

2016

Joshua Ryan Kim

ALL RIGHTS RESERVED

NaMn_{1.5+δ}Ni_{0.5-δ}O₄ SPINEL AS A HIGH-VOLTAGE POSITIVE ELECTRODE FOR SODIUM-ION
BATTERIES

by

JOSHUA RYAN KIM

A Dissertation submitted to the

Graduate School – New Brunswick

Rutgers, The State University of New Jersey

in partial fulfillment of the requirements

for the degree of

Doctor of Philosophy

Graduate Program in Materials Science and Engineering

Written under the direction of

Professor Glenn G. Amatucci

And approved by

New Brunswick, New Jersey

May 2016

ABSTRACT OF THE DISSERTATION

DELITHIATED $\text{LiMn}_{1.5+\delta}\text{Ni}_{0.5-\delta}\text{O}_4$ SPINEL AS A HIGH-VOLTAGE POSITIVE ELECTRODE FOR SODIUM-ION BATTERIES

By JOSHUA RYAN KIM

Dissertation Director:

Professor Glenn G. Amatucci

Sodium-ion batteries are an emerging technology aiming to significantly reduce the associated barriers of high performance batteries (high cost, and raw material abundance) in order to enable wide scale utilization of electrochemical energy storage devices. While being similar monovalent ions, Na^+ and Li^+ demonstrate considerably different characteristics when considering reversible ion-insertion materials, and it is of primary interest to ascertain whether or not analogous sodium chemistries can be derived from the well established lithium-ion compositions reported in literature.

A number of high-voltage cathode materials have been identified for Li-ion battery applications, and due to the intrinsic difference in standard redox potentials between Na/Na^+ and Li/Li^+ (*ca.* 0.3V), it is desirable to consider high-voltage sodium chemistries to overcome the inevitable lower voltages associated with sodium compositions. $\text{LiMn}_{1.5+\delta}\text{Ni}_{0.5-\delta}\text{O}_4$ spinel has been previously investigated for application in high performance Li-ion batteries, operating on a reversible redox reaction at *ca.* 4.7V vs. Li/Li^+ . Here, the spinel crystal structure provides a 3D-interconnected network of diffusional pathways, promoting facile Li^+ diffusion; and is considered for study in an analogous Na-ion battery as the combination of facile diffusional pathways and a high-voltage redox reaction (theoretically at *ca.* 4.4V vs. Na/Na^+) would act as a significant improvement in sodium energy storage cathodes.

Herein, $\text{LiMn}_{1.5+\delta}\text{Ni}_{0.5-\delta}\text{O}_4$ spinel is utilized to form the $\lambda\text{-Mn}_{1-x}\text{Ni}_x\text{O}_2$ ($\lambda\text{-MNO}$) structure by electrochemical delithiation. The resulting materials are then investigated as a positive electrode for sodium-ion batteries, as the spinel framework enables facile 3D-interdiffusion *via* vacant crystallographic

sites. Three profound conclusions may be derived from this work: (1) Na^+ insertion into the λ -MNO structure is possible, with Na^+ demonstrating almost exclusive occupancy of the 8a tetrahedral sites. (2) The Na^+ insertion reaction occurs at *ca.* 3.6V (vs. Na/Na^+), enabling direct replacement of existing commercial Li-ion cells. (3) Na^+ can be reversibly inserted / deinserted from the spinel host structure, with the possibility of further optimization.

Acknowledgement

I would like to thoroughly thank my thesis advisor, Dr. Glenn Amatucci, who has provided me with the unique and profound opportunity to advance my research interests in energy storage research over the passed years; for the countless hours and patience he has shown throughout my development, and the numerous lessons and situations he has thus prepared me for in the future.

Additionally, I would like to show my appreciation to my committee members: Dr. Lisa Klein, Dr. Richard Riman, and Dr. Martha Greenblatt, as they have contributed to my development over the years.

I would like to thank acknowledge Panasonic for provided financial support and funding for this project.

I would like to thank the various members of the Energy Storage Research Group (ESRG), who have acted as both a significant knowledge base and support for my endeavors over the years. Dr. Nathalie Periera has provided meaningful advice and guidance throughout my development as a researcher, taking the time to demonstrate and discuss vital techniques and topics to which I am very grateful.

I would like to thank the past graduate students: Dr. Kimberly Scott, Dr. Andrew Gmitter, Dr. Jonathon Ko, Dr. Anthony Ferrar, Dr. William Yourey, and Dr. Matthew Parkinson; current staff members: Mr. Barry Vanning, Mr. John Gural, Ms. Fadwa Badway, Ms. Irene Plitz, Ms. Linda Wu, and Ms. Anna Halajko; and fellow graduate students/classmates: Mr. Nick Faenza, and Mr. Daniel Kopp for contributing to my entire educational ezperience.

Dedication

I dedicate this work to my family, whom has provided me with unwavering support in all of my endeavors, whom have sacrificed so much throughout my upbringing, and whom continue to drive and inspire me.

1 Table of Contents

ACKNOWLEDGEMENT	IV
DEDICATION	V
LIST OF TABLES	IX
LIST OF FIGURES	XI
2 INTRODUCTION	1
2.1 BACKGROUND	2
2.1.1 ELECTROCHEMISTRY	2
2.2 AREAS OF FOCUS	48
3 EXPERIMENTAL TECHNIQUES	49
3.1 SYNTHESIS METHODS	49
3.2 CHARACTERIZATION TECHNIQUES	52
3.2.1 X-RAY DIFFRACTION (XRD)	52
3.2.2 FOURIER TRANSFORM INFRARED SPECTROSCOPY (FTIR)	61
3.2.3 BRUNAUER-EMMETT-TELLER (BET) SURFACE AREA	63
3.2.4 COULOMETRIC TITRATION TECHNIQUES	65
4 DELITHIATION OF LITHIUM SPINELS: Λ-$\text{Mn}_{1-x}\text{M}_x\text{O}_2$ STRUCTURE	69
4.1 INTRODUCTION	69
4.2 EXPERIMENTAL TECHNIQUES	69
4.3 RESULTS & DISCUSSION	71
4.4 CONCLUSION	76
5 Na^+ INSERTION INTO Λ-MO, Λ-MNOF, F Λ-MNO, AND P Λ-MNO	77
5.1 INTRODUCTION	77
5.2 EXPERIMENTAL CONSIDERATIONS	77
5.3 RESULTS	78
5.3.1 Na^+ INSERTION INTO Λ - MnO_2	78
5.3.2 Na^+ INSERTION INTO Λ -MNOF	81
5.3.3 Na^+ INSERTION INTO F Λ -MNO	94
5.3.4 Na^+ INSERTION INTO Λ - $\text{Mn}_{0.75}\text{Ni}_{0.25}\text{O}_2$ (P Λ -MNO)	111
6 Na^+ DEINSERTION, Na^+ REVERSIBILITY, AND REACTION MECHANISMS	125
6.1 INTRODUCTION	125
6.2 RESULTS	125
6.2.1 CONSTANT CURRENT / CONSTANT VOLTAGE CYCLING	125
6.2.2 Na^+ DE/INSERTION REACTION PATHWAY	129
6.2.3 POTENTIOSTATIC INTERMITTENT TITRATION TECHNIQUE	132
6.2.4 <i>Ex-SITU</i> X-RAY DIFFRACTION (XRD)	138

6.2.5	<i>OPERANDO</i> X-RAY DIFFRACTION (XRD)	143
6.3	DISCUSSION	161
6.4	CONCLUSION	163
7	$\text{Li}_{1-x}\text{Na}_x\text{Mn}_{2-y-z}\text{M}_y\text{Ni}_z\text{O}_4$ SPINEL SYNTHESIS	165
7.1	INTRODUCTION	165
7.2	EXPERIMENTAL METHODS	166
7.3	RESULTS	167
7.3.1	MATERIAL SYNTHESIS & CHARACTERIZATION	167
7.3.2	ELECTROCHEMICAL RESULTS: SYNTHESIZED SODIUM PHASES	178
7.4	DISCUSSION	181
7.5	CONCLUSION	183
8	FUTURE WORK	185
8.1	FUTURE WORK RELEVANT TO HIGH VOLTAGE ELECTRODE MATERIALS	185
8.2	FUTURE WORK RELEVANT TO HIGH-VOLTAGE SPINEL	185

List of Tables

Table 1-1: Representative sodium cells.....	18
Table 1-2: Electrolyte additives for lithium batteries	22
Table 1-3: Examples of commercially available ionic liquid compositions for sodium ion batteries.....	24
Table 1-4: Ordered phases of $P2-Na_xCoO_2$	37
Table 1-5: General NASICON chemical formula.....	40
Table 1-6: Overview of iron and vanadium polyanionic structures used in sodium batteries. Reformatted from Ref. ²⁸⁰	43
Table 4-1: Rietveld refinement on galvanostatically discharged electrodes	86
Table 4-2: Calculated diffusion coefficients of $F\lambda$ -MNO vs. Na/Na^+ PITT cells.....	107
Table 4-3: Calculated diffusion coefficients for the initial Na^+ insertion reaction into $P\lambda$ - MNO.....	114
Table 4-4: Calculated diffusion coefficients for $F\lambda$ -MNO and $P\lambda$ -MNO throughout the initial Na^+ insertion reaction	123
Table 5-1: Constant current, constant voltage protocol of $F\lambda$ -MNO and $P\lambda$ -MNO cells cycled using 1M $NaClO_4$ -PC:FEC2% electrolyte at 24°C	126
Table 5-2: Calculated diffusion coefficients for key Na^+ de/insertion reactions in FNa- MNO and PNa-MNO spinels	138
Table 5-3: Rietveld refined lattice parameters for FNa-MNO vs. Na/Na^+ cells. Reported (E/X) Na_x values are based off electrochemical and refined XRD data respectively.	141
Table 5-4: Rietveld refined lattice parameters for PNa-MNO vs. Na/Na^+ cells cycled at 3 mA/g, 50°C. Reported (E/X) Na_x values are based off electrochemical and refined XRD data respectively	143
Table 6-1: Transition metal cation radii from Ref. ³⁷⁵	166
Table 6-2: Multipoint BET surface area measurements of Zr-doped spinel compositions	172
Table 6-3: Comparison of Ti-doped $LiMn_{1.5-x}Ti_xNi_{0.5}O_4$ ($x = 0.1, 0.3, 0.5, 1.0, 1.3$) as compared against previous reports in literature	175

List of Figures

Figure 1-1: Schematic showing key components of an electrochemical cell (a) and the flow of electrons/ions throughout discharge (b) and charge (c) processes	3
Figure 1-2: Representative conductivity and viscosity values based on 1M NaClO ₄ electrolytes of co-blended inorganic solvents adapted from ref. ¹⁷⁹	21
Figure 1-3: Spider plot of select commercial Li-ion battery chemistries comparing common performance metrics between three select cathode compositions	26
Figure 1-4: Layered NaMO ₂ structures (M = Mn, Fe, Ni, Co) exhibiting trigonal prismatic Na-coordination (a-b) of the P2 and P3-type structures respectively, and octahedral coordination (c-d) for the O2 and O3-type structures respectively.	29
Figure 1-5: Voltage profile of O3-type NaCoO ₂ . Reproduced from ref. ²²⁰	30
Figure 1-6: Structural phase progression of NaCrO ₂ . Reproduced from Ref. ²³⁴	31
Figure 1-7: Chromium migration process during electrochemical Na ⁺ extraction. Reproduced from Ref ²³⁸	32
Figure 1-8: Typical voltage profile of Na _x VO ₂ in a sodium metal cell. Reproduced from Ref. ²⁴¹	33
Figure 1-9: Representative voltage profile of monoclinic O'3-NaNiO ₂ in a sodium metal cell. Reproduced from Ref. ²⁴⁶	35
Figure 1-10: Calculated reversible capacity and operating voltage comparison for layered sodium insertion materials reprinted from Ref. ²⁵¹	36
Figure 1-11: in-situ diffraction measurements of P2-Na _x CoO ₂ showing the phase progression of the (008) diffraction peak. Reproduced from Ref. ²⁷²	37

Figure 1-12: $\text{Na}_x\text{Mn}_y\text{O}_2$ structures for given Na/Mn ratios. Reformatted from Ref. ²⁷⁶	39
Figure 1-13: Comparison between NASICON and layered type cathode materials for sodium ion batteries. Reproduced from Ref. ²⁸¹	42
Figure 1-14: Crystal structure of NaCoF_3	44
Figure 1-15: LiMn_2O_4 normal spinel structure. Li and Mn ions are located on the centers of the tetrahedral (green) and octahedral (purple) sites respectively	45
Figure 1-16: Solid-state redox potentials (vs. Li/Li^+) estimated by slow-scan voltammetry for $\text{Li}[\text{Mn}_{1.5}\text{M}_{0.5}]\text{O}_4$ compositions. Reprinted from Ref. ²⁹⁷	47
Figure 2-1: Mechano-chemical synthesis schematic, demonstrating the different types of processes taking place during high-energy milling procedures	50
Figure 2-2: Generic material synthesis flow-diagram including solid-state synthesis ($a \rightarrow d \rightarrow e$), co-precipitation method ($a \rightarrow b \rightarrow c \rightarrow d \rightarrow e$), and Pechini synthesis ($a \rightarrow b \rightarrow c_2 \rightarrow d_2 \rightarrow e$)	52
Figure 2-3: Bragg-Brentano geometry used for a typical X-ray diffractometer. Reproduced from Ref. ³²²	53
Figure 2-4: Infrared spectra for $\text{LiMn}_{2-x}\text{Ni}_x\text{O}_4$ spinel annealed in air at 700°C . Reproduced from Ref. ³⁰⁶	62
Figure 2-5: Schematic of an <i>in-situ</i> transmission FTIR electrochemical cell. Reproduced from Ref. ³⁴⁷	63
Figure 2-6: core-shell model for phase transformation of a spherical particle illustrating the migrating species, original phase (alpha) and reaction products (beta) with a thin and sharp interface	68

Figure 3-1: CV scans for LMO, LMNOF, F-LMNO, and P-LMNO spinels vs. Li/Li ⁺ . Cyclic voltammetry scans are performed with a 1M LiPF ₆ -EC/DMC electrolyte within 3.0 – 5.0V at 24°C and 0.01 mV/s scan rate.	72
Figure 3-2: Transmission FTIR (Fourier Transform Infrared Spectroscopy) data of Fd-3m (dashed) and P4 ₃ 32 (solid) lithium spinels showing characteristic vibrational modes of Ni-O and Mn-O bonds.	73
Figure 3-3: Characteristic voltage profiles of lithium spinel positive electrodes with 1M LiPF ₆ -EC/DMC electrolyte at 24°C cycled with a 3 mA/g current.....	74
Figure 3-4: Powder X-ray Diffraction patterns of as prepared lithium spinel powders taken using Cu-K α incident radiation with a 0.02° step size and 1.5 second dwell time.	74
Figure 3-5: Electrochemical delithiation of F λ -MNO against a lithium and sodium metal anode in 1M NaClO ₄ -PC:FEC2% electrolyte at 24°C.....	75
Figure 3-6: Ex-situ XRD measurements on electrochemically delithiated spinel cathodes	76
Figure 4-1: Voltage profile of λ -MnO ₂ (λ -MO) with a 3mA/g discharge current at 24°C, 1M NaClO ₄ -PC:FEC2%.....	79
Figure 4-2: Voltage profile of Na-MnO ₂ showing the first cycle (red) and subsequent cycles (black) Cycled at 3 mA/g at 24°C, 1M NaClO ₄ -PC:FEC2%	80
Figure 4-3: Galvanostatically discharged sodium cells at 24°C, 1M NaClO ₄ -PC:FEC2% (a) and <i>ex-situ</i> XRD (b) measurements of λ -MNOF and C/100 discharged λ -MNOF	82

Figure 4-4: Spherical particle model of λ -MNOF spinel considering differences in grain boundary migration and Na^+ diffusion	83
Figure 4-5: combined <i>ex-situ</i> and <i>operando</i> XRD data for macrocrystalline λ -MNOF. <i>Ex-situ</i> data (a-b) was cycled at a C/10 rate at 24°C while <i>operando</i> XRD data was separately collected at a C/40 rate at 24°C, 1M NaClO_4 -PC:FEC2% (c-d)	87
Figure 4-6: Simplified core/shell model of discharged λ -MNOF cathode particle(s)	92
Figure 4-7: C/10 and C/100 discharge rates of Pechini derived $\text{F}\lambda$ -MNO spinel at 24°C, 1M NaClO_4 -PC:FEC2% (a) and <i>ex-situ</i> XRD of deconstructed cathodes (b)	94
Figure 4-8: Galvanostatic intermittent titration technique (GITT) of $\text{F}\lambda$ -MNO at 24°C with 1M NaClO_4 -PC:FEC2% electrolyte. First discharge (a) and subsequent charge/discharge voltage profiles (b).....	95
Figure 4-9: Voltage and specific current response of the sodium insertion of $\text{F}\lambda$ -MNO spinel utilizing a PITT protocol between 2 – 4.25V and a 0.25mA/g current cutoff with 1M NaClO_4 -PC:FEC 2% electrolyte at 24°C.....	97
Figure 4-10: Working and counter electrode voltages vs. a Na-metal reference electrode. $\text{F}\lambda$ -MNO cathode cycled at 24°C using 1M NaClO_4 PC:FEC2% electrolyte	98
Figure 4-11: <i>Ex-situ</i> XRD measurements throughout two-phase reaction region discharged at 3 mA/g, 24°C using 1M NaClO_4 -PC:FEC2%	99
Figure 4-12: C/60 <i>operando</i> XRD results of Na^+ insertion into $\text{F}\lambda$ -MNO spinel. Full XRD 2 θ range (a) and discharge profile cycled at 24°C, 1M NaClO_4 -PC:FEC2% electrolyte (b). Spinel diffraction peaks are labeled with their respective (<i>hkl</i>) Miller indices, and peaks marked by asterisks denote contributions from the aluminum current collector and beryllium window	102

Figure 4-13: Selected diffraction peaks from C/60 discharged F λ -MNO given in Figure 4-12 including the (111) (a), (311) (b) and (400) (c) spinel reflections and voltage profile (d). Dashed lines are provided as a guide to depict the onset in peak shift that occurs beyond the knee in the voltage profile. Diffraction patterns shown in red correlate to the knee in the voltage profile as shown by the red arrow of (d). Peaks marked by asterisks denote diffraction contributions from the current collector/beryllium window	105
Figure 4-14: Relative a-lattice parameter throughout Na ⁺ insertion into F λ -MNO spinel at 24°C, at 2.25mA/g	106
Figure 4-15: Voltage profile comparison between F-MNO vs. Li/Li ⁺ and F λ -MNO vs. Na/Na ⁺ with guidelines showing capacity contributions associated with the Mn ³⁺ /Mn ⁴⁺ redox	108
Figure 4-16: Discharge profiles of F λ -MNO and λ -MnO ₂ in Li-metal (dashed) and Na-metal cells (solid) respectively. λ -MnO ₂ vs. Na/Na ⁺ (a) F λ -MNO vs. Na/Na ⁺ (b), λ -MnO ₂ vs. Li/Li ⁺ (c), and F λ -MNO vs. Li/Li ⁺ (d) cells were discharged at a C/100 rate at 24°C using 1M NaClO ₄ -PC:FEC2% and 1M LiPF ₆ -EC/DMC electrolytes for sodium and lithium metal cells respectively	111
Figure 4-17: Voltage profile of PNa-MNO vs. Na/Na ⁺ . The first discharge/charge cycle (a) 5 th , 10 th , and 50 th cycles (b) are cycled at 3 mA/g at 24°C using 1M NaClO ₄ -PC:FEC2% electrolyte.	112
Figure 4-18: Potentiostatic intermittent titration technique (PITT) discharge/charge cycle for P λ -MNO vs. Na/Na ⁺ using 1M NaClO ₄ -PC:FEC2% at 24°C and a 0.25 mA/g current cutoff.....	113

Figure 4-19: Ex-situ XRD comparison between P λ -MNO and sodiated P λ -MNO using a 3.0 mA/g discharge current at 24°C with 1M NaClO ₄ -PC:FEC2% electrolyte. Note: XRD pattern of the PNa-MNO <i>ex-situ</i> sample observes a slight 2 θ shift relative to the P λ -MNO sample due to sample height displacement from the thickness of the cathode disk.	115
Figure 4-20: P λ -MNO (P4 ₃ 32) spinel discharged at 24°C and 3mA/g using 1M NaClO ₄ -PC:FEC2%. XRD scans are taken on a Δx interval of 0.02 in order to avoid significant peak broadening contributions. Dashed vertical lines are provided to illustrate the minor peak shift that occurs during single-phase Na ⁺ insertion, most clearly identified by the (511) and (440) Bragg reflections.....	119
Figure 4-21: Selected diffraction peaks from P λ -MNO vs. Na/Na ⁺ given in Figure 4-20 including the (111) (a), (311) (b) and (400) (c) spinel reflections and galvanostatically cycled voltage profile (d). Diffraction patterns shown in red correlate to the knee in the voltage profile as shown by the red arrow of (d). Peaks marked by asterisks denote diffraction contributions from the current collector/beryllium window.....	120
Figure 4-22: Relative lattice parameters of P λ -MNO vs. Na/Na ⁺ <i>in-operando</i> XRD data given in Figure 4-20. Lattice parameters are normalized according to the d-spacing of the P λ -MNO phase.....	121
Figure 5-1: Constant current/Constant voltage F λ -MNO and P λ -MNO vs. Na/Na ⁺ cells at 24°C, 1M NaClO ₄ -PC:FEC2%. Discharge capacities of F λ -MNO (a) and P λ -MNO (c) are given for cells using both a 2.0 and 2.5V lower potential cutoff, and a 1.0/2.0 mA/g constant voltage current cutoff as described in.....	128

Figure 5-2: Schematic reaction pathway of dis/ordered sodium spinel cathodes

constructed from a compilation of *ex-situ/operando* X-ray diffraction, and potentiostatic intermittent titration technique (PITT) data. Cells were held at open circuit in the fully discharged state for 10 hours, 24°C (a), discharged, and charged continuously at 24°C (b), and charged/discharged at 50°C (c). Red segments indicate two-phase regions, and black arrows indicate single-phase de/insertion mechanisms. Dashed arrows imply an additional 10 hour open circuit voltage (OCV) period imparted at the end of the first discharge. Schematic not drawn to scale. 131

Figure 5-3: Potentiostatic intermittent titration technique (PITT) of FNa-MNO vs. Na/Na⁺

during the first (a) and second (b) cycles within 2.0 - 4.25V followed by an additional high-voltage charge/discharge cycle (c) between 2.0 - 4.5V at 24°C, 1M NaClO₄-PC:FEC2%..... 134

Figure 5-4: Potentiostatic intermittent titration technique (PITT) charge/discharge PNa-MNO cathodes vs. Na/Na⁺ at 24°C using 0.25M NaBF₄-EC/DMC (a) 1M NaClO₄-PC (b) 1M NaClO₄-PC:FEC2% (c) and 1M NaClO₄-PC:FEC10% (d). FEC

electrolyte additives are based off volume percentages. PITT protocol consists of 10 mV potential steps with a 0.25 mA/g (active material) current cutoff. Labeled voltages correlate to non-Cottrellian current responses seen in the measured current response..... 135

Figure 5-5: Potentiostatic intermittent titration technique (PITT) of PNa-MNO vs. Na/Na⁺

during the first (a) and second (b) cycles. Cell was cycled at 24°C using 10 mV potential steps and a 0.25 mA/g current cutoff between 2.0 - 4.25 and 2.0 - 4.5V between (a) and (b) respectively with 1M NaClO₄-PC:FEC2% electrolyte..... 137

Figure 5-6: <i>Ex-situ</i> XRD of FNa-MNO cathodes cycled at 3 mA/g, 50°C using 1M NaClO ₄ -PC:FEC2% (a) and representative voltage profile (b)	140
Figure 5-7: <i>Ex-situ</i> XRD of PNa-MNO spinel cycled at 3 mA/g, 50°C using 1M NaClO ₄ -PC:FEC2%(a) and representative voltage profile (b).	142
Figure 5-8: Scaled intensity plot (a) and corresponding voltage profile (c) of <i>in-operando</i> XRD FNa _x -MNO within the first two cycles (2.0 – 4.25V) at 24°C, 1M NaClO ₄ -PC:FEC2%. Scaled intensity plot (b) and voltage profile (d) of high voltage charge/discharge cycle following relaxation at full discharge (4.5 – 2.0V) at 24°C. Bragg peaks are labeled at the top of (a-b) with asterisks marking aluminum and beryllium diffraction peaks from the in-situ cell. Dashed lines are added to regions pertaining to a single-phase reaction, and solid lines are oriented towards the product of the two-phase reaction. Lines M1 through M5 serve as guidelines with respect to the voltage profile. M3 and M5 indicate the onset of a two-phase reaction.....	146
Figure 5-9: <i>in-operando</i> XRD charge/discharge cycle of FNa-MNO vs. Na/Na ⁺ <i>in-situ</i> cell at 3 mA/g, 50°C, 1M NaClO ₄ -PC:FEC2% (a) and voltage profile (b) The FNa-MNO cathode was presodiated at 50°C in a coin cell prior to assembly in the <i>in-situ</i> electrochemical cell. Dashed arrow are provided marking the shift in diffraction peaks in accordance with the single-phase Na ⁺ de/insertion reaction, while solid arrows mark the abrupt peak shift described by a two-phase reaction. Markers M1 – M3 are provided to relate the two-phase reactions with the voltage profile.	149
Figure 5-10: Scaled intensity plot (a) and corresponding voltage profile (d) of <i>in-operando</i> XRD PNa-MNO vs. Na/Na ⁺ throughout the first two discharge/charge cycles at 3 mA/g, 24°C, 1M NaClO ₄ -PC:FEC2%, 2.0 – 4.25V. Scaled intensity plot	

(b - c) and corresponding voltage profile (e) of high voltage charge/discharge cycle 4.45 – 2.0V, 24°C at 3 mA/g. Peak intensities for the 311, 222, and 400 Bragg reflections are marked by (hkl) and $(hkl)'$ for the PNa-MNO and P λ -MNO phases respectively. Dashed lines are given to regions pertaining to a single-phase reaction, and solid lines are oriented towards the product of the two-phase reaction. Lines M1-M8 serve as guidelines with respect to the voltage profile. M1, M3, M4, M6, M7, and M8 indicate the onset of a two-phase reaction..... 153

Figure 5-11: Charge/discharge cycle *in-operando* XRD of PNa-MNO at 3mA/g, 50°C, 1M NaClO₄-PC:FEC2%. 2 θ range showing 311, 222, 400 peaks (a) and the 511 spinel peak (b) with the corresponding constant current voltage profile (c). Dashed lines are given to regions pertaining to a single-phase reaction, and solid lines are oriented towards the product of the two-phase reaction. Lines M1-M3 serve as guidelines with respect to the voltage profile. M1 and M2 mark the onset of a two-phase reaction..... 156

Figure 5-12: Combined *operando* XRD data for disordered (a - c) and ordered (d - f) sodium spinel cathodes under varying cycling conditions: continuous operation at 20°C (a + d), 10 hour open circuit (OCV) rest period following initial discharge at 20°C (b + e) and continuous operation at 50°C (c + f) all cycled at a current rate of 3mA/g with 1M NaClO₄-PC:FEC2% electrolyte. Vertical arrows mark the shift in relative lattice parameter of the various two-phase reactions taking place described by the (F/P)Na_x values reported. 160

Figure 5-13: Estimated mass-attenuation coefficients of λ -MNO and Na-MNO with respect to common X-ray diffractometer K α radiation sources..... 163

Figure 6-1: Powder X-ray diffraction data of a hexagonal layered sodium rich phase of nominal composition $\text{Na}_{0.67}\text{Ni}_{0.25}\text{Mn}_{0.75}\text{O}_2$ formed by solid-state synthesis at 900°C in air for 12 hours.....	168
Figure 6-2: Powder X-ray diffraction data for $\text{LiMn}_{1.5-x}\text{Zr}_x\text{Ni}_{0.5}\text{O}_4$ spinel samples ($x = 0.02, 0.04, 0.06, 0.08, 0.1, 0.2, 0.3$, and 0.4) for (a) - (h) respectively annealed at 500°C for 10 hours in air	170
Figure 6-3: Powder X-ray diffraction data for $\text{LiMn}_{1.5-x}\text{Zr}_x\text{Ni}_{0.5}\text{O}_4$ spinel samples ($x = 0.02, 0.04, 0.06, 0.08, 0.1, 0.2, 0.3$, and 0.4) for (a) - (h) respectively annealed at 700°C for 10 hours in air	170
Figure 6-4: Powder X-ray diffraction data for $\text{LiMn}_{1.5-x}\text{Zr}_x\text{Ni}_{0.5}\text{O}_4$ spinel samples ($x = 0.02, 0.04, 0.06, 0.08, 0.1, 0.2, 0.3$, and 0.4) for (a) - (h) respectively annealed at 800°C for 10 hours in air	171
Figure 6-5: Refined lattice parameters of $\text{LiMn}_{1.5-x}\text{Zr}_x\text{Ni}_{0.5}\text{O}_4$ ($x = 0.02, 0.04, 0.06, 0.08, 0.1, 0.2, 0.3, 0.4, 0.5$, and 0.6) samples across considered annealing temperatures	171
Figure 6-6: Powder X-ray diffraction data of sodium substituted $\text{Li}_{1-y}\text{Na}_y\text{Mn}_{1.44}\text{Zr}_{0.06}\text{Ni}_{0.5}\text{O}_4$ ($y = 0.1$ and 0.2) compositions (a) and (b) respectively. Arrows mark a sodium rich phase, and indexed peaks correlate to the lithium spinel. The vertical dashed line is provided to demonstrate no significant shift in peak positions as a function of increasing Na content.....	172
Figure 6-7: Powder X-ray diffraction data of titanium doped spinel samples of nominal composition $\text{LiMn}_{1.5-x}\text{Ti}_x\text{Ni}_{0.5}\text{O}_4$ ($x = 0.1, 0.3, 0.5, 1.0, 1.3$) for (a) – (e) respectively synthesized at 800°C in air	173

Figure 6-8: Powder XRD of $\text{Li}_{1-y}\text{Na}_y\text{Mn}_{0.5}\text{TiNi}_{0.5}\text{O}_4$ target compositions annealed at 800°C in air for 12 hours	176
Figure 6-9: Powder XRD of $\text{Li}_{1-y}\text{Na}_y\text{Mn}_{0.5}\text{TiNi}_{0.5}\text{O}_4$ target compositions annealed at 800°C under pure oxygen flow for 12 hours.....	176
Figure 6-10: Powder XRD of $\text{Li}_{1-y}\text{Na}_y\text{Mn}_{0.5}\text{Ti}_{1.3}\text{Ni}_{0.5}\text{O}_4$ target compositions annealed at 800°C in air for 12 hours	177
Figure 6-11: Powder XRD of $\text{Li}_{1-y}\text{Na}_y\text{Mn}_{0.5}\text{Ti}_{1.3}\text{Ni}_{0.5}\text{O}_4$ target compositions annealed at 800°C under pure oxygen flow for 12 hours.....	177
Figure 6-12: Voltage profile of $\text{LiMn}_{1.44}\text{Zr}_{0.06}\text{Ni}_{0.5}\text{O}_4$ spinel (500°C anneal) cycled at 3mA/g, using 1M LiPF_6 -EC/DMC electrolyte	178
Figure 6-13: Galvanostatically cycled λ - $\text{Zr}_{0.06}$ vs. Na/Na^+ using 1M NaClO_4 -PC:FEC2% at 24°C at 10 mA/g. 2.0 – 4.25V	179
Figure 6-14: Galvanostatic voltage profiles of $\text{LiMn}_{1.5-x}\text{Ti}_x\text{Ni}_{0.5}\text{O}_4$ ($x = 0.3, 0.5, 1.0$, and 1.3) compositions cycled at 10 mA/g at 24°C using 1M NaPF_6 -EC/DMC electrolyte	180
Figure 6-15: Galvanostatic voltage profile of electrochemically delithiated $\text{Mn}_{1.2}\text{Ti}_{0.3}\text{Ni}_{0.5}\text{O}_4$ cycled against a sodium metal anode using 1M NaClO_4 -PC:FEC2% electrolyte at 24°C, 10 mA/g	180
Figure 6-16: Galvanostatic voltage profiles of $\text{Li}_{1-y}\text{Na}_y\text{Mn}_{1.5-x}\text{Ti}_x\text{Ni}_{0.5}\text{O}_4$ ($x = 1.0$ (a), $x = 1.3$ (b); $y = 0.1, 0.5, 1.0$) compositions cycled at 10 mA/g at 24°C using 1M NaClO_4 -PC:FEC2% electrolyte.....	181

2 Introduction

The development of next generation energy storage technologies is essential towards meeting the growing energy demands of modern society. Conventional modes of power generation are largely based on combustion of fossil fuels, making power production a relatively straightforward process as decades of research and developments surrounding fossil fueled engines/turbines have yielded considerable improvements in terms of efficiency and ‘clean’ emissions. The problem however, comes with respect to providing uninterrupted electrical power throughout the entire electrical grid. As demand for electricity is by no means a known or constant value, generally resulting in one or more peak loads on the electrical grid throughout a given day; forcing utility companies to periodically startup and shutdown ‘peaker’ plants in order to meet the increased load on the system. This has proven to be the most efficient system based off current infrastructure, as continuous operation at peak loads results in excessive/wasted energy and raw materials, as only high output is needed during certain portions of the day. This problem becomes further exacerbated as phasing in of renewable energy sources such as wind/solar occurs; where only intermittent power production prompts a huge need for reliable and cost efficient energy storage technologies.

Over the passed decades, energy storage methodologies have significantly diversified, offering a range of suitable energy storage strategies including pumped hydro, compressed gas, and flywheel energy storage, all of which utilize stored mechanical energy for conversion into electrical energy.¹⁻⁸ However, it is desirable to utilize electrochemical storage devices, as they can be implemented as stand-alone storage solutions; not requiring servicing or serious maintenance due to the lack of moving parts/need of a human operator.

Simple electrochemical storage devices have been around for hundreds of years, however, recent societal advances including mobile electronics and electric vehicles have spurred a drastic increase in research activity, producing highly engineered devices designed for optimal lifetime and performance. Electrochemical cells are often constructed in series or parallel to produce an overall battery of suitable operating voltage and output current for the given application.

In order to meet the growing demand for electrochemical energy storage, it is crucial to develop high-performance batteries that are economically competitive with traditional fossil fuels. While lithium-ion

batteries have found many applications ranging from mobile electronics to electric vehicles, sodium-ion batteries are of primary interest for large-scale applications due to the huge economic benefits in switching to a sodium-based chemistry as shown by the large discrepancy between costs of raw materials ($\text{Na}_2\text{CO}_3 = 0.07\text{-}0.37 \text{ \$/kg}$; $\text{Li}_2\text{CO}_3 = 4.11\text{-}4.49 \text{ \$/kg}$).^{9,10} The following sections of this chapter consider in greater depth, the working principles behind electrochemical devices, and key examples throughout existing literature of novel chemistries being developed for sodium-ion batteries.

2.1 Background

2.1.1 Electrochemistry

Electrochemistry is a term that encompasses all phenomena that relate chemical change to an electric potential, electric forces produced by a chemical process, and so on. Generally speaking, electrochemical cells are complex devices, designed to convert chemical energy into electrical energy *via* an oxidation and reduction reaction. In practice, this generally requires very careful environmental controls; as to ensure that undesired side-reactions do not compete with the primary cell chemistry.

Four main components are of particular importance for electrochemical cells. They are:

- (1) The positive electrode (cathode)
- (2) The negative electrode (anode)
- (3) The electrolyte
- (4) The separator

A typical sandwich battery structure is shown schematically in Figure 2-1. Here, and throughout the following chapters, discharge is defined as the flow of electrons through the external circuit (L) from the anode to the cathode, and charge is defined as the flow of electrons through the external circuit from the cathode to the anode as shown by Figure 2-1b-c respectively. As such, the anode and cathode undergo reduction/oxidation reactions in accordance with the direction of electron flow.

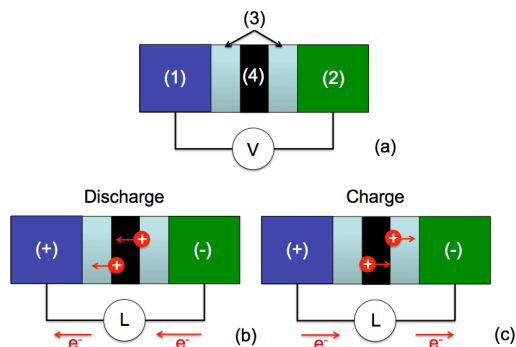


Figure 2-1: Schematic showing key components of an electrochemical cell (a) and the flow of electrons/ions throughout discharge (b) and charge (c) processes

The voltage of an electrochemical cell can be visualized as the driving force behind the intrinsic redox reaction; being determined by the composition of the positive and negative electrodes, or more specifically, the differences in chemical potentials between the two electrodes. As mentioned earlier, each electrode undergoes reduction/oxidation (redox) reactions depending on the direction of electron flow in what are known by convention as ‘half-cell’ reactions. Since only relative potential differences can be measured, half-cell potentials are by convention, established relative to a standard electrode under normal conditions (the standard hydrogen electrode (SHE) and with all electroactive species assuming unity activity). The overall equilibrium voltage between the two electrodes is then determined by the difference in half-cell potentials, or by consideration of the chemical activity of the electroactive species through the Nernst equation. The equilibrium cell potential (E°_{cell}) is related to the standard potential (E°) expressed in terms of chemical activity and concentration where $a_i = \gamma_i c_i$:

Equation 2-1:
$$E^\circ_{\text{cell}} = E^\circ - \frac{RT}{nF} \sum v_i \ln a_i = E^\circ - \frac{RT}{nF} \sum v_i \ln c_i$$

The overall Gibb’s free energy (Equation 2-3) of the electrochemical cell is thus related to the standard cell potential by combination of Equation 2-1 and Equation 2-2. A positive cell potential describes a galvanic cell, which correlates to a negative value of the Gibbs free energy, and thus meaning that a quantifiable amount of work can be extracted from the system. A negative cell potential denotes an electrolytic cell, where the positive Gibbs free energy describes the amount of energy required to drive the described electrochemical reaction.

Equation 2-2:
$$E^\circ_{\text{Cell}} = E^\circ_{\text{Cathode}} - E^\circ_{\text{Anode}}$$

Equation 2-3:
$$\Delta G^\circ = -nFE^\circ_{\text{Cell}}$$

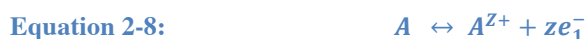
From this relationship, it is clear that simple measurements on the thermodynamics of an electrochemical cell can be made with little effort; and likewise, we can drive specified reactions in a controllable manner provided that no unprecedented electrochemical processes are taking place (*e.g.* contaminants, moisture, etc). It is also important to note that these relationships only hold at equilibrium conditions, and are highly dependent on the electrode surface and specific medium of the electrochemical cell; as is evident by the logarithmic relationship to the activity coefficient.

Simple measurement of the Gibbs free energy of the galvanic/electrolytic cell is possible given that we can describe the overall reaction in terms of its half-cell reaction. Below is an example for the formation of HCl from H₂ gas and Cl₂ gas:



The described reactions result in a potential difference between the two electrodes that is related to the driving force of the net reaction. Here, high voltage electrode materials offer a considerable benefit, as they are inherently more suitable for high power applications; requiring fewer individual cells linked in series that may further complicate devices through advanced battery management systems. However, this is often nontrivial in nature, as high-voltage materials must still operate within the electrochemical window of the electrolyte; a topic that will be touched upon in future chapters.

Considering the electrochemical activity at the interface, which will be used to describe the region of separation between the electrolyte and the electrode surface, the electrochemical processes can be described by Equation 2-8 to Equation 2-10. ‘A’ denotes the migrating ion in the electrode, A^{Z+} the migrating ion in the electrolyte, z is the number of electrons involved in the redox process, μ is the chemical potential, and φ describes the galvanic potential.^{11,12}



Equation 2-9: $\Delta\tilde{\mu}_i = \tilde{\mu}_{2,i} + \tilde{\mu}_{1,i} = \mu_{2,i} + \mu_{1,i} + z_i F(\phi_2 - \phi_1)$

Equation 2-10:

$$\mu_{1,A}^{\circ} = \mu_{2,A^{z+}}^{\circ} + RT \ln \left(\frac{a_{A^{z+}}}{a_{A^{z+}}^{\circ}} \right) + z\mu_{1,Ae-}^{\circ} + zF(\phi_2 - \phi_1)$$

These relations make the important distinction that the chemical potential, and thus the cell voltage are directly dependent on the electrode surface, and its ability to accept and donate the migrating species 'A'. Additionally, the act of applying or drawing a load from the electrochemical cell places it beyond equilibrium, making measurements between the anode and cathode significantly less meaningful. There are however, ways in which to overcome these shortcomings; the most common being to employ an additional third electrode to act as a reference. And since no load is applied/drawn between the reference electrode and the anode/cathode, its potential remains constant, allowing the user to measure the potential of either electrode relative to the reference with added accuracy. The third electrode, or reference electrode (E_{ref}) is situated in close proximity to the working electrode as to minimize polarization of the electrolyte.

Electrochemical cells involve a concerted interaction between a multitude of materials: active materials, binders, conductive additives, electrolyte salt/solvent/additives, cell casing, etc. All of which require careful consideration during assembly/fabrication, as certain materials may not suit the electrochemical window in which the cell will be operating at, often resulting in material breakdown or unwanted corrosion. Since the cell voltage, and ultimately the cell capacity, are characteristic of the specific chemistry of the electrodes, electrochemical cells are generally tailored to a specific application based on metrics such as cost, reliability, and energy density.

While certain applications such as mobile electronics and electric vehicles target high energy density, these types of compounds often reflect a high cost and environmental impact, making them unattractive for wide-scale usage. Commercial high-performance electrochemical cells used today utilize lithium-based compositions, taking advantage of the small ionic size of Li^+ ; as well as its high specific, and high gravimetric capacities. Although these types of energy storage devices have proven to be well suited to the mobile, and even automotive applications, concerns surrounding the abundance and geographic scarcity of raw materials have thus motivated additional research interested into sodium batteries.

Sodium ion batteries are of principle interest for large scale energy storage needs, as sodium precursors are both significantly more abundant and cheaper than lithium alternatives; making them an ideal candidate to meet grid-level storage needs for alternative energy power supplies such as wind and solar;¹³⁻²⁰ Such is the motivation for this work; the following sections are aimed to establish the well-

studied Li-ion industry in order to draw meaningful analogues/strategies toward optimization of sodium-ion batteries.

2.1.1.1 *Lithium batteries*

Lithium-ion batteries (LIBs) operate on the same basic electrochemical principles mentioned thus far, however, in contrast to the simplified case of metal electrodes, the chemical potential of the respective electrodes is constantly changing as Li^+ is reversibly inserted and deinserted into both the anode and cathode. It is worth discerning the differences between lithium-ion, and lithium-metal cells, as the two are used almost exclusively throughout commercial and research settings respectively. The term lithium-ion is used to identify electrochemical cells whose lithium content solely exists in the ionic state eliminating some of the safety concerns around active lithium metal. Lithium-metal cells are commonplace throughout the majority of research, as they provide a stable voltage, (-3.01 V vs. SHE) as opposed to graphite or other carbonaceous electrodes typically used in Li-ion cells, whose potentials deviate in accordance to the degree of lithiation.

While the lithium metal anode offers a very favorable standard reduction potential, the high reactivity of lithium metal with ambient oxygen and moisture is a primary safety concern, and thus commercial lithium-ion chemistries aim to keep all lithium in its ionic state, thereby greatly reducing the chance of a lithium-related fire in the event of a cell puncture/leak. There however, is still concern related to the inherent flammability of the inorganic solvents used in conventional inorganic electrolytes, motivating additional advances in low vapor pressure electrolytes, and solid-state electrolytes that will be touched upon in future sections.

While a large number of electrochemically active materials have been identified, the majority of Li-ion research can be identified by four main categories:

- (1) Insertion electrode materials^{21–30}
 - a. *e.g.* LiCoO_2 , LiMn_2O_4 , LiFePO_4 , Graphite, etc.
- (2) Conversion electrode materials^{31–36}
 - a. *e.g.* Li-S , CuF_2 , FeF_2
- (3) Alloying electrode materials
 - a. *e.g.* Li-Si , Li-Al , Li-Zn , etc.

(4) Lithium-air/hybrid fuel cells³⁷⁻⁴⁶

Insertion/intercalation compounds generally consist of an electrochemically active species (generally a transition metal cation) dispersed throughout an ordered array, or crystal lattice that has empty sites capable of accommodating the migrating ion species during the reduction/oxidation reaction. In this sense, the migrating ion species is inserted or intercalated onto the vacant sites of the host structure of the electrode, placing a high level of dependence on the types of structures used in electrode compositions; specifically the size, number, and level of inter-connectivity of the vacant sites within the host structure.

Conversion electrodes involve a phase transformation reaction; requiring nucleation and growth of a chemically (and usually structurally) different phase than the originating electrode material(s).

Conversion based chemistries generally utilize a nanocomposite structure, typically formed by high-energy milling processes generating an intimate mixture of the active species and an electronically conductive additive. Conductive additives are generally required for conversion materials, as they are for the most part, electronically insulating or intrinsically very poor conductors such that additives are required in order to achieve reasonable performance. Compared to insertion/intercalation compounds, the redox reaction occurs at the particle surface, converting the starting material into a completely different phase, (of either different chemical or structural identity). Formation of the nanocomposite further aids in the cell performance, as a greater surface area is able to react at a given time, making it possible to engineer high rate capability into these types of cells. Conversion materials have garnered a large amount of attention over the years as the redox reaction utilizes the full range of oxidation states (of the electroactive species) is utilized. Producing more electrons per electroactive species, and thereby a higher capacity when compared against typical insertion/intercalation materials.

Alloying electrodes are similar to conversion type materials, as one or more phase-transformation reactions are typically involved. However, they can be differentiated by the fact that they are limited to generally elemental compositions (Al, Zn, Si, Sn)⁴⁷⁻⁴⁹ that share a solid-solubility with Li. Such electrodes generally exhibit high theoretical capacities, but are largely limited by the large volumetric changes that occur; resulting in eventual cell failure as will be discussed in the following sections.

Lastly, lithium-air and similar hybrid fuel cell type electrochemical cells have been of considerable interest throughout the energy storage community as they are generally capable of delivering

5-10 times greater specific energy (~3500 Wh/kg) as compared to conventional transition metal oxide compositions. Lithium-air cells are typically constructed with a porous carbon cathode, and lithium metal anode, with the redox reaction being driven by the supply of ambient air (oxygen); shown by any one of the possible oxygen reduction reactions describing the primary discharge reaction.



The reverse reaction, involves the decomposition of Li_2O_2 to Li and O_2 during charge:



And while both aqueous and non-aqueous electrolytes have been reported,^{37,42,44} serious considerations of Li-air batteries for automotive and other high-performance applications favor non-aqueous compositions due to the need for precious metal catalysts in aqueous systems. The main drawback from these cell chemistries however become the overall cell lifetime, often suffering from a number of different failure modes that arise from the dendritic nature of metallic lithium.

2.1.1.2 Sodium Batteries

Falling directly beneath lithium in the periodic table, sodium can be expected to exhibit similar behavior, and thus, it is anticipated that considerable similarities may exist between Li and Na battery materials. However, differences in ionic size and charge density introduce various complications, making the application of the existing knowledge base regarding LIBs a non-trivial effort, as certain chemistries and crystal structures are physically incapable of accommodating the high volumetric strains associated with Na^+ de/insertion processes. Furthermore, Ong *et al.* have examined the specific voltage and diffusion barrier differences between Li/Na de/insertion into select layered, olivine, maricite and NASICON structures,⁵⁰ demonstrating large drops in reaction voltages attributed predominantly to effects occurring within the cathode material itself, while also exhibiting high dependence on the specific host structure(s) used.

As mentioned previously, sodium-ion batteries have attracted considerable attention as of late due to the rising need for reliable and cost effective energy storage solutions. Sodium-ion batteries offer a range of key benefits that enable them to be a direct replacement for existing lithium-ion technology. They are:

- (1) Na-ion materials have lower material costs than Li-ion counterparts
 - a. Sodium carbonate is < 10% the cost of lithium carbonate
 - b. Cathode and electrolyte costs can account for *ca.* 50% of cell costs
- (2) Sodium is more abundant in the Earth's crust (Na ~ 2.6% vs. Li ~ 0.005%) and is not geographically sparse
- (3) Na-ion materials can leverage existing infrastructure/fabrication techniques for Li-ion materials
- (4) Current collectors may utilize aluminum rather than copper as is used in Li-ion cells

As a whole, sodium batteries are of considerable interest for utilization in large-scale energy storage systems due to the inherent reduction in volumetric/gravimetric capacities when comparing against existing lithium technology. Here, sodium batteries intrinsically suffer from lower capacity metrics in comparison to lithium based chemistries due to the differences in their respective molar masses/densities. And while high performance sodium batteries may eventually replace commercial Li-ion cells, the majority of attention is being directed towards large-scale energy storage solutions that hinge on cost analyses.

Developed in the early 1960's, sodium sulfur batteries emerged as an incredibly simple battery chemistry utilizing elemental sodium and sulfur electrodes with a solid β'' - Al_2O_3 electrolyte. The unique use of a ceramic electrolyte makes it necessary to maintain the cell between 280°C – 350°C in order to facilitate high Na^+ diffusivity through the solid electrolyte, while maintaining both electrodes in a molten state. While these considerations place additional engineering considerations into the various methods/techniques of temperature regulation/insulation of an overall sodium-sulfur cell, they have been demonstrated to be exceedingly resilient against a number of failure scenarios including external short circuits, fire, and flooding damage protection.⁵¹ Cells of this type are highly competitive in terms of their coulombic efficiency (~100%) and service life, demonstrating excellent capacity retention beyond 5000 cycles, making this an attractive technology for large scale energy storage solutions. In fact, further development of sodium-sulfur batteries have widely focused on the implementation of room-temperature

sodium-sulfur batteries (RT Na-S), potentially opening up this cell chemistry for additional commercial/consumer type applications.^{52,53}

Additional work into molten sodium cell chemistries by the Zeolite Battery Research Africa Project (ZEBRA) group, has identified a similar chemistry. In the charged state, the negative electrode consists of molten sodium metal, and the positive electrode is a molten Ni/NiCl mixture. An additional molten salt eutectic NaCl/AlCl₃ is used to promote transport of Na⁺ from the positive electrode to the β"-alumina separator as shown by the equations listed below.



Further emphasizing the potential applications of ZEBRA batteries, the cell can be assembled in the discharged state, using only Ni and NaCl as starting materials. Additions of aluminum and iron sulfide further improve the performance of the cell, as they protect against sudden polarization of the cell and to intentionally poison the surface of the nickel particles such to prevent Ni deposition and particle growth throughout subsequent cycles respectively.⁵⁴



While ZEBRA batteries and similar molten electrode cells offer high capacities and excellent lifetime metrics, they require temperatures in excess of 150°C to maintain the molten state of the electrodes, requiring additional cell design to accommodate heating elements and insulating jackets, etc. Such illustrates the need for high performance sodium-ion cells operating at room temperature. The following subsections consider the various components and structures used for solid-state electrodes for sodium batteries, while drawing specific correlations and comparisons between analogous lithium compositions where applicable.

2.1.1.2.1 Negative Electrodes

Design and development of suitable negative electrodes is centered around several ideal properties:

- (1) Low redox voltage, such that the calculated full cell potential (Equation 2-2) is a maximum.
- (2) High capacity, *i.e.* accommodation of a large number of sodium ions.
- (3) High reversibility and stability.
- (4) Low cost.
- (5) Low volumetric change during cycling.

In practice, optimization of overall anode properties considers a combined sum of these main concerns, with special emphasis placed on certain aspects according to the intended application.

Generally speaking, motivations for Li-ion and Na-ion cells are centered around the reactivity of lithium and sodium metal anodes, with the latter being considerably more reactive, giving rise to a number of safety concerns surrounding cells using sodium metal anodes. While it is convenient to utilize sodium metal electrodes for laboratory scale measurements development of a high performance Na-ion anode material is necessary to enable the safe operation of commercial large format cells. Here, the use of an insertion material ensures that sodium metal may not be exposed to ambient air/moisture in the event of a cell rupture/leak.

2.1.1.2.1.1 Carbon Anodes

Carbonaceous materials are utilized for low cost/high capacity anodes across a variety of battery chemistries including alkaline cells, and advanced lithium-ion batteries. Containing a number of unique chemical properties, there are a considerably large number of carbon allotropes worthy of investigation for anode applications.

Graphitic materials, consisting of coherent graphene layers, have demonstrated certain limitations in specific capacity regarding Na⁺ de/insertion processes. Early reports by Doeff *et al.* consider sodium insertion properties of carbonaceous anodes derived from common crude carbon sources (petroleum coke, Shawinigan black, and microcrystalline graphite) demonstrating a significant dependence on the specific electrolyte(s) used and specific microstructure of the active material(s).⁵⁵ In fact, the extent of sodium

insertion was found to be drastically lower than that of lithium, producing approximate compositions *ca.* NaC₃₀, NaC₁₅ and NaC₇₀ for petroleum coke, Shawinigan black, and graphite derived anodes respectively.

The relatively poor performance of graphite is somewhat surprising, as complexes for lithium are commonly reported to *ca.* LiC₆,^{56–58} indicating that the physical size differences between Li⁺ and Na⁺ offer considerable challenges to designing suitable sodium ion insertion materials. *In-situ* Raman and *ex-situ/in-situ* X-ray Diffraction offers additional insight into the structural evolution of graphite under Na⁺ de/insertion, resembling the electrochemical features in LIBs,^{59–61} and suggests an additional intercalation of solvated sodium complexes in the presence of linear ether-based electrolytes, leading to exfoliation and degradation of the graphite electrode.

Additionally, Zhu *et al.* propose that Na⁺ insertion begins by a high-stage (n>2)* intermediate compound (NaC_x) followed by successively lower order intermediates (NaC_x) resulting in the transition from a flat voltage plateau to various sloping regions, indicating substantial energy differences between the different graphite intercalation compounds (GICs).⁶² Due to size restrictions surrounding the interlayer spacing (*ca.* 3.4Å) of graphite, additional modifications of the structure of graphite anodes have proven to enable significantly higher specific capacities by nature of the expanded interlayer structure, enabling facile Na⁺ intercalation. In fact, hard-carbon (non-graphitizable carbon) has demonstrated further advantages over traditional graphite anodes, demonstrating upwards of 220 mAh/g.⁶³ Hard-carbons such as these however, have demonstrated severe electrolyte degradation against common ethylene carbonate (EC) and propylene carbonate (PC) based electrolytes, requiring careful modification of the electrode interface by suitable electrolyte additives. While vinylene carbonate (VC) has been demonstrated to suitably passivate the electrode interface in analogous lithium cells, VC has been shown to exhibit deleterious effects on the Na⁺ insertion into hard-carbon electrodes. Further comments are provided in section 2.1.1.2.2.

More recent works^{64–67} have demonstrated the enhanced capability of porous carbon anodes derived from organic precursors for sodium ion storage. Introduction of nanoporosity coupled with high defect densities within graphene layers has since brought carbonaceous sodium anodes back into focus, exhibiting reversible capacities in excess of 300 mAh/g throughout the first 1000 cycles.

* Stage order (n) refers to the number of graphene layers between Na⁺ intercalation layers

Furthermore, graphene nanosheets (3-4 layers) are an interesting subcategory of graphitic anodes, introducing significantly higher surface areas and similar bulk characteristics to graphitic anodes. Capacities up to 220-260 mAh/g have been reported^{68,69} within the 0.01 – 2.0V potential range vs. Na with two main Na⁺ storage mechanisms being identified: (1) electro-adsorption/desorption and (2) bulk de/insertion. Limited by their insufficient d-spacing to accommodate Na⁺ de/insertion, carbon nanotubes and mesocarbon microbeads (MCMB) have not demonstrated as much utility toward Na⁺ storage. However, considerable improvement has been noted in pyrolyzed hollow carbon nanowires; exhibiting excellent cycling stability over 400 cycles and high reversible capacities *ca.* 250mAh/g.⁷⁰

Graphite derivatives have commanded considerable attention over the passed few years and have prompted the development of expanded graphite structures in order to overcome the shortcomings of traditional graphitic materials. Taking a computational approach, Kang *et al.* investigated the de/sodiation properties of expanded graphite structures considering both epoxide and hydroxide functional groups, discovering considerably greater performance across modified graphite oxides using epoxide functional groups, arising from strong interaction energies between Na⁺ and the respective functional group(s).⁷¹ Similar structural modifications can be achieved by introduction of covalently bonded sulfur. Sulfur bonded graphene (3-4 layers) has demonstrated 0.13Å increase in interlayer distance with respect to that of graphite, providing improved cycling performance and high capacity (291 mAh/g) corresponding to an NaC_{7.7} intercalation product; remarkably close to the LiC₆ compositional limit for Li-ion batteries.⁷²

2.1.1.2.1.2 Sodium alloys: Group-14 Na Anodes (Si, Sn, Pb)

Relative to carbonaceous materials, silicon is an attractive alternative anode material for LIBs (4200 mAh/g theoretical capacity) due to its high theoretical capacity. However, due to the large volumetric changes that occur during reversible Li⁺ de/insertion, implementation of Si based anodes has been largely inhibited. Although considerable difficulty surrounding reversible Na⁺ de/insertion into analogous sodium structures has proven to be largely limited by the significant differences in ionic sizes between Li⁺ and Na⁺, comparative examination of the insertion energetics of Li/Na/Mg into crystalline and amorphous silicon demonstrate the reduced volumetric changes and more-favorable insertion processes of amorphous silicon anodes for SIBs.^{73–75} However, more recent experimental considerations^{76,77} have demonstrated the relative inactivity of silicon for SIB anode applications, likely limited by poor reaction kinetics at ambient and even

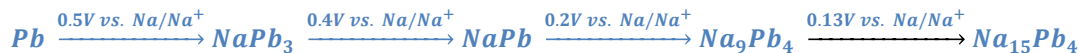
elevated (60°C) temperatures. Despite some of this controversy, focus towards alloy-based anode materials for SIBs has been largely devoted to Si, due to the considerably low volumetric expansion when compared against other alloy anode compositions based on Ge, Sn, and Sb. Shimizu *et al.* have demonstrated electrochemical activity of SiO thick film electrodes, producing initial capacities *ca.* 200 mAh/g.⁷⁸ In fact, finely dispersed Si within SiO₄ matrix has demonstrated high activity of Si compared to bulk Si anodes, demonstrating potential routes for future utilization of silicon-based anodes for SIBs.

Likewise, tin-based compounds have been shown to form solid-solutions with lithium and sodium, making them potential high capacity anodes for SIBs.^{79–81} Due to similar investigations for lithium anodes, metallic Sn have shown equal promise for anode materials, and initial DFT calculations have predicted several phase transitions including NaSn₅, NaSn, and Na₉Sn₄.⁸² before reaching a theoretical capacity of 847 mAh/g (Na₁₅Sn₄). However, much like the analogous Li-Sn anodes, failure mechanisms surrounding the large volumetric changes during the de/sodiation process (upwards of 420%) result in pulverization of the active material, leading to extensive degradation in electrode quality.^{83,84} Suitable nanocomposites/nanostructuring has, and may continue to improve the capacity retention of metallic Sn-based anodes. However, the enormous volumetric expansion during cycling has largely limited the practical implementation of metallic Sn anodes.

Alloying of Sn with additional sodium-active elements provides a potential route for utilization of Sn-based compositions without significantly sacrificing the intrinsically high discharge capacity. As such, group IV-VI Sn alloys,^{85,86} oxides⁸⁷, and similar intermetallic compounds^{88,89} have been investigated as potential anode materials for SIBs. While electrochemical properties of Sn-Ge lithium anode alloys^{90–92} are not fully understood, studies of Sn-Ge electrodes produced by glancing angle deposition have demonstrated the increased performance benefits of nanostructured thin films,⁸⁶ with investigations into tin oxide compounds^{83,87,93,94} demonstrating superior performance of SnO over SnO₂ and SnO₂/C composites attributable to vast differences in electrical conductivity. As a whole, active/inactive intermetallics/composites are widely used as a buffering matrix to accommodate the large volumetric strains that arise under normal operating conditions. Dispersion of Sn within metallic Cu₆Sn₅ and Cu₆Sn₅-TiC-C composites have demonstrated excellent rate capability and reversible capacities up to ~400 mAh/g, providing a suitable pathway towards optimization of Sn-based compounds.^{88,95}

Lead (Pb) has also been investigated as a potential alloying electrode material, with sputtered/composite lead electrodes exhibiting four distinct voltage plateaus⁹⁶ reaching full capacity (485mAh/g; Na₁₅Pb₄) as demonstrated by Ellis *et al.*⁷⁷ An overall phase progression is described as:

Equation 2-19:



The large Na:Pb ratio in the final alloy identifies a high intrinsic Na storage capability of Pb electrodes. However, due to catalytic electrolyte decomposition that has been documented on pure Pb surfaces, it is necessary to design a suitable protective layer to prevent cell degradation. It has been proposed that maintaining the Pb electrode in a sodiated state may limit the amount of catalytic decompositions, with additional utilization of suitable SEI additives exhibiting considerable improvements over the bare Pb surfaces.⁹⁶ Additional investigations into a number of M(NO₃)₂ structures has identified electrochemical activity of Pb(NO₃)₂/Carbon composites within lithium metal cells demonstrating a high reversible capacity of >450mAh/g and 82.9% capacity retention at 50 mA/g after 45 cycles.^{97–99} While no known reports on utilization of Pb(NO₃)₂ in analogous sodium cells exist, it is expected that similar electrochemical activity exists, potentially offering an alternative to the pure Pb electrodes while still maintaining nearly equal capacity.

2.1.1.2.1.3 Sodium alloys: Group-15 Na anodes (P, As, Sb, Bi)

In addition to the aforementioned compounds, group-15 elements (P, As, Sb, Bi) also form alloying compositions with sodium. Particularly advantageous over some of the group-14 electrodes, various group-15 elements have demonstrated considerable elastic softening (upwards of 60%) during sodiation, acting to mitigate the pulverization process that most group-14 compounds demonstrate.¹⁰⁰ Variation in the Young's and shear moduli of Na-P, Na-As, and Na-Sb phases arise primarily from the elastic anisotropy of their respective monoclinic crystal structures, producing 40-60% elastic softening at full sodiation. Changes in the intrinsic mechanical properties of group-15 sodium compounds are still notably improved over those of similar group-14 compounds,¹⁰¹ indicating that suitable optimization with buffering elements/composites can offer further improvements in reversibility and capacity retention. Such has already been demonstrated by investigations into Sb-C, NiSb, and FeSb₂ composites.^{102–106}

Multiple reports^{100,107–109} have demonstrated the improved capacity retention of Bi and Bi-based compounds due to minimal changes in mechanical behavior as a function of sodiation. However, observations by *ex-situ* XRD and DFT calculations imply the Na⁺ storage mechanism occurs by an intercalation process (by nature of the large 003 interlayer spacing of 3.95Å) rather than the formation of alloying compounds¹⁰⁷ suggesting minimal nanostructuring necessary to achieve high reversible capacities.

2.1.1.2.1.4 Oxides (Anodes)

Several layered and 3D-interconnected oxide structures have been identified as potential high performance sodium anodes. Lithium titanate (LTO) spinels have been widely investigated for lithium anodes, demonstrating excellent cycling stability attributable to the optimal diffusional pathways and structural stability of the spinel framework.¹¹⁰ Additionally, sodiated titanium oxides form a variety known layered structures demonstrating relatively stable storage capacities of 93-112 mAh/g at high rates up to 5C, making a compelling case for its implementation as an advanced anode material (Na₂Ti₃O₇, Na_{0.66}[Li_{0.22}Ti_{0.78}]O₂, and Na₂Ti₃O₇-C composites).^{111,112}

Stemming from the multiple polymorphs of TiO₂, several sodium de/insertion mechanisms have been proposed. Wu *et al.* have demonstrated the partial reduction to metallic Ti, Na₂O, and amorphous sodium titanate by a conversion type reaction,¹¹³ along with considerably different electrochemical features as compared to Li⁺ de/insertion.¹¹⁴ Similar TiO₂ bronze structures have shown electrochemical activity,¹¹⁵ but with considerably poor capacity retention within the first 100 cycles. Separate studies on TiO₂ nanorods/tubes have demonstrated improved capacity retention, and reversibility,¹¹⁶ with improvement in performance of large diameter (>80nm) nanotubes being demonstrated for amorphous TiO₂. Additional improvements of LTO based electrodes have been made through improving bulk conductivity by transition metal doping (Li_{4-x}MTi₅O₁₂)¹¹⁷ and carbon nanocomposites.¹¹²

The spinel structure is an ideal candidate for insertion based electrodes due to the 3D diffusional pathways, allowing for facile Li⁺/Na⁺ mobility through the host structure. Focus into Me₃O₄ (Me = Co, Fe, Mn, Mg, Zn, Ca) based spinels have demonstrated high capacities (>200mAh/g) and structural stability during reversible cycling in sodium cells, while offering a low cost highly abundant alternative chemistry.^{118–121} Additional comments on spinel structured electrodes is covered in a following section.

2.1.1.2.1.5 Sulfides (Anodes)

Investigations on layered carbonaceous anode structures have revealed that successful adaptation of well studied lithium-based layered structures revolves around the larger interlayer spacings required for reversible Na⁺ de/insertion. Graphene/Transition-metal-dichalcogenide conversion-typed layered nanostructures have demonstrated promising results as electrode materials in Li-ion batteries,^{122–128} with similar attention being directed to MoS₂/graphene and WS₂/graphene composites.^{129,130} Despite the relatively open layered structure, Li⁺ insertion into MoS₂ occurs distinctly by a conversion reaction:



2.1.1.2.1.6 Fluorides (Anodes)

Considering some of the fluoride chemistries, CoF₂ has been reported in a number of lithium-ion cells, demonstrating high discharge capacities up to 595 mAh/g when being implemented as a cathode material.¹³¹ However, when operating within 1.0 - 0.01V (vs. Li/Li⁺) a reversible interfacial intercalation reaction is observed providing up to 400 mAh/g during the initial discharge reaction.¹³² Tan *et al.* further demonstrate CoF₂ as a feasible anode material for sodium-ion batteries, demonstrating an initial discharge capacity of 402 mAh/g at a current density of 553 mA/g. However, capacity retention is notably poor at 47 mAh/g after just 30 cycles. While fluorides are generally attractive due to their high electronegativity of the M-F bonds, current investigations of sodium-based chemistries are limited for anode applications.

2.1.1.2.2 Electrolytes

It has been noted^{133,134} that Na metal and certain carbon-based anodes do not form a stable surface-electrolyte-interface (SEI) layer, leading to substantial coulombic inefficiencies and cell degradation for common inorganic sodium electrolytes. Therefore, in order to further advance the field of SIBs, additional work on stable electrolyte compositions and additives (designed to form a stable SEI layer) is needed to provide high-performance SIBs. Moreover, particular design and optimization of suitable electrolyte compositions are highly dependent on the specific anode/cathode compositions utilized, and thus specific tailoring is needed. Generally requiring that the electrochemical potential of the anode/cathode are lower/higher than the lowest/highest un/occupied molecular orbitals (LUMO/HOMO) respectively.

Four general classes of electrolytes can be identified for sodium electrolytes: (1) inorganic electrolytes, (2) aqueous electrolytes, (3) ionic liquid electrolytes and (4) solid (polymer) electrolytes. Here brief sections are provided for these main electrolyte categories. Table 2-1 gives a representative look on select anode/electrolyte/cathode compositions reported in literature.

Table 2-1: Representative sodium cells

Anode	Cathode	Electrolyte salt	Solvent	Reference
Graphite	P2: $\text{Na}_{0.66}[\text{Ni}_{0.33}\text{Mn}_{0.66}]\text{O}_2$	Na_2SO_4	H_2O	135
$\text{NaTi}_2(\text{PO}_4)_3/\text{Activated Carbon}$	$\lambda\text{-MnO}_2$	$\text{Li}_2\text{SO}_4 + \text{Na}_2\text{SO}_4$	H_2O	136
SnO_2	Na	NaBF_4	tetraethylene glycol dimethyl ether	137
Na	$\text{NaV}_6\text{O}_{15}$ nanorods	NaClO_4	EC:DEC	138
TiO_2 : Anatase $\text{Li}_4\text{Ti}_5\text{O}_{12}$: Cu doped	Na	NaClO_4	EC:DMC	113,117
Na	NaCrO_2	NaClO_4	EC:DMC	139
TiO_2 : Anatase $\text{SnO}_2@\text{MWCNT}$ Hard Carbon	Na	NaClO_4	EC:PC	140–142
$\text{Fe}_3\text{O}_4/\text{C}$	$\text{Na}[\text{Ni}_{0.25}\text{Fe}_{0.5}\text{Mn}_{0.25}]\text{O}_2$	NaClO_4	EMS:FEC	143
Spherical Carbon Co_3O_4	Na	NaClO_4	PC	144 145
Na	Oligopyrene (OPr) $\text{Na}_2\text{FeP}_2\text{O}_7$ $\text{Na}_{2-x}(\text{Fe}_{1-y}\text{Mn}_y)\text{P}_2\text{O}_7$ $\text{Na}_2\text{C}_6\text{O}_6$ (disodium rhodizonate) FeS_2 VO_2 $\text{Na}_3\text{V}_2(\text{PO}_4)_3$ $\text{Na}_3\text{M}_2(\text{PO}_4)_2\text{F}_3$ (M=Ti,Fe,V) $(\text{NH}_4)_2\text{V}_6\text{O}_{16}$	NaClO_4	PC	9,146–154
Na	P2: $\text{Na}_{0.66}[\text{Ni}_{0.33}\text{Mn}_{0.66}]\text{O}_2$ $\text{Na}_{0.7}[\text{Fe}_{0.7}\text{Mn}_{0.3}]\text{O}_2$	NaClO_4	PC:FEC	155,156
Hard Carbon	Na	NaClO_4	PC:FEC	142
Disordered carbon	$\text{Na}[\text{Ni}_{0.5}\text{Mn}_{0.5}]\text{O}_2$	NaClO_4	PC:FEC	157
Na	$\text{NaFe}_x(\text{Ni}_{0.5}\text{Ti}_{0.5})_{1-x}\text{O}_2$	NaFSI	PC	158
Na	$\text{NaNi}_{0.33}\text{Co}_{0.33}\text{Fe}_{0.33}\text{O}_2$ iron-nickel hexacyanoferrate P2: $\text{Na}_{0.67}[\text{Mn}_{0.65}\text{Fe}_{0.2}\text{Ni}_{0.15}]\text{O}_2$ $\text{Na}_4\text{Co}_{2.4}\text{Mn}_{0.3}\text{Ni}_{0.3}(\text{PO}_4)_2\text{P}_2\text{O}_7$ $\text{Na}_4\text{Co}_3(\text{PO}_4)_2\text{P}_2\text{O}_7$ $\text{Na}_2\text{FeP}_2\text{O}_7$ FeF_3 / reduced graphene oxide $\text{Na}_3\text{V}_2(\text{PO}_4)_3/\text{Carbon nanofibers}$	NaPF_6	EC:DEC	159–167

	NaCrO ₂			
Mn ₃ O ₄ / Fe ₂ O ₃ / Co ₃ O ₄	Na	NaPF ₆	EC:DEC:PC	168
TiO ₂ : Anatase	Na	NaPF ₆	EC:DMC EC:PC	140
Na	P2: Na _{0.66} Fe _{0.33} Mn _{0.66} O ₂	NaPF ₆	PC	169
Na	NaCrO ₂	NaPF ₆	PC	167
Na	(NH ₄) ₂ V ₆ O ₁₆	NaPF ₆	PC	154
Na	NaCrO ₂	NaTFSI	EC:DEC PC	167
TiO ₂ : Anatase	Na	NaTFSI	EC:DMC EC:PC	140
	Na ₄ Ni ₃ (PO ₄) ₂ P ₂ O ₇	2M NaOH-aqueous		170
Na	Cu	bis(trifluoromethylsulfonyl)amide (NaNTf2) : 1-butyl-1-methylpyrrolidinium bis(trifluoromethylsulfonyl)amide (C4mpyrNTf2)		171
Na	Na ₂ FeP ₂ O ₇	Na bis(fluorosulfonyl)amide : N-methyl-N-propylpyrrolidinium bis(fluorosulfonyl)amide		172
Na	Cu	Na[FSA]- [C2C1im][FSA]		173
Na	NaCrO ₂	Na[FSA]- [C3C1Pyr][FSA]		174
-	-	NaTFSI : 1-butyl-3-methylimidazolium bis(trifluoromethylsulfonyl)imide		175
-	-	NaTFSI : 1-ethyl-3-methylimidazolium bis(trifluoromethylsulfonyl)imide		175
Sn film	Na	NaFSA:KFSA (56:44 mol%)		176
Petroleum coke	Na	NaCF ₃ SO ₃	P(EO) ₈	55

2.1.1.2.2.1 Inorganic Electrolytes

Inorganic solvents utilize various polar groups (carbonyl (C=O), sulfonyl (S=O), ethers (-O-), etc.) to dissolve the electrolyte salt, and are widely used throughout commercial electrochemical devices due to their high dielectric strengths, excellent ionic conductivity, and large electrochemical window. Due to the differences in ionic radii and charge densities between Li⁺ & Na⁺, large differences in solvation properties

have been reported between analogous Li/Na electrolyte compositions owing to differences in conductivity and charge transfer kinetics.^{175,177,178} Here, the differences in solvation properties are largely due to the charge densities between Li^+ and Na^+ , with the former being significantly higher than the latter, leading to differences in solubility for a number of sodium electrolyte salts (NaBF_4 , NaPF_6 , NaClO_4 , *etc.*).

Decades of electrolyte research surrounding LIBs have identified a number of inorganic solvents, which have been dually applied to sodium electrolytes. Cyclic/linear carbonates such as propylene carbonate (PC), ethylene carbonate (EC), dimethyl carbonate (DMC), diethyl carbonate (DEC), and ethyl methyl carbonate (EMC) have been utilized in sodium metal/ion cells, but are generally plagued by poor capacity retention due to the catalytic degradation of the electrolyte at the electrode surfaces. The surface-electrolyte-interface (SEI) layer is a common problem throughout both lithium and sodium batteries, and often requires the formation of a stable passivating layer to promote long-term cycling.

Commonly employed sodium electrolytes are based off of sodium hexafluorophosphate (NaPF_6), sodium perchlorate (NaClO_4), sodium triflate (NaCF_3SO_3), sodium bis(trifluoromethylsulfonyl)imide (NaTFSI), and similar sodium salts mixed with an inorganic solvent capable of completely dissolving the electrolyte salt. Co-blending of inorganic solvents¹⁷⁹ is typically performed when optimizing rheological properties of the electrolyte, as illustrated by Figure 2-2, which considers the inverse relationship between ionic conductivity and viscosity.

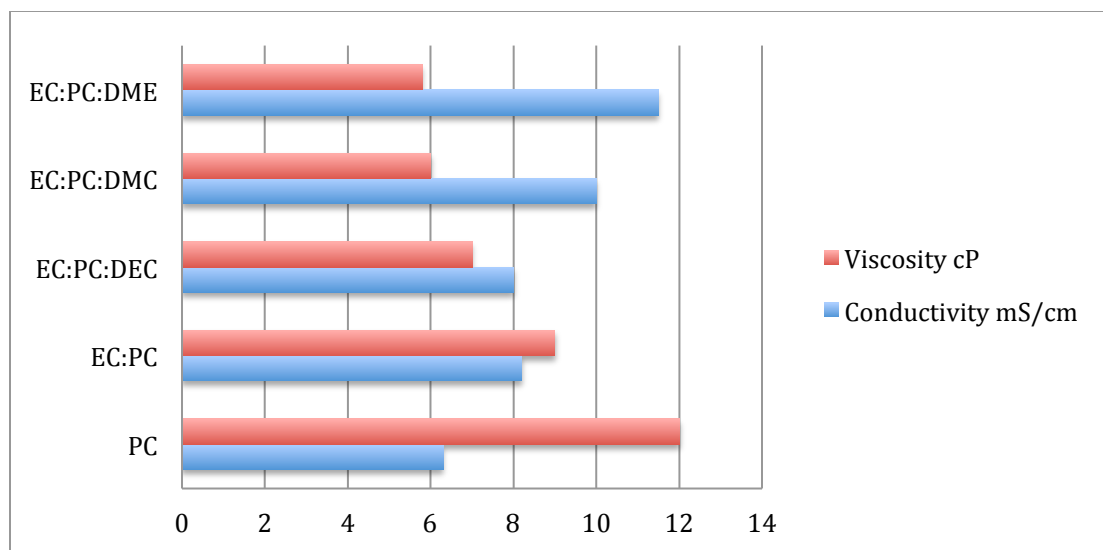


Figure 2-2: Representative conductivity and viscosity values based on 1M NaClO₄ electrolytes of co-blended inorganic solvents adapted from ref. ¹⁷⁹

However, due to the continuous corrosion that has been known to occur on metallic sodium electrodes¹³³ there is an inherent need to introduce electrolyte additives whose sole purpose is to preferentially decompose onto the electrode surfaces, forming a passivation layer protecting against additional electrolyte decomposition. Due to the overwhelming base of knowledge surrounding lithium electrolytes and novel SEI forming additives, it is both a convenient and reasonable starting point to consider established SEI forming additives for lithium metal/ion cells.

Initial investigations into similar electrolyte additives for sodium-based chemistries are comparatively limited, and have only identified fluorinated ethylene carbonate (FEC) as a stable SEI forming agent.^{143,157} Table 2-2 provides a short overview of established and newly tested electrolyte additives studied for lithium metal/ion cells. With further attention being drawn towards SIBs, it is expected that further progress in this field will rely upon interpolated data from Li-ion electrolytes.

Table 2-2: Electrolyte additives for lithium batteries

Anode	Cathode	Electrolyte Salt	Electrolyte Additive	Abbrev.	Ref
Li	LiCoO ₂	LiPF ₆	poly[dimethylsiloxane-co-(siloxane-g-acrylate)]	PDMS-A	180
Li	LiCoO ₂	LiPF ₆	poly(dimethylsiloxane-co-phenylsiloxane)	PDMS-P	180
Li	LiCoO ₂	LiPF ₆	poly[dimethylsiloxane-c-(siloxane-g-ethylene oxide)]	PDMS-EO	180
Li	LiCoO ₂	LiPF ₆	2,2'-Bithiophene	2TH	181
Li	LiCoO ₂	LiPF ₆	2,2':5',2''-Terthiophene	3TH	181
Li	LiCoO ₂	LiPF ₆	2,2'-Bis[4-(4-maleimidophenoxy)phenyl]propane	BMP	182
Li	LiMn _{1.5} Ni _{0.5} O ₄	LiPF ₆	N-methylpyrrole	MPL	183
Graphite	LiFePO ₄ & Li[Ni _{0.33} Co _{0.33} Mn _{0.33}]O ₂	LiPF ₆ / LiBF ₄ / LiTFSI / LiBOB	adiponitrile	ADN	184
Graphite	LiFePO ₄ & Li[Ni _{0.33} Co _{0.33} Mn _{0.33}]O ₂	LiPF ₆ / LiBF ₄ / LiTFSI / LiBOB	γ -butyrolactone	GBL	184
Graphite	Li[Li _{0.2} Ni _{0.15} Mn _{0.55} Co _{0.1}]O ₂	LiPF ₆	4-(perfluorooctyl)-1,3-dioxolan-2-one	PFO	185
Graphite	Li[Li _{0.2} Ni _{0.15} Mn _{0.55} Co _{0.1}]O ₂	LiPF ₆	4-(perfluorohexyl)-1,3-dioxolan-2-one	PFH	185
Graphite	Li[Li _{0.2} Ni _{0.15} Mn _{0.55} Co _{0.1}]O ₂	LiPF ₆	4-(perfluorobutyl)-1,3-dioxolan-2-one	PFB	185
Graphite	Li[Li _{0.2} Ni _{0.15} Mn _{0.55} Co _{0.1}]O ₂	LiPF ₆	4-trifluoromethyl-1,3-dioxolan-2-one	TFM	185
Graphite	Li[Ni _{0.33} Co _{0.33} Mn _{0.33}]O ₂	LiPF ₆	methyl phenyl carbonate	MPC	186
Graphite	Li[Ni _{0.33} Co _{0.33} Mn _{0.33}]O ₂	LiPF ₆	ethyl phenyl carbonate	EPC	186
Graphite	Li[Ni _{0.33} Co _{0.33} Mn _{0.33}]O ₂	LiPF ₆	diphenyl carbonate	DPC	186
Graphite	Li[Ni _{0.33} Co _{0.33} Mn _{0.33}]O ₂	LiPF ₆	vinylene carbonate / prop-1-ene-1,3-sultone / ethylene sulfite / trimethylene sulfate / 1,3,2-dioxathiolane-2,2-dioxide / methylene methanedisulfonate / tris(trimethylsilyl) phosphite	VC / PS / ES / TMS / DTD / MMDS / TMSP	187
Graphite	Li[Ni _{0.33} Co _{0.33} Mn _{0.33}]O ₂	LiPF ₆	di(methylsulfonyl) methane	DMSM	188
Li	LiMn _{1.5} Ni _{0.5} O ₄	LiPF ₆	ethyl methyl sulfone / dimethyl sulfone	EMS / DMS	189
Li	Li-rich NMC	LiPF ₆	tris(2,2,2-trifluoroethyl) phosphite	TTFP	190
Graphite	LiMn ₂ O ₄	LiPF ₆	methyl vinyl sulfone / ethyl vinyl sulfone	MVS / EVS	191
Li	Cyclam	LiPF ₆	1,4,8,11-tetraazacyclotetradecane	TACTD	192

2.1.1.2.2.2 Aqueous Electrolytes

Due to the highly exothermic reaction involving Na metal and H₂O, aqueous electrolytes are not compatible with alkali metal batteries. Due to overall costs and safety concerns surrounding inorganic solvents, utilization of an abundant and low cost solvent such as H₂O would be highly advantageous. However, aqueous electrolytes are typically limited by their narrow electrochemical window, making it necessary to carefully match anode/cathode compositions such that H₂ and O₂ evolution does not occur during normal cell operation.¹⁹³ Early reports of aqueous Na⁺-ion electrolytes utilized for Na_{0.44}MnO₂ (C_{th} = 160 mAh/g) have been demonstrated by Sauvage *et al.*, leading to the development of an Activated carbon/Na_{0.44}MnO₂ hybrid cell.^{194,195} Further improvements have been made by switching to λ -MnO₂ delivering specific capacities up to 390.7 mAh/g, with excellent capacity retention of 85 mAh/g after 500 cycles at 136 mA/g with NaSO₄ based aqueous electrolytes.¹³⁵

Similar large-format energy storage devices have been constructed with activated carbon/NaTi₂(PO₄)₃ composite anodes demonstrating the scalability and economic benefits of aqueous sodium batteries.^{136,196} More recent investigations on polyanionic compounds using aqueous sodium electrolytes have been reported for Na₂FeP₂O₇, Na₃Ti₂(PO₄)₃, and even LiFePO₄.^{197–199} While aqueous electrolytes are highly attractive due to the benign and low cost nature as compared to conventional electrolytes, they are overshadowed by conventional inorganic solvents due to the limited voltage stability of H₂O that restricts its usage to only low voltage cell chemistries.

2.1.1.2.2.3 Ionic Liquid (IL) Electrolytes

Commercial high-performance batteries generally employ inorganic electrolytes, and as such, have attributed LIBs as inherent safety risks due to the high volatility and flammability of inorganic solvents. The interest of developing ‘safe’ electrolyte compositions for LIBs has demonstrated a number of nonflammable molten eutectic electrolyte salts capable of addressing the needs for high safety margins in LIBs. General development of ionic liquid electrolytes focusing on a combination of desirable properties: low vapor-pressure, non-flammable, high thermal stability, high ionic-conductivity, and wide electrochemical window.¹⁷¹ As their name suggests, ionic liquids (ILs) are primarily composed of a mixture of two or more lithium/sodium salts, whose melting points are relatively close, or well below room temperature such that they are liquid at reasonable temperatures.

Chloroaluminate molten salts have seen notable interest over the years as an ambient temperature ionic-liquid, demonstrating high cycling efficiency of sodium.^{200–203} However, major considerations of sodium ionic liquid electrolytes have been centered around bis(fluorosulfonyl)amide and bis(trifluorosulfonyl)amide (FSA and TFSA respectively) based ionic liquids.^{173,175,204–206} Monti *et al.* have investigated the solvation characteristics of $[\text{Na}(\text{TFSI})_n]^{1-n}$ charge carriers in comparison to their lithium ionic liquid analogues. Detailed vibrational characterization identifies $[\text{Na}(\text{TFSI})_3]^{2-}$ as the primary charge carrier, compared to the $[\text{Li}(\text{TFSI})_2]^-$ charge carriers observed for lithium IL compositions. The increased solvation of the larger Na^+ cation has wide implications on ILs by impacting overall IL viscosity and ionic conductivity of the electrolyte as a whole, generally making sodium IL compositions increasingly viscous as compared to analogous lithium ILs.

Ionic liquids themselves, offer considerable thermal and electrochemical stability, yet are still generally outweighed by conventional inorganic electrolyte compositions due to the need for elevated temperatures to reach appreciable conductivity values.^{205,207} A short table of commercially available ILs is provided below for completeness.

Table 2-3: Examples of commercially available ionic liquid compositions for sodium ion batteries

Cation	Anion	Abbrev.	mp		mS/cm
1-butyl-1-methylpyrrolidinium	bis(fluorosulfonyl)imide	$[\text{C}_4\text{C}_1\text{pyr}][\text{FSI}]$	-17.7°C	5.7V @ 20°C	6.9 @ 20°C
1-butyl-1-methylpyrrolidinium	bis(trifluoromethylsulfonyl)imide	$[\text{C}_4\text{C}_1\text{pyr}][\text{TFSI}]$	-6°C	6.0V @ 25°C	2.7 @ 25°C
1-ethyl-3-methylimidazolium	bis(fluorosulfonyl)imide	$[\text{C}_2\text{C}_1\text{im}][\text{FSI}]$	-13°C	4.29V	15.4 @ RT
1-methyl-1-(2-methoxyethyl)pyrrolidinium	bis(fluorosulfonyl)imide	$[\text{C}_1\text{C}_1\text{-O-C}_2\text{pyr}][\text{FSI}]$	-	-	7.34 @ 25°C
1-methyl-1-(2-methoxyethyl)pyrrolidinium	bis(trifluoromethylsulfonyl)imide	$[\text{C}_1\text{C}_1\text{-O-C}_2\text{pyr}][\text{TFSI}]$	5.4°C	-	3.86 @ 25°C
1-methyl-1-(2-methoxypropyl)pyrrolidinium	bis(trifluoromethylsulfonyl)imide	$[\text{C}_1\text{C}_1\text{-O-C}_3\text{pyr}][\text{TFSI}]$	-	-	-

2.1.1.2.2.4 *Polymer gel Electrolytes*

Polymer-gel electrolytes aim to solve the same problem of volatile/flammable electrolyte compositions by immobilizing the liquid electrolyte within a free-standing body.^{208–210} Polymer-gel electrolytes stem from the formation of suitable micro/nano ceramic dispersions, which act to retain the electrolyte within a porous matrix. While immobilization of the electrolyte in this manner adds additional safety measures when considering cell ruptures & leaks, there exist several drawbacks toward typical polymer-gel electrolytes: (1) Low liquid retention capacity (2) poor dimensional stability, and (3) interfacial stability concerns.

Here it is necessary to highlight that while most polymer-gel electrolytes utilize inorganic electrolytes, they are still viewed as considerably safer than the former, as the polymer matrix works to prevent loss of the electrolyte in the event of a cell rupture/leak. Polymer compositions such as poly(methyl methacrylate), poly(vinylidene fluoride), poly(vinylidene fluoride-co-hexafluoropropylene), and poly(ethyleneoxide) are typically used throughout literature, with additions of colloidal dispersions of ceramic particles (SiO_2) being commonly performed to increase mechanical properties of the free-standing electrolyte.²⁰⁸

Since the polymer matrix serves as an immobilizing porous body, additional ionic liquid polymer-gel electrolytes can be formed, demonstrating good ionic conductivities on the order of conventional inorganic electrolytes (5.7 mS/cm).²⁰⁹

2.1.1.2.3 *Positive Electrodes*

Transition metal oxides make up the majority of cathode compositions considered for practical energy storage usage. While there are a number of possible stoichiometries and crystallographic structures capable of providing ample electrochemical activity, there exist fundamental properties ideal cathode chemistries should provide:

- (1) Low raw material/production cost
- (2) Low toxicity of precursors/active materials
- (3) High gravimetric & volumetric capacity (Ah)
- (4) High gravimetric & volumetric energy (Wh)
- (5) High rate capability

- (6) High thermal stability & safety
- (7) Long cycle/calendar life

Due to the inverse relationship these criteria generally have on one another, high-performance cathode compositions are generally tailored according to the specific operating conditions expected under real-load conditions. Figure 2-3 considers a spider plot comparing common cell metrics between existing commercial Li-ion batteries.

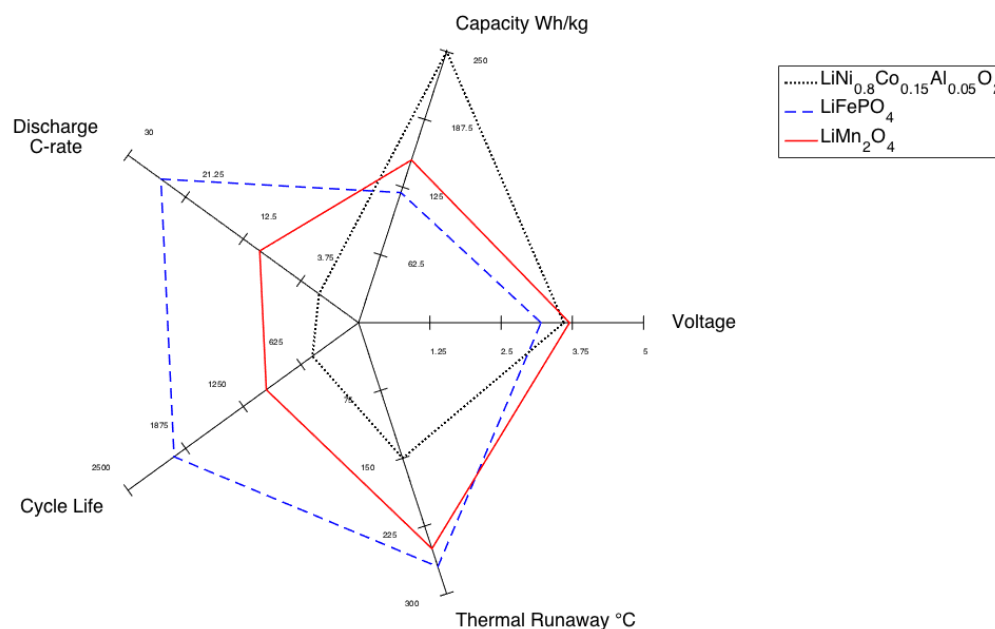


Figure 2-3: Spider plot of select commercial Li-ion battery chemistries comparing common performance metrics between three select cathode compositions

As individual electrode materials possess certain advantages and drawbacks, blended cathode compositions are yet another strategy towards developing optimal energy storage devices, combining advantageous properties from two or more specific compositions.²¹¹ This technique is more commonly practiced within established lithium-based chemistries, as understanding of the exact Na⁺ de/insertion process into many sodium-ion cathodes is not sufficiently understood/optimized for blended cathode compositions.

Overall, the end goal for SIBs is to offer a highly competitive alternative to existing lithium batteries. However, it is often the case that crystal structures/chemistries that have demonstrated excellent properties for LIBs are not easily adapted to analogous sodium chemistries. Jian *et al.* have proposed a methodology towards designing high-capacity cathode materials for SIBs, targeting the development of Li-rich layered compounds for direct application in an analogous Na-rich layered compounds.²¹² However, current synthesis techniques have not been able to produce direct sodium analogues, often requiring additional delithiation and subsequent sodiation by electrochemical or ion-exchange methods demonstrating potential barriers to commercialization of SIB technologies.^{212,213} The following sections are aimed at individual chemistries identified as potential cathode materials.

2.1.1.2.3.1 Transition metal oxides

Cathode compositions are commonly based on transition metal oxides, as MO_6 ($\text{M} = \text{Mn, Fe, Co, Ni, Cr}$) octahedra are capable of a variety of different packing schemes; forming edge/corner shared octahedral networks, double/triple octahedral chains, lamellar structures, and more.^{214–216} Transition metal oxide compounds provide a wide array of crystal structures/allotropes that have been investigated for electrochemical storage applications;

With respect to cathode compositions, it is desirable to utilize an open structure capable of accommodating reversible de/insertion of Na^+ with minimal volumetric change. However, structures with large interstitial sites are often less stable in their unpopulated (delithiated/desodiated) state, requiring electrochemical cycling within a restricted de/insertion range such to prevent collapse of the crystal structure. $\text{Li}_{1-x}\text{CoO}_2$ is commonly cycled within a narrow reversibility range ($0 < x < 0.5$) in order to prevent degenerative structural transformations that arise from the complete delithiation of the O3-type layered structure.^{217–219} Cobalt oxides have also been investigated for sodium batteries, with early investigations by Delmas *et al.* demonstrating multiple phase transitions that occur with reversible Na^+ de/insertion due to shifting of CoO_2 planes.^{220,221} While various transition metal oxides have proven to be suitable for sodium-ion batteries, the majority of focus has been directed towards layered manganese oxides which will be discussed in the following sections.^{155,161,222–224}

Parant *et al.* have identified a number of layered manganese oxide structures of interest for sodium-ion batteries,²¹⁴ and following works by Delmas have established a convenient notation to discern

between the subtle crystallographic differences between layered oxides based on the site preference of the alkali ion 'A'. As a whole, particular layered cathode compositions A_xMO_2 may be classified as one of the following structure types:

- (1) O3/O'3/P3-type structures^{225,226}
- (2) P2/P'2/O2-type structures^{214,215,223–229}
- (3) O6-type structures^{230–232}
- (4) T2-type structures^{223,225,228,229}

The P/O/T notation is provided to designate the coordination of the alkali metal 'A' (Li/Na), with P, O, and T indicating trigonal-prismatic, octahedral, and tetrahedral coordinations within the host structure respectively. The specific numbers (P2/P3/O2/O3) correlate to the number of MO_2 layers within a single unit cell, and primed superscripts describe a monoclinic structural distortion that typically arises due to cooperative Jahn-Teller distortion of the MO_6 octahedra. The close structural relation between the P3 and O3-type structures is realized as a gliding of the MO_2 layers, often resulting in easy transformation between the P3 and O3 structures when changing the A-M ratio; the same is the case for P2 and O2-type structures. Identification of the T2-structure has been documented only for layered lithium-based compositions,²²³ as Na^+ exhibits a high affinity towards P and O sites due to size considerations between Li^+ and Na^+ . Figure 2-4 considers the P2, P3, O2 and O3 structures. It is important to note that the α - $NaFeO_2$ structure is equivalent to the O3-structure, with the latter being the preferred notation throughout this section.

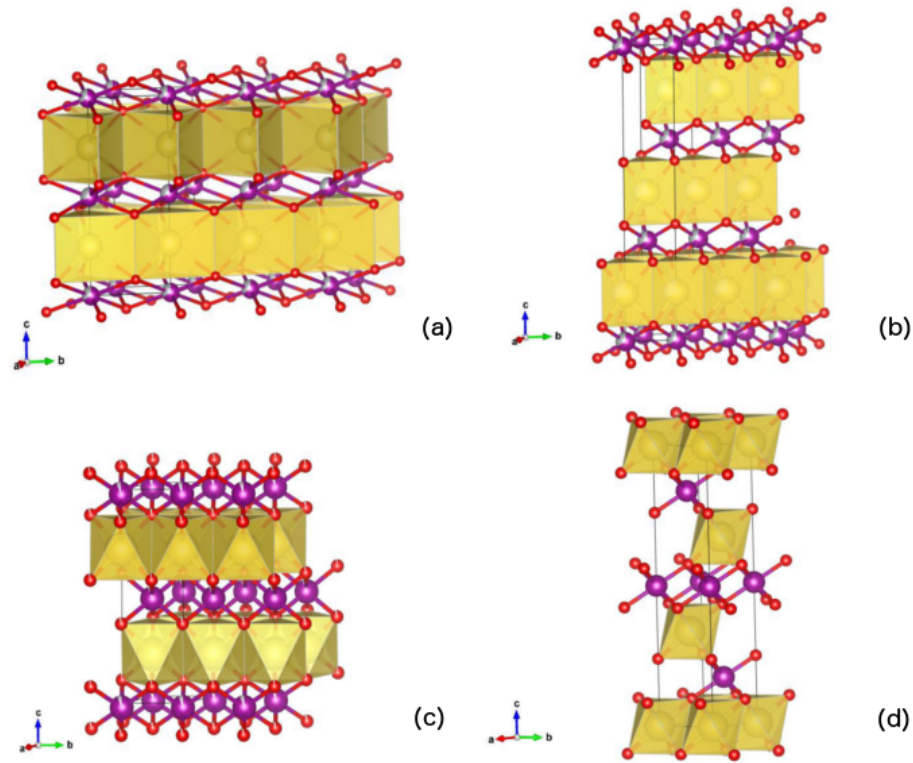


Figure 2-4: Layered NaMO_2 structures ($M = \text{Mn, Fe, Ni, Co}$) exhibiting trigonal prismatic Na-coordination (a-b) of the P2 and P3-type structures respectively, and octahedral coordination (c-d) for the O2 and O3-type structures respectively.

2.1.1.2.3.1.1 P3/O3-type structures

The O3-structure consists of alternating layers of trigonally distorted MO_6 ($M = \text{Li, V, Cr, Mn, Fe, Co, Ni}$) edge sharing octahedra with space group $R\bar{3}m$, with oxygen stacking sequencing:



With A, B, and C indicating oxygen layers and [M] denoting the transition metal. As will be discussed below, the O3 and P3 structures are very similar, only being distinguished by a small relative shifting of the metal oxide layers yielding trigonal-prismatic or octahedral sites between the oxide layers. The P3-structure has an oxygen stacking sequence of:



With Na1 and Na2 indicating one of two possible prismatic sites.

The O3-structure has demonstrated to be highly advantageous for electrochemical de/insertion materials, with early synthesis attempts for O3-type lithium chemistries often requiring soft chemistry techniques such as ion-exchange of the analogous NaCoO_2 in order to achieve the O3 structure.²²⁷ As mentioned previously, structural distortions of the O3-structure are systematically observed during electrochemical cycling. Figure 2-5 provides a general voltage profile for NaCoO_2 as it relates to the P'3/O'3/O3 structures. As the P2-type NaCoO_2 has demonstrated considerably better performance, additional comments on NaCoO_2 are provided in a latter section.

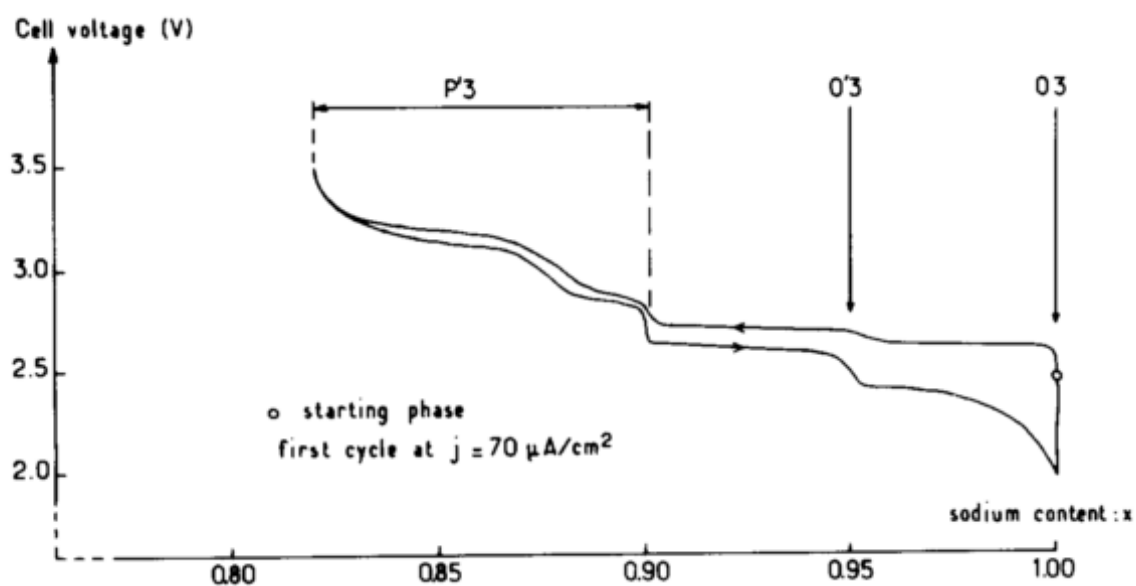


Figure 2-5: Voltage profile of O3-type NaCoO_2 . Reproduced from ref.²²⁰

NaCrO_2 also demonstrates an O3-structure, with early investigations by Braconnier *et al.* demonstrating minimal interest in the chromium oxides due to low discharge capacities.²³³ However, more recent considerations have demonstrated high reversible capacities of up to 120 mAh/g^{234–236} corresponding to reversible de/intercalation limits $\text{NaCrO}_2 - \text{Na}_{0.5}\text{CrO}_2$ with good capacity retention over 50 cycles.²³⁷ Further improvement in capacity retention has been demonstrated through carbon coating of NaCrO_2 particles with discharge capacities of 99 mAh/g at 150C rates being reported.^{139,235} Additionally, several *ex-situ/in-situ* XRD studies^{238,239} have demonstrated the structural transformations as described by Equation 2-21 and Figure 2-6, which follow a very similar progression as seen for NaCoO_2 .

Equation 2-21:

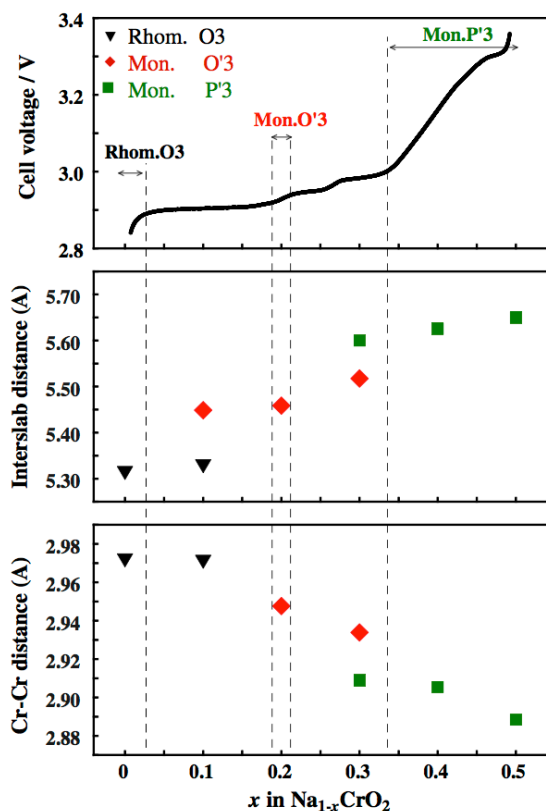


Figure 2-6: Structural phase progression of NaCrO_2 . Reproduced from Ref. ²³⁴

Kubota *et al.* have observed a migration of Cr^{4+} from the interslab layers into the interslab space confirmed by Rietveld refinement to a proposed $\text{Na}_{0.06}\text{Cr}_{\text{oct}0.1}\text{Cr}_{\text{tet}0.2}(\text{Cr}_{\text{oct}0.7})\text{O}_2$ structural model in which Cr_{oct} , Cr_{tet} , and (Cr_{oct}) denote the occupancy of chromium on octahedral/tetrahedral sites within the interslab space, and octahedral sites within the interslab space respectively. Drastic reduction in discharge capacity upon charging to a 4.5V cutoff, which corresponds to complete extraction of Na^+ , has been attributed to irreversible migration of chromium into the interslab layers.²³⁸ Figure 2-7 provides a visual representation of the proposed chromium migration process.

While NaCrO_2 presents itself as a potential sodium-ion insertion material, several drawbacks include (1) the need to restrict cycling within a narrow $0.5 < x < 1.0$ range, and (2) general concerns around the use of a chromium-based chemistry. Here, it is important to note that Cr^{4+} does not pose the same toxicological concerns as Cr^{6+} as pointed out by Xia and Dahn.²³⁶ However the majority of chromium minerals and chromium metal supplies within the U.S. are based off imports from South Africa, Kazakhstan, Russia and Mexico, making resources potentially limited and of relatively high cost when compared against other transition metals.¹⁰

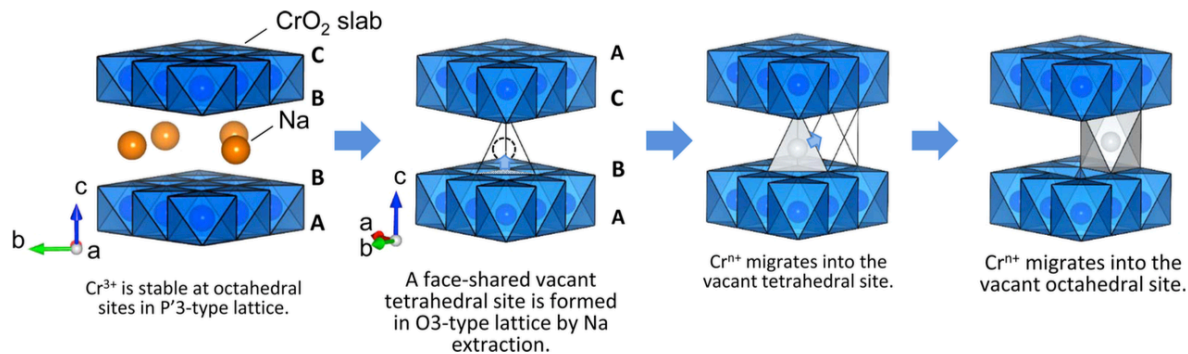


Figure 2-7: Chromium migration process during electrochemical Na^+ extraction. Reproduced from

Ref²³⁸

First investigations into vanadium oxides ($\text{O}3\text{-NaVO}_2$) originally synthesized by Barker *et al.*, demonstrated very low capacities and poor control over phase purity,²⁴⁰ with more recent works demonstrating phase pure samples and capacities up to 126 mAh/g^{241} generating a renewed interest in layered vanadium compounds. However, pure NaVO_2 is highly reducing, requiring it to be handled in a completely oxygen free atmosphere to prevent the spontaneous oxidation reaction described by Equation

2-22, where “ Na_xVO_2 ” denotes a combination of NaVO_2 and $\text{Na}_{0.66}\text{VO}_2$. Due to the difficulty in preparing O3-type NaVO_2 , cells are typically assembled with varying amounts of the O’3-type $\text{Na}_{0.66}\text{VO}_2$ with recovery of the O3 structure occurring upon discharge.²⁴¹ Due to a similar migration process described for $\text{NaTiO}_2/\text{NaCrO}_2$, the reversible range of NaVO_2 is limited to $0.5 < x < 1.0$ in Na_xVO_2 , as can be seen by the drastic drop in cell performance in Figure 2-8. Overall, NaTiO_2 & NaVO_2 does not present itself as a suitable cathode for common battery applications, as its difficult synthesis and relatively low voltages are considerable drawbacks in comparison to other transition metal compositions.^{242–244} Additional vanadium compounds, falling within the NASICON structural family are of more practical interest, and will be discussed in a following section.

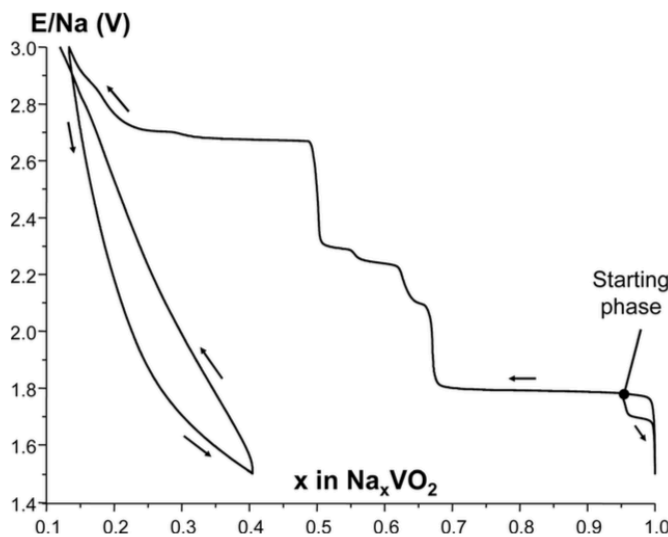


Figure 2-8: Typical voltage profile of Na_xVO_2 in a sodium metal cell. Reproduced from Ref. ²⁴¹

While O3/O’3/P’3/P3-type layered oxides have demonstrated considerable cell performance,^{221,235,236,238,241,245,246} the use of abundant, and environmentally ‘green’ transition metals such as Fe and Mn are of particular interest; especially when considering the growing demand for large-scale energy storage applications. NaFeO_2 is commonly found in two crystallographic forms; namely, the α and β phases. The α and β phases exhibit rhombohedral (O3-structure) and tetragonal crystal structures respectively, leading to drastically different electrochemical properties. $\beta\text{-NaFeO}_2$ has presented itself as a

multiferroic material,²⁴⁷ being of little interest for SIB cathodes due to the narrow 1-dimensional diffusional channels through which Na^+ diffuse. In fact, Takeda *et al.* have identified considerable kinetic limitations in the stabilization of the $\alpha\text{-NaFeO}_2$ phase, as $\beta\text{-NaFeO}_2$ is metastable below 760°C , typically requiring dissolution of the $\beta\text{-NaFeO}_2$ phase into a molten sodium source (Na_2O_2 or NaOH) to facilitate precipitation of the $\alpha\text{-NaFeO}_2$ phase.²⁴⁸

Investigations into layered iron oxide compositions for SIBs are promising for future cathode compositions. However, fully charged iron oxide cathodes are highly unstable, as the chemical instability of Fe^{4+} poses concerns around self discharge that must be addressed before realizing $\text{Fe}^{3+}/\text{Fe}^{4+}$ based electrodes.²⁴⁹ As such, O3-type iron compositions often require substitutional doping with Mn or Co to maintain structural stability^{250,251} leading to the underutilization of pure $\alpha\text{-NaFeO}_2$ over the years.^{252–254} Yabuuchi *et al.* have also noted such difficulties in utilizing $\alpha\text{-NaFeO}_2$ and have demonstrated considerable performance of $\text{Na}_x[\text{Fe}_{0.5}\text{Mn}_{0.5}]\text{O}_2$ O3 and P2-type structures.²²² Additionally, Tabuchi *et al.* have successfully synthesized $\alpha\text{-NaFeO}_2$ type LiFeO_2 by a hydrothermal synthesis technique, circumventing the traditional ion-exchange synthesis methods.^{255–257} And more recent investigations on LiFeO_2 cathodes have demonstrated high reversible capacities ($> 120\text{mAh/g}$) with further improvement by transition metal doping ($\text{A}_x[\text{Fe}_{1-x}\text{M}_x]\text{O}_2$ A = Na, Li; M = Co, Mn, Ni).^{250,258–260} Overall, renewed interests in LiFeO_2 are likely to trickle down into sodium cathode research as seen with previous analogous systems. And while a battery with a primary chemistry such as that offered by NaFeO_2 presents itself as an ideal case of highly abundant and low cost materials, further efforts are needed to ensure satisfactory capacity retention.

In particular, O3-type materials utilizing the $\text{NaFeO}_2\text{-NaNiO}_2$ solid solution have demonstrated a large increase in cell capacity and efficiency; with increasing nickel content resulting in greater capacities at high voltage.²⁶¹ Utilization of the $\text{Ni}^{2+}/\text{Ni}^{4+}$ redox reaction is of interest due to the attributed high voltages. However, pure NaNiO_2 observes a cooperative Jahn-Teller distortion of NiO_6 octahedra, resulting in potentially irreversible structural transformations.^{262–264} In fact, early investigations into the electrochemical behavior of monoclinic O'3- NaNiO_2 demonstrated very poor discharge capacities.²⁶⁵ However, more recent studies have reported considerable deintercalation limits, with capacities ranging up to 199mAh/g ($0.15 < x < 1.0$ in Na_xNiO_2).²⁴⁶ Figure 2-9 shows the step-wise voltage profile of O'3- NaNiO_2 . And despite frequent interests in NaNiO_2 as a potential cathode material, it is largely limited by

the careful synthesis methods needed to yield phase pure powders, and is often utilized in conjunction with additional transition metals in order to prevent cooperative Jahn-Teller distortions.^{224,261,266,267}

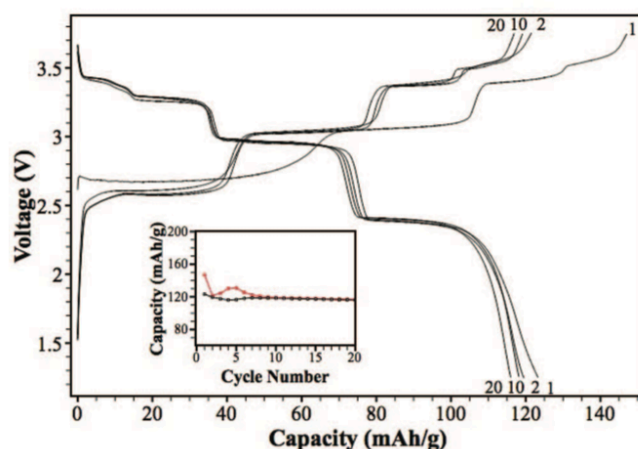
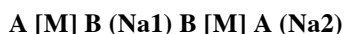


Figure 2-9: Representative voltage profile of monoclinic O'3-NaNiO₂ in a sodium metal cell. Reproduced from Ref.²⁴⁶

Re-emerging interests in iron and nickel based layered structures continue to demonstrate considerable improvement over initial cathode designs, and due to their desirable electrochemical properties, are of potential interest for high performance SIBs.

2.1.1.2.3.1.2 P2-type structures

While O3-type positive electrode materials have both demonstrated electrochemical activity and high rate capabilities; they are however, limited to approximately 50% of their theoretical capacities due to structural degradation that occurs when fully desodiating O3-NaMO₂ (M = Co, Ni, Cr, V, Mn) compositions. More recent investigations into layered cathode compositions have focused around the P2-type structure. The P2-structure consists of metal oxide layers with oxygen stacking sequence:



With Na1 and Na2 indicating occupancy of one of two possible trigonal prismatic sites. Side-by-side comparison of P2 and O3 sodium cathode compositions have demonstrated a significant advantage of the P2 structure as illustrated by Figure 2-10. The P2 structure commonly observes small structural distortions during cycling as previously demonstrated for P3/O3-type structures, with orthorhombic and monoclinic distortions occurring due to similar mechanisms involving the relative gliding of oxide layers.²⁶⁸ *In-situ* characterization by Xu *et al.* have further stabilized the P2 structure at high voltages by

introducing Li onto the transition metal sites; thereby allowing for greater Na^+ occupancy at high voltages, further stabilizing the P2 structure in $\text{Na}_x[\text{Li}_y\text{Ni}_z\text{Mn}_{1-y-z}]\text{O}_2$ ($0 < x, y, z < 1$).²⁶⁶ Utilizing similar compositions, Dahn *et al.* have formed O2-type $\text{Li}_{0.66}[\text{Li}_{0.16}\text{Mn}_{0.83}]\text{O}_2$ by ion-exchange of P2-type $\text{Na}_{0.66}[\text{Li}_{0.16}\text{Mn}_{0.83}]\text{O}_2$ bronzes.²⁶⁹ While the P2 and O2 structures vary only in their oxygen stacking sequences, the O2 structure is typically only found in such ion-exchanged lithium compositions,²²⁷ making P2-type structures of primary interest throughout this section.

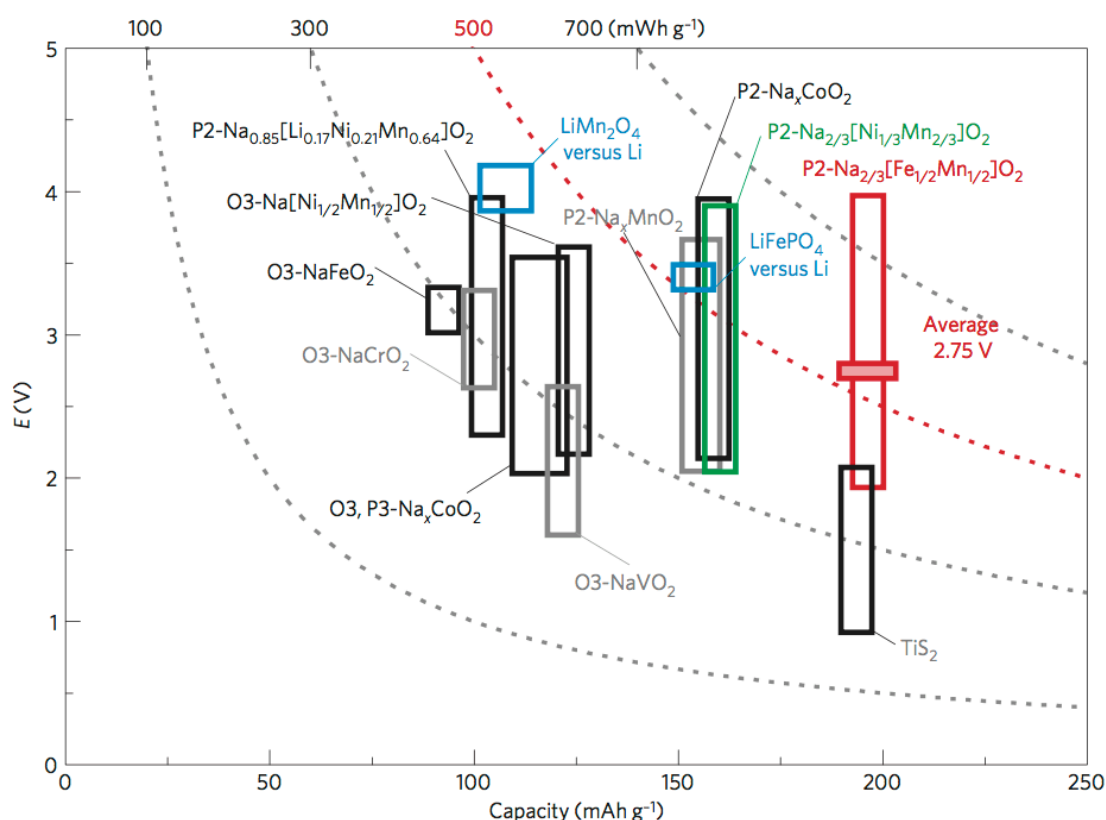


Figure 2-10: Calculated reversible capacity and operating voltage comparison for layered sodium insertion materials reprinted from Ref. ²⁵¹

A number of studies have been centered around the $\text{P2-Na}_x\text{CoO}_2$ phase due to its high electronic and ionic conductivities. Additionally, the large inter-dependence of Na^+ /vacancy ordering has proven to demonstrate a number of hexagonal/orthorhombic superstructures, illustrating a large contrast against the O3-NaCoO_2 .^{270–274} Delmas *et al.* have identified multiple bi-phasic domains throughout electrochemical de/intercalation of $\text{P2-Na}_x\text{CoO}_2$ as shown by Figure 2-11. Here, inflections in the voltage profile reflect the

different phase transitions occurring within $\text{P2-Na}_x\text{CoO}_2$. In particular, throughout the $0.55 < x < 1.0$ range, several distinct ordered phases have been identified, and are listed in Table 2-4.

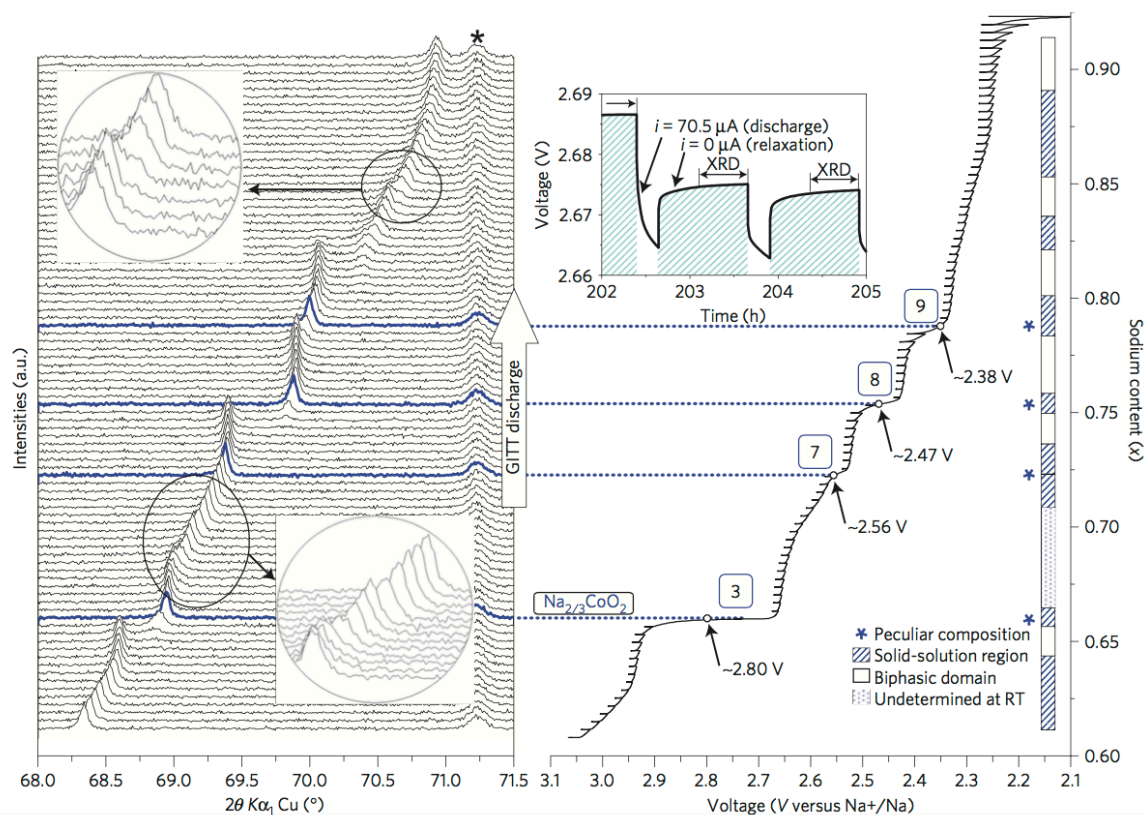


Figure 2-11: in-situ diffraction measurements of $\text{P2-Na}_x\text{CoO}_2$ showing the phase progression of the (008) diffraction peak. Reproduced from Ref. ²⁷²

Table 2-4: Ordered phases of $\text{P2-Na}_x\text{CoO}_2$

Phase	Voltage vs. Na/Na^+
$\text{Na}_{1/2}\text{CoO}_2$	3.45V
$\text{Na}_{4/7}\text{CoO}_2$	3.15V
$\text{Na}_{2/3}\text{CoO}_2$	2.80V
$\text{Na}_{0.72}\text{CoO}_2$	2.56V
$\text{Na}_{0.76}\text{CoO}_2$	2.47V
$\text{Na}_{0.79}\text{CoO}_2$	2.38V

While layered P2-NaCoO₂ is attributed with exceptional ionic and electronic conductivities, making it an ideal intercalation host material, attention has been shifted to alternative chemistries that circumvent the need for cobalt.

As such, P2-type layered compounds based on Mn/Fe chemistries are highly desirable with a number of reports demonstrating considerable performance gains over similar O3-type structures.^{155,161,169,222,224,266} While notable success has been had in the synthesis of O3-type NaMnO₂²⁷⁵ it is frequently observed that manganese-based oxides form a number of 3D or 2D structures based on sodium content as shown in Figure 2-12. Early studies into layered manganese oxides have reported three distinct layered phases: (1) α -Na_{0.7}MnO_{2+y}, (2) β -Na_{0.7}MnO_{2+y}, and (3) α -NaMnO₂, with an ideal P2-structure, an orthorhombic distorted P2-structure and the O'3-structures respectively; α -Na_{0.7}MnO_{2+y} has been observed in the range $0.05 < y < 0.25$ and β -Na_{0.7}MnO_{2+y} for $y < 0.05$ stable below and above 600°C (in air) respectively.²¹⁴ Here, an over-stoichiometric notation is used, which is equivalent to a manganese deficient Na_{0.7x}Mn_xO₂ with $x = 2/(2+y)$.

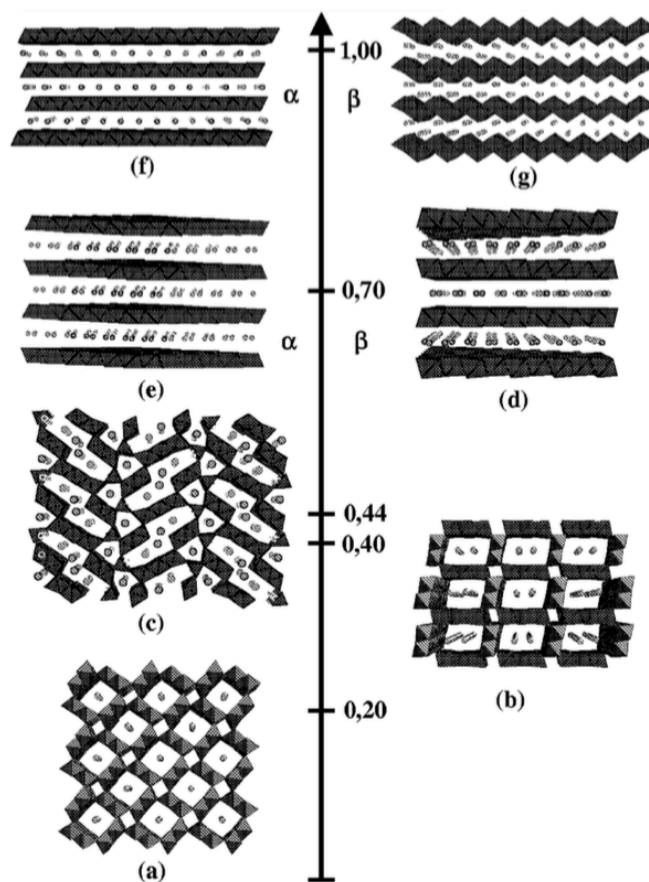


Figure 2-12: $\text{Na}_x\text{Mn}_y\text{O}_2$ structures for given Na/Mn ratios. Reformatted from Ref. ²⁷⁶

Early attention was placed on P2-type manganese bronzes for utilization in analogous Li-ion cathodes derived from ion-exchange techniques. Use of the sodium phases was historically chosen due to the lack of synthesis techniques capable of providing the lithium analogue; often resulting in the structural decomposition to a spinel phase.²²⁷ Moreover, P2-type sodium compositions typically do not observe an O2-type phase transition, resulting in smooth voltage profiles typical of solid-solution intercalation reactions.²¹⁵

Within current literature, investigations into P2-type structures can be largely regarded as the primary choice for commercial SIBs, as intercalation limits and discharge capacities are systematically higher as compared to P3/O3-type structures. As mentioned previously, cooperative Jahn-Teller distortions are frequently observed for layered phases consisting of a single transition metal, thereby relying on a mixture of transition metals to optimize both structural stability and voltage characteristics.

P2-type $\text{Na}_{0.66}[\text{Mn}_{1-x}\text{M}_x]\text{O}_2$ ($\text{M} = \text{Fe}, \text{Co}, \text{Ni}$) compositions have demonstrated considerably higher discharge capacities and capacity retention over undoped P2 layered oxides; with P2-type $\text{NaMn}_{1-x}\text{M}_x\text{O}_2$ ($\text{M} = \text{Ni}, \text{Fe}$) compositions demonstrating an optimal balance between benign materials and optimal electrochemical performance, with initial discharge capacities ranging upwards of 200mAh/g.^{161,222,224} Overall, P2-type structures are widely studied for their high capacities and cell performances, which exceed certain Li-ion technologies as previously highlighted.

2.1.1.2.3.2 NASICON (NAtrium Super Ionic CONductor) Structures

NASICON type structures are of particular interest due to the large open structure afforded by the large polyanionic chemistries. In general, NASICON structures consist of a general formula described by the table below.

Table 2-5: General NASICON chemical formula

$\text{AMM}'\text{X}_3\text{O}_{12}$ or $\text{AMM}'(\text{XO}_4)_3$	
A	$\text{Li}^+, \text{Na}^+, \text{K}^+, \text{Rb}^+, \text{Cs}^+, \text{Mg}^{2+}, \text{Ca}^{2+}, \text{Sr}^{2+}, \text{Ba}^{2+}, \text{H}^+, \text{H}_3\text{O}^+, \text{NH}_4^+, \text{Cu}^+, \text{Cu}^{2+}, \text{Ag}^+, \text{Pb}^{2+}, \text{Cd}^{2+}, \text{Mn}^{2+}, \text{Co}^{2+}, \text{Ni}^{2+}, \text{Zn}^{2+}, \text{Al}^{3+}, \text{Ge}^{4+}, \text{Zr}^{4+}, \text{Hf}^{4+}$
M/M'	$\text{Zn}^{2+}, \text{Cd}^{2+}, \text{Ni}^{2+}, \text{Mn}^{2+}, \text{Co}^{2+}, \text{Fe}^{3+}, \text{Sc}^{3+}, \text{Ti}^{3+}, \text{V}^{3+}, \text{Cr}^{3+}, \text{Al}^{3+}, \text{In}^{3+}, \text{Ga}^{3+}, \text{Y}^{3+}, \text{Lu}^{3+}, \text{Ti}^{4+}, \text{Zr}^{4+}, \text{Hf}^{4+}, \text{Sn}^{4+}, \text{Si}^{4+}, \text{Ge}^{4+}, \text{V}^{5+}, \text{Nb}^{5+}, \text{Ta}^{5+}, \text{Sb}^{5+}, \text{As}^{5+}$
X	$\text{P}, \text{S}, \text{Si}, \text{W}, \text{Mo}$

NASICON structures have been of particular interest for battery applications for a number of years, often being implemented as both solid-state electrolytes^{277,278} and electrode materials.²⁷⁹ While NASICON structures can form a number of different crystal structures, many are described by a rhombohedral structure (space group R-3c) of interconnected (M/M')O₆ octahedra and PO₄ tetrahedra where the conducting ions are situated on one of two interstitial sites: (1) between (M/M')O₆ octahedra along the c-axis (6b-sites), and (2) located between O₃MO₃ – O₃M'O₃ slabs, perpendicular to the c-axis with trigonal prismatic coordination (18e-sites).

Within the NASICON family, vanadium phosphates and fluorophosphates have seen considerable attention due to the large 3-dimensional structures that allow for facile diffusion of Na⁺, and relatively high

reported voltages due to polyanionic inductive effects. Overall, NASICON structures represent a wide range of feasible host structures for facile Na^+ de/insertion kinetics, with particular interest in iron-based compositions for reasons mentioned in earlier sections. Barpanda *et al.* report a novel $\text{Na}_2\text{Fe}_2(\text{SO}_4)_3$ structure, with an average operating voltage *ca.* 3.8V (vs. Na/Na^+), in the range of commercial Li-ion devices. An exhaustive review on NASICON structures for both lithium and sodium-ion batteries is provided by Masquellier *et al.*, with an account of interesting iron and vanadium-based NASICON structures provided in Table 1-6.²⁸⁰

As a whole, the NASICON and similar polyanion structures offer a large host structure capable of facile Na^+ de/insertion. However, when comparing against conventional layered structures, NASICON/polyanion structures suffer from lower specific and volumetric capacities, as illustrated by the relative differences between sulfate/phosphate compounds against the O3 and O2 layered compounds in Figure 2-13.

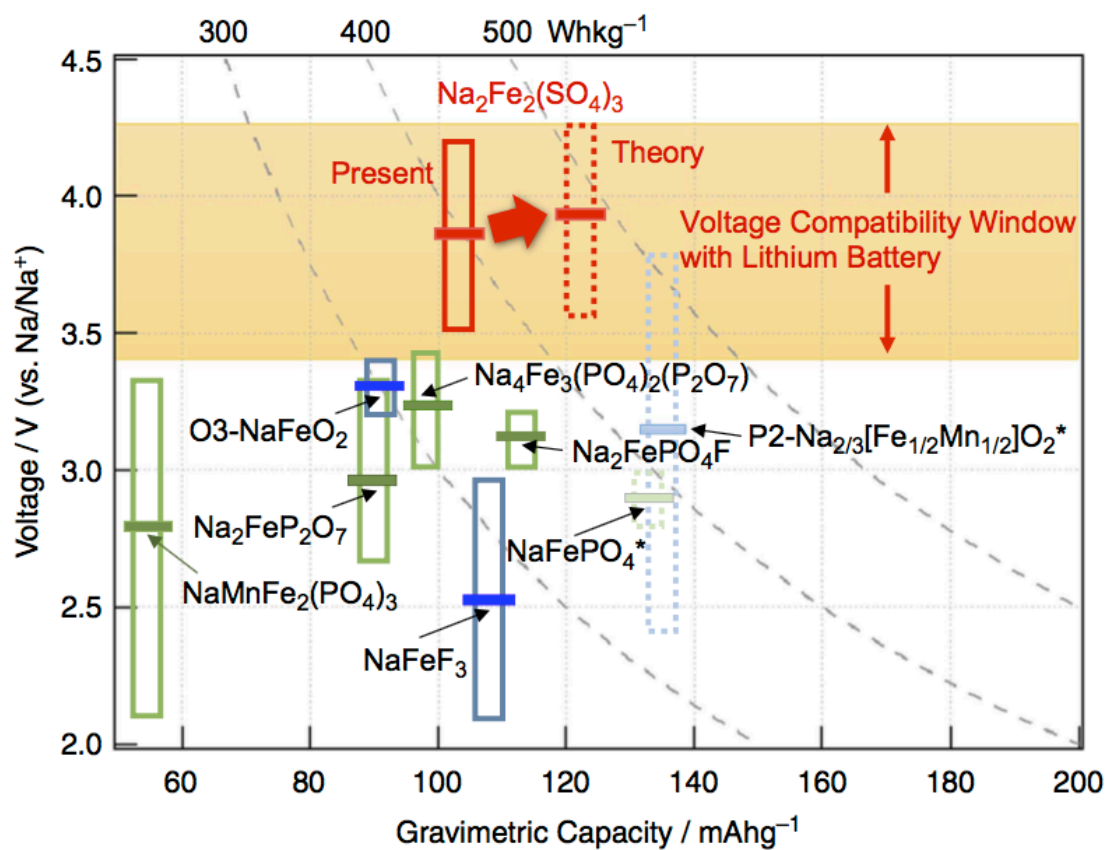


Figure 2-13: Comparison between NASICON and layered type cathode materials for sodium ion batteries. Reproduced from Ref. ²⁸¹

Table 2-6: Overview of iron and vanadium polyanionic structures used in sodium batteries.
Reformatted from Ref. ²⁸⁰

Structure Type	initial/final active material	redox couple	av. potential (vs. Na)	Theoretical capacity (mAh/g)	Energy density (W/kg)
NASICON	$\text{Fe}_2(\text{MoO}_4)_3/\text{NaFe}_2(\text{MoO}_4)_3$	$\text{Fe}^{3+}/\text{Fe}^{2+}$	2.7	91	246
NASICON	$\text{Fe}_2(\text{WO}_4)_3/\text{Na}_2\text{Fe}_2(\text{WO}_4)_3$	$\text{Fe}^{3+}/\text{Fe}^{2+}$	2.7	63	170
NASICON	$\text{Fe}_2(\text{SO}_4)_3/\text{Na}_2\text{Fe}_2(\text{SO}_4)_3$	$\text{Fe}^{3+}/\text{Fe}^{2+}$	3.3	134	442
NASICON	$\text{Na}_3\text{Fe}_2(\text{PO}_4)_3/\text{Na}_4\text{Fe}_2(\text{SO}_4)_3$	$\text{Fe}^{3+}/\text{Fe}^{2+}$	2.5	115	287
Hexagonal	$\text{Na}_3\text{Fe}_2(\text{AsO}_4)_3/\text{Na}_4\text{Fe}_2(\text{AsO}_4)_3$	$\text{Fe}^{3+}/\text{Fe}^{2+}$	2.4	90	216
olivine-type	$\text{NaFePO}_4/\text{FePO}_4$	$\text{Fe}^{3+}/\text{Fe}^{2+}$	3.0	154	462
layered	$\text{Na}_2\text{FePO}_4\text{F}/\text{NaFePO}_4\text{F}$	$\text{Fe}^{3+}/\text{Fe}^{2+}$	3.0	124	372
alluaudite	$\text{Na}_3\text{Fe}_3(\text{PO}_4)_4/\text{Na}_5\text{Fe}_3(\text{PO}_4)_4$	$\text{Fe}^{3+}/\text{Fe}^{2+}$	2.6	130	338
layered	$\text{NaFe}(\text{SO}_4)_2/\text{Na}_2\text{Fe}(\text{SO}_4)_2$	$\text{Fe}^{3+}/\text{Fe}^{2+}$	3.5	99	346
NASICON	$\text{Na}_3\text{V}_2(\text{PO}_4)_3/\text{NaV}_2(\text{PO}_4)_3$	$\text{V}^{3+}/\text{V}^{4+}$	3.4	118	401
NASICON	$\text{NaV}_2(\text{PO}_4)_3/\text{V}_2(\text{PO}_4)_3$	$\text{V}^{4+}/\text{V}^{5+}$	3.85	59	227
NASICON	$\text{Na}_3\text{V}_2(\text{PO}_4)_3/\text{Na}_5\text{V}_2(\text{PO}_4)_3$	$\text{V}^{2+}/\text{V}^{3+}$	1.6	118	189
NASICON	$\text{NaVPO}_4\text{F}/\text{VPO}_4\text{F}$	$\text{V}^{3+}/\text{V}^{4+}$	3.7	143	529
NASICON	$\text{Li}_{1.1}\text{Na}_{0.4}\text{VPO}_{4.8}\text{F}_{0.7}/\text{VPO}_{4.8}\text{F}_{0.7}$	$\text{V}^{3+}/\text{V}^{4+}, \text{V}^{4+}/\text{V}^{5+}$	4.0	142	568
NASICON	$\text{Na}_3\text{V}_2(\text{PO}_4)_2\text{F}_3/\text{NaV}_2(\text{PO}_4)_2\text{F}_3$	$\text{V}^{3+}/\text{V}^{4+}$	3.9	128	499

2.1.1.2.3.3 Fluorides

A number of metal trifluorides NaMF_3 ($\text{M} = \text{Fe}, \text{Mn}, \text{Ni}, \text{Co}, \text{Ti}, \text{V}$) have been identified as potential electrode materials for sodium ion batteries,²⁸² and are of particular interest due to the high electronegativity of the metal-fluorine bond, high theoretical capacity, and overall high safety (zero oxygen release from cathode). Metal trifluorides generally adopt a perovskite structure consisting of a 3-dimensional network of (tilted) corner shared MF_6 octahedra as shown in Figure 2-14.

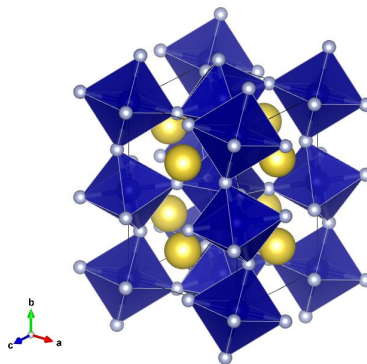


Figure 2-14: Crystal structure of NaCoF_3

In particular, FeF_3 is considered as a suitable cathode material for lithium and sodium batteries.^{283–285}

However, due to the overall insulating nature of metal fluorides, appreciable capacity is only realized when forming nanocomposites with conductive carbons; exhibiting discharge capacities from $< 100 \text{ mAh/g}$ to *ca.* 200 mAh/g .²⁸⁵

2.1.1.2.3.4 Spinel Structure

In addition to the aforementioned layered oxides, the spinel structure has demonstrated considerable utility in LIBs, and thereby is of potential interest for analogous SIBs. The chemical formula AB_2O_4 and $\text{B}(\text{AB})\text{O}_4$ describe the normal and inverse spinel structures respectively. The normal spinel structure describes the case where A ions exclusively occupy the tetrahedral sites, and B ions occupy the octahedral sites of the FCC stacked oxygen lattice. Alternatively, the term ‘inverse’ implies A ions lying solely on octahedral sites, while $\frac{1}{2}$ of the B ions occupy the tetrahedral sites.²⁸⁶ While certain exceptions exist, larger cations have a tendency to occupy the octahedral sites, with the smaller cation residing on the tetrahedral sites. Here it is important to note that specific oxidation states of the A & B cations are not solely restricted to $2^+/3^+$ oxidation states, and may/will change such to meet the condition of electroneutrality.

Komaba *et al.* have considered the inverse spinel Fe_3O_4 ($[\text{Fe}^{3+}]_{8a}[\text{Fe}_{1-3x}^{2+}\text{Fe}_{1+2x}^{3+}\square_x]_{16d}[\text{O}_4]_{32e}$ for $x < 0.05$) demonstrating more than 190 mAh/g throughout the first 10 cycles at 20 mA/g , and have speculated that Fe ion migration from 8a to adjacent 16c sites is responsible for the gradual amorphization with continual cycling in Na-ion cells using an acetylene black counter electrode.²⁸⁷ Here, iron-based spinels

offer considerable capacity, and provide a convenient and benign electrode chemistry meriting further future study.

Figure 2-15 considers the LiMn_2O_4 spinel structure, a cathode composition of interest for LIB applications due to the 3-dimensional diffusional pathways through which Li^+ ions diffuse. This section is primarily devoted to the LiMn_2O_4 spinel (space group Fd-3m) in which lithium and manganese occupy the 8a tetrahedral and 16d octahedral sites respectively. At the current writing of this manuscript, there exist only a limited number of reports on Na^+ insertion into spinel structured host materials,^{135,136,213,288,289} and thus the analogous lithium spinel is used as a frame of reference for potential future applications for sodium spinels.

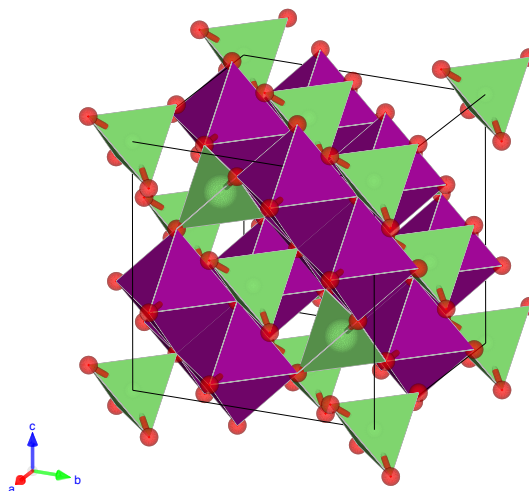


Figure 2-15: LiMn_2O_4 normal spinel structure. Li and Mn ions are located on the centers of the tetrahedral (green) and octahedral (purple) sites respectively.

Due to the multiple sites which the ‘A’ and ‘B’ cations may occupy, the Wyckoff letters (8a, 16c, 16d, 32e, etc.) are utilized to describe the respective site occupancies of the mono/multivalent cations that compose a typical spinel lattice. In the stoichiometric lithium spinel, Li^+ ions reversibly de/insert into the vacant 8a sites of the $(\text{Li})_{8a}[\text{Mn}_2]_{16d}[\text{O}_4]_{32e}$ network, throughout the $0 < \text{Li}_x < 1$ compositional range. This reaction takes place at *ca.* 4.0V (vs. Li/Li^+) with an additional insertion reaction occurring at *ca.* 3.0V (vs. Li/Li^+) as excess lithium thereby begins to insert onto adjacent 16c octahedral sites, inducing a first order transition to a rock salt phase $\text{Li}_2\text{Mn}_2\text{O}_4 = (\text{Li})_{8a}[\text{Li}]_{16c}[\text{Mn}_2]_{16d}[\text{O}_4]_{32e}$. The $\lambda\text{-MnO}_2$ phase (initially reported

by Hunter) can be synthesized by either chemical or electrochemical extraction of Li^+ from LiMn_2O_4 spinel,^{290–293} and is notably stable in the fully delithiated state. However, to the knowledge of the author, there exist no current reports on direct synthesis of the $\lambda\text{-MnO}_2$ phase.

Primary modes of capacity loss in manganese spinels are widely due to dissolution of Mn^{2+} , arising from the disproportionation of Mn^{3+} . Mn^{3+} is also a Jahn-Teller active cation, inducing cooperative distortional effects once surpassing a critical concentration of Mn^{3+} within the spinel structure. Several methodologies have been utilized to suppress the Jahn-Teller distortion, and ultimate degradation of the spinel structure; incorporating surface coatings²⁹⁴ and doping of the 16d sites such to (1) reduce the quantity of Mn^{3+} (2) increase the average oxidation state of Mn and (3) introduce a high-voltage redox reaction.^{24,26,295–306}

Regardless, manganese spinels have already demonstrated considerable electrochemical activity and utility for lithium cells, with similar progress being made in utilizing manganese spinels for sodium batteries.^{135,136,196,213,289} Commercial large-format energy storage cells utilizing $\lambda\text{-MnO}_2$ positive electrodes in an aqueous Na_2SO_4 electrolyte have demonstrated energy metrics of 19.7 Wh/kg at high power densities (3500 W/kg for potential application in grid-level storage).^{135,136,196} Several reports have investigated the modification of the LiMn_2O_4 spinel by Na substitution onto the tetrahedral sites.^{27,307} With reported spinel compositions demonstrating only minimal Na substitution is possible ($0 < \text{Na}_x < 0.01$ in $(\text{Li}_{1-x}\text{Na}_x)_8[\text{Mn}_2]_{16d}[\text{O}_4]_{32e}$) before a secondary $\text{Na}_{0.44}\text{MnO}_2$ phase begins to form. In fact, Guo *et al.* have noted that partial substitution of Na^+ onto the tetrahedral sites induces migration of Li^+ to the 16d octahedral sites by displacement of manganese.^{289,307}

Introduction of a lower valence cation onto the 16d octahedral sites has proven to enhance the stability of the spinel structure, by mitigating a first-order phase transition ($\text{Fd-3m} \rightarrow \text{I4}_1/\text{amd}$) caused by the accumulation of Jahn-Teller active Mn^{3+} .^{294,295,308,309} Actively increasing the manganese oxidation state in this manner circumvents the disproportionation reaction $2\text{Mn}^{3+} \rightarrow \text{Mn}^{4+} + \text{Mn}^{2+}$ which leads to eventual degradation in cell performance by dissolution of Mn^{2+} into the electrolyte. The disproportionation reaction is further exacerbated by large amounts of HF forming within the electrochemical cell as a result of the thermal decomposition of common LiPF_6 based electrolytes, often requiring salt stabilizers, and/or surface coatings to protect the electrode surfaces.²⁸

Ohzuku *et al.* have investigated the series of spinel structures $(\text{Li})_{8a}[\text{Mn}_{1.5}\text{M}_{0.5}]_{16d}[\text{O}_4]_{32e}$ ($\text{M} = \text{Ti}, \text{Cr}, \text{Fe}, \text{Co}, \text{Ni}, \text{Cu}, \text{Zn}$) identifying several $\sim 5.0\text{V}$ cathode materials of considerable interest for high-power applications shown in Figure 2-16.²⁹⁷ While Cr, Fe, Co, Ni, and Cu compositions all exhibit high-voltage redox reactions, $\text{Li}[\text{Mn}_{1.5}\text{Ni}_{0.5}]\text{O}_4$ demonstrates the largest high-voltage capacity, with a minimal $\sim 4.0\text{V}$ contribution ($\text{Mn}^{3+}/\text{Mn}^{4+}$) making it of primary interest for high-voltage lithium cells.^{26,296,298–306,310–313}

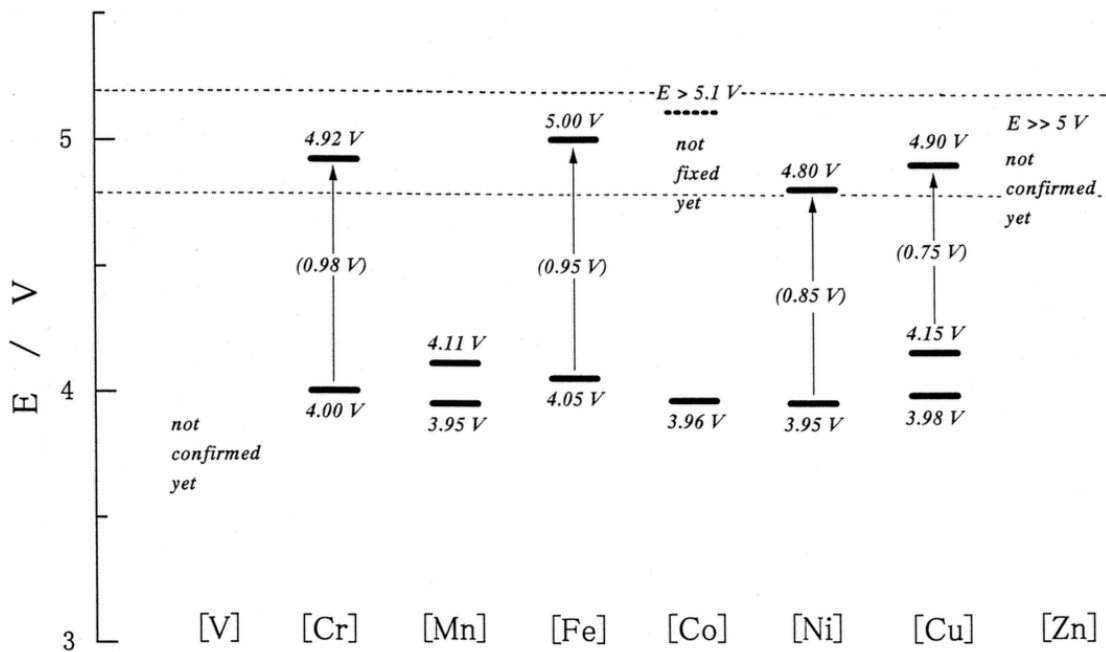


Figure 2-16: Solid-state redox potentials (vs. Li/Li^+) estimated by slow-scan voltammetry for $\text{Li}[\text{Mn}_{1.5}\text{M}_{0.5}]\text{O}_4$ compositions. Reprinted from Ref.²⁹⁷

The nickel doped $\text{Li}[\text{Mn}_{1.5}\text{Ni}_{0.5}]\text{O}_4$ (LMNO) spinel is fundamentally different from the pure manganese spinel, as all electrochemical activity lies on the $\text{Ni}^{2+}/\text{Ni}^{4+}$ redox, with manganese acting solely as a spectator ion; constantly in the 4^+ oxidation state. While the spinel structure is still retained with Ni substitution, additional cation ordering can be observed, where Ni occupies alternating MeO_6 octahedral layers along the $[1,1,1]$ direction, resulting in a primitive cubic crystal structure of space group P4_332 .²⁹⁶

In order to discern between the ordered (P4_332) and disordered (Fd-3m) lithium spinels, a convenient notation is suggested where P-LMNO and F-LMNO describe the ordered and disordered $\text{LiMn}_{1.5}\text{Ni}_{0.5}\text{O}_4$ spinels respectively, and (P/F) λ -MNO describes the ordered and disordered delithiated (vacant) spinels respectively. The current work proposes Na^+ insertion onto the 8a sites of the (F/P) λ -MNO

spinels, formulating a new cathode composition: (F/P)Na_x-MNO where Na_x describes the average 8a site occupancies of the (F/P)λ-MNO spinels respectively.

2.2 Areas of focus

The following chapters of this manuscript are devoted to the examination of the lithium spinel LiMn₂_xNi_xO₄ ($x = 0, 0.44, 0.5$) for application in analogous sodium-ion batteries. Specific challenges and characteristic behavior surrounding the Na⁺ insertion reaction, and subsequent cycling are discussed in detail using both electrochemical and physical characterization techniques; allowing for a coherent picture of the reaction phase-progression and overall evaluation of sodium spinel as a potential cathode material.

With these considerations additional research areas are identified and initial results into optimized spinel compositions are provided throughout the following chapters.

3 Experimental Techniques

3.1 Synthesis Methods

Material synthesis involves the successful conversion of raw materials to a finished product, with the majority of raw materials being provided in a powder/granular form. As this manuscript is primarily focused on material compositions for positive electrode applications in Li/Na-ion batteries, a number of different techniques have been utilized to produce high quality powder/thin-film electrodes, which will be discussed below.

Solid-state synthesis is a common method of preparing powder samples from two or more solid precursors. The majority of solid-state, and solid-state adapted synthesis methods share common steps including mixing of precursors, densification (to improve particle-to-particle contact), and calcination; where elevated temperatures are utilized to both drive chemical reactions and promote accelerated diffusional processes to form a uniform product. Mixing processes may be done in a variety of different ways, ranging from simple grinding with a mortar & pestle to high energy milling with hardened steel or ceramic media. In general, increasing the input energy into the mixing process yields a finer, more intimate mixture(s); making high-energy milling techniques preferred. Such describes mechano-chemical synthesis³¹⁴ (Figure 3-1) techniques, where precursors are pulverized by milling media, thereby generating a large amount of heat, which aids to induce chemical reactions and producing a homogenous nanocomposite..^{299,301,303,304} As such, mechano-chemical synthesis techniques such as this generally require significantly shorter annealing durations, and even lower temperatures than those relying on bulk diffusional processes, as diffusional distances are significantly shorter given the degree of mixing already afforded by the mechanical milling process.

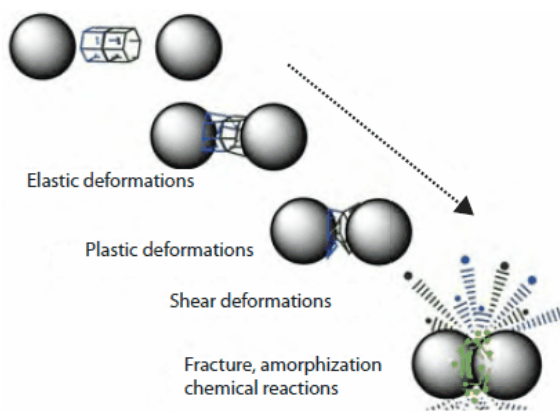


Figure 3-1: Mechano-chemical synthesis schematic, demonstrating the different types of processes taking place during high-energy milling procedures.

Here it is important to emphasize that traditional solid-state synthesis techniques involving mechanical mixing of powder precursors are generally the most economical and scalable, commonly being used throughout a number of industrial processes.

While solid-state synthesis techniques require considerable mechanical energy and/or high temperatures to promote completion of the desired reaction(s), a considerably higher degree of control and precision is offered when moving towards solution-based synthesis techniques. Alternative solution-based methods have proven to be equally effective at creating highly mixed precursors, only requiring further calcination to yield nano/macro-crystalline powders. The co-precipitation method is commonly utilized to synthesize a number of oxide powders of highly uniform particle size and morphology by precipitation of mixed hydroxide intermediates followed by several filtering/washing/drying/mixing steps prior to calcining at high temperature.²⁹⁶ While the co-precipitation method offers a huge degree of control over chemical composition, this technique is largely limited by the number and types of insoluble products that may form in solution, typically requiring additional mechanical mixing steps to produce the desired product. It then becomes obvious, that an ideal synthesis route would encompass the superior mixing capabilities of solution-synthesis, while eliminating additional mechanical mixing steps.

Molten-salt synthesis techniques have demonstrated further control over particle morphologies and crystallinity in addition to reducing trace level impurities by reaction with an sol-gel formed intermediates.³¹³

The Pechini synthesis technique is commonly used for fabricating high quality electrode materials³⁰⁰ for electrochemical devices, as it enables a highly uniform and finely mixed oxide upon final calcination. Initially intended for use for lead/alkaline-earth titanates/niobates,³¹⁵ the Pechini method encompasses the use of a hydrooxycarboxylic acid:polyhydroxy alcohol solution to chelate metal cations; forming a polymeric resin intermediate *via* an esterification reaction. The Pechini method greatly diverges from the co-precipitation method by effectively solidifying the dissolved metal cations in a polymeric intermediate resin, whereas the co-precipitation method would typically result in one or more mixtures of crystals of varying composition(s) forming upon evaporation of the solvent.

By nature of dissolving precursors into a suitable acid/alcohol solution, the Pechini technique allows for an intimate degree of mixing on the atomic level, superior to that obtained through energy-intensive mechanical milling. Instead, the polymeric resin binds the mixture of transition metal cations within a cross-linked network of bridging oxygen and organic radical bonds. In particular: alpha-hydroxycarboxylic acids (commonly citric acid) chelates with the transition metal precursors to form a polybasic acid, which further undergoes polyesterification when heated in the presence of a polyhydroxy alcohol. Specific choice of the polyhydroxy alcohol as reported in³¹⁶ controls the progression of the esterification reaction, yielding drastically different particle morphologies. Ethylene glycol is commonly chosen for Pechini synthesis of cathode materials^{300,317–321} producing a very fine and homogenous mesostructure that results from the evolution of micropores during final burn-off of excess organics. With regard to electrode materials, the Pechini technique is highly attractive, as it enables the synthesis of a high-quality, mesoporous network of nanocrystalline particles. The Pechini method itself is only largely limited by the types of compatible precursors, and with specific examples being discussed in later chapters.

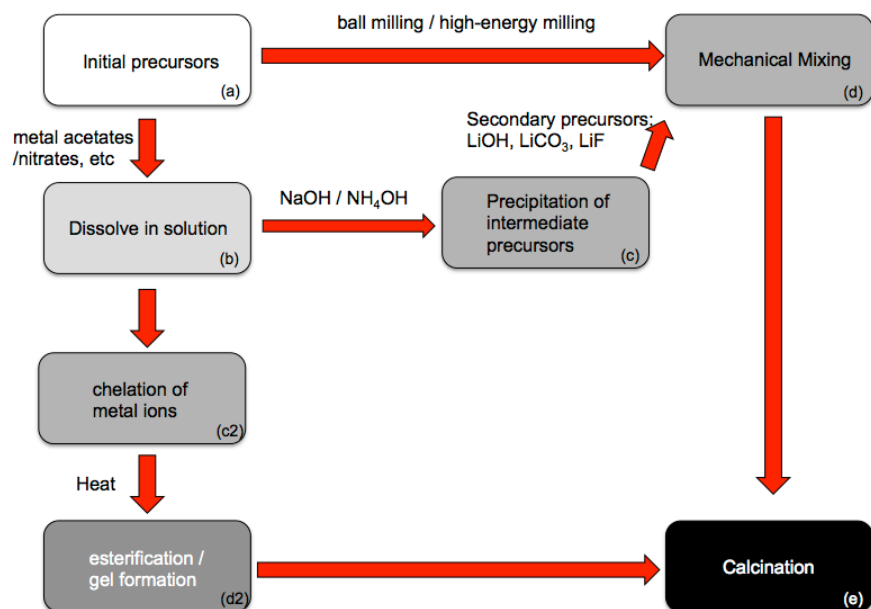


Figure 3-2: Generic material synthesis flow-diagram including solid-state synthesis (a→d→e), co-precipitation method (a→b→c→d→e), and Pechini synthesis (a→b→c2→d2→e).

3.2 Characterization Techniques

3.2.1 X-ray Diffraction (XRD)

The interaction between X-ray radiation and matter is the basis of a crucial scientific technique used to probe the fundamental and complex processes that occur within crystalline and non-crystalline bodies. While diffraction is a particularly powerful tool when utilized for crystalline bodies, fundamental and important information on liquids and amorphous solids can also be obtained through this simple, yet profound technique. This chapter will encompass the various subtleties surrounding X-ray diffraction (XRD) on crystalline materials, experimental considerations, and meaningful deductions that can be made from experimental diffraction data.

3.2.1.1 Powder diffraction, Bragg-Brentano geometry, and experimental considerations

As the Braggs' equation demonstrates, utilizing X-ray diffraction for material characterization is highly sensitive to the relative positioning between the sample and our measurement device. Early X-ray 'detectors' simply comprised of an X-ray sensitive film, producing dark spots/rings according to the respective intensities of the corresponding (*hkl*) planes. With the progression of X-ray detectors and computing power, it is commonplace to utilize a solid-state detector in what is termed Bragg-Brentano

geometry. Figure 3-3 illustrates the layout of the Bragg-Brentano geometry, seen almost unanimously throughout laboratory diffractometers. Compared to diffraction experiments utilizing film-based detection, (commonly referred to as cameras) diffractometers only sample a narrow range of the diffraction cone[†], generating a 2-dimensional plot of 2θ vs. diffracted intensity.

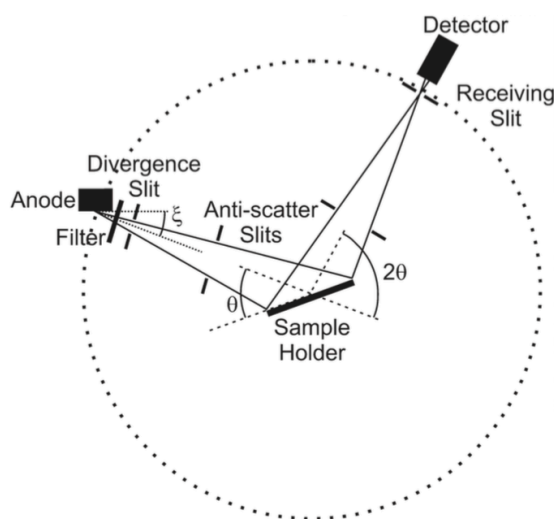


Figure 3-3: Bragg-Brentano geometry used for a typical X-ray diffractometer. Reproduced from Ref.

322

When considering diffraction of a crystalline body, descriptions and calculations are frequently based off of a single crystalline domain known commonly as a single crystal. While single crystal diffraction is a powerful technique, it is often incredibly difficult to fabricate high quality single crystals of sufficient size for diffraction analysis; as such, typical XRD samples are polycrystalline in nature, composed of many regions which can be said to be continuous with respect to the dimensions of a single unit-cell. Individual crystalline regions as described here are typically interrupted by an interface known as a grain boundary: an interface where the crystallographic orientations of two neighboring crystals are tilted by some angle.

[†] The diffraction cone is a term used to refer to the shape of the diffracted X-ray beam that satisfies the Bragg condition; for a given single-crystal/polycrystalline sample, a lattice plane which satisfies the Bragg condition will diffract X-rays in all directions at an angle equal to the incident beam, thereby creating a conical shape.

The overall size and morphology of the crystalline regions are widely controlled by the particular method of material synthesis and processing steps involved; yielding polycrystalline samples ranging from monodispersed nanocrystals to highly asymmetric columnar or plate shaped crystals on the order of hundreds of microns in diameter. Exotic crystal shapes such as these demonstrate the intrinsic symmetry within the crystalline phase under investigation, and introduces diffracted intensities that greatly differ from those of randomly distributed crystallites, which is taken as a general assumption of powder XRD. Such is the problem of preferential orientation, where the observed diffraction data of certain (hkl) planes are over/under-emphasized by nature of the statistically higher amount of a given (hkl) planes relative to another. Similarly, the number of coherent diffracting planes will influence the diffracted intensities, with larger particle sizes contributing to sharper, more defined peaks than crystallites of finer dimensions. In order to separate the contributions between particle size and preferred orientation, the Scherrer equation³²³ takes into account the half-peak broadening that occurs due to varying crystallite size. It can be stated as:

Equation 3-1:

$$t_{hkl} = \frac{K\lambda}{\sqrt{\beta_{obs}^2 - \beta_{ref}^2 \cos^2 \theta}}$$

The Scherrer equation describes how the mean crystallite size pertaining to a specific set of planes (t_{hkl}), X-ray wavelength (λ), peak breadth measured at half maximum intensity (β_{obs} , β_{ref}) for the observed and reference sample respectively, and the Bragg angle (θ) are interrelated. K is a dimensionless scalar known as the shape factor, with a value close to unity. Here it is important to note the inclusion of a reference/standard sample in the calculation of the crystallite size. This is done in order to account for broadening of XRD peaks arising from specific instrumental considerations. As such, the ideal reference sample for such analysis should possess a number of qualities:

- (1) Possess zero strain within the crystal lattice
- (2) Exhibit negligible broadening due crystallite size
- (3) Be consistently analyzed anytime changes in instrumental optics/stages/alignment are made.

In fact, a plot of X-ray intensities against their 2θ positions, should in theory, produce what is termed a ‘stick-pattern’ where diffracted beam intensities are only observed at those angles where the Bragg condition is satisfied. However, typical powder samples are generally, comprised of a random

distribution of crystallites, where certain (hkl) planes of differing particles are satisfying the Bragg condition at any given time, contributing a finite amount of background noise that is superimposed onto the measured intensities. Peak breadths can be easily visualized by considering two separate crystallites that are in almost identical orientations. As the first particle is aligned such that it satisfies the Bragg condition, the second particle, which is rotated slightly from particle 1 is not contributing any coherent diffraction, and thereby is not adding to the observed peak intensity. However, as the diffractometer continues to rotate through the given 2θ range, particle 2 will begin to coherently diffract, with particle 1 no longer satisfying the Bragg condition. It is clear that outside of a single-crystal sample, a finite amount of peak breadth is inevitable; making it experimentally difficult to analyze samples comprising of asymmetrically shaped particles or those that are nanocrystalline in nature. It is also important to note additional sources of peak broadening, which may arise from the temperature factor (B-factor, or B_{eq}), which consider the displacement of atoms due to thermal vibrations.

3.2.1.2 *Crystal structure solution & Rietveld refinement*

The discovery of unique elements, and the eventual composition of the periodic table, undoubtedly presented early researchers with the great mystery as to how are individual atoms are arranged within a solid body to contribute to the various properties of everyday objects. Such is the topic of crystal structure solution. In fact, early crystal structure ‘solution’, simply involved the inferring of the internal symmetry and atomic arrangement from the physical appearance of high quality crystals, and was not replaced until the early 1900’s. The first crystal structure to be successfully solved (NaCl) was performed by W. L. Bragg following the early and pioneering works of M. V. Laue, which was based on the geometric relationships of diffraction spots in a typical Laue diffraction pattern. While this technique was only successful for a handful of simple crystal structures with a high degree of symmetry, it has since opened the doorway to complex inorganic and organic crystal structures. The overall structure solution model consists of four (non-trivial) steps:

1. Collection of highly quality (single-crystal/powder) diffraction pattern
2. Indexing of diffraction pattern
3. Determination of diffraction peak intensities
4. Structure solution

It was only after the realization that the 3-dimensional crystal lattice may be easily represented by Fourier methods that the Patterson method was developed for the interpretation of Fourier maps, eventually leading to “direct method” software(s) for structure solution. Such methods give a picture of the internal atomic arrangement by mapping of the electron density within the crystal structure. While powder diffraction had demonstrated significant utility in phase identification and quantitative analysis, such methods were frequently left for analysis of single-crystal specimens, and full utility of powder diffraction was only realized through adaptation of neutron diffraction techniques developed simultaneously by Georg Will (1962) and Hugo Rietveld (1965).

Widely praised for his pioneering work on structure refinement, Rietveld established the method of structure refinement by least squares refinement in which a theoretical XRD pattern is fitted to all the measured intensities of the diffraction profile. Largely differing from structure solution methods, the Rietveld method requires preexisting knowledge on the specimen; namely a ‘best-guess’ crystal structure is needed to begin meaningful Rietveld analysis. Equation 3-2 describes the refinement process. M is the function being minimized, W_i is the statistical weight fraction of element i , and y_i^{obs} & y_i^{calc} are the intensities of the observed and calculated XRD patterns respectively.

This technique provides a significant step forward in ‘solving’ crystal structures, as structure determination previously could only be reliably done for very simple materials³²⁴ due to the problem of convoluted Bragg reflections, and the need to separate individual (hkl) intensities for implementation in one of the various structure solution techniques (Patterson methods, etc.). While this technique was initially developed for use with monochromatic neutron diffraction, it equally applies for time of flight, synchrotron, and monochromatic X-ray diffraction; the latter being the focus of this section.

Equation 3-2:

$$M = \sum_i W_i (y_i^{obs} - y_i^{calc})^2$$

The Rietveld method alone is incredibly efficient at dealing with convoluted peaks that may arise from overlapping peaks within a single or multiphase specimen given that certain care has been taking in the initial indexing of the diffraction pattern, with most ‘failed’ attempts of Rietveld refinement being the

result of a poorly conditioned initial structure, or due to insufficient data for the given number of refined parameters.

Differing from the high quality specimens utilized throughout single-crystal diffraction, powder diffraction samples introduce certain deviations in peak shape(s) to the overall diffraction pattern, with special consideration of the peak shape dependence of particle size and lattice stress/strain being necessary for high quality Rietveld refinement. Peak shape considerations have sprouted a number of different peak-shape functions to best describe the specific contributions both the instrumental setup and sample impart on the diffraction profile. While neutron diffraction experiments almost exclusively exhibit a Gaussian peak shape, implementation of the Rietveld technique for X-ray diffraction has also resulted in the utilization of additional peak shape functions becomes necessary.³²³ Equation 3-3 and Equation 3-4 describe the Gaussian, and Pseudo-Voigt (Lorentzian + Gaussian) peak shapes respectively.

Equation 3-3:

$$y_{obs} = I_{calc} e^{\frac{-4 \ln(2)}{H_{calc}^2} (2\theta_{obs} - 2\theta_{calc})^2}$$

Equation 3-4:

$$y_{obs} = I_{calc} [\eta L(2\theta_{obs} - 2\theta_{calc}) + (1 - \eta) G(2\theta_{obs} - 2\theta_{calc})]$$

Where y_{obs} describes the observed intensity at position $2\theta_{obs}$, H_{calc} is the full width at half maximum, $2\theta_{calc}$ is the peak center of the reflex, I_{calc} is the calculated intensity of the reflex, and η is a weighting term.

Meaningful structure refinement then becomes possible once the number of observations (observed diffraction peaks) exceeds the number of refined parameters such that minimization of M yields a global minimum, representing a solution of minimum variance.³²⁵ It is of particular importance to realize that in performing a least-squares fit, various local minima ‘solutions’ are likely to arise, and sensibility of the refined parameters should always be verified throughout each step of refinement in order to rule out such false solutions.

As the Rietveld method includes all measured data points, the background intensity and how it is accounted for, is a crucial step in the refinement process. Equation 3-2 assumes that the background intensities have been subtracted, which often becomes difficult when specimens contain a large background, or contain additional amorphous phases. Generally, the background is modeled by considering data points between diffraction peaks where no diffraction contribution is taking place, making it important to consider only high-quality diffraction data for Rietveld refinement, as minor diffraction peaks require a

sufficient incident X-ray/neutron intensity to be easily discernable from the background. However, such considerations always become exceedingly more difficult when dealing with amorphous phases, with various software packages (Topas, FULLPROF) allowing for modeling of additional amorphous/semi-crystalline phases during the refinement process.

Here it is important to emphasize that the Rietveld technique is a means of structure refinement rather than structure solution, as some initial ‘best guess’ is required to calculate diffraction intensities, and reach a meaningful result via the least squares approach. Assuming proper care has been taken to check for sensibleness in the refined parameters, the quality of the least squares refinement is generally measured by multiple residual values calculated as:

$$R_p = \frac{\sum[Y_{obs} - Y_{calc}]}{\sum Y_{obs}} ; R_{wp} = \sqrt{\frac{M}{\sum wY_{obs}^2}}$$

R_p and R_{wp} describe the ‘profile’ and ‘weighted profile’ residual values; more commonly summarized as X^2 or the Goodness-of-fit ($GOF = X$).

3.2.1.3 *In-situ diffraction electrochemical cells*

Dealing with structural changes resulting from the de/insertion of alkali ions (Li/Na) into a crystalline host, electrode materials are of prime interest for *in-situ* & *operando* XRD study. Particularly, *in-situ* diffraction is a very accurate means of measuring the lattice parameters during normal electrochemical cycling, providing valuable physical measurements which can be directly correlated to the characteristic voltage profile of the active material(s) under investigation.

In this case, *in-situ* diffraction is well suited for distinguishing between single-phase and two-phase reactions, which frequently occur within insertion/conversion type materials. While single-phase reactions are generally characterized by a smooth/sloping voltage profile indicative of a solid-solution type behavior, the latter demonstrates a very stable voltage plateau attributed to structural changes (typically compositional/structural) that occur throughout the de/insertion process. While, the voltage profile alone can distinguish the difference between the two reaction mechanisms, little can be said as to the extent of the structural change (volumetric change) by examination of the electrochemical data alone. Such is the case for $\text{Li}_4\text{Ti}_5\text{O}_{12}$,³²⁶ which observes a two-phase redox reaction, but with zero volumetric change; demonstrating the importance of *in-situ* and *operando* physical measurements of electrode materials.

In order to record meaningful *in-situ* measurements, one must consider the experimental setup; particularly the cell chemistry, and mode of measurement desired. Cell chemistry places important restrictions onto the general makeup of the electrochemical cell body with cell assemblies ranging from stainless steel casings to aluminized polymeric pouches depending on possible interactions cell body materials may have on the electrochemistry. This is highlighted when comparing the differences in material suitability between aqueous and conventional inorganic electrolytes; the latter requiring a completely dry and oxygen free environment due to the highly reactive nature of the Li/Na metal anodes typically used.^{59,327,328} The majority of *in-situ* electrochemical cells can be divided into two main categories based on the geometry with the incident radiation: (1) Transmission and (2) Reflection (standard diffraction). Within these two categories, only X-ray and neutron electrochemical cells are considered, with additional considerations on infrared spectroscopy covered separately.

3.2.1.3.1 Transmission-geometry *in-situ* electrochemical cells

When imaging samples in transmission geometry, it is foremost important to realize that the data obtained is an averaged summary of the bulk characteristics, as opposed to phenomena restricted to the outermost surfaces of the active particles under investigation. As such, *in-situ* measurements are typically limited to high intensity X-ray/neutron sources,^{329–340} as typical laboratory diffractometers are not able to produce X-rays capable of penetrating the entire cell stack[‡]. Differing from the conventional Bragg-Brentano geometry, utilization of a 2D area detector allows for fast collection times with additional spatial resolution as opposed to conventional 1D diffraction spectra. Generally speaking, utilizing high-intensity beams such as those provided by synchrotron/neutron user facilities seldom requires the used of a specially designed electrochemical cell, as the incident beam intensity is sufficient to penetrate the typical stainless steel casing of conventional coin cell type batteries, and it is customary to simply utilize commercial lithium/sodium-ion cells for *in-situ* characterization, eliminating potential concerns around quality/lack of hermetic seals in specially designed electrochemical cells.

[‡] The term cell stack is used to refer to the typical construction of an electrochemical cell: outer casing, current collector, positive electrode, separator + electrolyte, negative electrode, current collector, outer casing in that order

3.2.1.3.2 Reflection-geometry in-situ electrochemical cells

The reflection geometry is the same as that previously described for Bragg-Brentano based diffractometers, and is the most common cell design when utilizing laboratory X-ray sources. Compared to high intensity beam lines, which can produce X-ray energies in excess of several MeV, conventional laboratory diffractometers are limited to relatively ‘soft’ X-rays operating *ca.* 8 keV (Cu source), placing prime concern around the attenuation of the X-ray beam.

Due to attenuation of the incident beam, the typical stainless steel casing which acts as both a rigid support and current collector, are replaced with an X-ray transparent window, allowing for sufficient diffracted beam intensities to be measured. While Kapton, and similar polymeric films have been documented,^{341,342} beryllium is a commonly used X-ray window, as it provides suitable mechanical and electrical properties to ensure that the electrode of interest maintains a flat reference plane while also circumventing the need to use additional current collectors. Here it is important to distinguish, that due to the proportional relationship between X-ray attenuation and atomic number, selection of low Z-compounds for X-ray windows is necessary. In fact, movement away from beryllium windows is only necessary when considering high-voltage materials, often reporting aluminum foil windows on the order of a few microns,³⁴³ or implementing modified cell assemblies that act to electronically isolate the beryllium from the electrochemical cell,³⁴⁴ thereby preventing dissolution of the beryllium, and contamination of the electrolyte.

Despite these considerations, the large variety between laboratory X-ray diffractometers presents itself as an unsolvable problem with no single design capable of being deemed ‘ideal’. The individual design of the electrochemical cell is then only limited by the physical constraints of the individual sample mounts within the diffractometer and considerations of the experimentalist; with many reports designing custom machined assemblies designed for easy loading, cleaning, and mounting within their respective diffractometers.^{327,337,343,345}

While initial concerns are largely centered around the specifics of the cell construction, it is important to note that alignment of the in-situ cell within the diffractometer is a crucial step that will determine the intrinsic error in the measured diffraction data due to the relationship between sample height displacement from the diffracting plane and the measured d-spacings. A number of solutions are possible

including (1) correction/alignment of in-situ cell according to an internal standard (2) designing the in-situ cell to be accurately and reproducibly installed in between diffraction measurements or (3) to perform successive X-ray scans without altering the cell alignment to ensure zero relative change in sample height between XRD measurements. The latter is the preferred technique used throughout this manuscript, and allows for a reliable account for the phase evolution throughout electrochemical cycling.

3.2.2 Fourier Transform Infrared Spectroscopy (FTIR)

Infrared spectroscopy works off of the general interactions between the chemical bonds within a sample and electromagnetic radiation; in particular, the vibrational and rotational energy levels associated with the liquid/solid samples. The topic of infrared absorption and Raman spectroscopy has been covered by numerous texts,³⁴⁶ with only relevant applications towards battery components (electrode/electrode surfaces/electrolyte) being considered within this section.

As mentioned throughout the previous sections, electrode materials generally consist of a mixture of transition metal cations within their respective 3-dimensional networks (layered, spinel, NASICON, etc.). Fourier Transform Infrared Spectroscopy (FTIR) is particularly powerful in identifying cationic ordering within electrode materials (resulting from specific synthesis conditions) that would otherwise require advanced synchrotron or neutron sources. Taking the example of $\text{LiMn}_{1.5}\text{Ni}_{0.5}\text{O}_4$ (P-LMNO) spinel, FTIR allows for quick discrimination between the disordered (random distribution of Mn and Ni on octahedral sites) and ordered phases by nature of the increasing absorption of the Ni-O band around 588 cm^{-1} as illustrated by Figure 3-4.

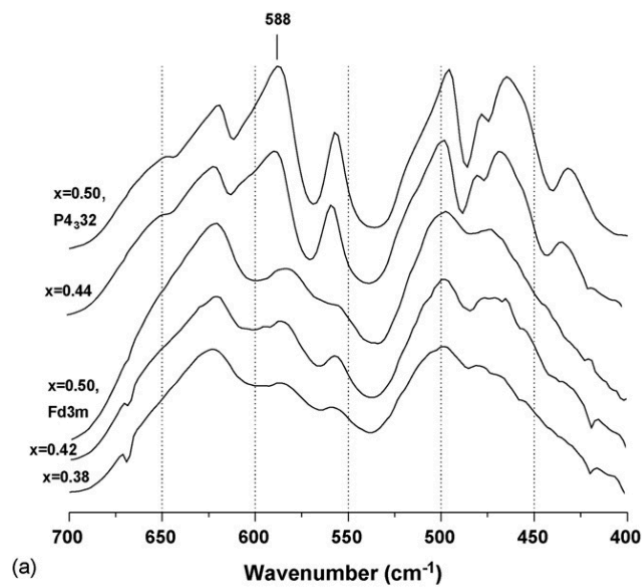


Figure 3-4: Infrared spectra for $\text{LiMn}_{2-x}\text{Ni}_x\text{O}_4$ spinel annealed in air at 700°C. Reproduced from Ref.

306

Various *in-situ* studies have also been made, particularly investigating the state of the electrolyte and the progression of the SEI layer under dynamic conditions.^{347–352} Experimental investigations of this type require specially designed electrochemical cells as shown by Figure 3-5, with careful assembly and control over thickness of the active electrode(s) being crucial due to the need to operate in a transmission geometry.

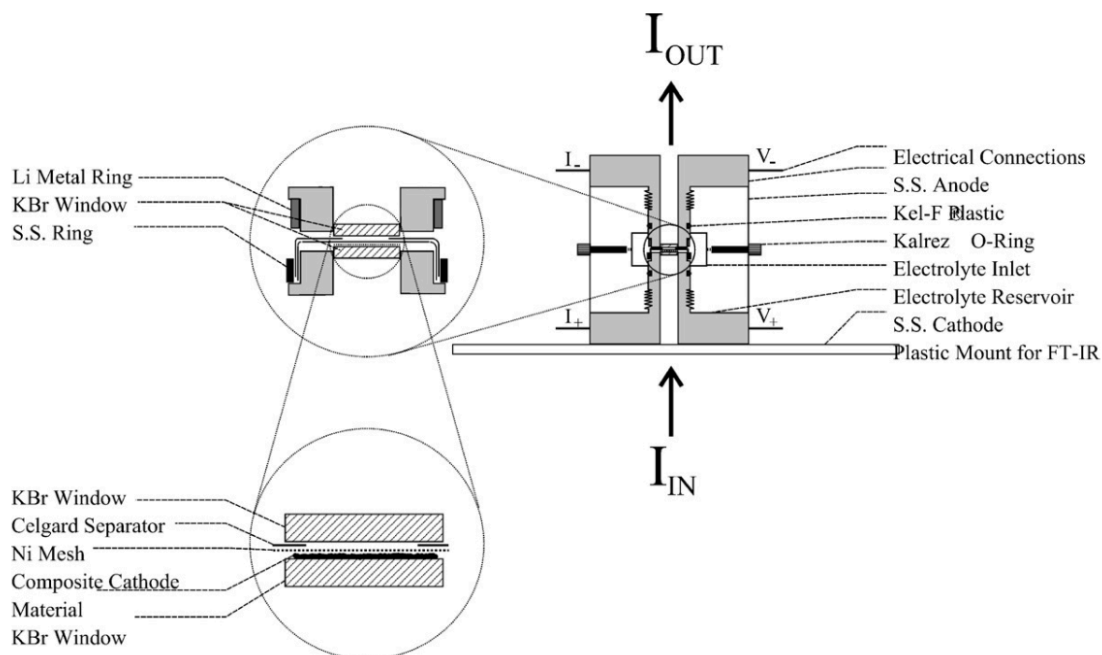


Figure 3-5: Schematic of an *in-situ* transmission FTIR electrochemical cell. Reproduced from Ref. ³⁴⁷

It is important to note, that considerable absorption/background noise takes place due to the electrolyte used within the electrochemical cell, placing further experimental limitations to the cell geometries compatible in *in-situ* measurements. Overall, FTIR/Raman are powerful tools, often used to characterize the very thin/fragile passivating SEI layer that enables long-term cyclability in the majority of electrochemical cells (excluding ionic-liquid based cells). Surface specific characterization techniques such as these are further being supplemented by *in-situ* atomic force microscopy (AFM)^{353,354} and similar microprobe techniques, to give a full picture of the unique chemistries that take place at the electrode surfaces.

3.2.3 Brunauer-Emmett-Teller (BET) surface area

In 1938, Brunauer, Emmett, and Teller described a theory of multilayer gas adsorption onto a solid surface, serving as the basis for modern surface area measurements.³⁵⁵ The BET theory is itself an extension of the Langmuir theory, which describes the monolayer adsorption of gas molecules onto a solid surface, and is based on a number of assumptions:³⁵⁶

- (1) Adsorption occurs solely on well-defined surface sites
- (2) Molecules can act as a single adsorption site for a molecule in an upper layer

- (3) The outermost layer is in equilibrium with the gas phase
 - a. Similar molecular adsorption/desorption rate
- (4) Desorption is a kinetically limited process
 - a. Heat of adsorption must be provided
- (5) At the saturation pressure, the molecule layer number tends towards infinity
 - a. Equivalent to the sample being surrounded by a liquid phase

As a whole, surface area calculations are based on the application of the adsorption isotherm described by:

Equation 3-5:
$$\frac{1}{v[(p_0/p)-1]} = \frac{c-1}{v_m c} \left(\frac{p}{p_0} \right) + \frac{1}{v_m c} ; \quad c = e^{(E_1 - E_L/RT)}$$

Here, p and p_0 indicate the equilibrium and saturation pressure of adsorbates at the adsorption temperature, v is the quantity of adsorbed gas, v_m is the quantity of gas resulting from monolayer adsorption, and c is a term called the BET constant; itself including E_1 and E_L : the heat of adsorption for the 1st and 2nd – n^{th} layers respectively. Within BET measurements, adsorbates are generally confined to non-corrosive gases (nitrogen, argon, helium, krypton), making routine surface area measurement a simple matter, by the conveniently linear form the adsorption isotherm provides:

Equation 3-6:
$$S_{BET} = \frac{v_m N_s}{V a}$$

S_{BET} describes the specific BET surface area, N is Avogadro's number, 'S' is the adsorption cross section of the adsorbing species, 'V' is the molar volume of the adsorbate gas, and 'a' is the mass of the sample.

BET surface area measurements play an important role in electrode design; enabling tuning of the specific rate capability of a material, to describing the poor electrochemical performance by nature of excessive surface area (that only acts to catalytically decompose the electrolyte). In either case, BET provides a quick and reliable means of measuring surface areas of nano/macro-crystalline samples, making it a crucial analytical tool for electrochemists. Additionally, average pore size distributions can be further elucidated by examination of multipoint BET measurements, and are of considerable importance when

considering the active surface area of a sample. Utilization of multiple p_0/p measurements, an inferred pore radius can be extracted considering the layers of adsorbed species.^{357,358}

3.2.4 Coulometric Titration Techniques

Early investigations into alloying-type anode materials utilizing coulometric titration techniques have grown into powerful electrochemical characterization tools, providing valuable information on reaction thermodynamics and kinetics of electrode materials. In particular, coulometric titration techniques including Galvanostatic intermittent titration (GITT), and potentiostatic intermittent titration (PITT) were designed to measure the chemical diffusion coefficients of solid alloy electrode materials. Movement from measurements by chemical tracer,³⁵⁹ and similar destructive evaluation methods has accounted for a large expansion into reported diffusion measurements of electrode materials. Previously, the measurement of diffusion coefficients have been made by inferred data from galvanostatically cycled electrodes,^{360–363} mainly taking into account only the time and current flow associated with the de/intercalation process.

Taking a first-principles approach, Wen *et al.* established the potentiostatic technique³⁶⁴ where sudden potential steps are imparted on a planar electrode with a uniform initial concentration (C_0) of the mobile species ‘A’ in the bulk. Once the potential is changed, a new activity of ‘A’ is imposed by the new concentration gradient at the electrode surface C_s . In order to maintain the surface concentration at a constant value C_s , a continual supply of ‘A’ through the electrolyte takes place as ‘A’ diffuses through the electrode until reaching a bulk concentration of C_s throughout the entirety of the electrode. The magnitude of the current response thereby provides a measure of the chemical diffusion flux, giving a simplified calculation of the diffusion coefficient by one of two approximations:

$$\text{Equation 3-7:} \quad I(t) = z_A F S (C_s - C_0) \sqrt{\frac{\tilde{D}}{\pi t}} \quad \text{for } t \ll L^2/D$$

$$\text{Equation 3-8:} \quad I(t) = \frac{2z_A F S (C_s - C_0) \tilde{D}}{L} e^{-\frac{\pi^2 \tilde{D} t}{4L^2}} \quad \text{for } t \gg L^2/D$$

Here, S is the cross-sectional area common to the sample electrode and electrolyte, z_A is the charge number of the electroactive species, F is Faraday’s constant, L describes the characteristic diffusional length, and C_s/C_0 described the surface and initial concentrations of ‘A’ within the electrode sample. Due to the tight control over potential ranges, PITT offers itself as a high-resolution

electrochemical technique as close examination of single/multi-phasic regions can be studied independently. However, ohmic potential drop within the electrolyte, and transient charge buildup at the electrode surfaces often cannot be avoided, providing subtle drawbacks of the PITT method. Utilization of a pulsed Galvanostatic technique^{365,366} further exceeds the shortcomings of the PITT method, where constant current pulses are provided to the electrochemical cell followed by prolonged rest periods where the system is allowed to return to equilibrium. Diffusion coefficients can be determined by the approximation:

$$\text{Equation 3-9:} \quad \tilde{D} = \frac{4L^2}{\pi t} \left(\frac{\Delta E_s}{\Delta E_t} \right)^2 \quad \text{for } t \ll L^2/D$$

Where ΔE_s and ΔE_t represent the change in the steady-state voltage and total change in voltage during the constant current pulse respectively. The GITT method overcomes the ohmic voltage drop, which is present as an added time-independent constant, easily subtracted by the extrapolation of E vs. $t^{1/2}$ to $t = 0$. However, due to the changing concentration gradient at longer time scales, the GITT method can only be utilized over a compositional range where the titration curve can be assumed to be linear:

$$\text{Equation 3-10:} \quad (E(t) - E(t = 0))_{t=0} = \frac{ILV_M}{3Z_A F S \tilde{D}} \quad \text{for } t > L^2/D$$

Where 'I' is constant current pulse, and V_M is the molar volume of the electrode sample. While these simple electrochemical techniques can yield valuable information on the reaction kinetics within electrode materials, these treatments are however, still limited to single-phase de/insertion type electrodes as only diffusional processes are accounted for. In order to extend this technique into materials that exhibit phase transformations during de/insertion, the consideration of the interphase boundary migration is needed. Due to this shortcoming, 'traditional' PITT, and especially GITT are generally regarded as unreliable methods for diffusion coefficient calculations within multiphasic compositions, frequently only providing apparent diffusional data, as considerations of the boundary migration become necessary.

As described 'traditional' PITT/GITT methods are modeled based on flat electrode geometry, requiring added considerations when moving toward spherical particle geometries, which are far more

common.³⁶⁷ Further extending on the traditional coulometric titration techniques, Funabiki and Levi, have proposed moving-boundary models taking into account added energetic interactions that occur during phase transformations for PITT and GITT.^{368,369} Here, the diffusion is considered to be the only factor controlling boundary migration during the phase transformation. However, it is important to realize that the phase transformation occurs under nonequilibrium conditions; being itself a combination of diffusion and interface migration, making it exceedingly difficult to accurately reflect true characteristics of the electrode material within the two-phase region still.

Further extending on this approach, Zhu and Wang³⁷⁰ introduce additional considerations on the strain energy imparted by the lattice mismatch between the two phases during the phase transformation process in LiFePO₄ electrodes. The mixed-control phase transformation model is based on the layer growth and interface migration of the secondary phase, as the diffusing species moves through the particle surface (secondary phase) to the interface; driving the gradual rearrangement of the crystal lattice of the parent phase into the secondary phase. Consideration of the strain energies within the interphase region further highlights the uncertainty in measuring the two-phase region by traditional PITT/GITT. While traditional coulometric titration techniques commonly report *ca.* 2-3 orders of magnitude difference between the single-phase and two-phase regions, the mixed-control method estimates the actual difference in diffusion coefficients to be within a factor of 10, with the large discrepancy in the former calculations being caused by not considering boundary migrational effects. While it is possible to separate the two factors, it is however often the case that only the boundary migration is of importance, as it is the rate limiting process throughout the described reaction.

Considering two phases α and β , the $\alpha \rightarrow \beta$ transformation requires two simultaneous processes: (1) β -phase layer growth & interface migration, and (2) diffusion of 'A' from the surface into the interface, and through the β -phase layer as shown schematically by Figure 3-6. The mixed control phase-transformation model demonstrates that the driving force ΔG_d for the $\alpha \rightarrow \beta$ transformation is primarily the sum of the chemical driving force ΔG_{chem} , strain accommodation energy ΔG_{strain} , and the interface energy ΔG_{int} :

Equation 3-11:
$$\Delta G_d = \Delta G_{chem} + \Delta G_{strain} + \Delta G_{int}$$

In the simplified case of a planar electrode, the interface energy may be ignored, with added geometric terms arising when considering spherical particles³⁶⁷ and additional geometries. Overall the terms for the chemical and strain components then become simple relations of the relative concentrations of 'A' in the α/β -phases and the equilibrium potential:

Equation 3-12:
$$\Delta G_{chem} = \left(\frac{C_{\beta}^i - C_{\alpha}^i}{C_{max}} \right) F E_d^i - \left(\frac{C_{\beta}^{eq} - C_{\alpha}^{eq}}{C_{max}} \right) F E_{eq}$$

Equation 3-13:
$$\Delta G_{accom} = \left(\frac{C_{\beta}^{eq} - C_{\alpha}^{eq}}{C_{max}} \right) F E_{eq} - \left(\frac{C_{\beta}^i - C_{\alpha}^i}{C_{max}} \right) F E_d^i = f(x_i)$$

With C_{β}^i and C_{α}^i representing the interfacial concentrations of 'A' in the β and α -phases respectively. C_{β}^{eq} and C_{α}^{eq} are the equilibrium concentrations of 'A' in the β and α -phases respectively. C_{max} is the maximum concentration of 'A' possible within the host structure, F is the Faraday constant, E_d^i is the dynamic interfacial potential measured during discharge, and E_{eq} is the strain-free equilibrium potential.

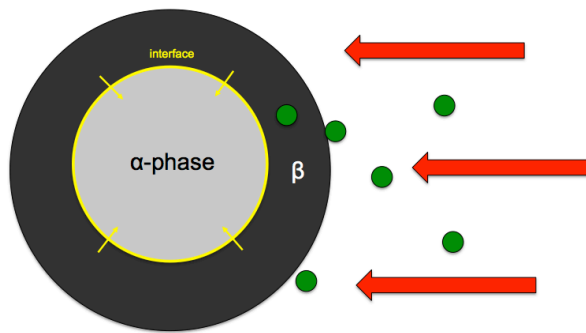


Figure 3-6: core-shell model for phase transformation of a spherical particle illustrating the migrating species, original phase (alpha) and reaction products (beta) with a thin and sharp interface

Coulometric titration is a valuable technique, as it enables detailed thermodynamic studies on electrode materials *in-situ/operando*; allowing for detailed studies on intercalation kinetics and order/disordered phase transformations.^{241,272}

4 Delithiation of lithium spinels: λ - $\text{Mn}_{1-x}\text{M}_x\text{O}_2$ Structure

4.1 Introduction

Early work by Hunter²⁹³ has identified the λ - MnO_2 structure as a stable crystallographic form of manganese oxide. Unlike the α , β , and δ - MnO_2 forms, λ - MnO_2 is a metastable phase, itself being the delithiated product of LiMn_2O_4 , carried out by either chemical or electrochemical delithiation.²⁹² In order to properly investigate the Na^+ de/insertion characteristics, the delithiated λ - MnO_2 is taken as a starting material. Chemical and electrochemical delithiation describe two common techniques used to extract the Li^+ ions, where the former generally yields a protonated spinel structure as H^+ replaces Li^+ , and the latter consists of electrochemically oxidizing the Mn cations during the Li^+ extraction process. Herein, lithium spinels of nominal composition $\text{LiMn}_{2-x}\text{Ni}_x\text{O}_4$ ($x = 0, 0.44, 0.5$) were used to produce their respective λ - $\text{Mn}_{1-y}\text{Ni}_y\text{O}_2$ ($y = \frac{1}{2}x$) structures for examination of the Na^+ insertion reaction into the λ - $\text{Mn}_{1-y}\text{Ni}_y\text{O}_2$ structure.

4.2 Experimental techniques

Lithium spinels for use in lithium/sodium cells were purchased and synthesized: $\text{Li}_{(1+x)}\text{Mn}_{(2-x)}\text{O}_4$ (LMO) was received from CHEMetal, while additional spinel samples: $\text{Li}_{1.1}\text{Mn}_{1.5}\text{Ni}_{0.5}\text{O}_{3.8}\text{F}_{0.2}$ (LMNOF), $\text{LiMn}_{1.5}\text{Ni}_{0.5}\text{O}_4$ (P-LMNO), and $\text{LiMn}_{1.56}\text{Ni}_{0.44}\text{O}_4$ (F-LMNO) were prepared according to solid state and Pechini methodologies respectively as described in^{299,315,321,371}. Spinel powders were dried at 300°C and stored in a dry room at 24°C and relative humidity $<1.0\%$. The spinel powder samples were cast into free standing positive electrodes consisting of 69.8% active material, 3.8% conductive carbon (SP, MMM) and 6% poly(vinylidene fluoride-*co*-hexafluoropropylene) (Kynar 2801, Elf Atochem) binder along with 20% propylene carbonate (PC) plasticizer. After successive extraction of PC with diethyl ether and drying under dry air, 3/8" disks were punched from the electrodes. Positive electrode disks were dried in a vacuum chamber at 120°C for a minimum of 10 hours and stored in an Argon filled glove box. Electrodes were initially charged vs. Na/Na^+ in order to extract Li^+ and to create a vacant host structure for Na^+ intercalation studies. Delithiated electrodes were removed from the initial 2032 type aluminum clad coin cells (Hohsen) and rebuilt with fresh glass fiber separator (Whatman GF/D) and Na metal (Sigma Aldrich: 262714) anodes

prior to the first discharge against Na/Na⁺. Within the following sections λ -MNO derived from disordered (Fd-3m) and ordered (P4₃32) lithium spinels and their corresponding sodiated analogues (Na_x-MNO) are abbreviated as F λ -MNO, P λ -MNO, FNa_x-MNO and PNa_x-MNO respectively.

While reports on sodium ion battery electrolytes have demonstrated a number of different aqueous, non-aqueous, ionic liquid and solid-state electrolytes, few optimal compositions have been identified. Direct analogues from existing lithium electrolytes are rarely successful, as the solvation and passivation properties of Na metal differ from that of Li. Due to these limitations, use of 1M NaClO₄-PC is chosen as a baseline electrolyte due to favorable solubility of the electrolyte salt and extensive use throughout other SIB studies^{135,372}. While maintaining good conductivity at room temperature, stability concerns associated with residual moisture of the perchlorate salt (45.5 ppm) and electrochemical limitations of the PC based electrolyte should be noted, leading to observation of competing oxidation of the electrolyte during high voltage and high temperature studies as will be discussed in detail throughout the following sections. Due to these concerns comparative analysis with additional sodium electrolytes and utilization of a monofluoro ethylene carbonate (FEC) electrolyte additive is chosen for the majority of the presented results, as PC does not form a stable SEI layer with the sodium metal anode. FEC has proven to successfully passivate Na metal cells⁶¹, and is utilized in a 2 vol% 1M NaClO₄-PC:FEC electrolyte throughout this study referred to as 1M NaClO₄-PC:FEC2% except when explicitly mentioned otherwise.

Multipoint BET surface area measurements were performed using a Micrometrics ASAP 2020 analyzer. Degassing conditions were run at 120°C for a minimum of 12 hours on the lithium spinel powder samples mentioned previously. Surface area and pore size distribution analysis was performed using N₂ gas.

Moisture content of electrolyte salts and powder samples were performed using a Karl Fischer Metrohm KF 831 Coulometer & 860 Thermoprep oven. Powder samples were heated to 200°C with a dry N₂ carrier gas flow rate of 80 mL/min. Electrolyte conductivity was measured with a Metrohm 6.0908.110 conductivity cell and a Solartron SI 1260 impedance analyzer under ambient conditions.

X-ray diffraction (XRD) characterization of powder and electrode disk samples was conducted on a Bruker D8 Advance diffractometer (Cu K α , λ = 1.5406 Å). *Ex-situ* XRD measurements were conducted on discharged and cycled (vs. Na/Na⁺) positive electrodes after disassembly and removal of electrolyte by

rinsing with dimethyl carbonate (DMC) in an Ar filled glove box. XRD samples were prepared by sealing the positive electrodes onto glass slides using Kapton film to minimize moisture contamination during the XRD scan. Rietveld refinement was run utilizing the TOPAS software package using a 5th order Chebychev polynomial function to fit the background, while also refining sample height displacement, atomic positions and occupancies assuming a pseudo-voigt peak shape. Initial refinement of delithiated λ -MNOF, and F λ -MNO samples provide the fixed oxygen atomic positions used throughout *ex-situ* XRD data analysis. Reported refined samples were modeled with a Fd-3m/P4₃32 space group assuming Na⁺ exclusively on the 8a tetrahedral sites. Corrections based on the quantities of the Kapton film cover, conductive and binder additives were not made, as their contribution to the XRD profile was negligible.

4.3 Results & Discussion

BET surface areas of LMO, LMNOF, F-LMNO, and P-LMNO powder samples were 1.1, 1.2, 5.7, and 4.6 m²/g respectively. Electrochemical characterization of the initial lithium spinels was conducted by Galvanostatic cycling and by cyclic voltammetry (CV) using a 3 mA/g cycling current and 0.01 mV/s scan rate respectively. Here, lithium spinel samples were cycled against a lithium metal positive electrode with a 1M LiPF₆-EC/DMC (50:50 vol) electrolyte. The corresponding CV curves are given in Figure 4-1.

Here, the CV curves demonstrate the electrochemically active redox couples throughout the LMO, LMNOF, P-LMNO, and F-LMNO samples respectively. Nickel doped spinel samples exhibit a high-voltage redox couple at *ca.* 4.7V with minor traces of the Mn³⁺/Mn⁴⁺ redox intended by the off-stoichiometric compositions chosen for the LMNOF and F-LMNO samples used throughout this study. Overall, CV scans indicate that the lithium spinel samples are both electrochemically active, primarily working on the Mn^{3+/4+} and Ni^{2+/4+} redox reactions, and are in agreement with the voltage profiles provided in Figure 4-3.

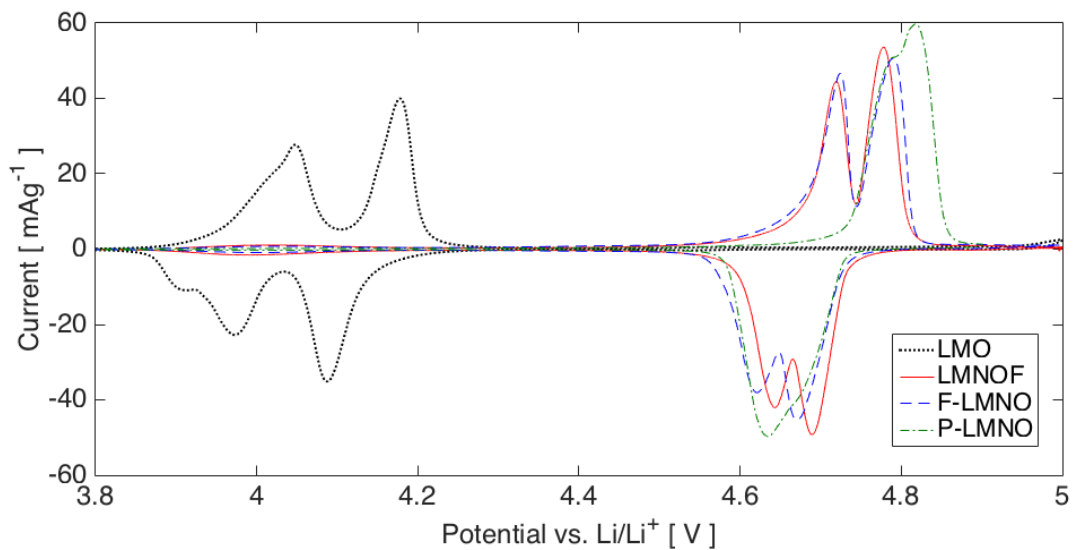


Figure 4-1: CV scans for LMO, LMNOF, F-LMNO, and P-LMNO spinels vs. Li/Li⁺. Cyclic voltammetry scans are performed with a 1M LiPF₆-EC/DMC electrolyte within 3.0 – 5.0V at 24°C and 0.01 mV/s scan rate.

Additional Fourier Transform Infrared Spectroscopy (FTIR) was performed on the lithium spinel cathode powders using a transmission geometry in order to validate the formation of the P₄32 (P_λ-MNO) spinel. Figure 4-2 considers the Ni-O and Mn-O vibrational modes indicating successful formulation of the ordered spinel, as demonstrated throughout previous literature.^{303,306}

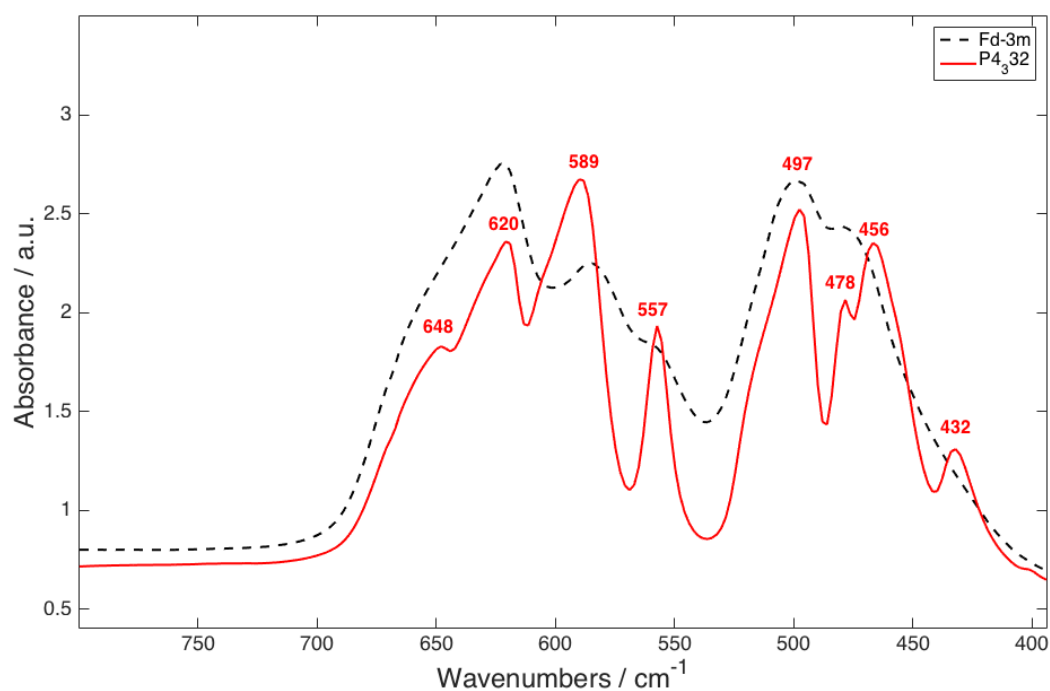


Figure 4-2: Transmission FTIR (Fourier Transform Infrared Spectroscopy) data of Fd-3m (dashed) and P4₃32 (solid) lithium spinels showing characteristic vibrational modes of Ni-O and Mn-O bonds.

X-ray diffraction (XRD) patterns, and corresponding Rietveld refined patterns of standard spinel samples LMO, LMNOF, F-LMNO, and P-LMNO are shown in Figure 4-4. All observed peaks can be assigned to Bragg reflections consistent with a Fd-3m/P4₃32 spinel crystal structure. The Rietveld refined lattice parameters of $a = 8.236\text{\AA}$, 8.169\AA , 8.167\AA , and 8.160\AA for LMO, LMNOF, F-LMNO and P-LMNO samples respectively are in good agreement with those previously reported^{63,179,207,295,300,304}.

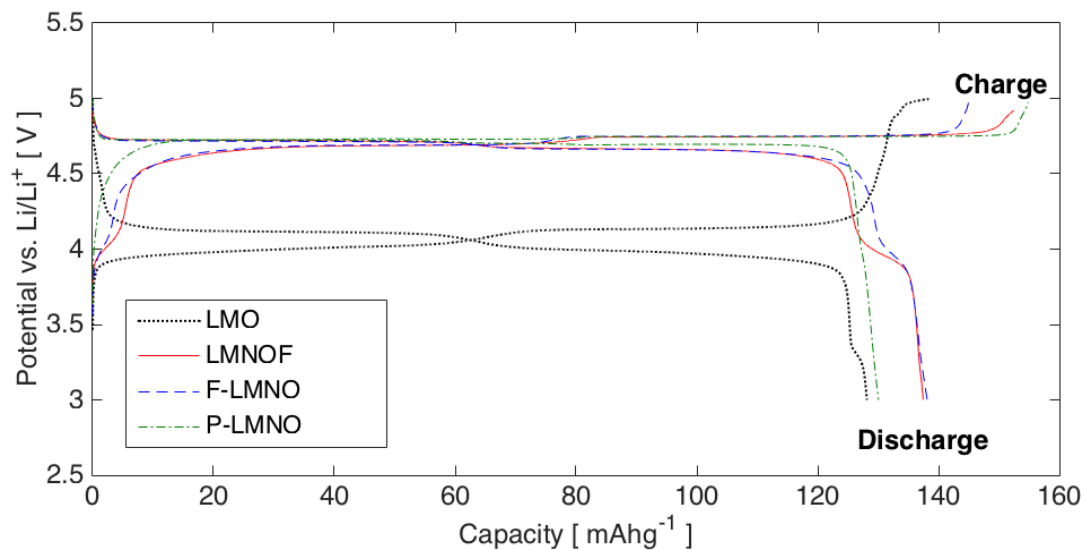


Figure 4-3: Characteristic voltage profiles of lithium spinel positive electrodes with 1M LiPF_6 -EC/DMC electrolyte at 24°C cycled with a 3 mA/g current

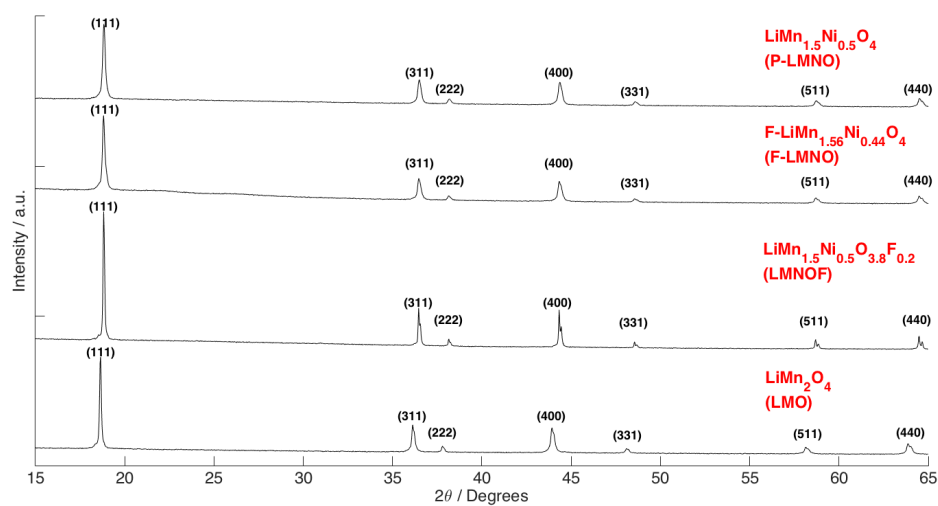


Figure 4-4: Powder X-ray Diffraction patterns of as prepared lithium spinel powders taken using $\text{Cu-K}\alpha$ incident radiation with a 0.02° step size and 1.5 second dwell time.

During delithiation, charge capacities consistently demonstrate between 145 – 150 mAh/g with and open circuit potential $>4.7\text{V}$ (vs. Na/Na^+) indicating that complete electrochemical delithiation has

taken place. The high open circuit voltages in the 4.4 - 4.7V range suggest extensive Li plating on the Na metal anode as seen in Figure 4-5. Although the concentration of Li^+ in the prepared sodium cells is extremely low following delithiation ($\sim 1\text{mol}\%$), fresh sodium anodes and electrolyte were provided in rebuilt Na/Na^+ cells to ensure the following intercalation studies are free of any mixed Li^+/Na^+ de/insertion effects.

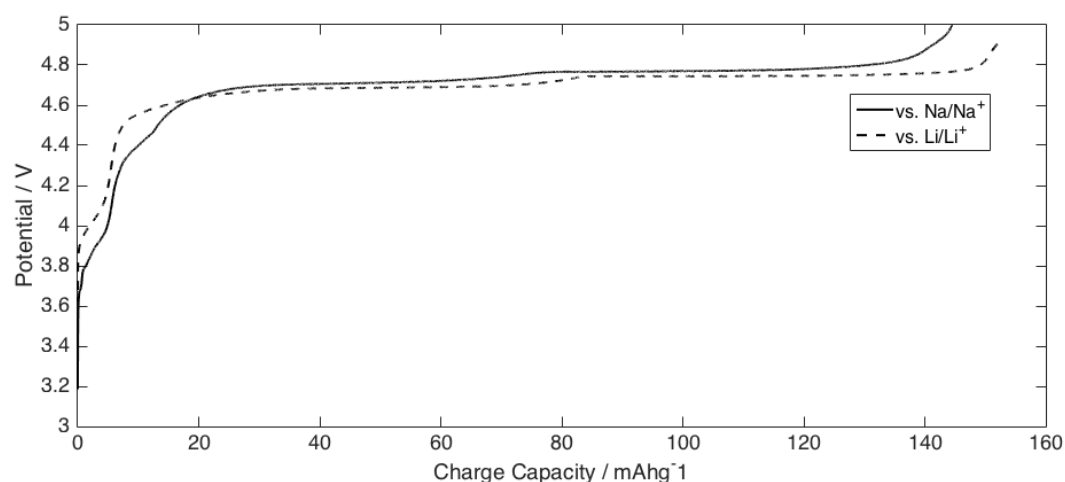


Figure 4-5: Electrochemical delithiation of $\text{F}\lambda\text{-MNO}$ against a lithium and sodium metal anode in 1M $\text{NaClO}_4\text{-PC:FEC2\%}$ electrolyte at 24°C

Figure 4-6 provides *ex-situ* XRD measurements following electrochemical delithiation. $\lambda\text{-MO}$, $\lambda\text{-MNOF}$, $\text{F}\lambda\text{-MNO}$, and $\text{P}\lambda\text{-MNO}$ notations are used here to indicate the delithiated spinel structure, which can be distinguished by the rightward shift in the diffraction peaks, indicating a substantial contraction in the lattice parameter consistent with the combined effect of depopulation of the 8a sites and smaller ionic radii of the Ni^{4+} cation.

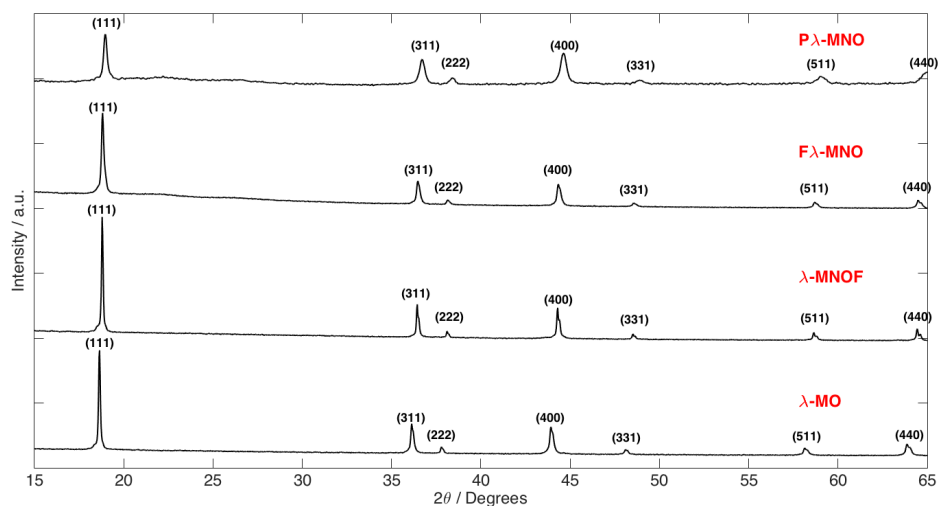


Figure 4-6: Ex-situ XRD measurements on electrochemically delithiated spinel cathodes

4.4 Conclusion

Electrochemical delithiation was utilized in order to form the λ -MO, λ -MNOF, $F\lambda$ -MNO, and $P\lambda$ -MNO spinels ($a = 8.052, 8.001, 8.000$, and 7.994\AA respectively) for further investigation as a potential sodium-ion electrode material. Electrochemical and structural characterization reveal that lattice parameters and active redox couples are in good agreement with those previously reported, and additional *ex-situ* XRD measurements on the λ -MO, λ -MNOF, $F\lambda$ -MNO, and $P\lambda$ -MNO phases exhibit a pure spinel phase of smaller lattice parameter indicating a significant contraction in the spinel lattice due to removal of lithium.

The following sections utilize the delithiated λ -MO, λ -MNOF, $F\lambda$ -MNO, and $P\lambda$ -MNO spinel compositions in order to investigate their potential use in future sodium-ion batteries.

5 Na⁺ insertion into λ -MO, λ -MNOF, F λ -MNO, and P λ -MNO

5.1 Introduction

In order to make direct comparisons between lithium and sodium spinel electrodes, the λ -spinel phase is produced by electrochemical delithiation as mentioned throughout the previous section. As described in the later chapters, the direct synthesis of the sodium spinel has proven to be exceedingly difficult due to differences in site preference and additional steric effects, often resulting in the formation of a layered structure. In particular, the λ -MO, λ -MNOF, F λ -MNO, and P λ -MNO compositions are chosen for the following reasons: (1) The undoped λ -MO provides a suitable benchmark against which a meaningful comparison to the nickel-doped spinels can be formed. (2) The λ -MNOF composition has demonstrated itself as an attractive Li-ion cathode, demonstrating considerable capacity retention at both ambient and elevated temperatures. (3) The F λ -MNO, and P λ -MNO spinels are both synthesized by a modified Pechini process, producing a mesoporous network of nanocrystallites, providing shorter diffusional pathways by nature of the relative differences in particle size compared to the solid-state derived λ -MNOF, while also considering the differences attributed to ordering of the transition metal cations between the F λ -MNO and P λ -MNO spinels respectively.

Throughout this section, two key features are demonstrated: that (1) the spinel structure is retained after insertion of Na⁺, and (2) that Na⁺ insertion occurs predominantly onto the 8a tetrahedral sites seen by complementary electrochemical and structural characterization; providing valuable insight into the reaction mechanisms at play throughout the initial discharge reaction, while demonstrating near theoretical capacity during the first discharge.

5.2 Experimental Considerations

Electrochemical characterization was performed on λ -MO, λ -MNOF, F λ -MNO, and P λ -MNO spinel positive electrodes, with bare sodium metal anodes in sodium electrolyte in 2032 type coin cells as mentioned previously. *Ex-situ* XRD was performed on discharged λ -MO, λ -MNOF, F λ -MNO, and P λ -MNO spinels following a delithiation and electrolyte extraction method discussed earlier.

An adjustable 3-axis stage and *in-situ* XRD electrochemical cell was assembled comprising a stainless steel cell base and beryllium window. LMO, LMNOF, F-LMNO, and P-LMNO positive electrodes were cast into free standing positive electrodes as described previously and punched into 5/16" diameter disks prior to removal of PC plasticizer. The resulting cathode disks were centered and laminated onto 5/8" carbon coated aluminum mesh disks that are designed to provide an electrical contact to the *in-situ* cell body. Extraction of the PC plasticizer was performed after lamination onto aluminum mesh disks at 120°C with 40 psi applied pressure. The cell parts and cathodes were dried under vacuum at 120°C prior to assembly to remove residual moisture. Cell assembly was performed as described in earlier work.³⁷³ Prior to *in-situ* and *operando* XRD measurements, the 3-axis stage was aligned with the incident X-ray beam to optimize the signal to noise ratio of the (111) spinel reflection. Electrochemical delithiation was performed prior to assembly in the *in-situ* cell.

Three-electrode cells were utilized to validate possible polarization of the sodium metal anode. These specially designed cells consist of modified Swagelok body using sodium metal as the reference and counter electrodes.⁴⁹ Cell bodies were dried at 120°C under vacuum prior to assembly in an Argon filled glovebox, and assembled using glass fiber separator and Mylar sleeves to insulate the electrodes from the cell body.

Galvanostatic and potentiostatic cycling was performed using a Bio-Logic VMP3 multichannel potentiostat/galvanostat and MacPiles galvanostat. Galvanostatic Intermittent Titration Technique (GITT) and Potentiometric Intermittent Titration Technique (PITT) were performed on 2032 Hohsen coin cells assembled in an Argon filled glovebox. GITT protocols consisted of 1-hour pulses of 7.58 mA/g of active material followed by 5-hour open circuit rest periods within the voltage range of 2.0-4.0V. PITT protocols were cycled with 10 mV steps with a current cutoff of 0.25 mA/g of active material within the voltage range of 2.0-4.25V.

5.3 Results

5.3.1 Na⁺ insertion into λ -MnO₂

Figure 5-1a considers the discharge profile of λ -MO at a 3mA/g current rate at 24°C. As opposed to the voltage profile seen for λ -MO vs. Li/Li⁺, there is a significant drop in the voltage plateau from *ca.*

3.7V (vs. Li/Li⁺) to 3.12V (vs. Na/Na⁺). The first plateau is attributed to Na⁺ insertion onto the 8a tetrahedral sites. Beyond the $0 < x < 1$ range, a second voltage plateau can also be identified at *ca.* 2.37V as Na⁺ begins to occupy the adjacent 16c octahedral sites, resulting in a structural decomposition into a layered structure shown by the *ex-situ* XRD profile of Figure 5-1b.

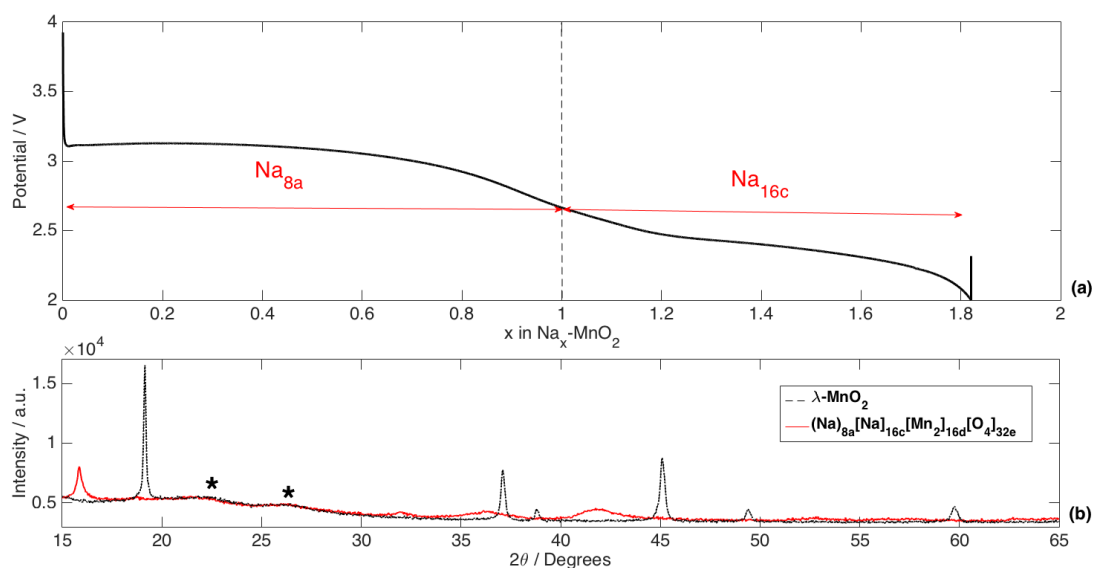


Figure 5-1: Voltage profile of $\lambda\text{-MnO}_2$ ($\lambda\text{-MO}$) with a 3mA/g discharge current at 24°C, 1M NaClO₄-PC:FEC2%

Figure 5-1b also considers the initial $\lambda\text{-MO}$ phase, demonstrating the abrupt change in crystal structure to a layered phase.²⁸⁹ Peaks marked by asterisks are attributable to the Kapton film used to encapsulate the cycled electrodes for *ex-situ* measurement. Although Na⁺ insertion onto the adjacent 16c sites allows for a large increase in capacity, excessive strain in the spinel lattice and critical buildup in Jahn-Teller active cations (Mn^{3+}) results in the irreversible decomposition into an Orthorhombic layered phase. This irreversible change is evident by the change in the characteristic voltage profile; as demonstrated in Figure 5-2. Here, the initial discharge/charge cycle is shown in red, which is then completely indistinguishable by the 3rd and later cycles shown in black. Structural decomposition into the layered phase has been well documented, especially in the case of reversible Li⁺ de/insertion, which is induced by the cooperative Jahn-Teller distortion of the MnO_6 octahedra.^{28,294,309}

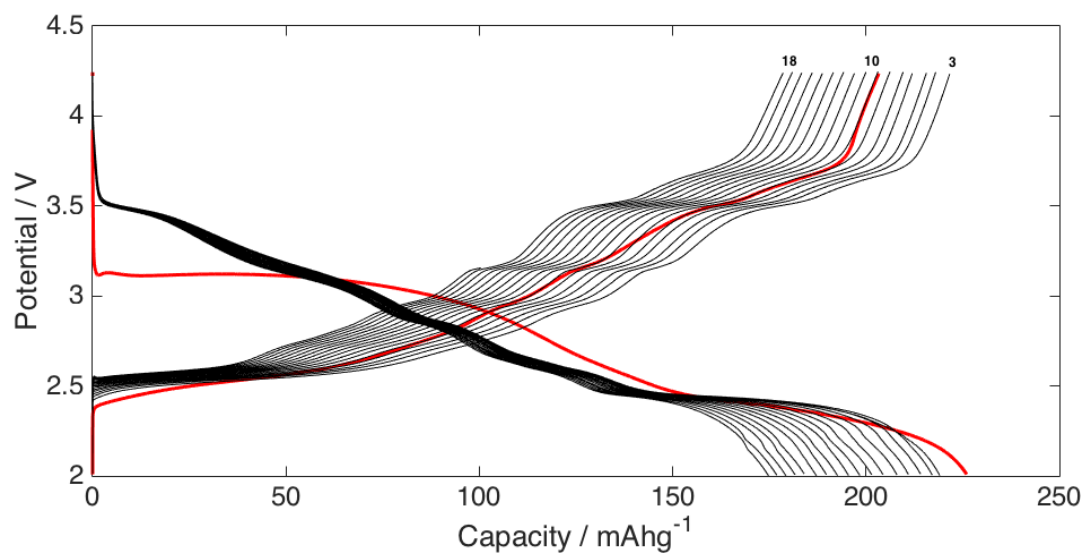


Figure 5-2: Voltage profile of Na-MnO₂ showing the first cycle (red) and subsequent cycles (black)
 Cycled at 3 mA/g at 24°C, 1M NaClO₄-PC:FEC2%

In summary, reversible Na⁺ de/insertion λ -MnO₂ structure induces irreversible structural transformations, which is readily apparent by the drastic change in the voltage profile described by Figure 5-2. This decomposition into a layered structure does not come as a surprise, as reversible Li⁺ de/insertion exhibits the same structural change, and is attributed to the critical accumulation of Mn³⁺, further resulting in distorted MnO₆ octahedra by nature of the cooperative Jahn-Teller distortional effects.

5.3.2 Na⁺ insertion into λ -MNOF

As discussed previously, the λ -MNOF spinel stoichiometry has been previously optimized²⁹⁹ for Li⁺ de/insertion, and its investigation as a suitable sodium insertion compound is of particular interest to contrast the different behaviors of Li⁺/Na⁺ ion de/insertion.

Figure 5-3 provides the discharge voltage profiles at C/10, C/25, C/50, C/100, C/200, and C/400 current-rates for λ -MNOF at 24°C demonstrating discharge capacities of 89.2, 102, 114.7, 118.8, 126.7, and 125.1 mAh/g respectively. Both the C/200 and C/400 discharge rates exhibit very similar capacity values, indicating complete reaction of λ -MNOF is feasible at a C/200 rate. Rietveld refinement was conducted on *ex-situ* XRD measurements, and is provided in Table 4-1.

The sodium insertion reaction occurs at *ca.* 3.6V vs. Na/Na⁺, which is notably lower than that expected when solely considering differences in standard redox between Na and Li. As will be discussed in greater detail in the following sections, this is largely due to added energetic ‘penalties’ that arise when incorporating Na⁺ into the spinel host structure, as the specific site and strain energies greatly differ between Na⁺ and Li⁺. In fact, this becomes further exemplified in the λ -MNOF samples, as the relatively large particle sizes (*ca.* 200-700 nm) of the λ -MNOF spinel inherently limits the rate-capability of the Na⁺ de/insertion reaction, and motivates the need to consider high surface area spinel samples used in the following sections.

Following complete discharge to 2.0V (vs. Na/Na⁺), the resulting cathodes were analyzed by *ex-situ* XRD. Of the considered discharge rates, the C/10 discharge rate shows the existence of three phases: (1) residual λ -MNOF spinel (*a*=8.009(2) Å) due to incomplete sodiation, (2) the sodiated spinel of expanded unit cell (*a*=8.414(2) Å), and (3) an additional phase which may also be indexed with an Fd-3m symmetry of intermediate lattice parameter (*a*=8.186(1) Å) between the vacant λ -MNOF and sodiated Na-MNOF structures. This is shown in Figure 4-5 and Table 4-1.

Due to the potential of lattice instability of Na spinels, additional known layered sodium phases were also modeled throughout the Rietveld refinements of discharged λ -MNOF vs. Na/Na⁺ cells. The relative poor fitting of the considered layered phases as compared to the Fd-3m Na-MNOF spinel support the retention of the spinel framework throughout Na⁺ insertion.

After discharge, the C/25 and C/100 discharged λ -MNOF vs. Na/Na⁺ cells only exhibit the existence of both the sodiated Na-MNOF spinel ($a=8.426(2)$ Å and $8.446(2)$ Å, respectively) and the intermediate spinel of approximate composition Na_(0.1-0.4)-MNOF spinel ($a=8.190(3)$ Å and $8.196(7)$ Å respectively). Whereas the C/200 discharged λ -MNOF vs. Na/Na⁺ cell only resulted in the presence of the fully sodiated Na-MNOF phase suggesting that complete insertion of Na⁺ onto the vacant 8a tetrahedral sites has taken place, consistent with the initial discharge capacity near its theoretical value.

Figure 5-3b provides the *ex-situ* XRD scans of the λ -MNOF samples after discharging at C/100. A significant shift in all the Bragg reflections to larger d-spacings are noted along with the appearance of the (220) Bragg reflection at *ca.* 30° 2 θ is consistent with an expansion of the spinel lattice, and occupation of a relatively higher atomic number element (as compared to Li) on the 8a tetrahedral sites. While Ni²⁺ has demonstrated the ability to occupy the 8a sites, the lack of sufficient thermal energy to break the existing Mn/NiO₆ octahedral network, and electrochemically active redox both indicate that the 8a sites are exclusively populated by Na⁺. XRD patterns are further quantified by Rietveld refinement given in Table 4-1, and discussed in detail below.

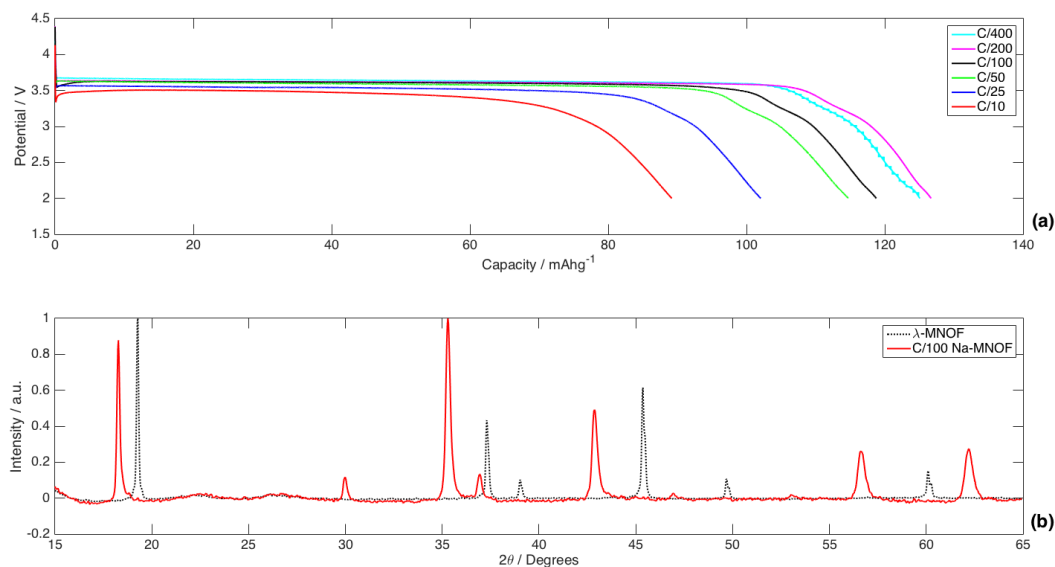


Figure 5-3: Galvanostatically discharged sodium cells at 24°C, 1M NaClO₄-PC:FEC2% (a) and *ex-situ* XRD (b) measurements of λ -MNOF and C/100 discharged λ -MNOF

Considering the multiphasic nature of *ex-situ* XRD samples at discharge rates higher than $C/25$, Figure 5-4 demonstrates a spherical particle, and provides a schematic representation as to the observed multiphasic electrode compositions. As will be discussed in detail, reaction kinetics associated with the Na^+ insertion processes are largely limited by grain boundary migration, posing considerable difficulties when dealing with low surface area electrodes at high charge/discharge rates. As noted by *ex-situ* XRD, three distinct spinel phases can be observed when cycling at progressively higher rates, as inhomogeneous regions begin to form within a single particle. Although this reaction model has yet to be validated directly, it provides a realistic account for the intermediate spinel phase without considering additional complex side reactions.

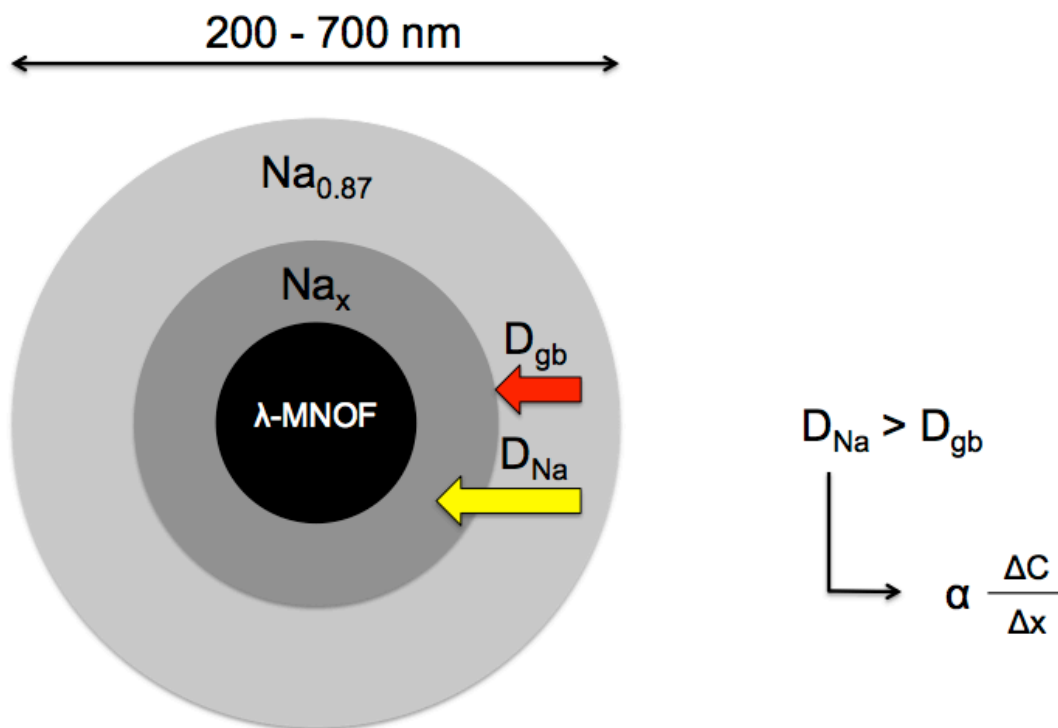


Figure 5-4: Spherical particle model of λ -MNOF spinel considering differences in grain boundary migration and Na^+ diffusion

Ex-situ and preliminary *in-situ* XRD of λ -MNOF vs. Na/Na^+ cells exhibit an additional third phase (presumably of an intermediate sodium content) that is likely the result of the kinetic limitations of the sodium insertion reaction.

Figure 5-5 shows the *ex-situ* XRD profile of λ -MNOF vs. Na/Na⁺ discharged to 2.0V at a C/10 with special emphasis in the 18° - 20° 2 θ range (b) in which the additional phase can be seen between the (111) Bragg reflections of the sodiated and non-sodiated spinel. This unknown composition (denoted as Na_x-MNOF) can also be assigned to an Fd-3m space group, possibly indicating that a separate two-phase reaction is initiated as a result of the relatively (as compared to diffusional kinetics) high discharge rate, or an intermediate spinel composition is formed due to large strain/concentration gradients forming within individual particles.

Refined parameters of the λ -MNOF are provided at the top of Table 4-1 in order to draw comparisons between the vacant λ -MNOF structure and the fully sodiated Na-MNOF. The fully sodiated cell result in a lattice parameter approximately 5% greater than the host λ -MNOF, and voltage profiles across the considered discharge rates all suggest that the $\text{Ni}^{4+} \rightarrow \text{Ni}^{2+}$ reaction is taking place at *ca.* 3.6V (vs. Na/Na⁺). Equation 5-1 illustrates the proposed insertion reaction in which Na⁺ is inserted onto the 8a tetrahedral sites of the λ -MNOF spinel, with the additional spinel phases of the discharged λ -MNOF cells being likely described by the large kinetic limitations of the λ -MNOF spinel as illustrated by Figure 5-4.

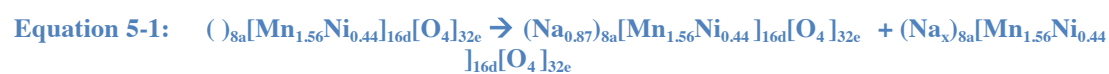


Table 5-1: Rietveld refinement on galvanostatically discharged electrodes

	Delithiated LMNOF	C/10 Discharge			C/25 Discharge		C/100 Discharge		C/200 Discharge
Phase wt%	λ -MNOF 100%	Na-MNOF 82.48%	Na _x -MNOF 4.90%	λ -MNOF 12.60%	Na-MNOF 97.32%	Na _x -MNOF 2.67%	Na-MNOF 98.09%	Na _x -MNOF 1.90%	Na-MNOF 100%
a (Å)	7.999(1)	8.414(2)	8.186(1)	8.009(2)	8.426(1)	8.190(3)	8.446(2)	8.196(7)	8.453(2)
Unit Cell Vol (Å³)	511.9(9)	595.9(0)	548.5(6)	513.7(7)	598.2(8)	549.4(2)	602.5(4)	550.7(1)	604.1(0)
Na (Occ)	(0,0,0) (0)	→ (0.8499)	→ (0.1)	→ (0)	→ (0.9465)	→ (0.3294)	→ (0.9465)	→ (0.1)	→ (1.0)
Mn (Occ)	(5/8,5/8,5/8) (0.75)	→ (0.75)	→ (0.75)	→ (0.75)	→ (0.75)	→ (0.75)	→ (0.75)	→ (0.75)	→ (0.75)
Ni (Occ)	(5/8,5/8,5/8) (0.25)	→ (0.25)	→ (0.25)	→ (0.25)	→ (0.25)	→ (0.25)	→ (0.25)	→ (0.25)	→ (0.25)
O (Occ)	(0.38809, 0.38809, 0.38809) (0.95)	→ (0.95)	→ (0.95)	→ (0.95)	→ (0.95)	→ (0.95)	→ (0.95)	→ (0.95)	→ (0.95)
F (Occ)	(0.38809, 0.38809, 0.38809) (0.05)	→ (0.05)	→ (0.05)	→ (0.05)	→ (0.05)	→ (0.05)	→ (0.05)	→ (0.05)	→ (0.05)
R_{exp}	1.50	1.35			1.39		1.35		1.41
R_{wp}	3.64	3.07			3.11		2.96		2.91
GOF	2.43	2.27			2.24		2.20		2.07

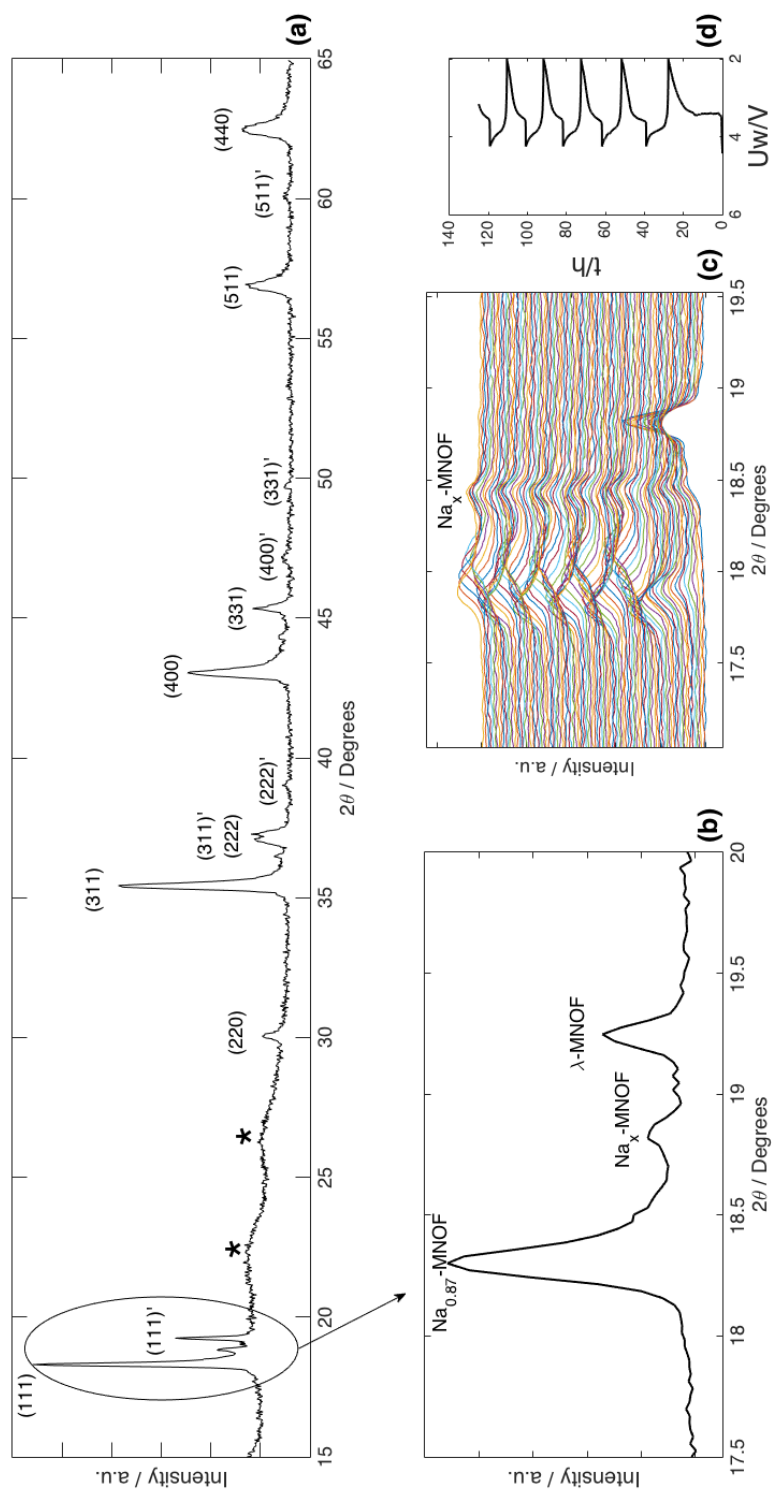


Figure 5-5: combined *ex-situ* and *operando* XRD data for macrocrystalline λ -MNOF. *Ex-situ* data (a-b) was cycled at a C/10 rate at 24°C while *operando* XRD data was separately collected at a C/40 rate at 24°C, 1M NaClO_4 -PC:FEC2% (c-d)

Close examination of Figure 4-5 indicates that the final peak position of the $\text{Na}_x\text{-MNOF}$ phase does not appreciably change beyond completion of the first discharge. This type of behavior may be explained by either (1) an intermediate sodium phase, potentially related to an ordering of Na^+ along the tetrahedral sites, or (2) incomplete extraction of lithium containing electrolyte during the initial electrochemical delithiation step.

Figure 5-5c exhibits a small shoulder peak at *ca.* $18.5^\circ 2\theta$, which proceeds by a small shift in position during the first discharge to 18.41° , and finally stabilizes at $18.45^\circ 2\theta$ after the first charge cycle

where it then becomes effectively 'inactive' throughout the remaining 4 cycles. While the shoulder peak described in

Figure 5-5c would suggest some degree of lithium remaining in the spinel. However, the consistency between *ex-situ* and *in-situ* XRD measurements suggest that this phase is either a sodium spinel or mixed Li/Na spinel as implied by the relatively high lattice parameter, with the initial shoulder observed in

Figure 5-5c potentially being described by residual lithium caused by the poor electrolyte extraction as described in Chapter 4.

The core/shell model proposed by Figure 5-4 can be further expanded to explain the apparent ‘inactivity’ of the intermediate spinel phase, as it is likely that the same multiphasic core/shell model can be applied to the *in-situ* XRD data shown in

Figure 5-5c. In this case, the absence of the λ -MNOF at the end of the discharge is likely a result of reduction in the λ -MNOF core beyond XRD detection limits (a result of the differences in discharge rate: C/10 vs. C/40). Here, direct validation of the multiphasic core/shell model is not suitable with the given experimental considerations, and a simplified core/shell particle model is provided in Figure 5-6 where the λ -MNOF and Na_x -MNOF regions can be summarized as a single domain of an average sodium content.

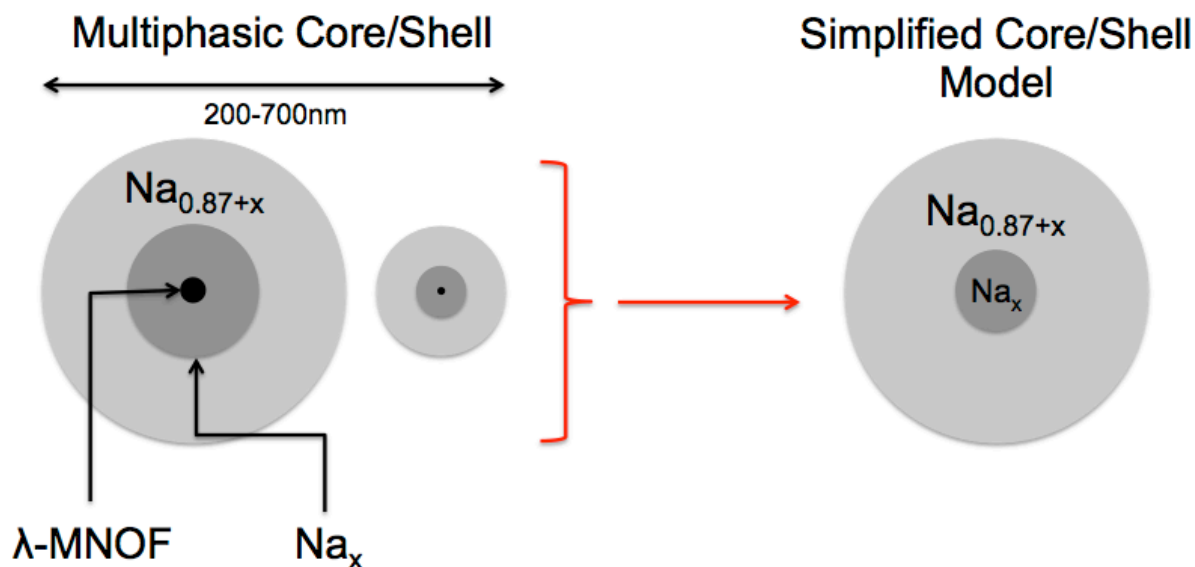


Figure 5-6: Simplified core/shell model of discharged λ -MNOF cathode particle(s)

The simplified core/shell model provides an intuitive explanation for the relative ‘inactivity’ of the Na_x -MNOF core, as the majority of Na^+ de/insertion is expected to take place predominantly throughout the volume of the particle shell due to the relatively large diffusional lengths of the 200-700 nm sized particles. This new model illustrates the important aspect of particle size and distribution when considering Na^+ de/insertion reaction kinetics, as the relatively large particle sizes of the λ -MNOF spinel results in a finite volume of material that becomes practically unusable due to the exceedingly low discharge/charge rates necessary to accommodate the low Na^+ bulk diffusivity.

Initial *in-situ* XRD results (Figure 4-5c-d) demonstrate that reversible cycling of Na-MNOF cathodes does not recover the initial λ -MNOF phase, as indicated by the relative peak positions of the observed diffraction peaks; motivating further study of the Na^+ deinsertion rate mechanism(s) preventing the complete removal of Na^+ from the spinel host lattice.

From these considerations, it is clear that full reaction of the λ -MNOF spinel is dependent on both the grain boundary migration and bulk Na^+ diffusion. Here the grain boundary migration and bulk diffusion coefficient are relatively constant (regardless of applied current rate), being only largely controlled by temperature and strain accommodation in the spinel host lattice. Although reduction of the average particle size is likely to observe the same phenomena, the effective volume of the intermediate spinel (Na_x) will be

negligible from considerations of the experimental detection limits of XRD. In fact, movement towards nanocrystalline (50-80nm) particle sizes no longer observes this apparent rate limiting behavior, indicating that reduction of the particle size is a necessary step towards reaching high discharge capacities due to the limiting kinetic considerations.

Movement to a Pechini synthesis route (covered in the next section) greatly improves the rate capability as evidenced by the high discharge capacities and phase purity of *ex-situ* XRD measurements on discharged cathodes. BET surface area analysis (5.8 m²/g vs. 1.2 m²/g for the LMNO-P and LMNOF samples respectively) and previous characterization of this material by FESEM and Williamson Hall technique show that the Pechini synthesis route has reduced the spinel crystallite size from 200-700 nm²⁹⁹ to 50-80 nm³⁰⁰, while creating a mesoporous network that is more suitable for wetting of the electrode surface and reversible ion intercalation.

5.3.3 Na⁺ insertion into F λ -MNO

Movement towards a Pechini synthesis technique was chosen to enhance the rate capability by greatly reducing the diffusional distances that appeared to greatly limit the λ -MNOF spinel mentioned previously. Here, a disordered spinel (F λ -MNO) is discussed in terms of the initial Na⁺ insertion reaction.

Figure 5-7 considers F λ -MNO vs. Na/Na⁺ cells discharged at a C/10 and C/100 rate, with their respective *ex-situ* XRD patterns. Refined lattice parameters are in close agreement with one another: $a=8.439(0)$ Å and $a=8.461(4)$ Å respectively, with no residual or intermediate phase observed by XRD. Although not definitive, this observation is consistent with the previous multiphasic core/shell model proposed in the previous chapter. Most importantly, both *ex-situ* XRD patterns depict a single phase, but differ greatly in their observed discharge capacity. It is therefore believed that a similar core/shell reaction mechanism is at play. However, due to the small particle sizes attributable to the Pechini derived F λ -MNO (50-80 nm), the inner core of individual particles large enough to satisfy the ~5 wt% detection limit of XRD. While it is once again, important to distinguish that there is insufficient data to fully support this reaction model, it is apparent that the Pechini derived F λ -MNO demonstrates a higher rate capability when considering Na⁺ insertion as determined by both the higher discharge capacities and larger average lattice parameter reported by XRD. Given current analyses, it is assumed that complete reaction of individual particles takes place throughout the following chapters.

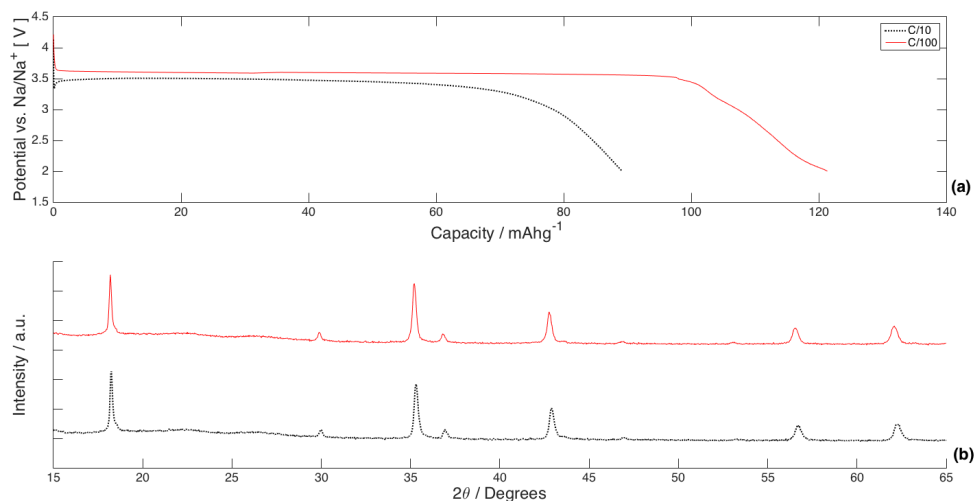


Figure 5-7: C/10 and C/100 discharge rates of Pechini derived F λ -MNO spinel at 24°C, 1M NaClO₄-PC:FEC2% (a) and *ex-situ* XRD of deconstructed cathodes (b)

5.3.3.1 Coulometric Titration: GITT/PITT

GITT was utilized as a low rate, near equilibrium electrochemical protocol to examine whether near theoretical specific capacities could be achieved as well as to gain insight on the voltage variation and phase progression associated with the Na^+ insertion mechanism; the results are shown in Figure 5-8.

During the initial Na^+ insertion reaction (Figure 5-8a), the open circuit potentials are relatively invariant at 3.65V across the majority of the discharge until $x \sim 0.8$ indicating that the two-phase reaction has completed within the confines of our applied electrochemical protocol. Further discharge then appears to proceed through a single-phase reaction between 3.5-2V, and a final discharge capacity of 134.2 mAh/g is observed (99.53% theoretical capacity) throughout the combined two-phase & single-phase insertion reactions. This demonstrates complete Na^+ insertion into the $\text{F}\lambda\text{-MNO}$ structure is possible given a sufficiently slow rate.

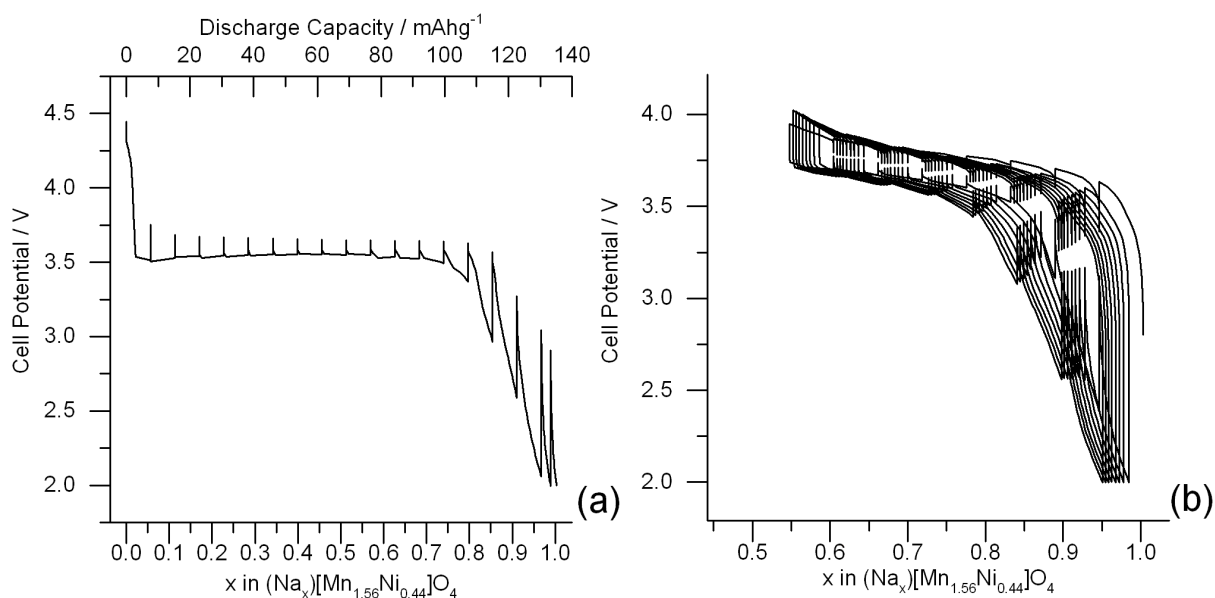


Figure 5-8: Galvanostatic intermittent titration technique (GITT) of $\text{F}\lambda\text{-MNO}$ at 24°C with 1M $\text{NaClO}_4\text{-PC:FEC2\%}$ electrolyte. First discharge (a) and subsequent charge/discharge voltage profiles (b)

After the initial insertion of Na^+ there is significant difficulty in extracting all the sodium from the sodiated structure considering the 4.0V cutoff (Figure 5-8b). Initial GITT results suggest a variation in the relaxed potential with Na^+ deinsertion characteristic of a single-phase process, and demonstrates a

reversible Na^+ window between $x = 0.55$ and $x = 1.0$. Here, GITT results illustrate that the following Na^+ de/insertion reaction is highly reversible, itself taking place throughout a single-phase de/insertion reaction process. However, only limited capacity is realized (*ca.* 60 mAh/g) due to the limited sodium extraction from the spinel host lattice, with further examination of the Na^+ deinsertion reaction mechanism being covered in the following chapters.

In order to further elucidate the onset of the single-phase reaction, potentiostatic intermittent titration technique (PITT) cycling conditions were imposed to provide quasi-equilibrium conditions throughout the Na^+ insertion process. Corresponding PITT data is given in Figure 5-9. The two-phase Na^+ insertion reaction occurs across multiple 10 mV steps in the 3.68-3.58V range, with the majority of the capacity occurring within a very narrow voltage range: 3.65 - 3.60V. The relative invariance supports a two-phase insertion behavior consistent with the GITT results presented above.

Superimposed in Figure 5-9 is the specific current response across the applied potentials. Within the 3.65-3.60V range of interest, each step is associated with a strong non-Cottrellian current response characteristic of a multiphasic reaction, with each potential step throughout the two-phase region demonstrating a peak in current followed by a gradual decay until reaching a 0.25 mA/g current cutoff(per gram of active material). This behavior is reported until the overall cell potential drops below *ca.* 3.58V at which the current response then follows a Cottrellian-like $t^{-1/2}$ dependence. This transition to a single-phase reaction occurs at *ca.* $x = 0.87$, just as the voltage drops below 3.6V at the knee in the recorded voltage profile; consistent with the previous GITT results. Combined with existing XRD data, the overall intercalation reaction of Na^+ into the $\text{F}\lambda\text{-MNO}$ structure is expected to occur *via* a two-phase intercalation reaction onto the vacant 8a tetrahedral sites up to an average sodium composition of *ca.* $x = 0.87$ followed by further Na^+ insertion onto 8a sites *via* a single-phase reaction until full sodiation has taken place ($x = 1.0$).

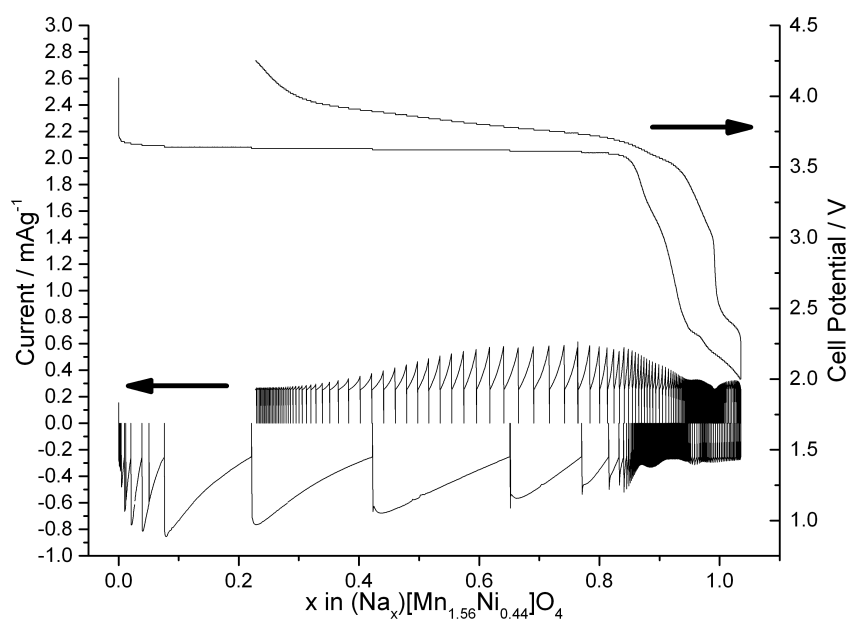


Figure 5-9: Voltage and specific current response of the sodium insertion of Fλ-MNO spinel utilizing a PITT protocol between 2 – 4.25V and a 0.25mA/g current cutoff with 1M NaClO₄-PC:FEC 2% electrolyte at 24°C

Since there is always concern regarding the accuracy of high-resolution electrochemical techniques in a two-electrode configuration, a 3-electrode Swagelok cell described in previous works³⁷¹ was used to determine the contribution to the overall cell potential from the sodium metal anode. Results are shown in the red voltage profile of Figure 5-10. The working potential of Fλ-MNO vs. Na/Na⁺ counter electrode (solid curve) and Fλ-MNO vs. Na/Na⁺ reference electrode (dashed) are nearly identical, indicating the negligible polarization of the negative electrode, and high level of confidence in the existing two-electrode data.

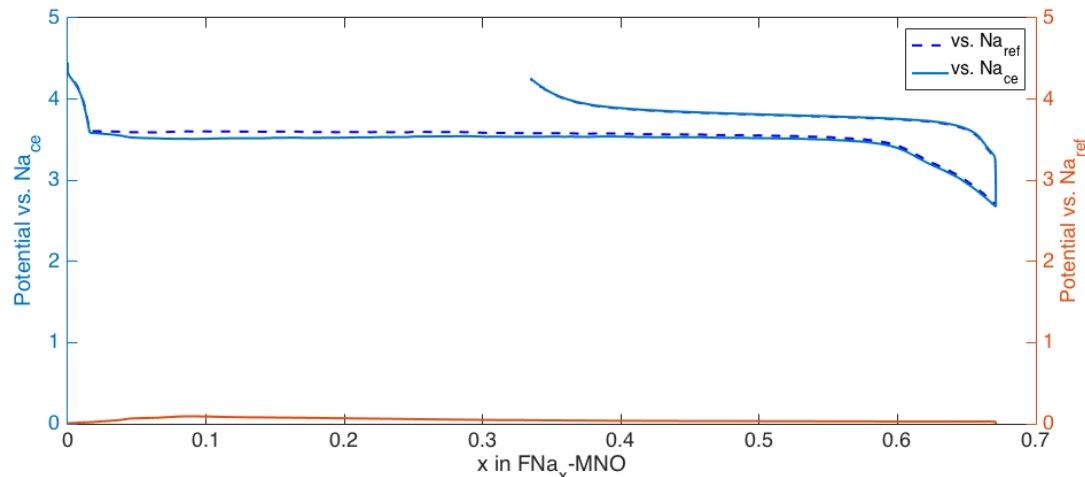
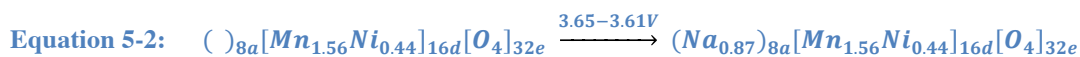


Figure 5-10: Working and counter electrode voltages vs. a Na-metal reference electrode. F λ -MNO cathode cycled at 24°C using 1M NaClO₄:PC:FEC2% electrolyte

5.3.3.2 *Ex-situ X-ray Diffraction (XRD)*

Additional F λ -MNO electrodes were galvanostatically discharged at a C/200 rate with Δx cutoffs of 0.4, 0.6, and 0.8 in order to validate the two-phase region previously observed with PITT. *Ex-situ* XRD measurements were taken at different points within the two-phase reaction regime. Refined Na⁺ occupancies for the sodiated phase (Na-MNO) of 0.894 and 0.890 along with similar lattice parameters ($a=8.391(7)$ Å & $a=8.412(1)$ Å respectively) for the $x=0.4$ and $x=0.6$ samples support the proposed two-phase insertion reaction process described in Equation 5-2. This conclusion is also supported by the high-resolution electrochemical techniques described above, suggesting that once the F λ -MNO phase is fully converted to the Na_{0.87}-MNO phase, the insertion reaction proceeds in a single-phase manner as described by Equation 5-3. Here, it is important to distinguish that although refined sodium occupancies suggest a higher degree of sodiation within the spinel, the relatively low scattering strength of Na makes it difficult to elucidate the exact Na occupancy by refinement techniques alone, and except where mentioned exclusively, Na occupancies are reported based off of electrochemical data.



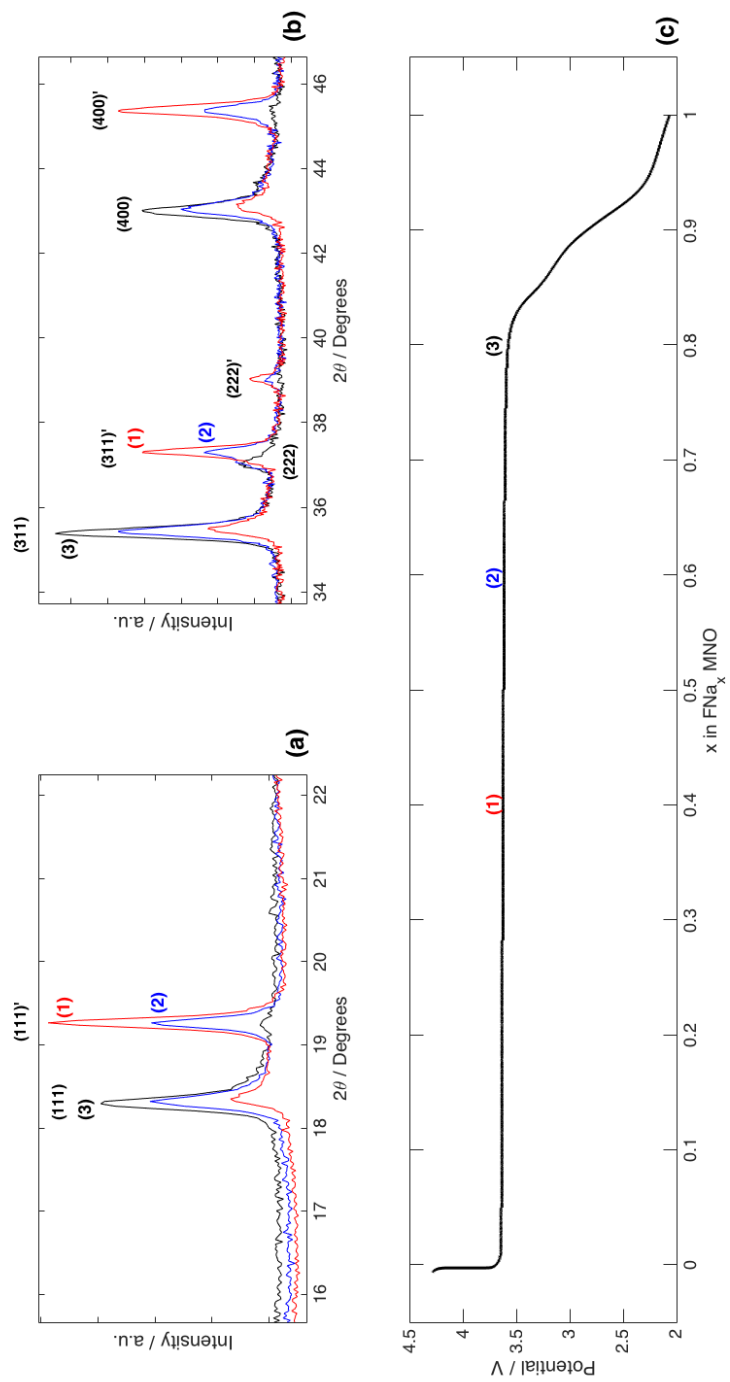


Figure 5-11: *Ex-situ* XRD measurements throughout two-phase reaction region discharged at 3 mA/g, 24°C using 1M NaClO_4 -PC:FEC2%

5.3.3.3 Operando X-ray Diffraction (XRD)

Further validation of the reaction mechanism was performed by *in-operando* at both a C/60 and C/40 (not shown) discharge rate.

Figure 5-12 considers a stacked XRD plot in which scans are taken on a continual basis with a maximum interval between sequential XRD scans of $x = 0.03$, which is presumed to produce negligible artifacts/peak broadening. Asterisks are provided to mark the diffraction peaks correlating to the aluminum current collector and beryllium window used for the *in-situ* cell. (111) (220) (311) (222) (400) (511) and (440) spinel reflections are labeled for the Na-MNO spinel.

Operando XRD measurements of Na⁺ insertion into Fλ-MNO at C/60 and C/40 discharge rates reveal a common progression of phase evolution: Initial insertion of Na⁺ results in the formation of a larger lattice parameter phase of high sodium content (Na_{0.87}MNO) as PITT results described above, followed by a single-phase insertion mechanism evidenced by a consistent shift in diffraction peaks to higher d-spacings. Here both the C/60 and C/40 discharge rates were utilized to potentially investigate the aforementioned core/shell reaction mechanism described in an earlier chapter. However, due to insufficient X-ray flux, such investigations were inconclusive, yet still validate the combined two-phase/single-phase reaction progression described by high-resolution electrochemistry independent of the chosen discharge rates.

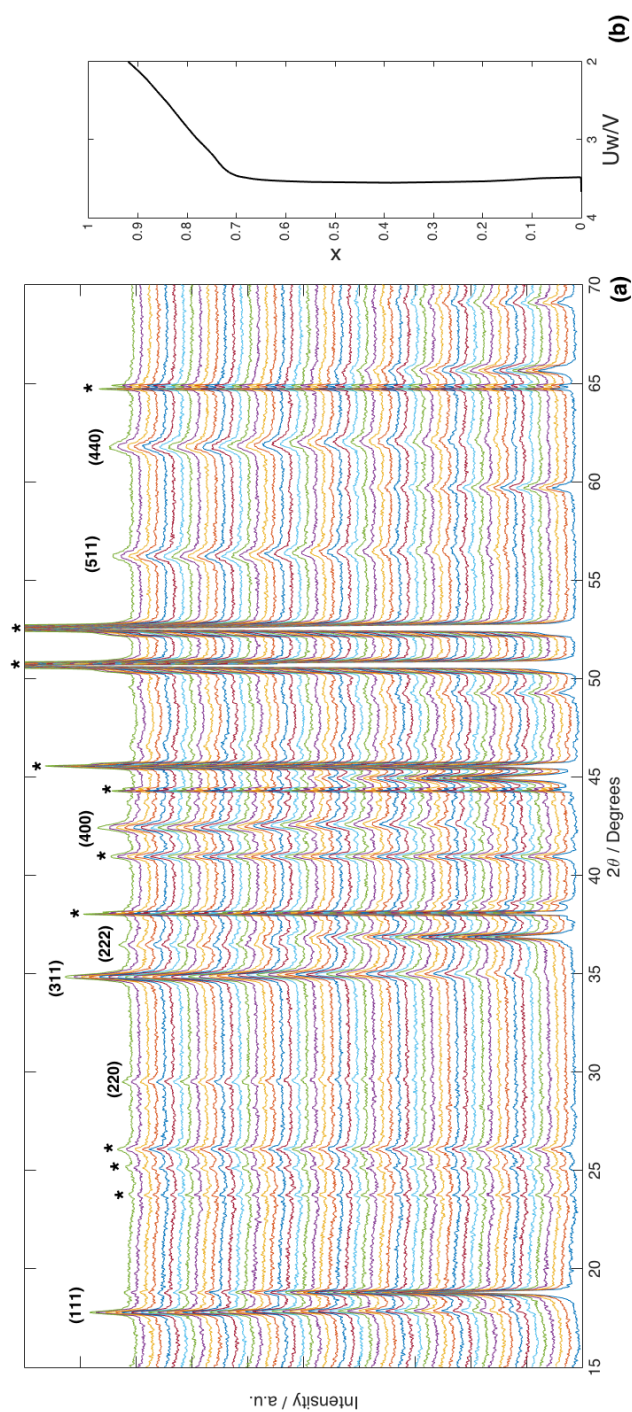


Figure 5-12: C/60 *operando* XRD results of Na^+ insertion into $\text{F}\lambda\text{-MNO}$ spinel. Full XRD 2θ range (a) and discharge profile cycled at 24°C , 1M $\text{NaClO}_4\text{-PC:FEC2\%}$ electrolyte (b). Spinel diffraction peaks are labeled with their respective (hkl) Miller indices, and peaks marked by asterisks denote contributions from the aluminum current collector and beryllium window.

A final discharge capacity of 124.04 mAh/g was achieved for the cell discharged at a C/60 rate, corresponding to *ca.* 92% theoretical capacity. *In-situ* XRD scans taken during open circuit periods following the C/60 discharge did not exhibit any relaxation of the observed sodium spinel peaks, indicating that the reaction does not proceed beyond the intended discharge, and that structural degradation does not appear to be an issue. The vertical guidelines of Figure 4-13 demonstrate the magnitude of the peak shift in the Na-MNO Bragg reflections, and as anticipated by the earlier *ex-situ* XRD results, it appears that the onset of the $\text{Mn}^{4+} \rightarrow \text{Mn}^{3+}$ reduction facilitates the dominating single-phase reaction as can be seen by the onset of peak shift marked at the voltage profile knee of Figure 4-13d.

Peak shift contributions from misalignment of the *in-situ* electrochemical cell may be easily ruled out, as the aluminum mesh current collector acts as an internal standard and indicates no such shift in peak position; thereby indicating that a partially sodiated spinel phase is nucleated, which then proceeds by a single-phase reaction to reach a final composition of $\text{Na}_{0.98}\text{MNO}$, and $\text{Na}_{0.91}\text{MNO}$ for the C/40, and C/60 discharged sodium cells respectively.

Comparison of the C/40 and C/60 *operando* cells provides further insight to the possible rate dependence on the observed onset of the single-phase reaction. The C/60 and C/40 results show the same evidence of a mixed two-phase/single-phase sodium insertion reaction, however, the ratios of the capacity contribution from the respective two-phase and single-phase regions do not directly correlate; potentially indicating inhomogeneous electrochemical processes occurring throughout the particle volume as discussed earlier.

Termination of the two-phase reaction for the C/40 and C/60 *operando* cells occurred at Na_x values of 0.78, and 0.70 respectively, which differs from the PITT measurements mentioned previously ($x = 0.87$). Due to the quasi-equilibrium conditions of the PITT protocol, and apparent kinetic limitations of the two-phase reaction, it is of no tremendous surprise that there is a considerable deviation between the PITT and galvanostatically cycled cells. Most importantly, *operando* measurements validate that the onset of the two-phase/single-phase insertion behavior occurs beyond the *ca.* 3.6V plateau. *Operando* C/60 and C/40 F λ -MNO vs. Na/Na⁺ cells provide valuable information into the structural evolution throughout electrochemical cycling: linking the observed shift in reaction mechanism to the voltage profile. *Operando*

XRD data supports the proposed insertion reactions of Equation 5-2 and Equation 5-3, suggesting that the shift in reaction mechanism occurs as a result of the $\text{Mn}^{4+}/\text{Mn}^{3+}$ reaction. This can potentially be explained by the relative size differences between Mn^{4+} and Mn^{3+} , with the latter acting to prop open the spinel structure, facilitating easier Na^+ diffusion through a single-phase reaction. Further remarks on the origins of the single-phase behavior are provided in following sections.

Figure 5-14 compares the relative change in the measured lattice parameter from the C/60 *in-situ* cell. Here, reported lattice parameters are normalized to the F λ -MNO spinel ($a = 8.000\text{\AA}$) and remain constant throughout the first *ca.* 33 hours of operation while generating a secondary spinel phase ($a \sim 8.44\text{\AA}$) in a typical two-phase insertion reaction. In agreement with the previous electrochemical data, the measured lattice parameter of the sodiated spinel thereby undergoes a systematic increase throughout the single-phase region upon completion of the two-phase reaction. Here it is also important to consider potential error in the measured lattice parameters, as the initial alignment of the *in-situ* electrochemical cell was performed to maximize the intensity of the diffraction peaks, rather than to focus the cathode onto the diffraction plane. Errors in the measured d-spacings are calculated to be less than 2.9% as given by Equation 5-4, where D is the sample displacement normal to the diffracting plane, and R is the goniometer radius. In order to avoid such errors, the relative change in lattice parameters are reported here, and in following sections, using either the vacant λ -phase spinel or the fully sodiated spinel as a point of reference.

Equation 5-4:

$$\frac{\Delta d}{d} = - \frac{D \cos^2 \theta}{R \sin \theta}$$

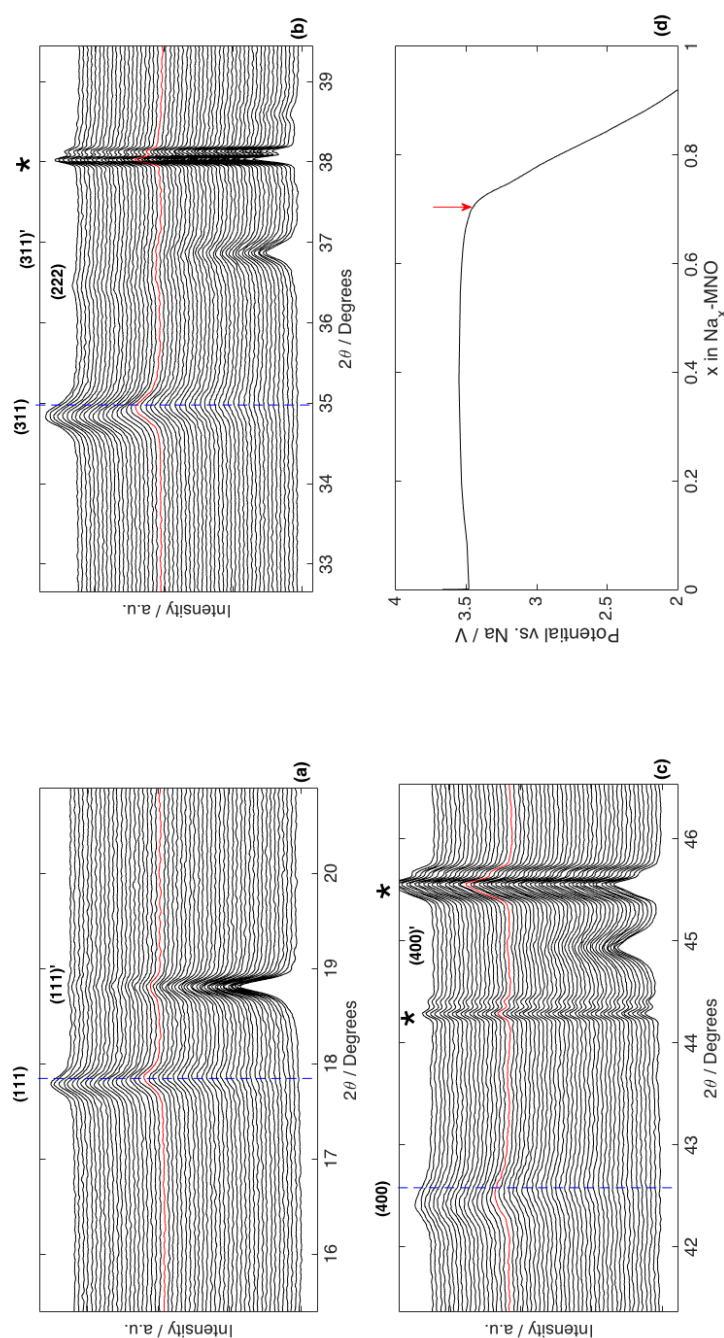


Figure 5-13: Selected diffraction peaks from C/60 discharged F λ -MNO given in Figure 4-12 including the (111) (a), (311) (b) and (400) (c) spinel reflections and voltage profile (d). Dashed lines are provided as a guide to depict the onset in peak shift that occurs beyond the knee in the voltage profile. Diffraction patterns shown in red correlate to the knee in the voltage profile as shown by the red arrow of (d). Peaks marked by asterisks denote diffraction contributions from the current collector/beryllium window.

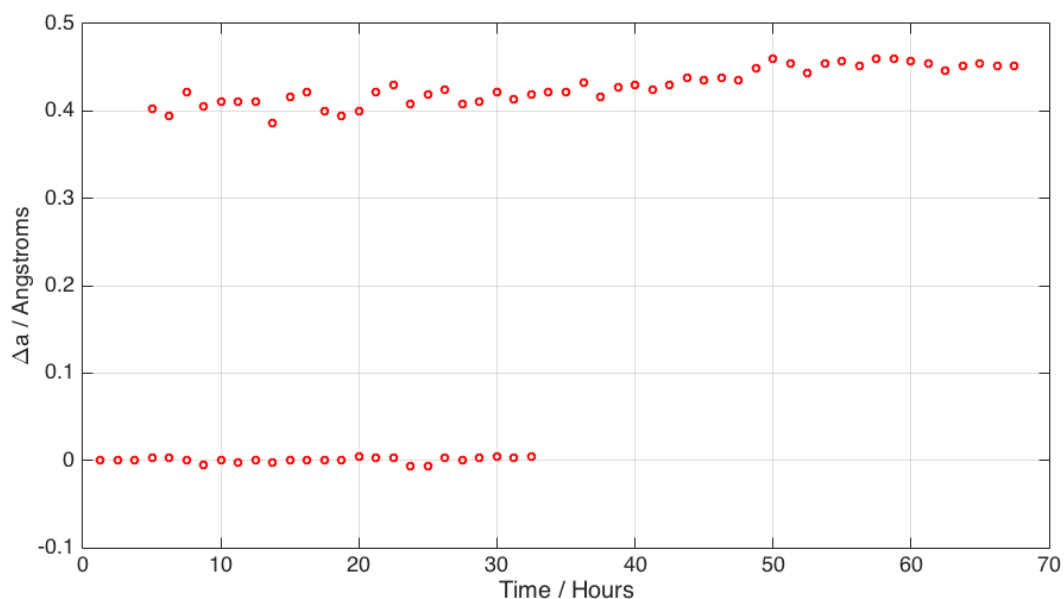


Figure 5-14: Relative a-lattice parameter throughout Na⁺ insertion into Fλ-MNO spinel at 24°C, at 2.25mA/g

5.3.3.4 Discussion

5.3.3.4.1 Reaction Mechanism

The combination of electrochemical and physical characterization techniques previously covered gives a complementary view of the different reaction pathways taking place throughout the initial Na⁺ insertion. The overall reaction pathway consists of both a two-phase and single-phase Na⁺ insertion reaction as described by Equation 5-2 and Equation 5-3. The observed two-phase behavior is sensible when considering to the significant mismatch in lattice parameters between the Fλ-MNO and the Na_{0.87}MNO phases and the subsequent strain energy associated with the Na⁺ insertion onto the 8a tetrahedral sites.

Following the completion of the initial two-phase reaction, the insertion process thereby proceeds along a solid-solution behavior as seen by both *in-operando* XRD and high-resolution electrochemistry data. The transition to a single-phase reaction mechanism significantly improves the reaction kinetics as demonstrated by the calculated diffusion coefficients in Table 5-2. Here, the observed differences in kinetics between the two-phase and single-phase insertion reactions are not entirely surprising, as additional limitations of the grain boundary between the sodiated and desodiated phases must be

considered. The reported diffusion coefficient for the two-phase region in fact, more accurately describes the grain boundary migration between the $F\lambda$ -MNO and the $Na_{0.87}$ MNO phases; explaining the *ca.* 3 order of magnitude difference. Although assumptions surrounding the calculation of the diffusion coefficient for the two-phase reaction here, and in following sections are based off an ideal solid-solution behavior, calculation within the two-phase region occurs without any loss of ‘significance’ in the data, as grain boundary migration will remain the dominant factor throughout the considered two-phase reaction(s).

Although not conclusive, preliminary data suggests some correlation of the initiation of the single-phase reaction with the $Mn^{4+} \rightarrow Mn^{3+}$ reduction reaction, as existing Na^+ within the spinel lattice and difference in ionic radii of Mn^{4+}/Mn^{3+} both act to prop open the spinel host lattice, allowing for facile Na^+ diffusion. While additional analysis may be done on the specific reaction pathways as a function of Mn^{3+} content (present in the $F\lambda$ -MNO due to the initial intended non stoichiometry of the spinel), such works are left for future investigations.

Figure 5-15 considers two discharge voltage profiles: (1) $F\lambda$ -MNO vs. Li/Li^+ and (2) $F\lambda$ -MNO vs. Na/Na^+ . Dashed lines are provided to demonstrate the electrochemical contribution from the Mn^{3+}/Mn^{4+} redox for the $F\lambda$ - $Mn_{1.56}Ni_{0.44}O_4$ composition in particular, which can be more accurately described by Equation 5-5.

Table 5-2: Calculated diffusion coefficients of $F\lambda$ -MNO vs. Na/Na^+ PITT cells

Na^+ insertion reaction	Diffusion Coefficient [cm^2/s]
$F\lambda$ -MNO \rightarrow $FNa_{0.87}$ MNO	1.61 E -16
$FNa_{0.87}$ MNO \rightarrow $FNa_{0.87+x}$ MNO	5.05 E -13

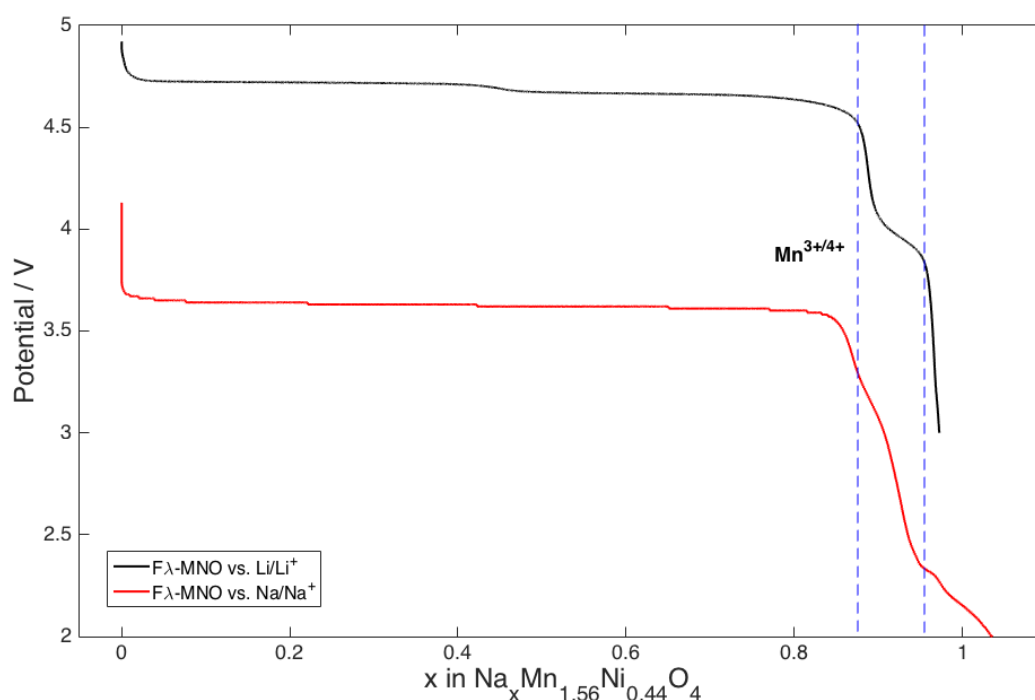


Figure 5-15: Voltage profile comparison between F-MNO vs. Li/Li⁺ and F_λ-MNO vs. Na/Na⁺ with guidelines showing capacity contributions associated with the Mn³⁺/Mn⁴⁺ redox



Considering Figure 5-15, it is also important to note that Na⁺ insertion also appears to occur onto the adjacent 16c octahedral sites, as can be seen by the shift in slope of the voltage profile between the $0.97 < Na_x < 1.03$ compositional range. Here, the ‘spilling’ of Na⁺ onto the adjacent lattice sites does not come as a drastic surprise, as the relative interatomic distances between 8a sites is relatively small when considering the large cationic radii of Na⁺, likely resulting in distorted tetrahedral coordinations of inserted Na⁺ or partial occupancy of the 16c sites in order to reduce repulsive and lattice strain effects from neighboring Na⁺. In fact an additional study on the lattice site occupancy of Na⁺ throughout the $0 < Na_x < 1.0$ compositional range would give valuable insight into the potential limitations of the sodium spinel, and origins of the two-phase/single-phase reaction transition. While in-situ vibrational studies as described in Chapter 1 may provide data related to the tetrahedral/octahedral nature of the sodium sites specifically, Na⁺ insertion is regarded as occurring predominantly on the 8a tetrahedral sites throughout the following sections based off of electrochemical and X-ray characterization.

Figure 5-8, Figure 5-9, and Figure 5-10 all illustrate that following the initial discharge reaction, Na^+ deinsertion is only successful in extracting a narrow range of Na^+ from the FNa-MNO spinel host. Further remarks are provided throughout the following chapter.

5.3.3.4.2 Insertion Potentials Associated With the Spinel Host Structure

As reported by^{301,312} Li^+ insertion into F λ -MNO occurs between 4.7-4.75V. The observed voltage for insertion of Na^+ into λ -MNOF and F λ -MNO shows a significantly different behavior than the anticipated 0.3V difference from considerations of the difference in standard reduction potentials of Li and Na. Overpotential contributions from the negative electrode were found to be negligible, indicating that the observed voltage differences between the Li and Na spinels are due solely to characteristics of the λ -MNOF/F λ -MNO host structure.

To gain insight into the nature of the significant voltage differences between the sodium and lithium spinels, a direct comparison between F λ -MNO and λ - MnO_2 was considered using both a lithium and sodium metal counter electrode. Their voltage profiles are given in Figure 5-16. Although not covered in detail, the additional reaction occurring at *ca.* 2.4V (vs. Na/Na^+) in Figure 5-16a is related to a structural decomposition into a layered phase induced by a cooperative Jahn-Teller distortion of Mn^{3+} cations.

The overall voltage difference between Li^+ and Na^+ insertion is approximately 1.1V (between Figure 5-16d & Figure 5-16b) for F λ -MNO and 1.0V (between Figure 5-16c & Figure 5-16a) for λ - MnO_2 . The observed difference in voltage between the lithium and sodium metal cells are approximately 0.7V larger than the 0.3V difference expected from simple derivation from the discrepancies in standard redox potentials of the respective metal anodes alone, suggesting energetic barrier(s) attributed to the Na^+ insertion into the spinel structure. This/these barrier(s) is/are similar between both the nickel substituted and unsubstituted spinels, and three electrode studies have shown (Figure 5-10) that the overpotential of the Na/Na^+ reaction is not a contributor to the overall cell potential, thereby attributing the disparity in potential to the ability of the host structure to accommodate the Na^+ . Since the nickel substitution of λ -MNOF and F λ -MNO acts to increase the observed potential by approximately 0.5V consistently relative to λ - MnO_2 regardless of the intercalating species (Li^+ or Na^+) further generalization of this behavior can be said to be characteristic of Na^+ insertion into the Fd-3m spinel structure.

This insertion occurs without structural decomposition or rearrangement as evidenced by the comparative voltage profiles and XRD data shown previously, as *ex-situ* XRD data indicates that insertion of Na^+ has been occurring solely on the vacant 8a tetrahedral sites. Here, it is also important to elucidate that potential Na^+ insertion onto the adjacent 16c octahedral sites is likely occurring (< 8%) below 2.2V (vs. Na/Na^+). However, throughout the remaining chapters, Na^+ insertion behavior will be described as occurring exclusively onto the 8a sites, as further in-depth characterization methods are necessary to elucidate the occupancy of the 16c sites.

Overall, a consistent *ca.* 0.6V difference is observed between the $\text{F}\lambda\text{-MNO}$ and $\lambda\text{-MnO}_2$ sodium cells; with an average voltage difference of 1.10V and 1.0V demonstrated between the lithium and sodium cells respectively. This simple comparison allows for two profound conclusions regarding the Na^+ insertion reaction onto the $\text{F}\lambda\text{-MNO}$ host lattice: (1) The $\text{Ni}^{2+}/\text{Ni}^{4+}$ redox reaction is still the predominant electrochemical reaction being considered, indicating that a similar insertion reaction is occurring between Li^+ and Na^+ , and (2) the high-voltage $\text{F}\lambda\text{-MNO}$ phase sees additional energetic penalties associated with the Na^+ insertion reaction attributed to the both steric and specific lattice site energy differences between Li^+ and Na^+ .

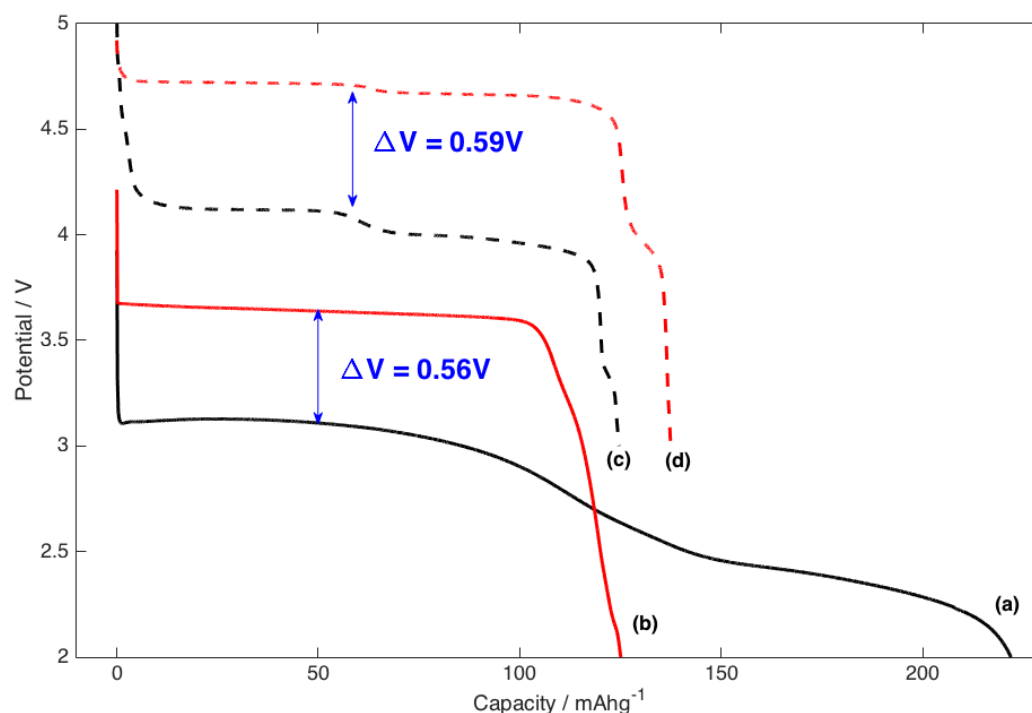


Figure 5-16: Discharge profiles of F λ -MNO and λ -MnO₂ in Li-metal (dashed) and Na-metal cells (solid) respectively. λ -MnO₂ vs. Na/Na⁺ (a) F λ -MNO vs. Na/Na⁺ (b), λ -MnO₂ vs. Li/Li⁺ (c), and F λ -MNO vs. Li/Li⁺ (d) cells were discharged at a C/100 rate at 24°C using 1M NaClO₄-PC:FEC2% and 1M LiPF₆-EC/DMC electrolytes for sodium and lithium metal cells respectively.

5.3.4 Na⁺ insertion into λ -Mn_{0.75}Ni_{0.25}O₂ (P λ -MNO)

5.3.4.1 Results

Lithium spinels have consistently demonstrated³⁷⁴ significantly different cycling characteristics as a function synthesis conditions due to formation of a primitive ordered P4₃32 spinel in which nickel substitutions are distributed along alternating layers along the [111] direction. It is therefore of particular interest to examine the characteristics that govern Na⁺ insertion into the P λ -MNO spinel. Here, P λ -MNO spinel was formed by additional heat treatment of F λ -MNO at 700°C in air for 12 hours. The resulting XRD and FTIR data are covered in Figure 4-2 and Figure 4-4, with the P λ -MNO spinel being formed by the same method as described throughout Chapter 4.

Initial galvanostatic cycling (3mA/g cycling current at 24°C between 2.0 – 4.25V) of P λ -MNO (vs. Na/Na⁺) demonstrates a similar voltage profile as that previously seen for F λ -MNO vs. Na/Na⁺ cells

throughout the initial discharge reaction of Figure 5-17a. Considerable change in the voltage profile following the initial discharge/charge cycle can be seen in Figure 5-17b and is discussed further in the following chapter. Here, the initial Na^+ insertion observes a final capacity of 112.3 mAh/g, (73% theoretical capacity) which is considerably low when considering the initial discharge capacities of typical $\text{F}\lambda\text{-MNO}$ cathodes ($\sim 90\%$ theoretical capacity) under similar galvanostatic conditions.

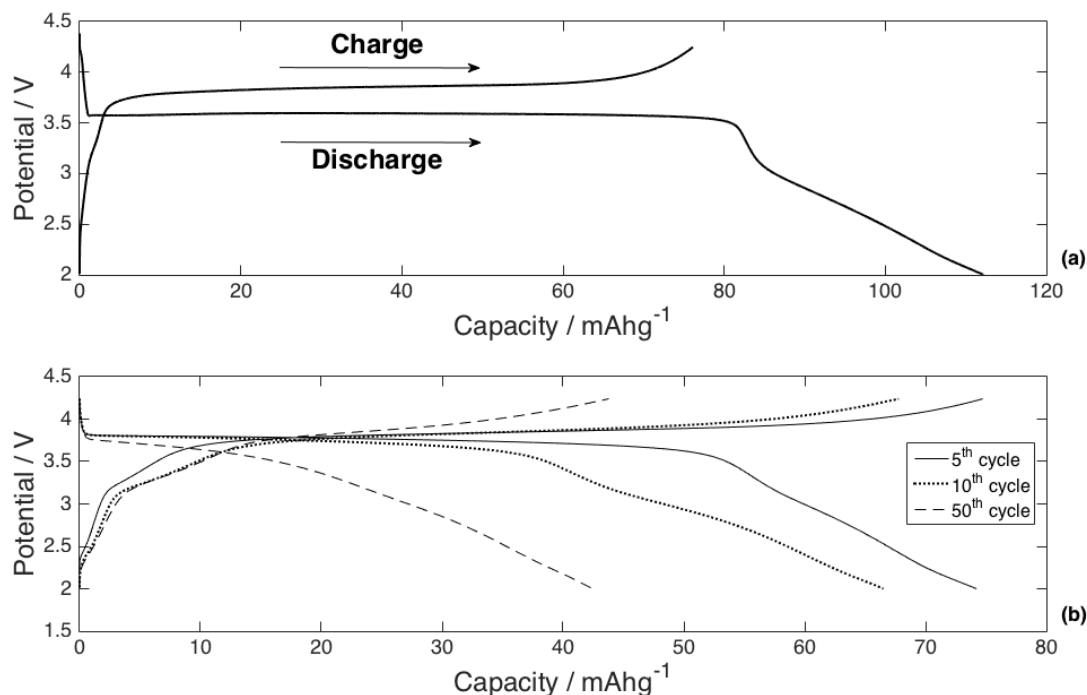


Figure 5-17: Voltage profile of PNa-MNO vs. Na/Na^+ . The first discharge/charge cycle (a) 5th, 10th, and 50th cycles (b) are cycled at 3 mA/g at 24°C using 1M NaClO_4 -PC:FEC2% electrolyte.

5.3.4.2 Coulometric Titration

PITT was used to determine Na^+ insertion kinetics and specific reaction mechanisms taking place within the $\text{P}\lambda\text{-MNO}$ spinel. Figure 5-18 considers both the voltage profile and current response throughout the first discharge/charge cycle operated between 2.5 – 4.25V (vs. Na/Na^+) at 24°C using a 1M NaClO_4 -PC:FEC2% electrolyte and a 0.25 mA/g current cutoff.

As Na^+ begins, a two-phase reaction is apparent by the non-Cottrellian current response throughout the ~ 8 10 mV potential steps within the 3.69 - 3.61V potential range. The two-phase reaction then comes to a stop at an average composition of $\text{PNa}_{0.63}\text{MNO}$, and thereby continues along a single-phase insertion reaction as evidenced by both the sloping voltage profile and the current response. Notably

different from the $F\lambda$ -MNO, $P\lambda$ -MNO reaches just over 81% theoretical capacity, suggesting that some additional Na^+ insertion barriers exist when considering the ordered $P\lambda$ -MNO spinel.

Judging from the PITT and galvanostatic data alone, the initial Na^+ insertion reaction appears to progress in a similar two-phase/single-phase reaction pathway as previously described for $F\lambda$ -MNO, except with a considerable difference in the amount of sodium in the spinel host lattice. Equation 5-6 and Equation 5-7 considers the two step reaction pathway for the initial Na^+ insertion into $P\lambda$ -MNO. However, considering the consistently low discharge capacities of the $P\lambda$ -MNO, despite the quasi-equilibrium conditions PITT cycling affords, it is expected that a considerable amount of unreacted $P\lambda$ -MNO phase is still present, making Equation 5-6 and Equation 5-7 inaccurate representations of the Na^+ insertion reaction, as is highlighted and discussed in the following sections.

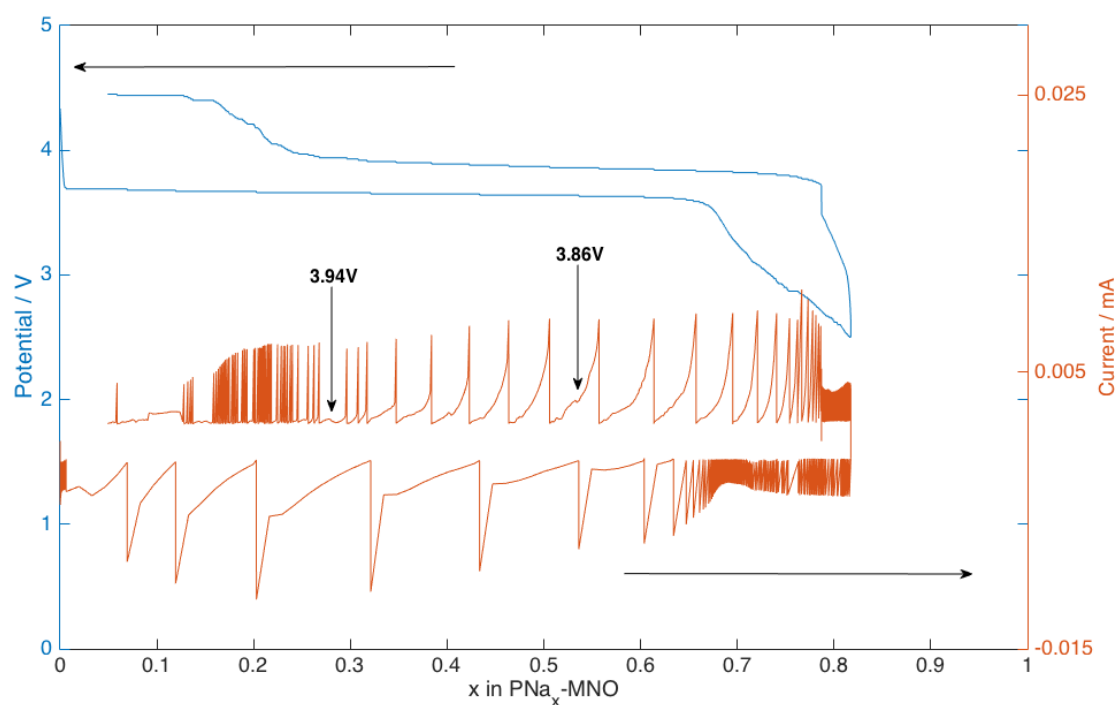
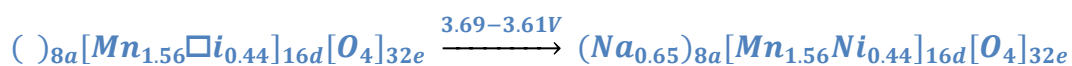


Figure 5-18: Potentiostatic intermittent titration technique (PITT) discharge/charge cycle for $P\lambda$ -MNO vs. Na/Na^+ using 1M NaClO_4 -PC:FEC2% at 24°C and a 0.25 mA/g current cutoff

Equation 5-6:



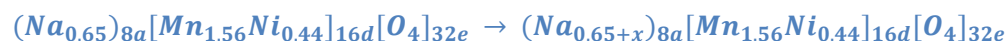
Equation 5-7:

Table 5-3 provides the calculated diffusion coefficients throughout the initial Na⁺ insertion reaction for both the two-phase and the single-phase reactions. Here, the reported Na⁺ insertion reactions are based off of *in-situ* XRD data due to incomplete reaction of the Pλ-MNO under normal galvanostatic and PITT cycling conditions. It is once again important to illustrate that calculation of the diffusion coefficients in this manner is based on assumptions around a solid-solution behavior, and only realistically describes the grain boundary migration between the Pλ-MNO/PNa_{0.93}MNO phases for the two-phase reaction described. This however does not diminish the meaningfulness of the data, as the grain boundary migration is the rate-limiting process throughout the considered two-phase reaction, as can be seen by the *ca.* 3 orders of magnitude difference in the calculated diffusion coefficients of Table 5-3.

Table 5-3: Calculated diffusion coefficients for the initial Na⁺ insertion reaction into Pλ-MNO

Na ⁺ insertion reaction	Diffusion Coefficient [cm ² /s]
Pλ-MNO → PNa _{0.93} MNO	4.67 E -16
PNa _{0.93} MNO → PNa _{0.93+x} MNO	8.26 E -13

The following charge (desodiation) occurs primarily by a single-phase Na⁺ deinsertion reaction as indicated by the PITT and *in-situ* XRD data of the following sections. However, Figure 5-18 sees an additional non-Cottrellian current response at *ca.* 3.92V (vs. Na/Na⁺) indicating a minor two-phase reaction taking place during the Na⁺ deinsertion process. Additional reactions can be seen above 4.2V, however, due to the inherent limitations of the PC based electrolyte, further contrasting data is needed to elucidate the specific processes taking place during desodiation. Further discussion on the desodiation process is left for the following chapter.

5.3.4.3 Ex-situ X-ray Diffraction (XRD)

Figure 5-19 considers a discharged Pλ-MNO vs. Na/Na⁺ cathode using the same *ex-situ* XRD sample preparation techniques described previously. The cell was discharged to 2.0V (vs. Na/Na⁺) using a

3.0 mA/g current at 24°C using a 1M NaClO₄-PC:FEC2% electrolyte, reaching a final discharge capacity of 106.7 mAh/g (~79% theoretical capacity). Asterisks pertain to diffraction peaks from the Kapton film, and $(hkl)'$ and $(hkl)''$ Bragg reflections are used to indicated the initial P λ -MNO and an intermediate PNa_x-MNO phase respectively. This behavior is very similar to that observed for λ -MNOF cathodes in which multiple spinel phases have been demonstrated as a result of the kinetic limitations of the active material.

As will be discussed in the following chapter, in order to draw further comparisons between the ordered (PNa-MNO) and disordered (FNa-MNO) sodium spinels, P λ -MNO cathodes are initially discharged at 50°C in order to facilitate complete reaction of the P λ -MNO particles; achieving similar discharge capacities to F λ -MNO (24°C). Various limitations of the P λ -MNO spinel are also expected from the comparatively low surface area of the P λ -MNO powder samples: 4.6 m²/g vs. 5.7 m²/g for the ordered and disordered spinels respectively. Additional comments are provided in the following chapter.

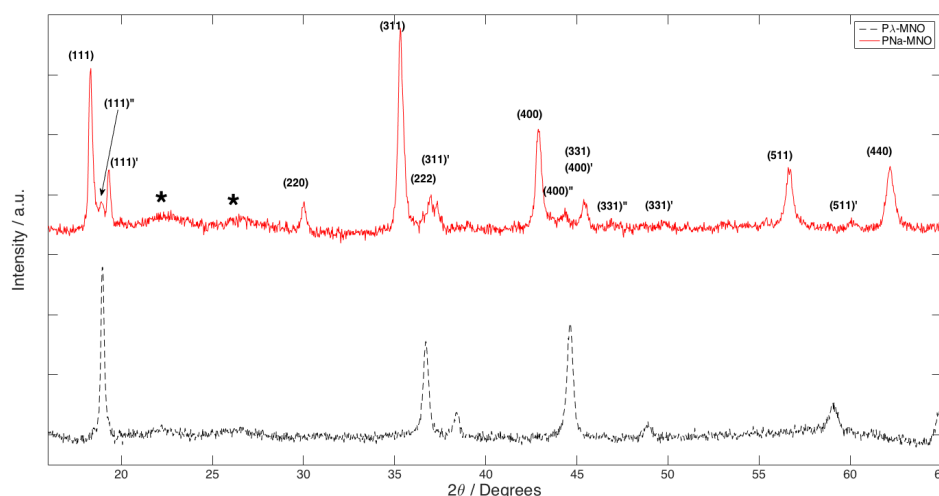


Figure 5-19: Ex-situ XRD comparison between P λ -MNO and sodiated P λ -MNO using a 3.0 mA/g discharge current at 24°C with 1M NaClO₄-PC:FEC2% electrolyte. Note: XRD pattern of the PNa-MNO *ex-situ* sample observes a slight 2θ shift relative to the P λ -MNO sample due to sample height displacement from the thickness of the cathode disk.

Nevertheless, discharged P λ -MNO (vs. Na/Na⁺) cathodes exhibit three key features: (1) Na⁺ insertion is occurring on the 8a tetrahedral sites, as can be inferred by the significant growth in intensity of the (220) Bragg reflection as compared to P λ -MNO. Due to both the reversibility of the PNa-MNO spinel, and the relatively low temperatures used, possible migration of Mn/Ni onto the 8a tetrahedral sites is ignored as insufficient thermal energy is provided to break the M-O bonds. (2) Na⁺ insertion begins by a

two-phase reaction as indicated previously by galvanostatic and PITT electrochemical data, which can be easily observed in Figure 5-19 due to the remaining $P\lambda$ -MNO phase as marked by the $(hkl)'$ Bragg peaks. And (3) there exist significant kinetic limitations of the ordered ($P\lambda$ -MNO) spinel as compared to the disordered ($F\lambda$ -MNO) spinel, which limits the initial Na^+ insertion reaction, and subsequent cycles, as will be discussed later.

5.3.4.4 Operando X-ray Diffraction (XRD)

Continuous XRD scans were performed under *in-operando* conditions on a $P\lambda$ -MNO vs. Na/Na^+ cell using a 3mA/g current at 24°C and a 1M $NaClO_4$ -PC:FEC2% electrolyte. X-ray scans were taken on a $Na_x = 0.02$ interval, which is assumed to introduce negligible contribution on the resulting diffraction data. Bragg peaks are labeled with asterisks and are indexed as $(hkl)/(hkl)'$ in accordance with the previous section. Vertical guide-lines are provided to demonstrate a minor peak shift in the PNa -MNO spinel Bragg reflections indicating a single-phase Na^+ de/insertion behavior.

Figure 5-20 provides the stacked XRD scans throughout the first discharge/charge cycle of the P λ -MNO vs. Na/Na⁺ cell.

Figure 5-21 considers only the (111), (311) and (400) spinel reflections, and more clearly demonstrates the two-phase and single-phase Na^+ insertion reactions taking place during the initial discharge. Further remarks regarding the successive Na^+ de/insertion processes depicted in Figure 4-21 is reserved for the following chapter.

In Figure 4-21 the Na^+ insertion reaction initiates by a two-phase reaction producing a sodiated spinel of larger lattice parameter as indicated by the relative peak positions between the $(hkl)'$ and the (hkl) reflections. As compared to the earlier *ex-situ* XRD data, no $(hkl)''$ phase can be identified, possibly due to the relatively low diffraction intensities resulting from the specific experimental setup of the *in-situ* electrochemical cell discussed within the experimental section. Nonetheless, the *operando* XRD data clearly validates the combined two-phase/single-phase reaction pathway throughout the initial Na^+ insertion as shown earlier by the PITT data. In fact, the *operando* XRD data enables a more definitive look at the initial two-phase reaction that is occurring, as the initial $\text{P}\lambda\text{-MNO}$ phase offers a convenient internal reference peak from which a precise lattice parameter can be calculated for the two-phase reaction product.

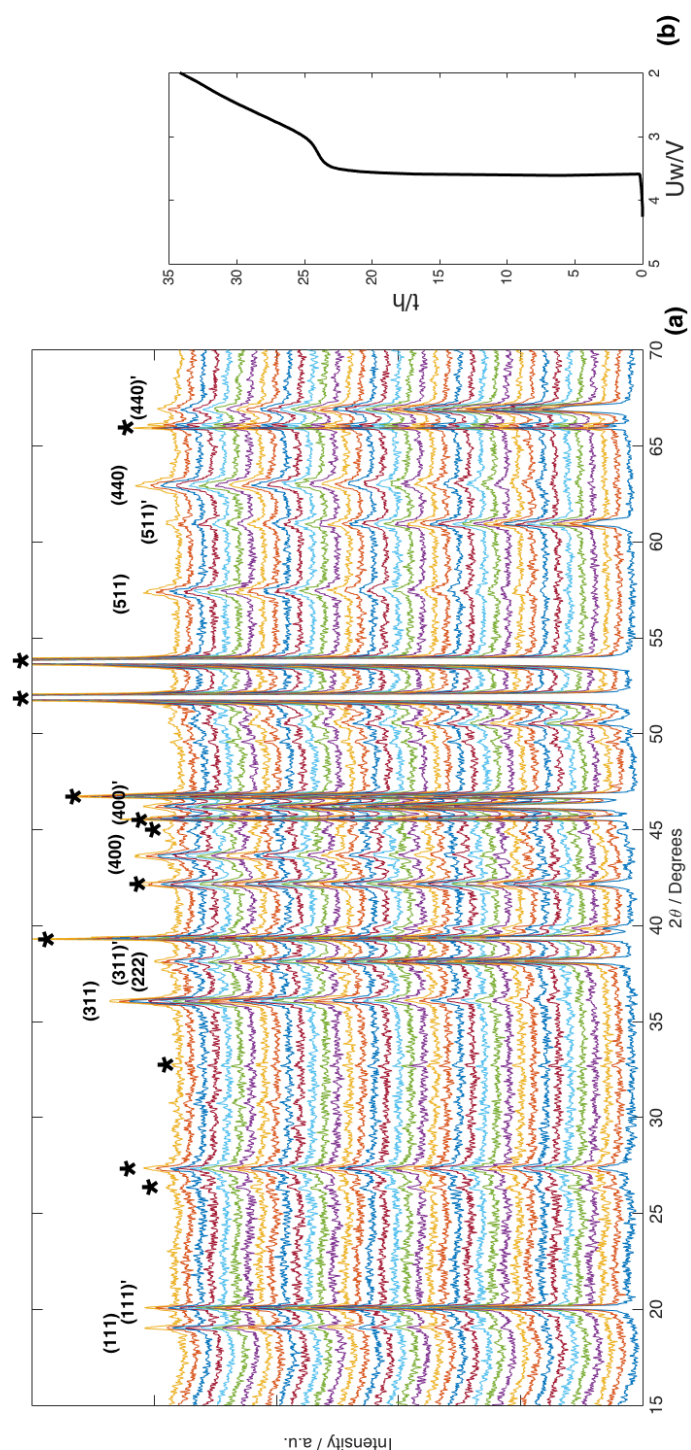


Figure 5-20: $P\lambda$ -MNO ($P4_32$) spinel discharged at 24°C and 3mA/g using 1M NaClO_4 -PC:FEC2%. XRD scans are taken on a Δx interval of 0.02 in order to avoid significant peak broadening contributions. Dashed vertical lines are provided to illustrate the minor peak shift that occurs during single-phase Na^+ insertion, most clearly identified by the (511) and (440) Bragg reflections.

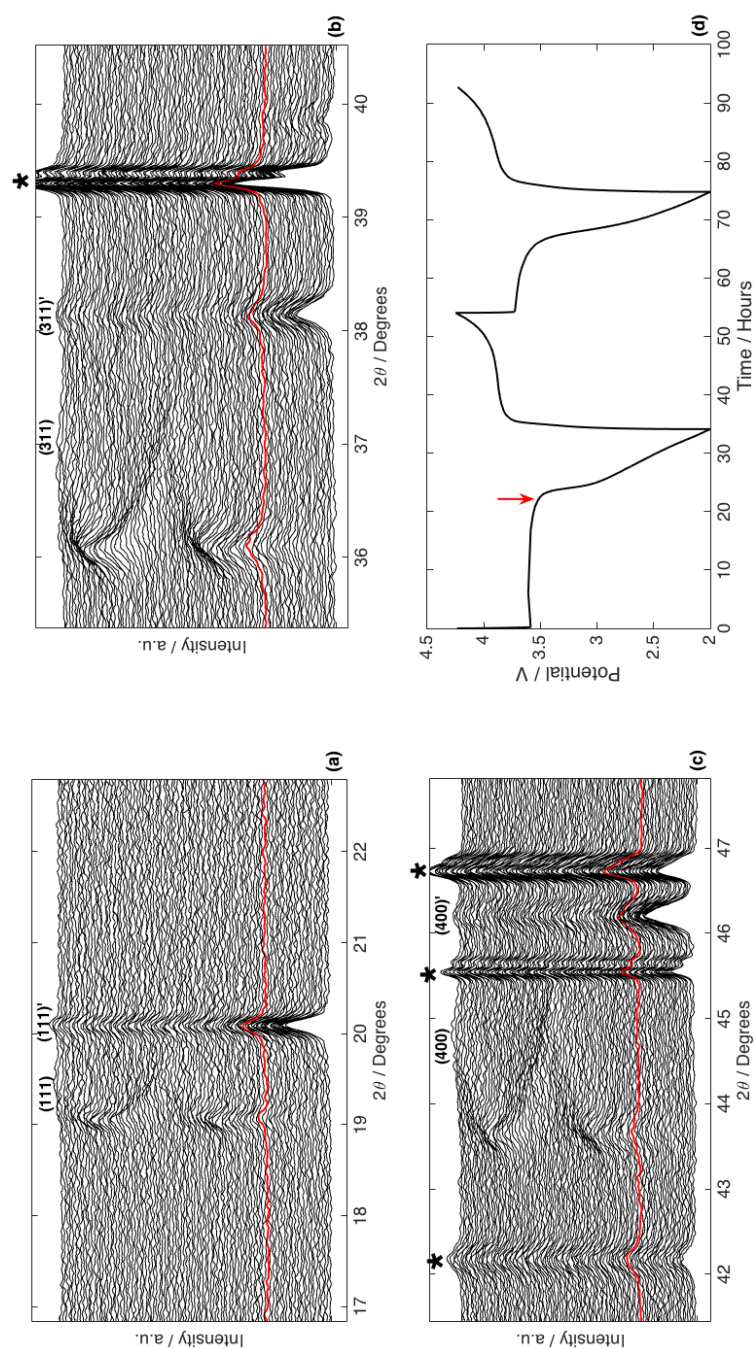


Figure 5-21: Selected diffraction peaks from P λ -MNO vs. Na/Na⁺ given in Figure 4-20 including the (111) (a), (311) (b) and (400) (c) spinel reflections and galvanostatically cycled voltage profile (d). Diffraction patterns shown in red correlate to the knee in the voltage profile as shown by the red arrow of (d). Peaks marked by asterisks denote diffraction contributions from the current collector/beryllium window.

Figure 5-22 considers the relative change in lattice parameter throughout the initial Na⁺ insertion reaction. As the initial two-phase reaction begins, a second spinel phase (PNa-MNO) of approximate lattice parameter *ca.* 8.419Å is formed, and undergoes further expansion of the spinel lattice to a value of *ca.* 8.433Å by the end of discharge. As noted previously, full theoretical capacity is seldom achieved at ambient (24°C) conditions when considering the Pλ-MNO spinel. The fully sodiated PNa_{1.0}MNO spinel is quantified by the Pλ-MNO vs. Na/Na⁺ coin cells discharged at 50°C, which produce a sodiated spinel phase with an approximate lattice parameter of *ca.* 8.453Å. Considering the relative changes in lattice parameter between the vacant and fully sodiated spinel structures, an approximate value of the initially formed two-phase reaction product can be assigned as described by Equation 5-8 and dEquation 5-9.

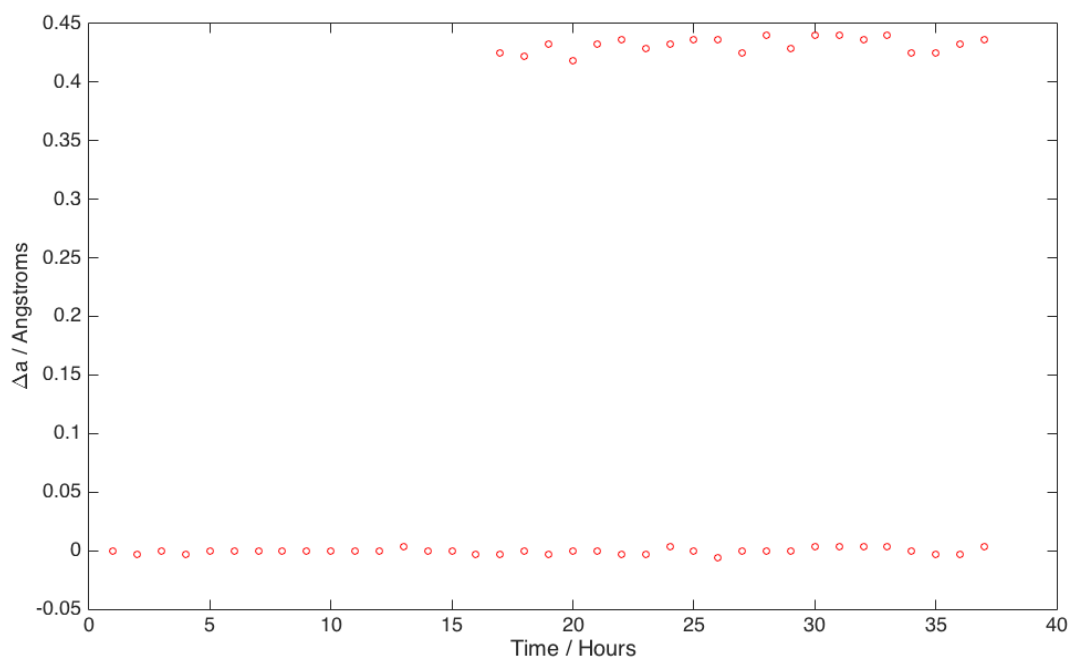
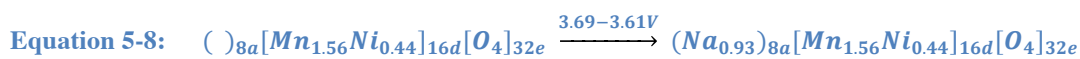


Figure 5-22: Relative lattice parameters of Pλ-MNO vs. Na/Na⁺ *in-operando* XRD data given in Figure 4-20. Lattice parameters are normalized according to the d-spacing of the Pλ-MNO phase.



5.3.4.5 PNa-MNO Discussion/Summary

Both galvanostatic and potentiostatic electrochemical data of Figure 5-17 and Figure 5-18 demonstrate that Na^+ de/insertion into the ordered P λ -MNO host structure is a reversible process. However, it is apparent that there exist some further kinetic barriers preventing the complete Na^+ insertion reaction into the P λ -MNO phase as compared to that previously considered for the F λ -MNO spinel, as both the voltage profile characteristics and observed discharge capacities see a significant change following the initial discharge.

Considering the Na^+ deinsertion process, and the subsequent cycles beyond the initial discharge, the ordered PNa-MNO spinel demonstrates that further difficulties arise when extracting Na^+ from the spinel host structure; resulting in low charge capacities, and sodiated spinel phases that deviate from the initial P λ -MNO as apparent by the final peak positions of the diffraction peaks at the end of charge throughout Figure 4-21. The expanded lattice parameter, and limited discharge capacities of successive cycles demonstrate only a narrow reversible compositional range within the ordered spinel of $ca. 0.61 < \text{Na}_x < 0.99$ prompting further investigation of the specific Na^+ deinsertion reaction mechanisms, which is the subject of the following chapter.

Two intrinsic properties of the ordered spinel can be offered as a potential source for the difference in the initial two-phase reaction between the F λ -MNO and P λ -MNO spinels at this point: (1) the P λ -MNO spinel has a notably smaller lattice parameter as compared to the F λ -MNO; 7.994 Å vs. 8.000 Å respectively. And (2) existing literature^{26,304,313} on the ordered PLi-MNO spinel has suggested that the likewise relatively poor performance of the ordered (vs. disordered) spinel may arise from a reduction in electrical conductivity of the ordered spinel resulting from the specific electronic band structure differences between the ordered and disordered spinel.

As the origins of the initial two-phase reaction are attributed to the large difference in lattice parameter between the vacant and sodiated spinels, specific differences between the ordered and disordered spinels are not readily apparent. It is proposed that the relatively smaller lattice parameter of the P λ -MNO phase presents itself with considerably smaller 8a tetrahedral sites; explaining the relatively poor Na^+ insertion kinetics of the ordered spinel, and potentially explaining the P λ -MNO \rightarrow PNa_{0.93}MNO two-phase reaction, as poor insertion kinetics would result in some degree of Na^+ ‘pile-up’ as compared to the F λ -

MNO \rightarrow FNa_{0.87}MNO two-phase reaction. This theory however does not correlate with the existing calculated diffusion coefficients from the PITT data given in Table 5-4. The reported diffusion coefficients suggest that Na⁺ diffusivity in the ordered spinel is significantly higher as compared against F λ -MNO, which largely contrasts with previous considerations based solely on the differences in lattice parameters between the vacant and sodiated spinels respectively.

Table 5-4: Calculated diffusion coefficients for F λ -MNO and P λ -MNO throughout the initial Na⁺ insertion reaction

Na ⁺ insertion reaction	Diffusion Coefficient F λ -MNO [cm ² /s]	Diffusion Coefficient P λ -MNO [cm ² /s]
Two-phase reaction	1.61 E -16	4.67 E -16
Single-phase reaction	5.05 E -13	8.26 E -13

Due to the disagreement between these considerations, it is therefore suspected that predominant differences between the F λ -MNO and P λ -MNO spinels are due to the differences in electronic band structure, which has demonstrated characteristically different behavior within analogous lithium cells. Further investigation into these differences is however, beyond the scope of this work, and is left for future considerations.

The initial two-phase insertion reaction described by Equation 5-8 is solely based off XRD data, and provides a more accurate account to the reaction mechanisms within the P λ -MNO spinel as compared to that inferred by the PITT data, and will be referred to in the following chapters. Here, the combined use of high-resolution electrochemistry and physical characterization techniques illustrates the large kinetic limitations of the ordered spinel, and provides a number of important points for further consideration. (1) The initial two-phase reaction occurs between the P λ -MNO phase and a sodiated phase of approximate composition PNa_{0.93}MNO, which contains considerably more Na⁺ than the analogous two-phase reaction into the F λ -MNO spinel. (2) Even under quasi-equilibrium conditions (24°C) complete sodiation of the P λ -MNO phase is not attainable, only being achieved when cycling at elevated temperatures (50°C). (3) Initial galvanostatic and potentiostatic cycling has illustrated that the Na⁺ de/insertion reaction mechanism(s) of successive cycles deviate from those seen throughout the initial Na⁺ insertion reaction; primarily occurring along a single-phase Na⁺ de/insertion reaction. (4) Desodiation from the ordered spinel does not produce

the original $P\lambda$ -MNO phase, effectively limiting the attainable discharge capacity of successive cycles within the narrow $0.61 < Na_x < 0.99$ compositional range; indicating that there exist additional kinetic limitations of the PNa-MNO spinel when considering Na^+ deinsertion.

6 Na⁺ deinsertion, Na⁺ reversibility, and reaction mechanisms

6.1 Introduction

The previous chapter has considered the insertion of Na⁺ into the vacant λ -MnO₂, λ -MNOF, F λ -MNO, and P λ -MNO spinel host structures, through both electrochemical and physical characterization techniques. Due to the robust spinel framework, the large volumetric strains associated with the Na⁺ insertion reaction can be accommodated, and demonstrate moderate capacities and excellent reversibility within a narrow compositional range of *ca.* $\Delta\text{Na}_x = 0.5$. This narrow cycling compositional range presents itself as one of the key limiting factors in considering λ -Mn_{2-x}Ni_xO₄ spinel for high power sodium-ion batteries, as a substantial amount of Na⁺ remains locked in the spinel host, thereby limiting the theoretical capacity of successive cycles.

In order to fully utilize the potential of a sodium spinel cathode, further investigations into the energetic barriers preventing the complete extraction of Na⁺ from the spinel host structure are necessary, and should eventually result in the optimization of the spinel crystal structure such that factors such as the discharge capacity, rate capability, reversibility and cost are considered.

Throughout this chapter, the specific desodiation reaction(s) for the F λ -MNO and P λ -MNO will be discussed. Although the λ -MnO₂, and λ -MNOF spinels are excluded from this analysis, their individual characteristics are expected to be similar to that of the F λ -MNO spinel with some considerable deviations due to specific differences in their respective active redox reactions, and particle sizes/surface areas.

6.2 Results

6.2.1 Constant current / constant voltage cycling

In order to promote the desodiation reaction from both the F λ -MNO and P λ -MNO spinels, (F/P) λ -MNO vs. Na/Na⁺ cells were cycled using a constant current (3mA/g), constant voltage electrochemical protocol while examining the effect of increasing charging potentials. The specific potential cutoffs and current cutoffs for the constant voltage segments are outlined in Table 5-1 Table 6-1.

Table 6-1: Constant current, constant voltage protocol of F λ -MNO and P λ -MNO cells cycled using 1M NaClO₄-PC:FEC2% electrolyte at 24°C

	1st Cycle	2nd Cycle	3rd – nth Cycle
Charge	4.25V; 1.0 & 2.0 mA/g	4.35V; 1.0 & 2.0 mA/g	4.45V; 1.0 & 2.0 mA/g
Discharge	2.0V	2.0V	2.0V

Charge	4.25V; 1.0 & 2.0 mA/g	4.35V; 1.0 & 2.0 mA/g	4.45V; 1.0 & 2.0 mA/g
Discharge	2.5V	2.5V	2.5V

Figure 6-1 considers the discharge capacities and characteristic voltage profiles of F λ -MNO (a-b) and P λ -MNO (c-d). For F λ -MNO samples (Figure 5-1a), cells discharged to 2.0V had an initial discharge capacity between 132-141 mAh/g ($N_{ax} = 0.867 - 0.928$ respectively), and 124-129 mAh/g ($N_{ax} = 0.813 - 0.849$ respectively) when discharged to 2.5V. And for P λ -MNO cells (Figure 5-1c), initial discharge capacities are notably low at 112 mAh/g and 97 mAh/g for both the 2.0 and 2.5V potential cutoffs respectively.

The relatively low initial capacity of the P λ -MNO suggests a finite amount of unreacted P λ -MNO phase remaining at the end of the initial discharge, consistent with previous operando XRD data discussed throughout the earlier text. While the P λ -MNO cells demonstrated relatively poor cycling characteristics when compared against F λ -MNO, P λ -MNO cells discharged to 2.0V exhibit a comparatively high discharge capacity throughout the first ca. 10 cycles of operation than those (P λ -MNO) discharged to 2.5V. This suggests that the residual P λ -MNO is contributing to minor additions in discharge capacity beyond the first cycle, also seen by changes in relative intensities throughout *operando* studies, which will be covered in the following sections.

Differences in cycling performance across the various constant voltage protocols may also suggest contrasting failure mechanisms between the disordered and ordered spinels; chiefly, the FNa-MNO spinel observes a more drastic reduction in capacity when discharging to 2.0V, which has been previously demonstrated involve some minor Na⁺ insertion onto the adjacent 16c octahedral sites. While no evidence of an irreversible structural transformation has been found, partial irreversible decomposition to an orthorhombic phase could explain the disparity between FNa-MNO vs. Na/Na⁺ cells discharged to 2.0 and 2.5V.

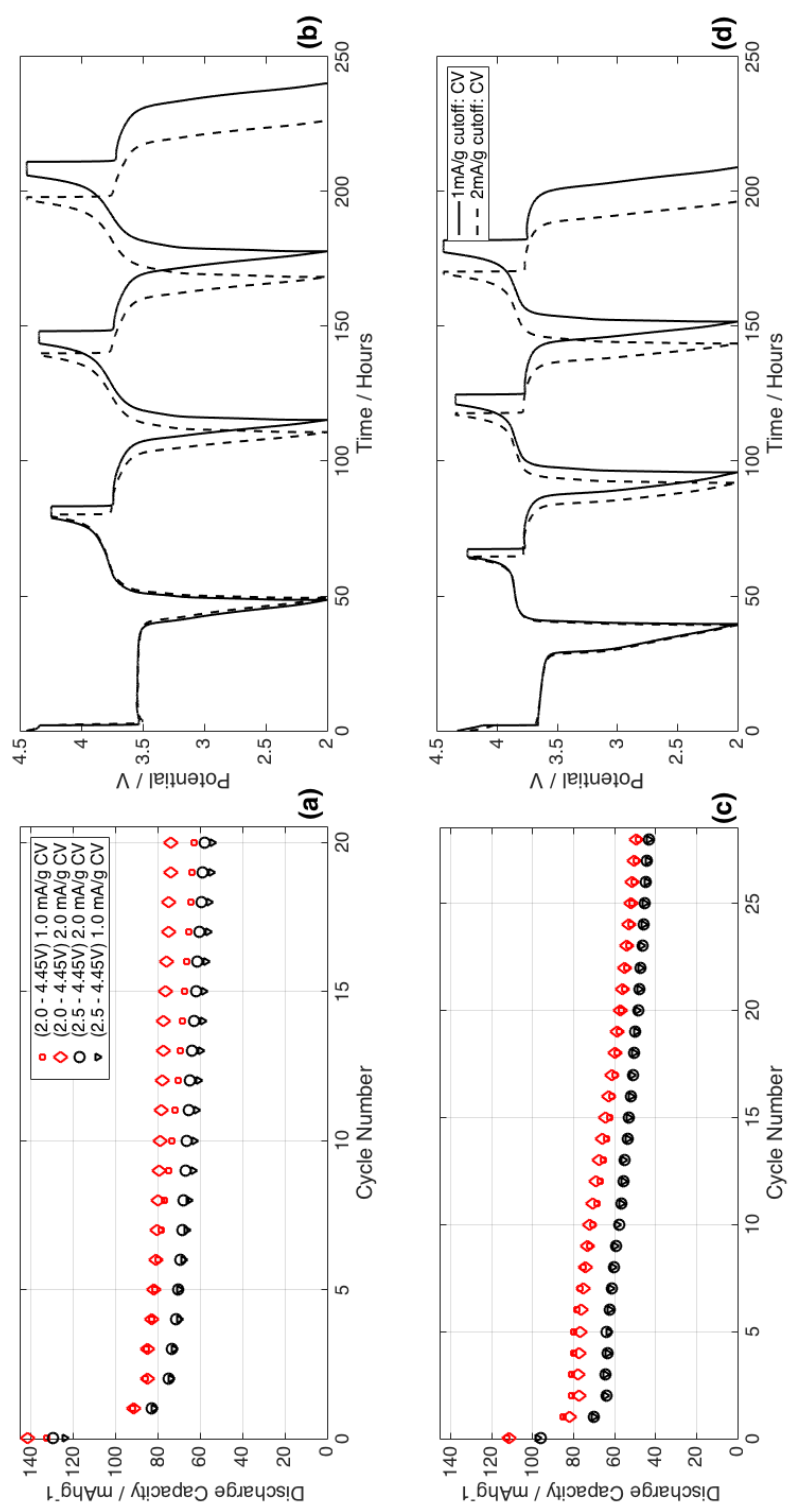


Figure 6-1: Constant current/Constant voltage Fλ-MNO and Pλ-MNO vs. Na/Na⁺ cells at 24°C, 1M NaClO₄-PC:FEC2%. Discharge capacities of Fλ-MNO (a) and Pλ-MNO (c) are given for cells using both a 2.0 and 2.5V lower potential cutoff, and a 1.0/2.0 mA/g constant voltage current cutoff as described in

Overall, cells maintain appreciable cycle efficiency of ca. 90-95%, with a gradual reduction in performance. Most of this reduction in performance is likely associated to the degradation of the NaClO₄-PC:FEC2% electrolyte as evidenced by the discoloration of electrolyte upon cell disassembly. Additional *ex-situ* XRD analysis on cells cycled beyond 50 cycles indicate that the spinel structure is maintained without evidence of structural decomposition or formation of additional phases, clearly demonstrating that the Na⁺ insertion reaction into the (F/P)Na_x-MNO structure is highly reversible.

6.2.2 Na⁺ de/insertion reaction pathway

Despite utilizing increasing charging potentials, and a range of constant voltage charging techniques, it appears that the desodiation reaction is still largely limited by additional energetic barriers, as the discharge capacities do not see any appreciable improvement as a function of voltage cutoff/constant voltage segment, which would be expected to arise from increased amounts of desodiation. This result may in fact be due to the limited stability of the PC based electrolyte used, in which efforts of the increasing potential cutoffs and prolonged exposure at high voltage predominantly contribute to oxidation of the electrolyte rather than to drive the desired Na⁺ deinsertion reaction.

While additional desodiation strategies are covered in the following sections, Figure 6-2 is provided in order to assist and guide the reader through the mechanistic pathways described for both the disordered and ordered sodium spinels within the following sections. Within Figure 6-2, segments marked by red arrows indicate a two-phase Na⁺ de/insertion reaction occurring between two spinel compositions, and those shown by black arrows denote Na⁺ de/insertion by a solid-solution reaction mechanism. Dashed segments correlate to data collected following an extended open circuit period at full discharge for the (F/P)λ-MNO spinels respectively. Parts (a – c) for the (F/P)λ-MNO will be discussed in detail throughout the following sections, and pertain to unique reaction pathways observed dependent on cycling conditions.

The initial Na⁺ insertion of FNa_x-MNO takes place by a two-phase reaction (Fλ-MNO → FNa_{0.88}MNO) followed by Na⁺ insertion by a single-phase reaction (0.88 < x < 1.0 in FNa_x-MNO) saturating the remaining 8a tetrahedral sites as discussed in the previous Chapters. Recovery of the original Fλ-MNO structure is only realized when activating a kinetically sluggish two-phase reaction that occurs beyond 4.25V, after which, the following discharge then proceeds in the same manner as the original Na⁺ insertion shown in reaction pathway (c1). These kinetic limitations prevent complete desodiation of the

$\text{FNa}_x\text{-MNO}$ structure under normal operating conditions, thereby largely limiting discharge capacities of successive cycles to a narrow Na^+ de/insertion range of *ca.* $0.55 < x < 1.0$ as discussed previously.

When operating under standard conditions (*i.e.* 24°C , $2.0 - 4.25\text{V}$) the desodiation reaction remains largely incomplete, and an alternative pathway is identified during the following sodiation. This is shown by reaction pathway (a1), which is purely single-phase in nature, as entrapped Na^+ acts to prop open the spinel structure facilitating a relatively fast solid-solution type behavior.

The ordered $\text{PNa}_x\text{-MNO}$ spinel follows a similar trend in which the final reformation of the $\text{P}\lambda\text{-MNO}$ structure is dependent on an additional two-phase reaction occurring beyond 4.25V (reaction pathway c2). Additional two-phase reactions are also observed below 4.25V (pathways a2 – b2) indicating a difference in the reaction pathway between ordered and disordered spinels during Na^+ de/insertion. As will be discussed, $\text{FNa}_x\text{-MNO}$ begins to follow a very similar trend when relaxing at open circuit in the fully discharged state (pathway b1), suggesting additional kinetic/phase stability considerations, which will be covered in detail below.

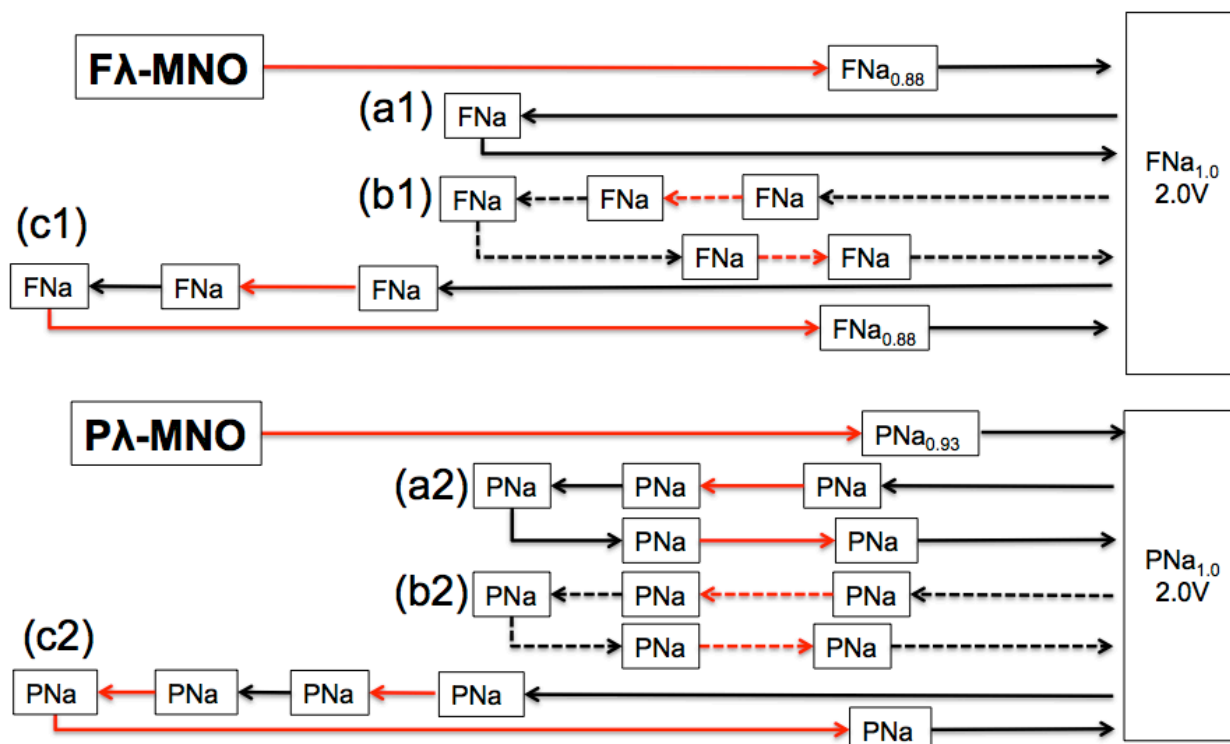


Figure 6-2: Schematic reaction pathway of dis/ordered sodium spinel cathodes constructed from a compilation of *ex-situ/operando* X-ray diffraction, and potentiostatic intermittent titration technique (PITT) data. Cells were held at open circuit in the fully discharged state for 10 hours, 24°C (a), discharged, and charged continuously at 24°C (b), and charged/discharged at 50°C (c). Red segments indicate two-phase regions, and black arrows indicate single-phase de/insertion mechanisms. Dashed arrows imply an additional 10 hour open circuit voltage (OCV) period imparted at the end of the first discharge. Schematic not drawn to scale.

6.2.3 Potentiostatic Intermittent Titration Technique

6.2.3.1 *F λ -MNO/FNa-MNO spinel*

Potentiostatic intermittent titration technique (PITT) was utilized as a low rate, near equilibrium electrochemical technique to identify the Na⁺ de/insertion reaction mechanisms. Figure 6-3 shows the PITT data of F λ -MNO during the first two discharge/charge (2.0-4.25V) cycles (Figure 6-3a and Figure 6-3b respectively) and a following high-voltage (4.5-2.0V) charge/discharge cycle (Figure 6-3c).

During the first discharge, a non-Cottrellian current response is observed across a range of 10 mV steps (3.65 – 3.60V) indicating a multi-phasic reaction taking place during the initial Na⁺ insertion reaction (F λ -MNO \rightarrow FNa_{0.87}MNO) followed by Na⁺ insertion *via* a solid-solution mechanism to a final composition FNa_{1.0}MNO; consistent with previous data shown in Section 1.1.1. The following deinsertion reaction to 4.25V is characteristically single-phase, as seen by the current response.

Although the rate of the PITT protocol is extremely low, the deinsertion reaction reaches only 82% charge capacity with the remaining 18% of tetrahedral sites being occupied by Na⁺ (Na_{0.18}MNO). The limited extent of the charge reaction provides a direct explanation for the large drop in observed discharge capacities beyond the initial discharge (Figure 5-1), and due to the extremely slow-rate afforded by the PITT protocol, it is likely that additional energetic barriers are preventing the complete desodiation reaction.

During the second cycle (Figure 6-3b) a small multi-phasic reaction is initially observed during discharge, otherwise proceeding by a single-phase insertion mechanism. Across the 3 PITT cycles, discharge capacities show gradual degradation, presumably due to the concerns with electrolyte stability and the prolonged exposure at high voltage during PITT cycling. Similar to the first cycle, the extent of desodiation for Figure 6-3b reaches the same upper limit as in the previous cycle, providing confidence that additional energy barrier(s) is/are preventing further desodiation. The following discharge taking place between Figure 6-3b and Figure 6-3c (not shown) no longer demonstrates any multiphasic characteristics, showing a purely single-phase insertion mechanism occurring throughout the entire potential range. It is therefore assumed that Na⁺ de/insertion within FNa_x-MNO occurs primarily by a single-phase reaction mechanism within 2.0 – 4.25V under the quasi equilibrium conditions imparted by the PITT protocol.

Figure 6-3c considers the effects of increasing the potential cutoff to 4.5V during the PITT protocol. Charging to 4.5V induces additional two-phase reactions that can be observed both during charge and discharge. The reformed two-phase reaction during discharge is remarkably similar to the two-phase reaction seen during the initial sodiation of the $\text{F}\lambda\text{-MNO}$; indicating that the previous charge was successful in extracting a significant amount of the entrapped Na^+ . Two non-Cottrellian regions are seen in Figure 6-3c: (1) during charge at 4.37V and (2) during the subsequent discharge at 3.65V. It should be noted that due to the extent of desodiation, which extends the desodiation to negative “ Na_x ” values, there is also a significant amount of electrolyte decomposition that is evident. While the observed reaction at high-voltage may be due to reaction(s) occurring within the electrolyte, the re-established non-Cottrellian region at 3.65V during the subsequent discharge is a good indication that the observed reaction at 4.37V during desodiation is related to reformation of the original $\text{F}\lambda\text{-MNO}$ structure. In other words, the high-voltage charge was successful in extracting the majority of the 18% of entrapped Na^+ , and the two-phase reaction seen at 3.65V describes a similar reaction as seen during the first cycle.

In addition to the high-voltage PITT data shown in Figure 6-3c, cells subjected to the same PITT protocol using additional electrolytes have demonstrated similar characteristics, as is shown by Figure 5-4. This was performed to see if any improvements in the anodic electrolyte decomposition component of the high voltage reaction could be enabled. While the alternative electrolytes demonstrated significant electrolyte decomposition, cells exhibited a single large two-phase re-sodiation region following the 4.5V charge segment. This finding gives further confidence that the high-voltage non-Cottrellian current response observed in Figure 6-3c is not simply a side reaction associated with the composition of the electrolyte. This conclusion will be further supported by XRD results presented later in this Chapter.

Of the electrolyte compositions investigated, none afforded an appreciable improvement in the anodic oxidation of the electrolytes over the 1M $\text{NaClO}_4\text{-PC:FEC2\%}$ (2 vol%) composition used herein. In summary, the PITT results indicate that full desodiation of the spinel structure is limited by the need to initiate an additional two-phase reaction to yield the $\text{F}\lambda\text{-MNO}$ phase. Initiation of the two-phase desodiation reaction is only apparent above 4.3V under near equilibrium PITT conditions, motivating elevated temperature/voltage-cutoff studies throughout the following sections.

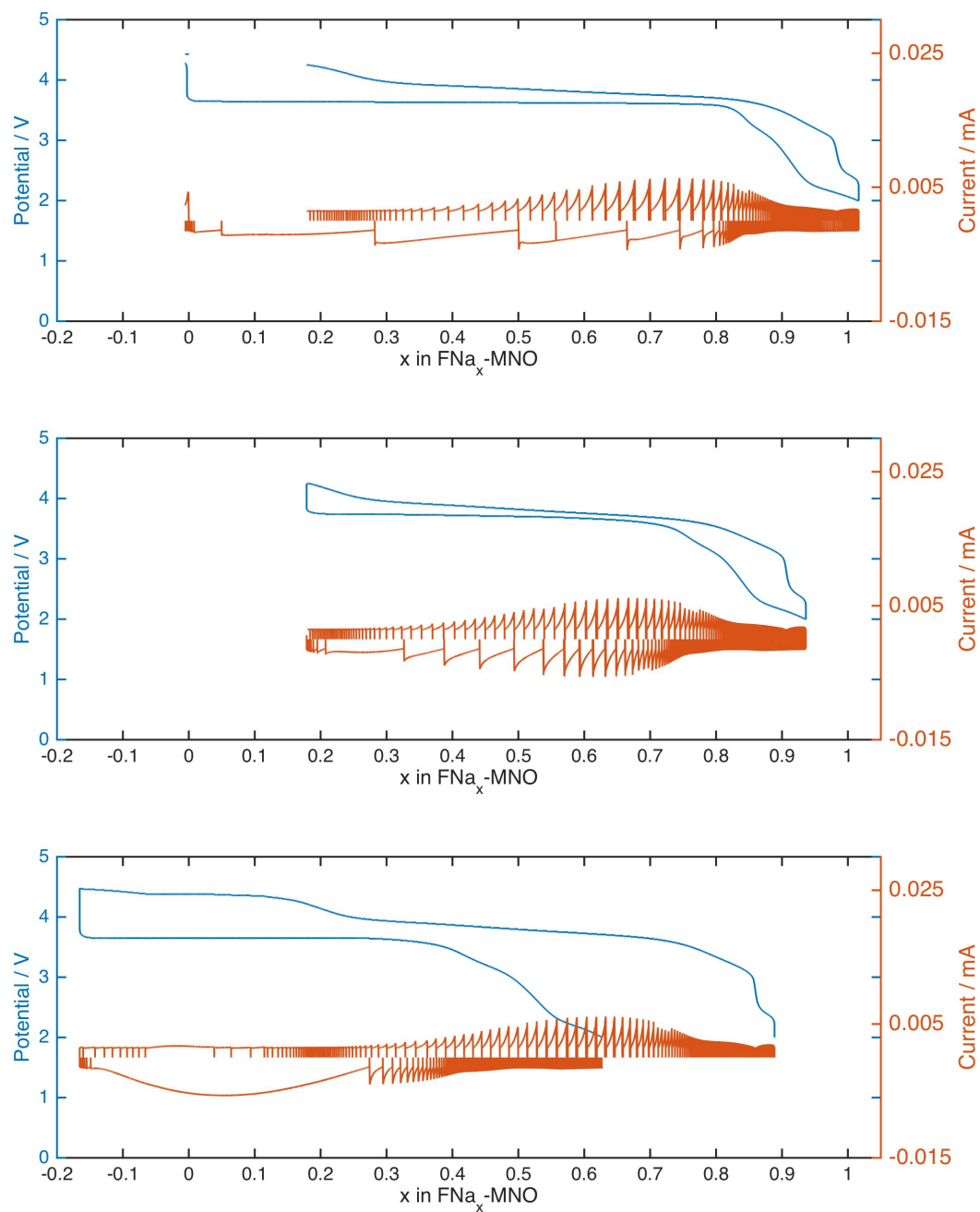


Figure 6-3: Potentiostatic intermittent titration technique (PITT) of FNa-MNO vs. Na/Na⁺ during the first (a) and second (b) cycles within 2.0 - 4.25V followed by an additional high-voltage charge/discharge cycle (c) between 2.0 - 4.5V at 24°C, 1M NaClO₄-PC:FEC2%

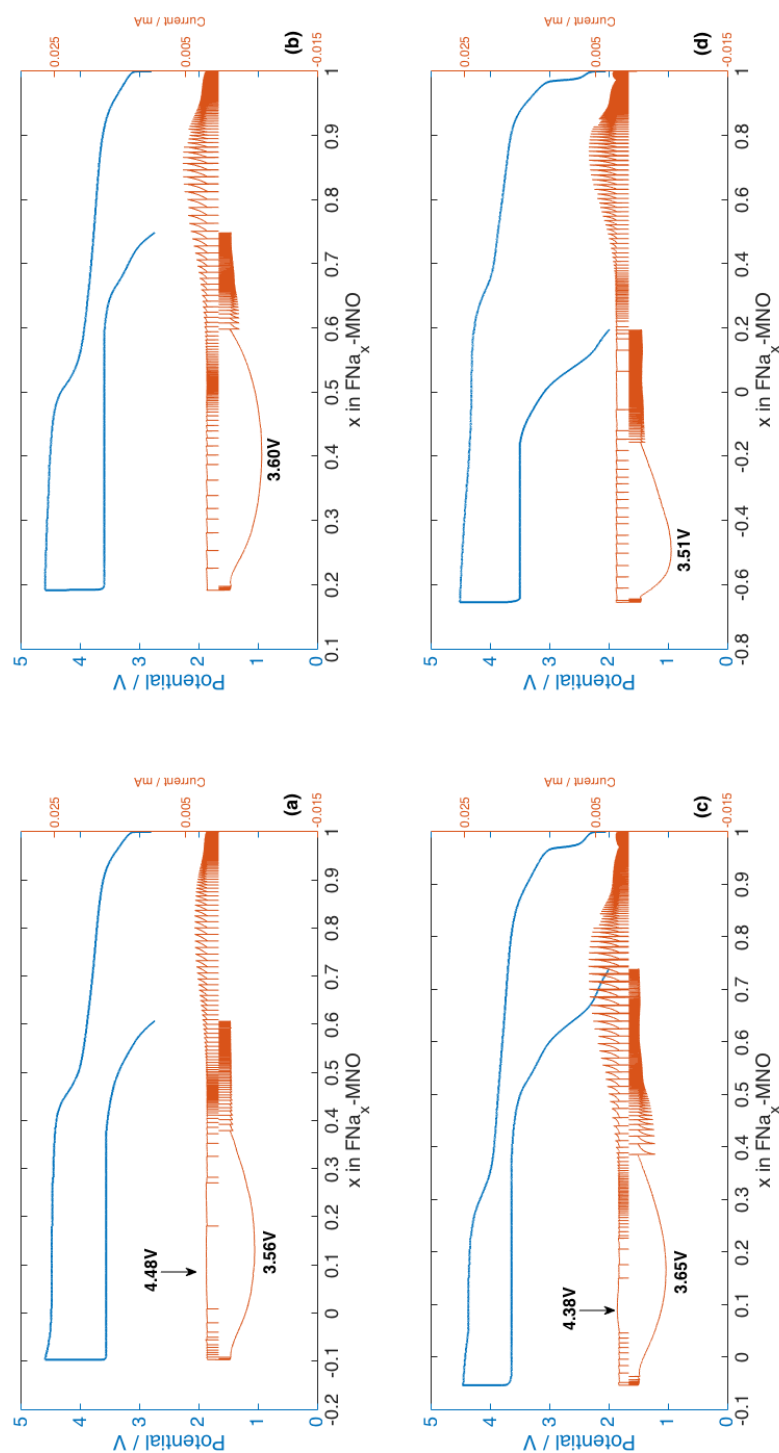


Figure 6-4: Potentiostatic intermittent titration technique (PITT) charge/discharge PNa-MNO cathodes vs. Na/Na⁺ at 24°C using 0.25M NaBF₄-EC/DMC (a) 1M NaClO₄-PC (b) 1M NaClO₄-PC:FEC2% (c) and 1M NaClO₄-PC:FEC10% (d). FEC electrolyte additives are based off volume percentages. PITT protocol consists of 10 mV potential steps with a 0.25 mA/g (active material) current cutoff. Labeled voltages correlate to non-Cottrellian current responses seen in the measured current response.

6.2.3.2 $P\lambda$ -MNO/PNa-MNO spinel

Similar PITT conditions were also utilized for $P\lambda$ -MNO vs. Na/Na⁺ sodium cells in order to probe the desodiation reaction mechanism(s) at progressively higher voltage cutoffs under quasi-equilibrium conditions. Figure 6-5 provides the first two PITT discharge/charge cycles of $P\lambda$ -MNO vs. Na/Na⁺ at 24°C between 2.5 – 4.45V. $P\lambda$ -MNO progresses initially by a two-phase Na⁺ insertion reaction onto the 8a tetrahedral sites across a voltage range of 3.69 – 3.62V, similar to the disordered spinel discussed above. Despite the slower rate afforded by the PITT conditions, initial discharge capacity only realizes *ca.* 81% theoretical capacity (123.6 mAh/g), implying that a considerable amount of residual $P\lambda$ -MNO remains in the following cycle. As discussed previously, residual $P\lambda$ -MNO plays a minor role throughout the successive charge/discharge cycles, and illustrates the significant differences in rate capability between the $F\lambda$ -MNO and $P\lambda$ -MNO spinels.

Following the first discharge (Figure 6-5a), the voltage profile during the charge reaction closely resembles that of a two-phase reaction, with a very flat profile and prolonged duration at individual 10mV steps. However, the only non-Cottrellian regions throughout the entire charge are observed at 3.86V and 3.94V; indicating a minor multi-phasic reaction. This reaction proceeds to completion relatively quickly, (compared to the initial discharge reaction) and the remaining voltage steps reveal relatively slow solid-solution deinsertion behavior. A distinct voltage plateau can be seen at 4.44V during charge (of Figure 6-5a), which also displays a non-Cottrellian current response, however due to concerns around the electrolyte stability at these relatively high voltages, it remains unclear as to whether this correlates to a reaction occurring within the electrode, or the electrolyte.

The second discharge (Figure 6-5b) demonstrates a single large non-Cottrellian response at 3.75V, and although occurring at a higher voltage than the initial discharge reaction, it is attributed to the reformation of the initial discharge reaction ($P\lambda$ -MNO \rightarrow $PN_{a_{0.93}}$ MNO) (as shown later by *operando* XRD) as additional PITT cycling of $P\lambda$ -MNO within 2.0 – 4.25V does not demonstrate the same two-phase behavior beyond the initial discharge. The reformation of a non-Cottrellian response following the high-voltage cutoff is believed to imply that a significant amount of Na⁺ has been removed from the spinel structure, enabling the second cycle to follow a similar reaction pathway as the initial discharge, with additional support provided in the later sections. The continued presence of a non-Cottrellian response

throughout the second charge (3.88 and 3.90V) is in agreement with observations made during the first cycle, likely indicating a ‘small’, yet reversible, two-phase reaction interrupting an overall single-phase deinsertion mechanism.

Additional *operando* data (provided in later sections) further supports the formation of a two-phase reaction during desodiation, which characterizes the previously discussed ‘energetic barriers’ preventing the complete desodiation from the (F/P)Na-MNO spinel as an additional kinetically limited two-phase reaction occurring at *ca.* 3.9V. Due to the previous electrolyte study performed on FNa-MNO, additional electrolytes were not considered, as the PC:FEC2% composition has been demonstrated to be the ideal choice amongst those considered.

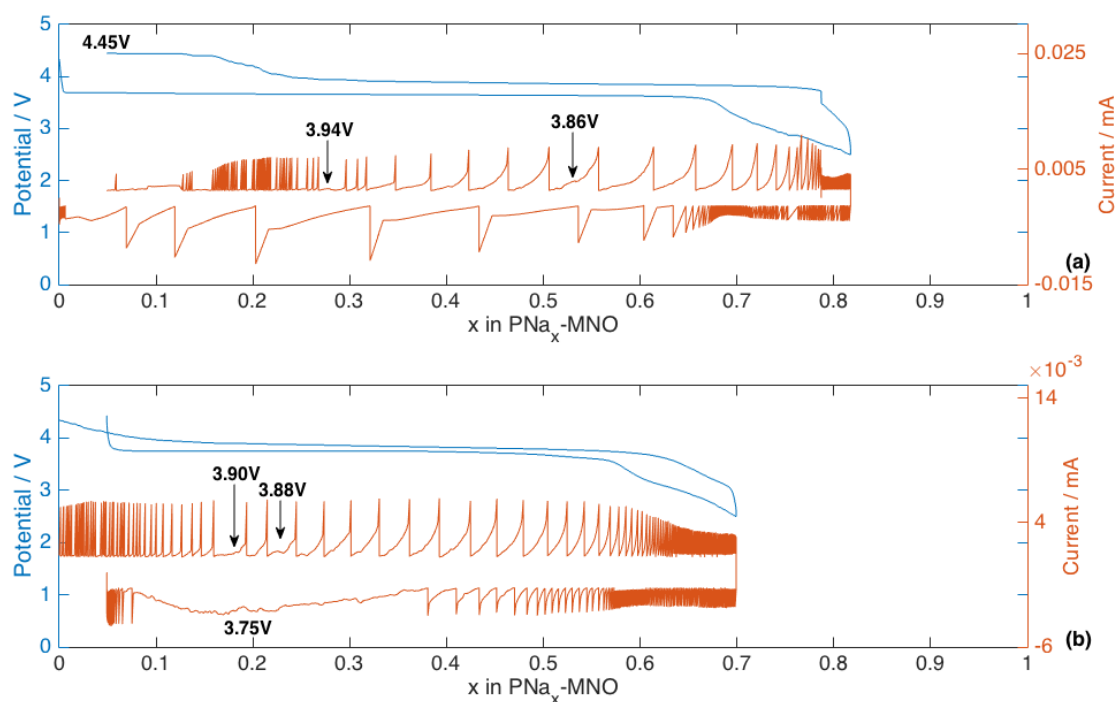


Figure 6-5: Potentiostatic intermittent titration technique (PITT) of PNa-MNO vs. Na/Na⁺ during the first (a) and second (b) cycles. Cell was cycled at 24°C using 10 mV potential steps and a 0.25 mA/g current cutoff between 2.0 - 4.25 and 2.0 - 4.5V between (a) and (b) respectively with 1M NaClO₄-PC:FEC2% electrolyte

6.2.3.3 (F/P)Na-MNO PITT Summary

Considering the observed reaction mechanisms thus far, Table 6-2 provides calculated diffusion coefficients for the respective Na⁺ de/insertion processes for the ordered and disordered spinel samples. Further comments are provided in the discussion section.

Table 6-2: Calculated diffusion coefficients for key Na⁺ de/insertion reactions in FNa-MNO and PNa-MNO spinels

Diffusion Coefficient [cm ² /s]	F λ -MNO	P λ -MNO
1 st cycle, two-phase sodiation	1.61 E -16	4.67 E -16
1 st cycle, single-phase sodiation	5.05 E -13	8.26 E -13
2 nd cycle, two-phase desodiation	6.32 E -17	1.96 E -16
2 nd cycle, two-phase sodiation	1.84 E -16	6.93 E -17

6.2.4 Ex-Situ X-ray Diffraction (XRD)

6.2.4.1 F λ -MNO/FNa-MNO spinel

An *ex-situ* XRD characterization study was performed in order to gain a more detailed analysis of the reaction pathway throughout the desodiation reaction. Figure 6-6 provides a stacked plot of the *ex-situ* XRD measurements across various states of charge (SOC) as monitored by the galvanostatic cycling conditions. Cells were initially discharged at 3mA/g (50°C) reaching full theoretical capacity prior to being stopped during charge at incremental Δx values before undergoing disassembly and electrolyte extraction for *ex-situ* XRD measurement.

Table 6-3 provides Rietveld analysis on the *ex-situ* diffraction data. As concerns surrounding the electrolyte stability has been mentioned throughout the preceding sections, it is assumed that the reported SOC and Na_x values throughout Table 6-3, which are based solely on electrochemical data, may deviate from their actual values; especially so towards higher voltages. Evidence of this deviation arises in the refined lattice parameters, which are utilized to calculate approximate Na occupancy values given as 'XNa_x'.

Considering Figure 6-6, *ex-situ* measurements at 70% Na occupancy still demonstrates the 111, 220, 311, 222, 400, 511 and 440 spinel reflections, given in order of 2 θ position respectively, indicating

that 8a sites are still highly populated by Na^+ . Further extraction of Na^+ to 60% Na^+ occupancy, shows that the $\text{FNa}_x\text{-MNO}$ 220 reflection (at *ca.* $30^\circ 2\theta$) is no longer discernable from the background intensity, indicating a reduction in 8a site occupancy as anticipated. Significant peak shifts can be seen systematically throughout the various *ex-situ* samples, indicating that the overall dimensions of the spinel lattice contracts an appreciable amount as Na^+ is extracted. Although the (220) spinel reflection is no longer discernable (Na is not particularly strong at scattering X-rays) from the background at the higher states of charge, the relative occupancy of successive *ex-situ* XRD scans may still be inferred by the relative change in the lattice parameter. Overall, the observed peak shifts are in good agreement with the PITT data, which indicate a predominantly single-phase deinsertion mechanism.

At 30% Na occupancy (3.98V), the $\text{Na}_x\text{-MNO}$ peaks become significantly broad before returning to approximately the same FWHM. Here, the emergence of a very broad set of spinel diffraction peaks is believed to mark the onset of a small two-phase reaction occurring between two $\text{FNa}_x\text{-MNO}$ compositions of similar lattice parameter. Although the existing PITT data has only demonstrated two-phase desodiation behavior towards voltages exceeding 4.0V, it is feasible that cycling at elevated temperatures has acted to improve the reaction kinetics of the proposed high-voltage two-phase reaction. Additional support is provided when considering the following *operando* XRD studies.

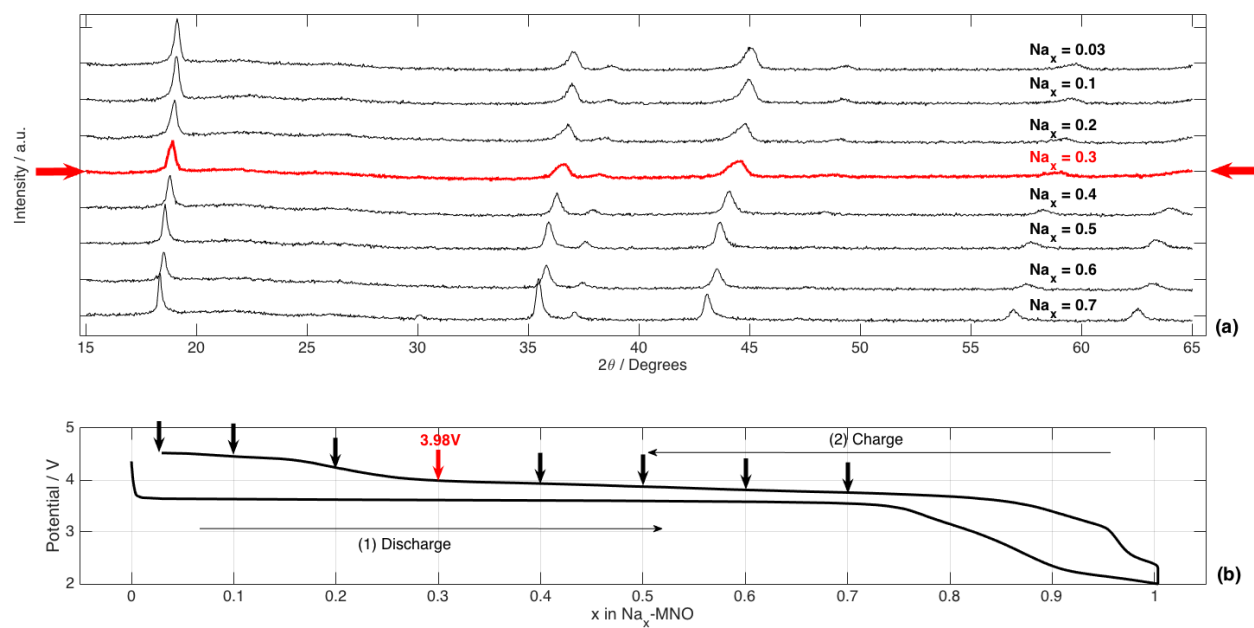


Figure 6-6: Ex-situ XRD of FNa-MNO cathodes cycled at 3 mA/g, 50°C using 1M NaClO₄-PC:FEC2% (a) and representative voltage profile (b)

Table 6-3: Rietveld refined lattice parameters for FNa-MNO vs. Na/Na⁺ cells. Reported (E/X)Na_x values are based off electrochemical and refined XRD data respectively.

X ²	a1 (Å)	a2 (Å)	ENa _x	XNa _x
2.49	8.408(7)	-	0.7	0.84
2.04	8.330(3)	-	0.6	0.68
2.46	8.304(7)	-	0.5	0.63
2.62	8.242(1)	-	0.4	0.50
2.56	8.198(1)	8.132(2)	0.3	0.41 / 0.27
2.28	8.155(5)	8.094(4)	0.2	0.32 / 0.19
2.75	8.075(7)	-	0.1	0.15
2.34	8.061(2)	-	0.03	0.12

6.2.4.2 Pλ-MNO/PNa-MNO spinel

Previous data on the FNa-MNO spinel demonstrated that the movement towards high temperature and high-voltage potentials enabled further desodiation from the spinel structure. The same approach has been adopted for the PNa-MNO spinel within this section.

Similar to the previous PITT data, high temperature cycling has evidently facilitated further desodiation from the PNa-MNO structure. However, based on the refined lattice parameters of the *ex-situ* XRD measurements, desodiation efforts remain unable to recover the Pλ-MNO phase ($a = 7.994\text{Å}$). While it is projected that *ca.* 25% of 8a sites are still populated, Figure 6-7 observes what appears to be a distinct sign of a two-phase reaction occurring during charge.

At the early stages of charge, the Na_x-MNO peaks are notably asymmetric, which is considered to be the onset of a multi-phasic reaction, as indicated by the multiple lattice parameters reported in Table 6-4. At 40% occupancy, (highlighted in red) it is clear that the excessively broad peaks are a result of the growth in intensity from the shoulder peaks seen in the earlier *ex-situ* measurements. Beyond Na_x = 0.4, peak shapes are considerably more symmetric, no longer indicating the presence of convoluted/shoulder peaks. The *ex-situ* data is in agreement with the prior PITT data, as it suggests that the reaction mechanism switches between a two-phase and a single-phase deinsertion mechanism following the initial discharge reaction.

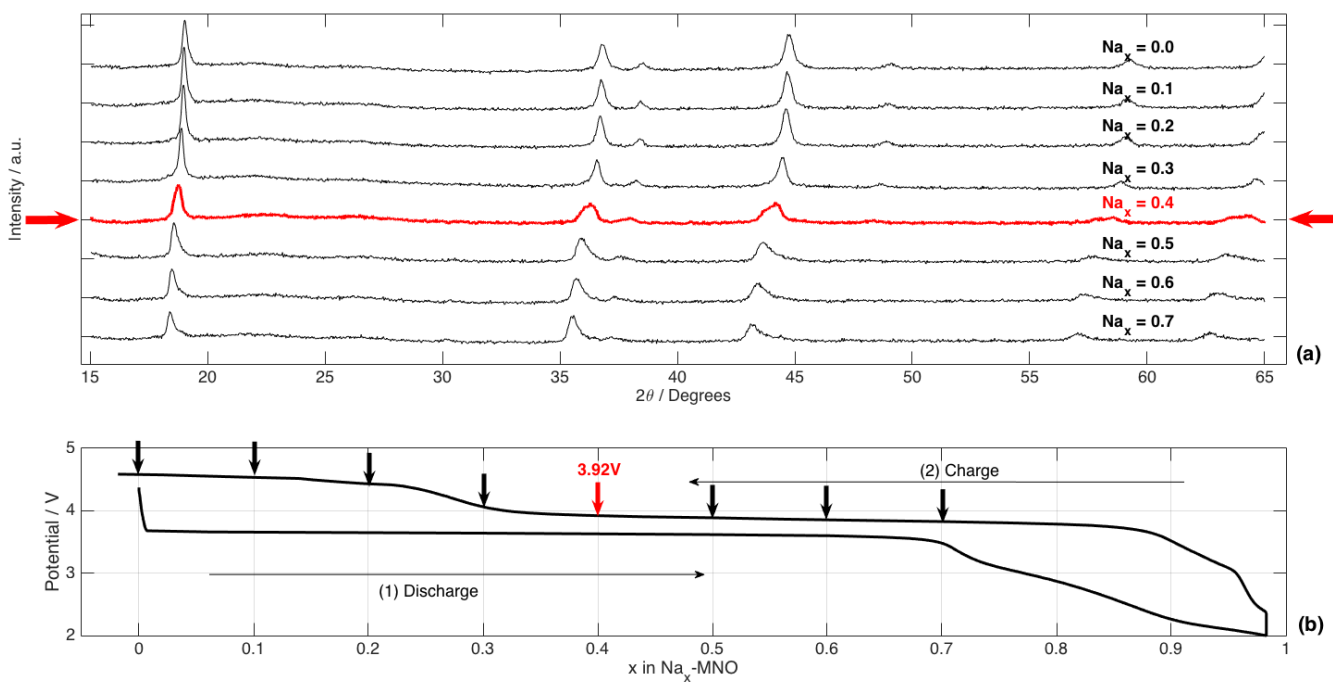


Figure 6-7: *Ex-situ* XRD of PNa-MNO spinel cycled at 3 mA/g, 50°C using 1M NaClO₄-PC:FEC2% (a) and representative voltage profile (b).

Table 6-4: Rietveld refined lattice parameters for PNa-MNO vs. Na/Na+ cells cycled at 3 mA/g, 50°C. Reported (E/X)Na_x values are based off electrochemical and refined XRD data respectively.

X ²	a1 (Å)	a2 (Å)	ENa _x	XNa _x
2.89	8.391(6)	-	0.7	0.84
2.62	8.346(5)	8.190(4)	0.6	0.74 / 0.41
2.34	8.318(9)	8.235(2)	0.5	0.68 / 0.50
2.52	8.275(9)	8.199(5)	0.4	0.59 / 0.42
2.13	8.154(2)	-	0.3	0.33
2.62	8.131(3)	-	0.2	0.28
2.59	8.118(2)	-	0.1	0.25
2.92	8.109(2)	-	0.0	0.23

6.2.5 Operando X-ray Diffraction (XRD)

6.2.5.1 Experimental Considerations

To further validate the reactions seen in the previous PITT and *ex-situ* XRD results, *operando* XRD was utilized during galvanostatic cycling (3mA/g) at 24°C and 50°C. XRD measurements were taken on a continuous basis such that the change in composition (Na_x) throughout each scan was less than 3%, presumably introducing negligible effects on the diffraction spectra. A removable heating element was used to bring the body of the *in-situ* electrochemical cell up to 50°C (±1°C) and was maintained throughout the entire duration of the experiment.

Specifically considering cells operating at 50°C, the (F/P)λ-MNO cathode was previously discharged (50°C) in a coin cell prior to assembly in the *in-situ* cell due to the limited hermeticity of the *in-situ* cell.

6.2.5.2 Fλ-MNO/FNa-MNO spinel

Figure 6-8(a, b) considers only the (311), (222), and (400) spinel reflections as they offer the greatest signal-to-background ratio. Within Figure 5-8, (*hkl*) and (*hkl*)' reflections denote the initial FNa-MNO and F λ -MNO phases respectively. Markers and arrows are used to indicate the reaction progression, with solid and dashed arrows representing two-phase and single-phase reaction mechanisms respectively. Here, and in similarly constructed scaled intensity figures, diffraction peaks are visualized from a top-down view (best read left-to-right, bottom-to-top), observing peak position as a function of both time and cell voltage.

During the first two cycles (shown in Figure 5-8 a, c) the F λ -MNO phase is consumed by a two-phase reaction, further succeeded by a Na⁺ insertion reaction via solid-solution within the sodiated FNa_x-MNO spinel during the first discharge. The following desodiation, and second cycle all together, follow a strictly single-phase Na⁺ de/insertion mechanism as can be seen by the systematically shifting nature of the Bragg peaks. *Operando* measurements are in good agreement with the first two-cycles seen within the PITT data mentioned earlier, consistently describing a similar reaction mechanism progression, and building further confidence in the proposed reaction pathway of Figure 6-2 (a1).

Following the continuous cycling shown in Figure 5-8a, the *in-situ* cell was left in the fully discharged state for *ca.* 12 hours prior to being restarted within a larger potential window (4.5 – 2.0V). The resulting *operando* XRD data, and voltage profile are given in Figure 5-8b, and Figure 5.8d. Here, the FNa-MNO phase can be seen to deviate from the purely single-phase Na⁺ de/insertion reaction previously seen during continuous cycling. As the desodiation begins, diffraction peaks similarly begin to shift towards higher 2 θ angles, implying the reduction in the FNa-MNO lattice parameter. At *ca.* 11 hours (marker M3), diffraction peaks become exceedingly broad, which is believed to be due to a minor two-phase reaction

occurring between two FNa-MNO spinels of similar composition. Previous *ex-situ* XRD data also exhibited a similar peak broadening feature *ca.* 4.0V, building further confidence in this finding.

Following the minor two-phase deinsertion reaction, the diffraction peaks once again exhibit a systematic/gradual peak shift throughout the remainder of the charge protocol; characteristic of a single-phase deinsertion reaction. Marker M4 visually highlights the end of the charge protocol, and demonstrates the relative positions of the spinel diffraction peaks; all of which are at their respective highest 2θ values, indicating some minimum in the Na^+ occupancy within the FNa-MNO spinel.

Upon switching to discharge, the diffraction peaks thereby demonstrate a consistent shift in position to lower 2θ values, indicating that the spinel lattice parameter is increasing through a single-phase Na^+ insertion reaction. Marker M5 highlights an additional two-phase reaction, seemingly related to the minor two-phase reaction seen during the previous charge reaction. Following the short two-phase Na^+ insertion reaction, diffraction peaks once again exhibit a systematic shift in 2θ position, indicating a single-phase Na^+ insertion mechanism.

The deviation in the Na^+ de/insertion reaction pathway (shown schematically by Figure 6-2b), comes without any apparent loss in Na^+ de/insertion reversibility, as both the capacities and relative lattice parameters at the end of charge/discharge remain approximately the same between Figure 5-8a and Figure 5-8b. However, the additional two-phase reactions are suspected to introduce significant concerns surrounding the kinetics of the Na^+ de/insertion reaction as illustrated by the calculated diffusion coefficients of Table 6-2. Further comments are provided in the following sections.

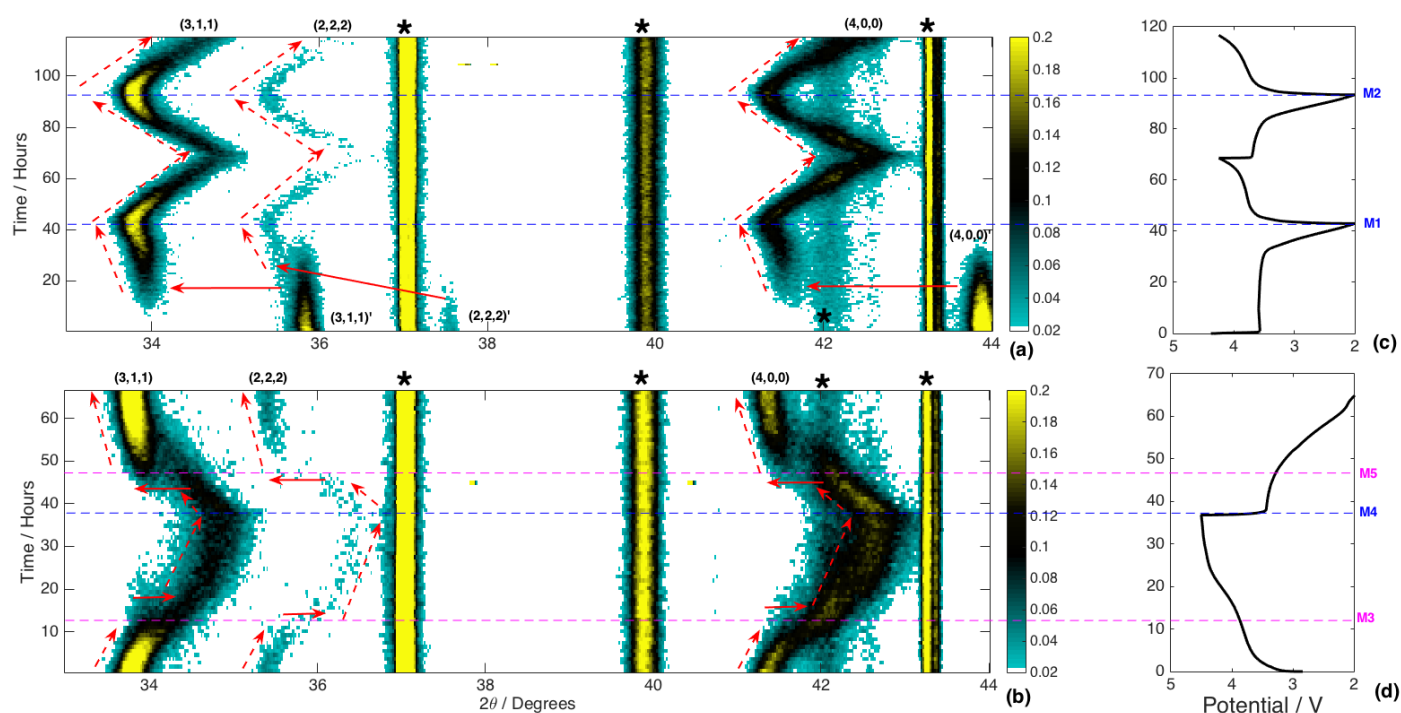


Figure 6-8: Scaled intensity plot (a) and corresponding voltage profile (c) of *in-operando* XRD FNa_x-MNO within the first two cycles (2.0 – 4.25V) at 24°C, 1M NaClO₄-PC:FEC2%. Scaled intensity plot (b) and voltage profile (d) of high voltage charge/discharge cycle following relaxation at full discharge (4.5 – 2.0V) at 24°C. Bragg peaks are labeled at the top of (a-b) with asterisks marking aluminum and beryllium diffraction peaks from the in-situ cell. Dashed lines are added to regions pertaining to a single-phase reaction, and solid lines are oriented towards the product of the two-phase reaction. Lines M1 through M5 serve as guidelines with respect to the voltage profile. M3 and M5 indicate the onset of a two-phase reaction.

In order to further enhance the Na⁺ deinsertion kinetics, additional *operando* XRD measurements were made at 50°C.

Figure 6-9 provides a scaled intensity plot of the (311), (222), and (400) Bragg reflections; with the corresponding voltage profile for the FNa-MNO spinel. The following data pertains to the reaction pathway described by Figure 6-2 (c1).

During charge, Na⁺ deinsertion takes place within a single-phase seen by the constantly shifting Bragg peaks. At 4.0V, (shown by marker M1) a two-phase reaction is initiated, generating a second spinel phase with an approximate lattice parameter of 8.04Å. As shown through previous PITT and *ex-situ* XRD data, it is clear that a two-phase reaction is consistently initiating at *ca.* 4.0V.

Elevated temperature provides a tremendous advantage in terms of the relative ‘strength’ of the two-phase reaction, as the newly formed secondary phase is nearly completely desodiated. It is expected that complete recovery of the Fλ-MNO is possible by these means, as a gradual shift in the diffraction peak positions is evident upon completion of the two-phase reaction; however, the *in-situ* cell was forcibly switched to discharge prior to reaching a 4.5V cutoff in order to preserve the electrolyte from further oxidation.

As the discharge reaction is initiated, an immediate decrease in intensity and large overpotential is observed, both supportive of a two-phase reaction. Due to sensitivity limitations of the XRD setup, the secondary spinel phase is not measurable by XRD until some time after the discharge is initiated (Marker M3). This resulting two-phase reaction occurs at *ca.* 3.3V, and despite occurring at a lower voltage compared to the initial Na⁺ insertion reaction, (which is somewhat expected due to the large extent of electrolyte degradation) it is presumed to be equivalent to the initial Na⁺ insertion reaction described in Chapter 1 based on the relative difference in lattice parameters between the two spinel compositions. Further considerations are covered in the discussion section.

In summary, the collection of ambient and elevated temperature *operando* XRD studies support the development of a two-phase discharge reaction upon sufficient desodiation of the FNa_x-MNO spinel. The high voltage two-phase reaction presents itself as the rate limiting step, preventing easy desodiation of

the spinel structure, thereby contributing to the major cause of poor cell performance beyond the first discharge.

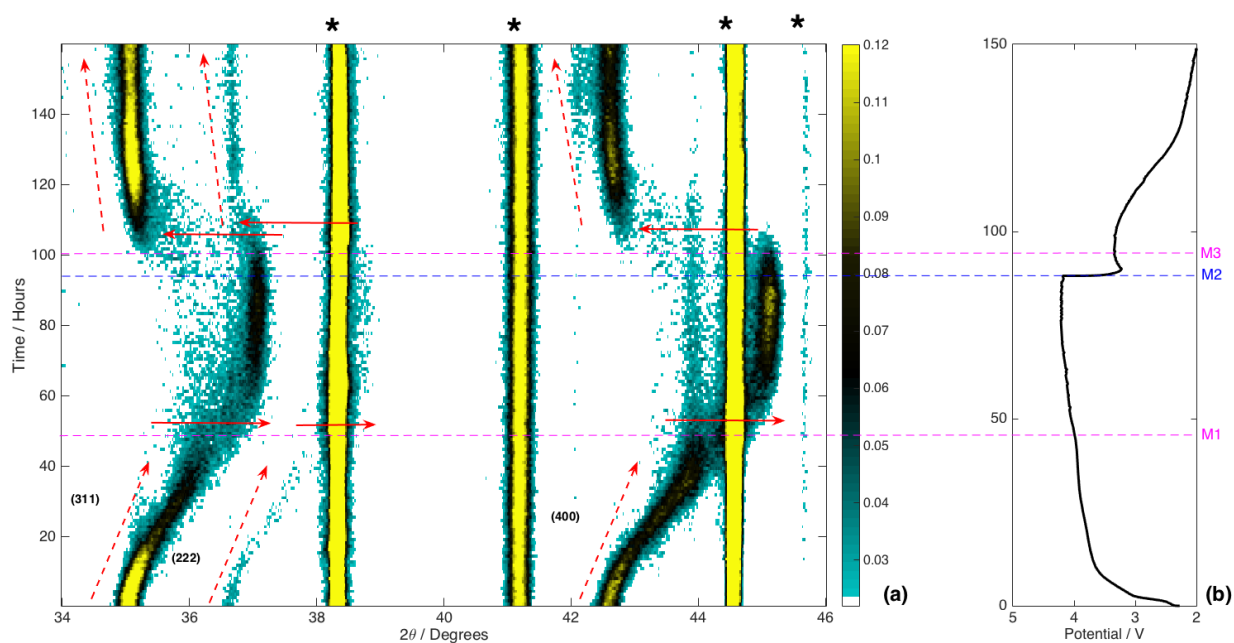


Figure 6-9: *in-operando* XRD charge/discharge cycle of FNa-MNO vs. Na/Na⁺ *in-situ* cell at 3 mA/g, 50°C, 1M NaClO₄-PC:FEC2% (a) and voltage profile (b) The FNa-MNO cathode was presodiated at 50°C in a coin cell prior to assembly in the *in-situ* electrochemical cell. Dashed arrow are provided marking the shift in diffraction peaks in accordance with the single-phase Na⁺ de/insertion reaction, while solid arrows mark the abrupt peak shift described by a two-phase reaction. Markers M1 – M3 are provided to relate the two-phase reactions with the voltage profile.

6.2.5.3 $P\lambda$ -MNO/PNa-MNO spinel

Due to the widely differing electrochemical characteristics obtained *via* PITT (between $Fd\text{-}3m$ and $P4_332$), *operando* XRD was used in a similar fashion as described for FNa-MNO, to contrast the behaviors between the ordered and disordered spinel structures. As the ordered spinel structure only differs in the arrangement of the manganese and nickel cations, XRD patterns are nearly indistinguishable (albeit with differing lattice parameters induced by a small amount of Mn^{3+} in the disordered spinel).

Figure 6-10 provides a scaled intensity plot of the $P\lambda$ -MNO vs. Na/Na^+ *in-situ* cell cycled at a 3mA/g rate (2.0 – 4.25V) at 24°C. Figure 5-10a & Figure 5-10d combine the *operando* XRD and electrochemical data for the (311), (222), and (400) spinel reflections, and the overall reaction pathway are illustrated by Figure 6-2 (a2). Markers M2 and M5 are visual guidelines to indicate the end of discharge for the respective cycles; markers M1, M3, M4, M6, M7, and M8 all indicate the beginning of two-phase reactions taking place. Beryllium and aluminum peaks are seen as constant vertical lines marked by asterisks, and scaled intensities are normalized to each respective 2θ range.

The initial Na^+ insertion reaction is consistent with the PITT data from Figure 6-5, as it progresses initially by a two-phase reaction (shown by solid arrows) with the (311), (222), and (400) $P\lambda$ -MNO diffraction peaks diminishing in intensity to produce the sodiated spinel ($PNa_{0.93}MNO$) at lower 2θ angles. The $PNa_{0.93}MNO$ phase can be seen relatively early on (marker M1) and progresses along a single-phase reaction pathway once the cell voltage drops below *ca.* 3.4V. Dashed arrows up to marker M2 indicate a small shift in peak position consistent with the single-phase insertion onto residual 8a tetrahedral sites of the PNa-MNO spinel occurring during the initial discharge. It is important to note that the (222) spinel reflection exhibits the same de/insertion mechanisms as described in this section, however, due to the proximity and convolution of the PNa-MNO (222) reflection with the $P\lambda$ -MNO (311)' diffraction peak, annotations & analyses of the (222) peak are excluded.

During the following charge, Na^+ deinsertion occurs within a single-phase seen by consistent peak shifts toward higher 2θ angles. At *ca.* 3.9V, (marker M3) (*hkl*) diffraction peaks become exceedingly broad along with a dramatic change in observed peak intensities, suggesting that a small two-phase reaction is taking place. This reaction goes to completion comparatively quickly before resuming along a single-phase deinsertion mechanism shown by the gradual shift in diffraction peak positions. These results are in good

agreement with the PITT data shown in Figure 6-5, where a small non-Cottrellian region was observed at 3.86V. Here, it is once again apparent that the shift in (*hkl*) diffraction peaks does not continue to their original 2θ positions, indicating that a substantial amount of Na^+ remain on the 8a tetrahedral sites of the PNa-MNO spinel.

The second discharge of

Figure 6-10a follows a reversed phase progression as that previously described for the initial desodiation reaction; being mostly single-phase in nature, interrupted by a minor two-phase reaction shown by marker M4. The second charge reaction proceeds in the same fashion as the first charge reaction described above.

After 3 complete cycles, the *in-situ* electrochemical cell was left in the fully discharged state for *ca.* 12 hours before being restarted at 3 mA/g, 24°C, 4.5 – 2.0V as shown schematically in Figure 6-2 (b2).

Figure 6-10b considers the 2θ range containing the (311), (222), and (400) PNa-MNO diffraction peaks, and

Figure 6-10c considers the (511) and (440) peaks. Desodiation proceeds by a solid-solution behavior seen by the changing positions of the PNa-MNO peaks marked by dashed arrows for the respective (*hkl*) diffraction peaks. Similar to the earlier cycles shown in

Figure 6-10a &

Figure 6-10d, a short two-phase reaction can be seen (marker M7), as a large amount of peak broadening occurs across all (*hkl*) reflections; marking the presence of two PNa-MNO spinels of similar lattice parameter. This two-phase reaction can be most clearly seen by consideration of the (511) and (440) PNa-MNO diffraction peaks (

Figure 6-10c). This two-phase reaction initiates around *ca.* 3.9V and resumes along a single-phase pathway to the end of charge.

Similar to that seen during the continuous cycling of

Figure 6-10a, (1) minor two-phase reactions can be observed both during the Na^+ deinsertion and Na^+ insertion reactions, and (2) peak positions do not return to their original 2θ values (P λ -MNO phase), indicating that 8a sites are still populated by residual Na^+ . Considering

Figure 6-10a, $(hkl)'$ diffraction peaks demonstrate an interesting change in intensities throughout the charge/discharge cycles. Further discussion is provided in the following sections.

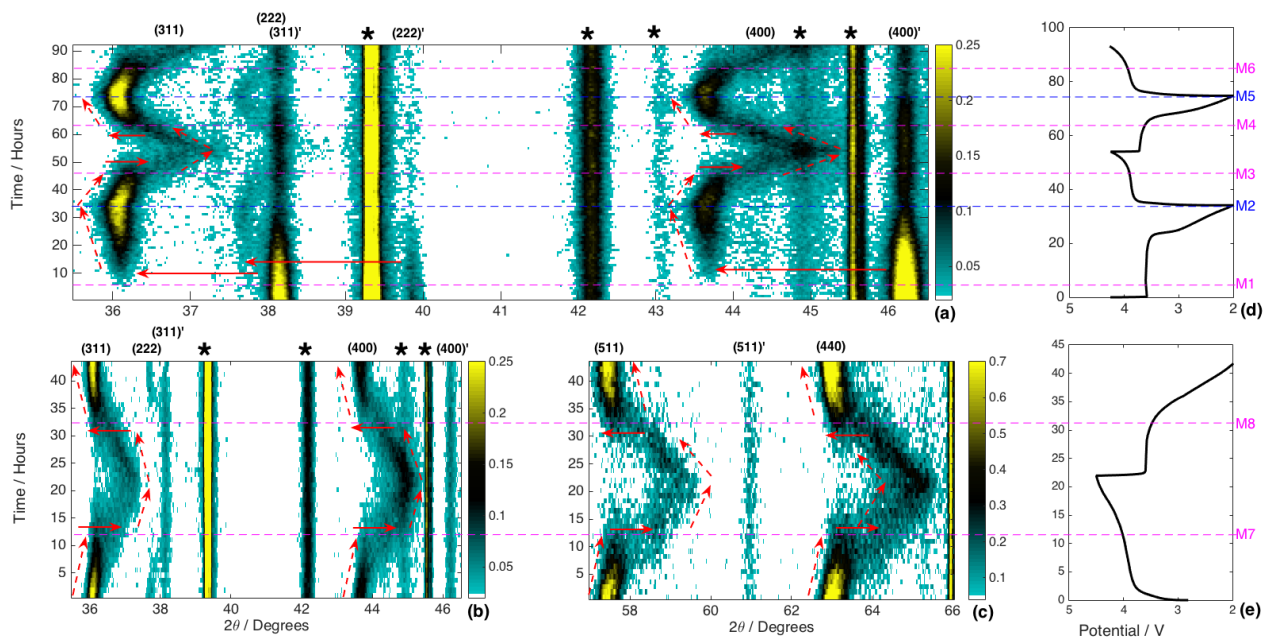


Figure 6-10: Scaled intensity plot (a) and corresponding voltage profile (d) of *in-operando* XRD PNa-MNO vs. Na/Na⁺ throughout the first two discharge/charge cycles at 3 mA/g, 24°C, 1M NaClO₄-PC:FEC2%, 2.0 – 4.25V. Scaled intensity plot (b - c) and corresponding voltage profile (e) of high voltage charge/discharge cycle 4.45 – 2.0V, 24°C at 3 mA/g. Peak intensities for the 311, 222, and 400 Bragg reflections are marked by (hkl) and $(hkl)'$ for the PNa-MNO and P λ -MNO phases respectively. Dashed lines are given to regions pertaining to a single-phase reaction, and solid lines are oriented towards the product of the two-phase reaction. Lines M1-M8 serve as guidelines with respect to the voltage profile. M1, M3, M4, M6, M7, and M8 indicate the onset of a two-phase reaction.

High temperature (50°C) *operando* XRD and electrochemical results are reported in

Figure 6-11. The following results describe the reaction pathway shown in Figure 6-2 (c2). As seen previously in the PITT/*ex-situ/operando* XRD results reported earlier, there is an observed two-phase region that occurs during charge at *ca.* 3.9V illustrated by marker M1. This reaction is in agreement with previous PITT data, which suggests a small multi-phasic region occurring at *ca.* 3.88V; further validated by similar results obtained by the earlier *ex-situ* (50°C) and *operando* XRD (24°C) data.

Upon completion of an initial minor two-phase Na⁺ deinsertion reaction at *ca.* 4.0V, the reaction mechanism immediately changes back to single-phase behavior, and continues until reaching a second two-phase reaction at *ca.* 4.27V (marker M2). The two-phase reaction marked by M2 is notably more pronounced as evidenced by the larger change in diffraction peak position, indicating a substantial difference in lattice parameter between the two separate spinel phases. Due to the limited stability of the electrolyte used, it is expected that the electrochemical efficiency of the Na⁺ deinsertion reaction is relatively poor, requiring a significant amount of time to drive the desodiation reaction to completion. The two phases involved are once again, of very similar lattice parameter, as the subtle reaction can only be clearly seen by examination of the high angle peaks as in

Figure 6-11b.

The final two-phase reaction produces a PNa-MNO spinel with a lattice parameter of *ca.* 8.02Å. Throughout the charge, diffraction peaks continue to grow in intensity, and begin to demonstrate a minor degree of peak shift, suggesting that the reaction once again switches to a single-phase deinsertion mechanism until full recovery of the Pλ-MNO phase (*a* = 7.994Å) is achieved. However, the electrochemical protocol is forcibly switched to discharge in order to preserve the condition of the electrolyte, but is anticipated to proceed in the manner described to produce the fully vacant spinel. It is also important to note that although an extensive amount of electrolyte decomposition has taken place, the XRD measurements are only sensitive to the structural evolution of the cathode itself, therefore giving a reliable account of the relative changes in the crystal structure throughout the desodiation reaction.

Marker M3 indicates the beginning of the following discharge, where a clear two-phase reaction is observed; producing a spinel phase of significantly larger lattice parameter. In accordance with similar data obtained for FNa_x-MNO, the re-formation of the initial two-phase reaction appears to be primarily dependent on depopulating the 8a sites. While electrochemistry typically offers tremendous sensitivity in discerning the degree of Na⁺ de/insertion, obvious stability concerns introduce fundamental limitations to the precision of such experimental techniques; requiring the compilation of the many experimental techniques presented herein to construct a coherent account of the Na⁺ de/insertion behavior into (F/P)Na_x-

MNO. In summary, PNa-MNO follows a considerably different reaction pathway as compared to FNa-MNO, with additional two-phase reactions, likely accounting for the relatively poor performance of the PNa-MNO spinel. Further considerations are provided in the discussion section.

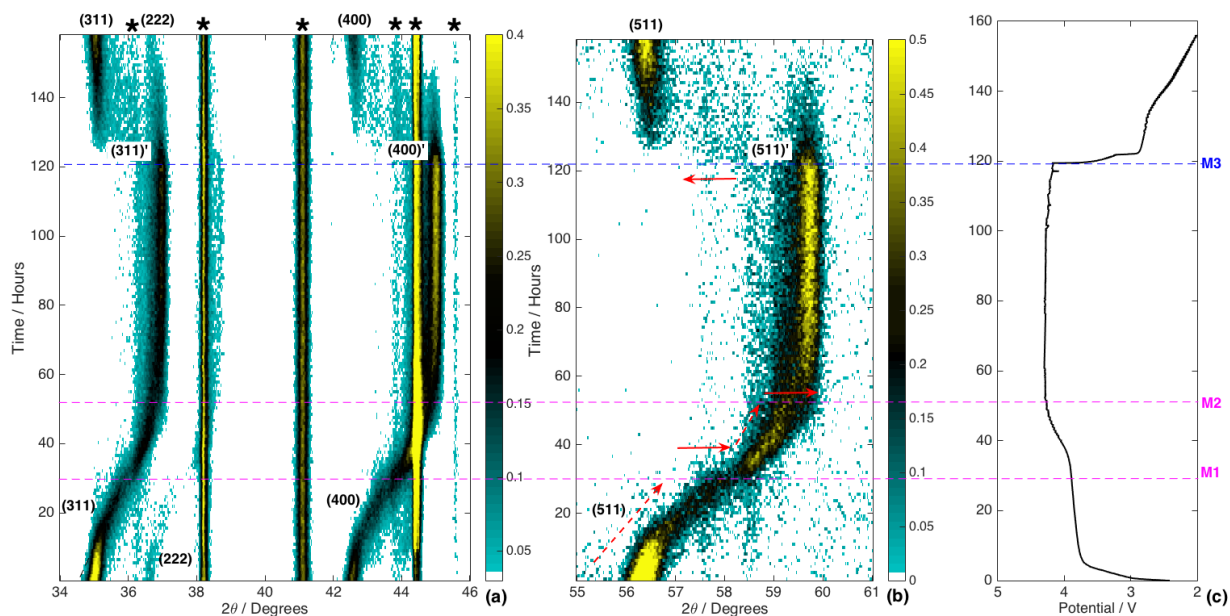


Figure 6-11: Charge/discharge cycle *in-operando* XRD of PNa-MNO at 3mA/g, 50°C, 1M NaClO₄-PC:FEC2%. 2θ range showing 311, 222, 400 peaks (a) and the 511 spinel peak (b) with the corresponding constant current voltage profile (c). Dashed lines are given to regions pertaining to a single-phase reaction, and solid lines are oriented towards the product of the two-phase reaction. Lines M1-M3 serve as guidelines with respect to the voltage profile. M1 and M2 mark the onset of a two-phase reaction.

6.2.5.4 Operando XRD Comparisons: FNa-MNO vs. PNa-MNO

Operando XRD was used to systematically measure structural changes within the dis/ordered spinel cathodes under both ambient (24°C) and elevated temperatures (50°C). A comparative summary of *operando* XRD measurements across (F/P)Na-MNO cells is provided in

Figure 6-12. Relative changes in lattice parameters are calculated with respect to the initial (F/P) λ -MNO and fully sodiated (F/P)Na-MNO spinels for

Figure 6-12 (a, b, d, e) and

Figure 6-12 (c, f) respectively. Data presented within

Figure 6-12 are compiled from *in-situ* data as described within the previous sections.

Figure 6-12 (a, d) provide the relative lattice parameters for the (F/P)Na-MNO spinels under continuous cycling (24°C, 2.0 – 4.25V) conditions respectively.

Figure 6-12 (b, e) consider (F/P)Na-MNO cells left in the fully discharged state for *ca.* 10 hours (24°C, 2.0 – 4.25V). And

Figure 6-12 (c, f) provide (F/P)Na-MNO vs. Na/Na⁺ *operando* XRD data at elevated temperature (50°C, 4.5 – 2.0V) respectively. Inserted sodium (Na_x) values are based off of relative lattice parameters assuming a linear relationship as described by Vegard's law.

Figure 6-12 (a, d) consider the change in relative lattice parameter for the disordered (FNa-MNO) and ordered (PNa-MNO) spinels, respectively, throughout the first two cycles within 2.0 – 4.25V at 24°C. During the initial discharge, a two-phase reaction is observed between the disordered and ordered spinels, producing sodiated spinels 0.44Å and 0.43Å larger than the (F/P) λ -MNO phases respectively. Contrasting behaviors between the disordered and ordered spinels can be readily observed, as sodiation within the P λ -MNO phase proceeds only to *ca.* PNa_{0.95}MNO as opposed to the disordered spinel which reaches full sodiation to FNa_{1.0}MNO. Vertical arrows throughout

Figure 6-12 indicate two-phase reactions occurring between respective (F/P)Na-MNO phases. The limited rate capability of the P λ -MNO leaves appreciable amounts of P λ -MNO behind, providing incremental capacity throughout the following cycles as shown later on. The remaining P λ -MNO phase provides a physical account for the reduced discharge capacity of P λ -MNO, only providing incremental capacity to subsequent cycles as demonstrated in section 6.2.1.

Following charge/discharge cycles further emphasize the difference in reaction pathway between (F/P)Na-MNO, as PNa-MNO observes a combined single-phase/two-phase de/insertion behavior as evidenced by the gradual and abrupt shifts in lattice parameter of

Figure 6-12d. The Na⁺ de/insertion behavior of PNa-MNO draws a sharp contrast against the purely single-phase nature of FNa-MNO in

Figure 6-12a. However, much like PNa-MNO, additional minor two-phase reactions can be observed in FNa-MNO when relaxing at open circuit in the fully discharged state as seen in

Figure 6-12b. While FNa-MNO consistently demonstrates this hysteric dependence on relaxation time, PNa-MNO retains the same reaction pathway independent of relaxation time (

Figure 6-12e). This behavior may be related to possible migration of Na^+ onto adjacent 16c sites and is the subject of future investigations. It should be noted that the lower voltage cutoff is sufficient to initiate insertion onto the 16c sites, as a lower voltage reaction is apparent in Figure 6-3 at *ca.* 2.2V.

Overall, all cells (dis/ordered) cycled at ambient temperatures consistently observe desodiation limitations, as lattice parameters are consistently *ca.* 0.20 - 0.25 Å larger than their respective (F/P)λ-MNO spinels at the end of charge, indicating residual Na^+ occupancy; consistent with earlier galvanostatic and PITT results.

The remaining Na^+ in the FNa-MNO structure demonstrate an additional energetic barrier preventing complete desodiation, which is not realized until activating an additional two-phase reaction as seen by *operando* XRD (

Figure 6-9a) and PITT (Figure 6-3c and Figure 6-3b). Considering PNa-MNO, similar energetic barriers are apparent, as recovery of the original Pλ-MNO phase requires activation of a high voltage two-phase reaction as previously described for FNa-MNO.

(F/P)Na-MNO cathodes demonstrate an abrupt change in lattice parameter during charge (at 50°C) as kinetic barriers surrounding the desodiation reaction are largely mitigated (

Figure 6-12 c, f). Here, relative lattice parameters are reported relative to that of the fully sodiated FNa-MNO and PNa-MNO structures. Following an extended charging period, both the FNa-MNO and PNa-MNO spinels exhibit a two-phase reaction during the subsequent discharge, which is believed to be identical to the Na^+ insertion reaction described by Equation 5-2 and Equation 5-8.

The two-phase reaction seen on discharge produces a sodiated spinel phase of approximate composition $\text{Na}_{0.88}\text{MNO}$ and $\text{Na}_{0.93}\text{MNO}$ for the disordered and ordered spinels respectively. The sodiated spinels formed during the two-phase reaction are equivalent to those observed during the initial discharge reaction for (F/P)λ-MNO, and provides further support that full theoretical capacity can be maintained beyond the first discharge. These findings suggest that the observed two-phase reactions during the initial sodiation are primarily a result of the large difference in lattice parameter between the vacant and sodiated spinel structures, potentially indicating that rate capabilities can be further optimized by enlarging the

(F/P) λ -MNO unit cell such that the slow two-phase reactions are suppressed in favor of single-phase insertion mechanisms.

It is apparent that the two-phase reactions may impart considerable kinetic barriers to practical performance. In order to quantify the extent of these contributions, diffusion coefficients were calculated from the obtained PITT data and shown in Table 5-4. While calculations are based on ‘traditional’ coulometric titration³⁶⁴ considerations, their results offer a relative benchmark between the ordered and disordered spinels. Na⁺ mobility exhibits a consistent difference of *ca.* 3 orders of magnitude when relating the diffusion coefficients between the two-phase and single-phase regions described herein, prompting a desire to push Na⁺ de/insertion mechanisms toward a purely single-phase behavior throughout the entire $0 < \text{Na}_x < 1$ compositional range. Further considerations are provided in the following chapter.

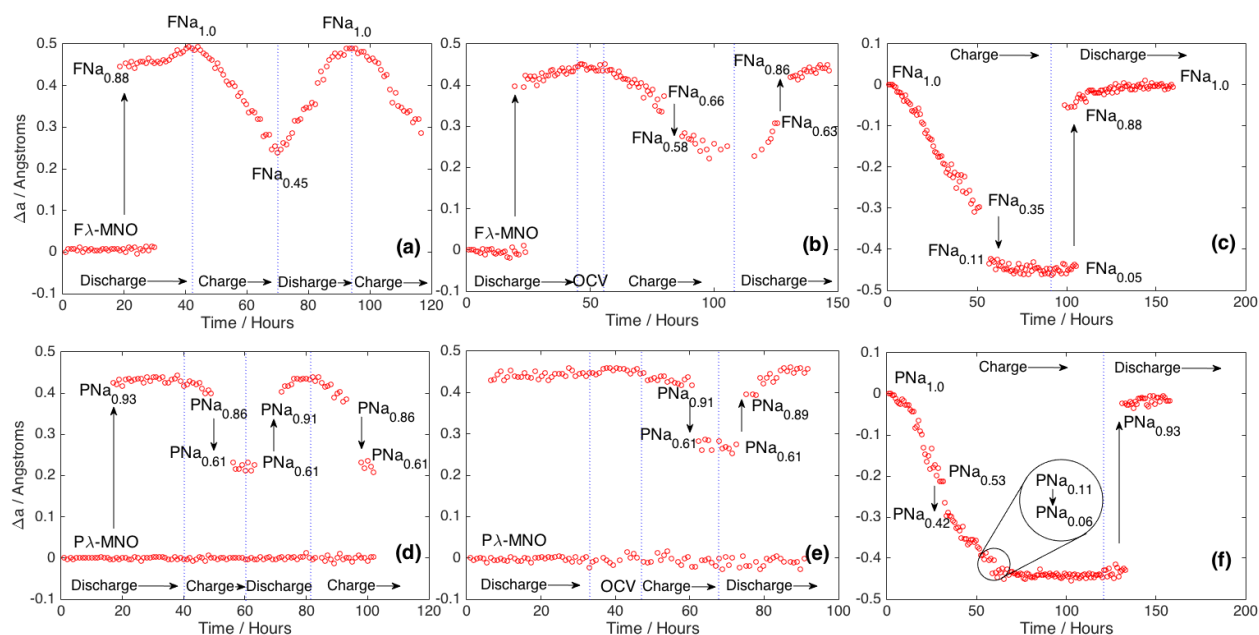


Figure 6-12: Combined *operando* XRD data for disordered (a - c) and ordered (d - f) sodium spinel cathodes under varying cycling conditions: continuous operation at 20°C (a + d), 10 hour open circuit (OCV) rest period following initial discharge at 20°C (b + e) and continuous operation at 50°C (c + f) all cycled at a current rate of 3mA/g with 1M NaClO₄-PC:FEC2% electrolyte. Vertical arrows mark the shift in relative lattice parameter of the various two-phase reactions taking place described by the (F/P)Na_x values reported.

6.3 Discussion

Considering the *in-operando* XRD data for the FNa-MNO and PNa-MNO spinels, a number of important remarks are provided to clarify the scaled intensity plots; particularly with regard to the observed intensities shown throughout

Figure 6-8 to
Figure 6-11. Within

Figure 6-8 FNa-MNO demonstrates a combined single-phase/two-phase reaction pathway as previously described, with relatively large fluctuations in the observed diffraction peaks throughout the respective charge/discharge cycles. At the end of discharge (markers M1 & M2) intensities of the (311), (222), and (400) diffraction peaks are notably more pronounced than measurements taken during charge. This result is believed to be a combined effect of the increased mass-attenuation coefficient of the sodiated (F/P)Na-MNO spinel, and potential ordering of Na^+ that occurs on the available 8a (or combined 8a/16c) sites.

Figure 6-10 shows the PNa-MNO spinel, and contains a number of XRD features in addition to those previously mentioned for FNa-MNO. Due to the partial reaction of the $\text{P}\lambda\text{-MNO} \rightarrow \text{PNa}_{0.93}\text{MNO}$ two-phase reaction, a considerable amount of the $\text{P}\lambda\text{-MNO}$ phase remains throughout the discharge/charge cycles within

Figure 6-10, which are marked by $(hkl)'$. Here, of key interest are the fluctuations in the diffraction peak intensities of the $(311)'$ and $(400)'$ peaks within

Figure 6-10a. Throughout the discharge/charge cycles, both the $(311)'$ and $(400)'$ diffraction peaks undergo a reversible de/increase in measured intensity, indicative of fluctuating amounts of the $\text{P}\lambda\text{-MNO}$ phase.

This however, largely contrasts with the previously proposed Na^+ de/insertion reactions, as reformation of the $\text{P}\lambda\text{-MNO}$ phase requires an additional two-phase deinsertion reaction; only achieved herein by utilization of quasi-equilibrium cycling conditions and/or elevated temperatures. This gives further support that the previously described intensity fluctuations are primarily due to the changing mass-attenuation of

the cathode as Na^+ is reversibly inserted and deinserted into the (F/P) λ -MNO host structure; demonstrated by Figure 6-13.

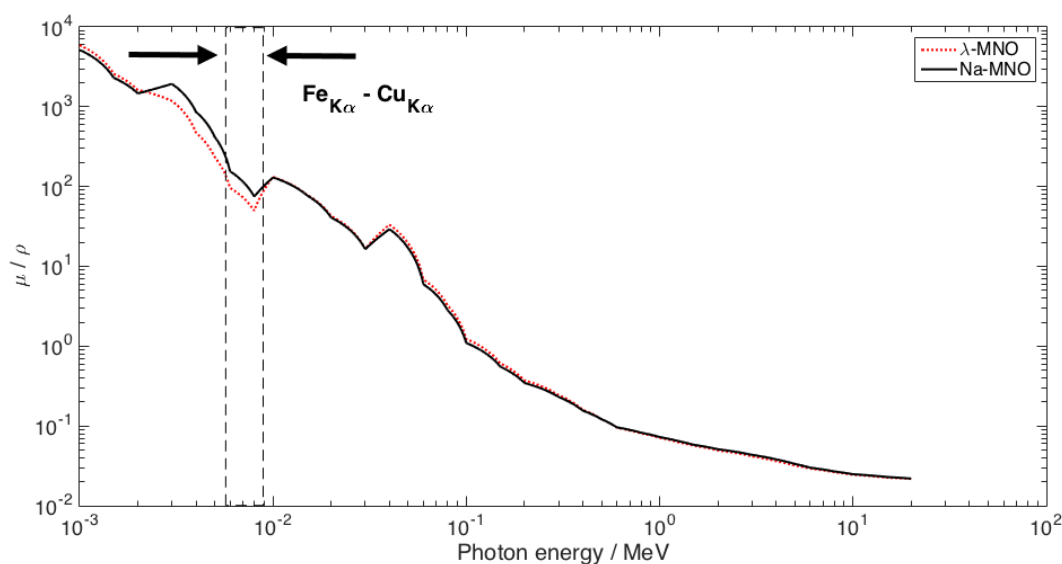


Figure 6-13: Estimated mass-attenuation coefficients of λ -MNO and Na-MNO with respect to common X-ray diffractometer $K\alpha$ radiation sources.

In the case of the PNa-MNO *operando* XRD data mentioned previously (

Figure 6-10a), the apparent fluctuations in the (311)' and (400)' diffraction peaks can be explained by the increased mass-attenuation coefficient of the PNa-MNO phase. Here, the increased mass-attenuation coefficient acts to 'shield' the P λ -MNO phase from the incident radiation, owing to the apparent minimum and 'maximum' in intensity of the (311)' and (400)' diffraction peaks throughout the discharge/charge cycles of

Figure 6-10a. These considerations also support the core/shell reaction mechanism described by Figure 5-6, and suggest that complete Na^+ insertion into the (F/P) λ -MNO structure can be further optimized by sufficient nanostructuring of the (F/P)Li-MNO spinel precursors.

6.4 Conclusion

Both the FNa-MNO (disordered) and PNa-MNO (ordered) sodium spinels exhibit uniquely different de/insertion reaction mechanisms as compared to their lithium analogues, and highlight key reaction mechanisms/pathways whose understanding is central to further optimizing the spinel structure for reversible Na^+ de/insertion. Overall, Na^+ insertion into the disordered and ordered spinels initiates by a two-

phase reaction ($\text{F}\lambda\text{-MNO} \rightarrow \text{FNa}_{0.87}\text{MNO}$ and $\text{P}\lambda\text{-MNO} \rightarrow \text{PNa}_{0.93}\text{MNO}$ respectively) followed by Na^+ insertion onto the remaining 8a tetrahedral sites by a solid-solution type reaction.

Both sodiated spinels demonstrate a number of different reaction mechanisms by nature of a kinetically limiting two-phase deinsertion reaction which produces the original (F/P) λ -MNO structure. As this reaction has only been described herein by utilization of slow quasi-equilibrium cycling conditions, or by elevated temperature studies, separate reaction pathways are frequently observed; as the reversible Na_x de/insertion range is considerably restricted to *ca.* $0.55 < \text{FNa}_x < 1.0$ and $0.6 < \text{PNa}_x < 1.0$ for the disordered and ordered spinels respectively.

High-resolution PITT electrochemical cycling also illuminates the considerable differences in reaction kinetics between the single-phase and two-phase processes described throughout chapter 1, and further indicates that the utilization of sodium spinels for high power Na-ion cathodes can further benefit from the superior single-phase reaction; chiefly, if optimization/modification of the spinel structure can be performed such that the Na^+ de/insertion mechanism occurs primarily by a single-phase mechanism, a significant increase in rate capability, and increased capacity retention is predicted. Such is the topic of the following chapter.

7 $\text{Li}_{1-x}\text{Na}_x\text{Mn}_{2-y-z}\text{M}_y\text{Ni}_z\text{O}_4$ spinel synthesis

7.1 Introduction

As demonstrated throughout the previous chapters, the spinel structure has proven to be a robust and stable platform for reversible Na^+ cycling. However, due to the physical size of Na^+ relative to the 8a tetrahedral sites of the (F/P) λ -MNO structure, the Na^+ insertion/deinsertion reaction(s) is/are considerably hindered by poor diffusional kinetics as reflected by calculated diffusion coefficients, and limited reversible capacities. Considering the comparatively high diffusivity of Li^+ within the spinel framework, it is feasible to predict that enlarging the crystal lattice of the vacant (F/P) λ -MNO structure would provide substantial improvements in cell performance regarding Na^+ de/insertion, due to the enlarged diffusional pathways that are more capable of accommodating the Na^+ .

Considering the nickel doped high-voltage spinel $\lambda\text{-Mn}_{0.78}\text{Ni}_{0.22}\text{O}_4$ (F λ -MNO) and $\lambda\text{-Mn}_{0.75}\text{Ni}_{0.5}\text{O}_4$ (P λ -MNO), expansion of the unit cell should ideally be performed such that it does not interfere with the electrochemically active species, *i.e.* the nickel content should ideally remain unchanged. Considering the (F/P) λ -MNO parent spinel, the nickel substitution acts to push the average oxidation state of manganese to *ca.* a +4 oxidation state, where its presence can be largely regarded as a ‘spectator cation’ as it does not contribute to any significant portion of the electrochemical redox reaction. Due to its relatively inactive role, direct substitution of manganese for a suitably larger transition metal cation may potentially enlarge the spinel structure sufficiently, and in the process facilitate more beneficial Na^+ de/insertion kinetics.

Considering the available +4 transition metals, Table 7-1 compares the ionic radii of key transition metals of interest. Throughout this chapter, Zr and Ti are selected as substitutional dopants, as Zr demonstrates the largest ionic radii of those considered, and Ti offers an intermediate sized dopant and also meets necessary criteria concerned with environmental toxicity, and raw material abundance as compared to other 4d-transition metals.

Table 7-1: Transition metal cation radii from Ref. ³⁷⁵

Element	Ionic Radius [Å]	% Difference Relative to Mn ⁴⁺	Comments
Ti	0.605	+ 14.1	Highly abundant
V	0.58	+ 9.4	-
Cr	0.55	+ 3.7	Toxicity concerns (Cr ⁺⁶)
Fe	0.585	+ 10.3	Unstable in +4 oxidation state
Zr	0.72	+ 35.8	-
Nb	0.68	+ 28.3	-
Mo	0.65	+ 22.6	-
Tc	0.645	+ 21.6	Costly
Ru	0.62	+ 16.9	Costly
Hf	0.71	+ 33.9	Costly
Ta	0.68	+ 28.3	-
W	0.66	+ 24.5	-

7.2 Experimental methods

Material synthesis was carried out by two separate methods described within Section 3.1; namely by solid-state synthesis and a modified Pechini technique. The modified Pechini technique consisted of dissolving stoichiometric quantities of metal acetates (lithium acetate, sodium acetate) and metal nitrates (manganese nitrate, nickel nitrate, zirconium oxynitrate) into aqueous solution followed by a chelation and esterification reaction within a 4:1 ethylene glycol (EG) / citric acid (CA) mixture (mol%). Weights of acetate/nitrate precursors were determined such to give a 4:1:1 ratio of EG:CA:M where M denotes the total moles of dissolved cations.

Reported solid-state synthesized samples were prepared by mixing stoichiometric quantities of transition metal oxides/hydroxides (sodium carbonate, nickel(II) oxide, manganese(IV) oxide, lithium hydroxide, sodium peroxide, nickel(II) hydroxide, manganese oxide hydroxide, titanium oxide: anatase) by either a wet-milling or high-energy milling process. Wet-milling consisted of roll milling initial oxide precursors (*i.e.* sodium carbonate, nickel(II) oxide, manganese(IV) oxide) with zirconia milling media in acetone for a minimum of 5 hours. High energy milled samples were mixed *via* a zirconia high energy planetary mill (Retsch) for 1 hour at 400 rpm. The resulting powder samples were annealed in an alumina crucible in either ambient air, or under pure oxygen flow as stated in the following section.

Phase identification of powder samples was performed using X-ray diffraction on a Bruker D8 Advance diffractometer using Copper K α radiation. Reported lattice parameters are based off of Rietveld

refinement of XRD data using the TOPAS software package, assuming a 5th order Chebychev polynomial background, sample height displacement correction, and pseudo-voigt peak shapes. Refinement models assume an Fd-3m space group, and random distribution of Mn/Ni/M (M = Zr, Ti) cations along the 16d octahedral sites.

Cathodes were fabricated by the same casting technique as described in the earlier chapters, with the exception of the $\text{LiMn}_{1.5-x}\text{Ti}_x\text{Ni}_{0.5}\text{O}_4$ ($x = 0.3, 0.5, 1.0, 1.3$) spinel samples which were SPEX milled for 15 minutes with 10 wt% conductive carbon (SP, MMM) prior to mixing with poly(vinylidene fluoride-co-hexafluoropropylene (Kynar 2801), SP, and a propylene carbonate (PC) plasticizer to form a similar free standing electrode.

7.3 Results

7.3.1 Material Synthesis & Characterization

Throughout the following sections doped spinel samples are commonly referred to as M_x or equivalently, $\text{LiMn}_{1.5-x}\text{M}_x\text{Ni}_{0.5}\text{O}_4$ where M denotes the specific transition metal cation of interest. In fact, $\text{Li}_{1-y}\text{Na}_y\text{Mn}_{1.5-x}\text{M}_x\text{Ni}_{0.5}\text{O}_4$ compositions reported herein correlate to a ‘target composition’ that is meant to distinguish the relative ratios of the transition metal cations prior to annealing, and does not reflect the actual stoichiometry of the formed phase(s).

In order to investigate the phase stability of a sodium spinel, solid-state synthesis techniques used to fabricate the analogous lithium spinel (LMNO) were adapted with sodium precursors. Na_2CO_3 , NiO, and MnO_2 were mixed in a 2:1:3 molar ratio throughout a multi-step wet milling process described by Hagh.³⁰³ Figure 7-1 provides the powder XRD data following a 900°C air anneal for 12 hours. Indexed peaks correlate to a hexagonal layered phase of approximate composition $\text{Na}_{0.67}\text{Mn}_{0.75}\text{Ni}_{0.25}\text{O}_2$, which is in good agreement with previous sodium-rich layered oxides reported throughout Section 2.1.1.2.3.1. Here, an analogous synthesis technique used to form the LMNO spinel has demonstrated that the significantly larger ionic size of Na^+ destabilizes the spinel crystal structure, forming a layered compound. A minor secondary phase can also be seen (as shown by arrows) which signifies an unknown sodiated manganese phase that is ignored throughout the remainder of this work, as only the formation of spinel phases are of primary interest.

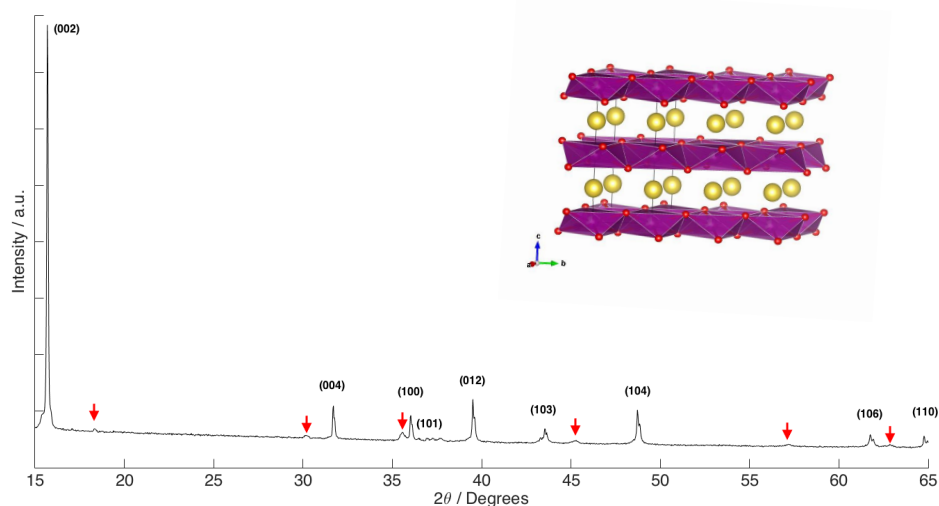


Figure 7-1: Powder X-ray diffraction data of a hexagonal layered sodium rich phase of nominal composition $\text{Na}_{0.67}\text{Ni}_{0.25}\text{Mn}_{0.75}\text{O}_2$ formed by solid-state synthesis at 900°C in air for 12 hours.

In order to incorporate Na^+ into the tetrahedral sites of the spinel crystal structure, it is clear that modification of the average size of the tetrahedral sites need to be sufficiently increased such that steric destabilization effects do no arise as seen in Figure 7-1.

Modification of the unit cell in this sense is performed by substitutional doping of the transition metal cations: specifically Mn^{4+} , as it contributes to no appreciable electrochemical redox reaction. By substitutional doping with a physically larger transition metal, the average size of the 16d octahedral sites is expected to increase; thereby increasing the overall tetrahedral sites in the process. As depicted by Table 7-1, a number of +4 transition metals may serve as a feasible dopant. However, only Ti and Zr are chosen due to the combined considerations of electrochemically active redox reactions, relative ionic size, and environmental considerations (essential for promising Na-ion compositions).

Figure 7-2, Figure 7-3, and Figure 7-4 consider 500°C, 700°C and 800°C 10 hour air anneals for $\text{LiMn}_{1.5-x}\text{Zr}_x\text{Ni}_{0.5}\text{O}_4$ ($x = 0.02, 0.04, 0.06, 0.08, 0.1, 0.2, 0.3, 0.4$) compositions (a) – (h) respectively. Arrows throughout Figure 7-2, and Figure 7-3 show evidence of an orthorhombic ZrO_2 phase, which become more distinguishable as the annealing temperature is increased, eventually resulting in a cubic ZrO_2 phase shown in Figure 7-4. Considering only the spinel phase, Figure 7-5 provides the refined lattice parameters of the 500°C, 700°C, and 800°C air anneals mentioned previously. Here, it is clear that the

lattice parameter of the synthesized spinel reaches a maximum at a composition of *ca.* $\text{LiMn}_{1.44}\text{Zr}_{0.06}\text{Ni}_{0.5}\text{O}_4$ across all considered annealing temperatures suggesting some maximum in solid-solubility.

As shown throughout Figure 7-2 through Figure 7-4, secondary phases become exceedingly more prominent as a function of increased Zr content, suggesting that beyond the $\text{Zr}_{0.06}$ composition, the spinel crystal structure is unable to accommodate the relatively large Zr^{4+} cations, and a precipitated ZrO_2 phase forms at the particle surfaces. However, as demonstrated by the 500°C annealed samples, refined lattice parameters see an additional peak at a compositions of *ca.* $\text{LiMn}_{1.0}\text{Zr}_{0.5}\text{Ni}_{0.5}\text{O}_4$. This observation is seemingly due to the relatively low annealing temperature (500°C), preventing significant loss of the Zr due to poor diffusion kinetics, and also resulting in much broader diffraction peaks due to combined particle size and strain considerations. However, due to the multiphasic nature of compositions beyond $\text{Zr}_{0.06}$ ($\text{LiMn}_{1.44}\text{Zr}_{0.06}\text{Ni}_{0.5}\text{O}_4$) across all temperatures, it is believed that this composition represents the solid-solubility limit for Zr within the LMNO spinel. Here, it is important to distinguish that formation of the Li-Mn-Zr-Ni spinel was produced throughout a single annealing process as opposed to a multi-step solid-state reaction as described for LMNO stoichiometries by Nader *et al.*³⁰³ This is also supported by the systematic increase in measured surface area as a function of Zr content given in Table 7-2.

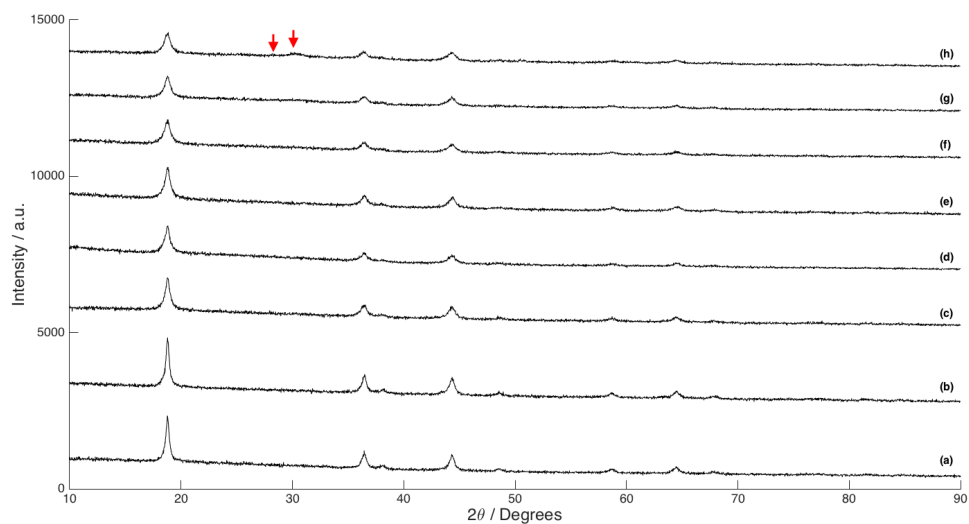


Figure 7-2: Powder X-ray diffraction data for $\text{LiMn}_{1.5-x}\text{Zr}_x\text{Ni}_{0.5}\text{O}_4$ spinel samples ($x = 0.02, 0.04, 0.06, 0.08, 0.1, 0.2, 0.3$, and 0.4) for (a) - (h) respectively annealed at 500°C for 10 hours in air

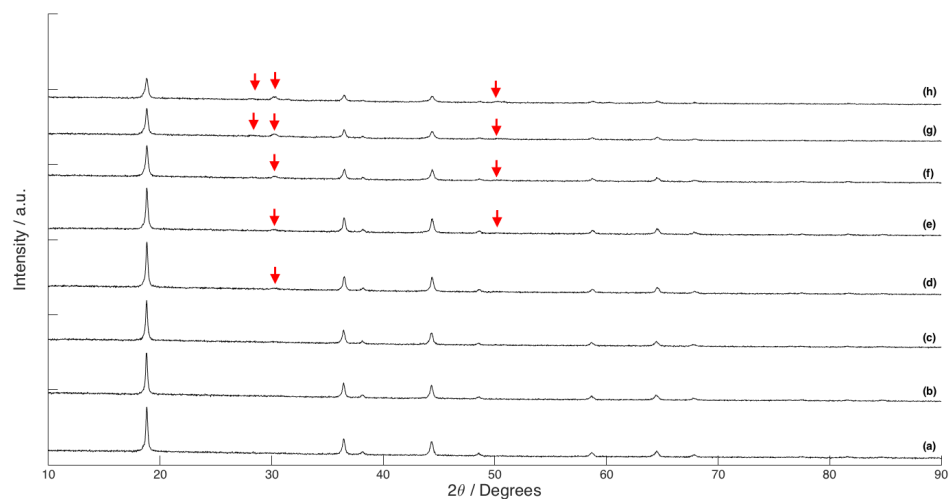


Figure 7-3: Powder X-ray diffraction data for $\text{LiMn}_{1.5-x}\text{Zr}_x\text{Ni}_{0.5}\text{O}_4$ spinel samples ($x = 0.02, 0.04, 0.06, 0.08, 0.1, 0.2, 0.3$, and 0.4) for (a) - (h) respectively annealed at 700°C for 10 hours in air

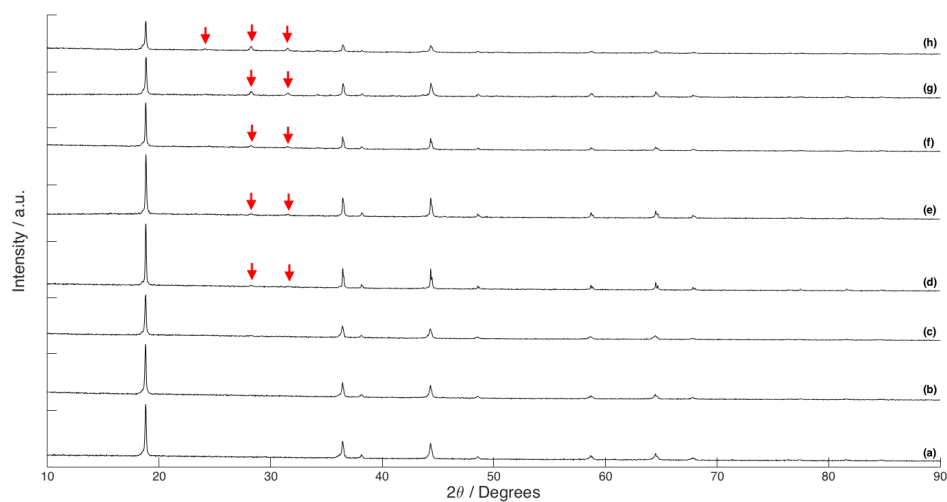


Figure 7-4: Powder X-ray diffraction data for $\text{LiMn}_{1.5-x}\text{Zr}_x\text{Ni}_{0.5}\text{O}_4$ spinel samples ($x = 0.02, 0.04, 0.06, 0.08, 0.1, 0.2, 0.3$, and 0.4) for (a) - (h) respectively annealed at 800°C for 10 hours in air

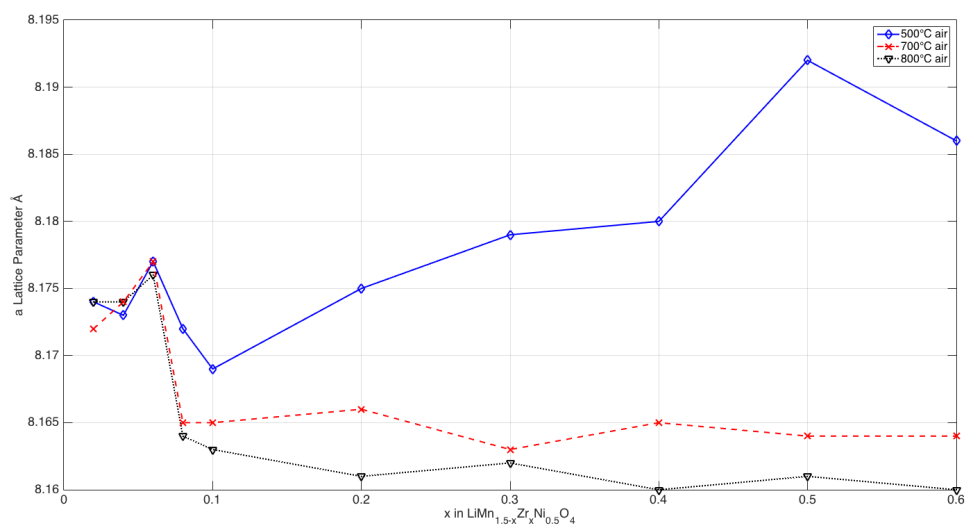


Figure 7-5: Refined lattice parameters of $\text{LiMn}_{1.5-x}\text{Zr}_x\text{Ni}_{0.5}\text{O}_4$ ($x = 0.02, 0.04, 0.06, 0.08, 0.1, 0.2, 0.3, 0.4, 0.5$, and 0.6) samples across considered annealing temperatures

Table 7-2: Multipoint BET surface area measurements of Zr-doped spinel compositions

Anneal Temperature	Zr _{0.02}	Zr _{0.6}
500°C air	27.83 m ² /g	41.55 m ² /g
600°C air	21.51 m ² /g	29.82 m ² /g
700°C air	8.223 m ² /g	13.85 m ² /g
800°C air	2.650 m ² /g	3.874 m ² /g

Given that the Zr_{0.06} composition has demonstrated itself as the practical limit of solid-solubility within the manganese-nickel spinel, systematic substitution of Li for Na was performed in order to assess whether the incorporated Zr has sufficiently enlarged the spinel crystal structure to accommodate the larger Na⁺ cations. Figure 7-6 provides powder XRD data for Li_{1-y}Na_yMn_{1.44}Zr_{0.06}Ni_{0.5}O₄ (y = 0.1, 0.2) target compositions. While the major crystalline phase can be indexed as a cubic spinel, the systematic growth of a secondary sodiated manganese oxide phase (marked by arrows in Figure 7-6) suggests that further expansion of the spinel lattice is necessary. The dashed line provides a visual indication of the similar lattice parameters between the two samples, suggesting that little to no change in lattice parameter has occurred. In fact, refined lattice parameters of the spinel phases suggest that no appreciable amounts of Na have been successfully incorporated into the spinel phase, promoting the increasing amount of secondary sodiated phase(s) as a function of increasing sodium content.

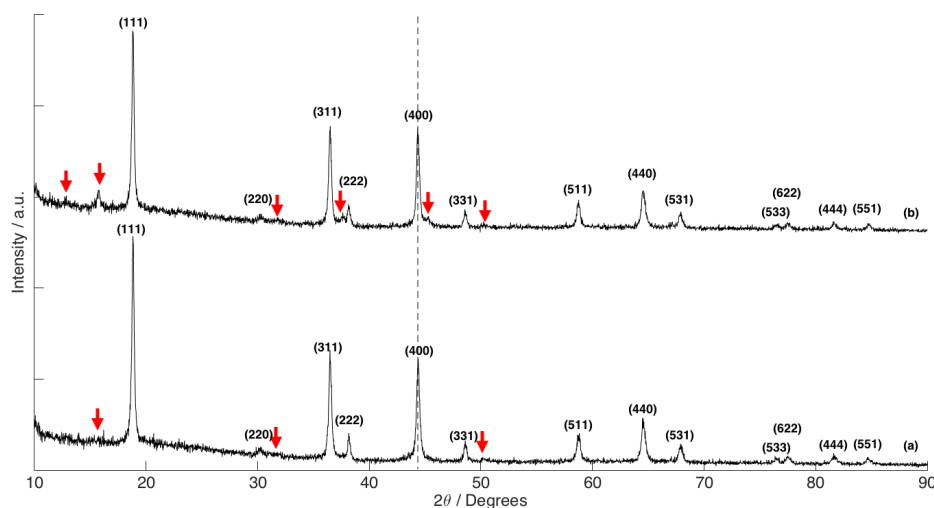


Figure 7-6: Powder X-ray diffraction data of sodium substituted Li_{1-y}Na_yMn_{1.44}Zr_{0.06}Ni_{0.5}O₄ (y = 0.1 and 0.2) compositions (a) and (b) respectively. Arrows mark a sodium rich phase, and indexed peaks correlate to the lithium spinel. The vertical dashed line is provided to demonstrate no significant shift in peak positions as a function of increasing Na content.

Additionally, Ti was investigated as a similar dopant cation. Figure 7-7 shows powder XRD data of Ti-doped $\text{LiMn}_{1.5-x}\text{Ti}_x\text{Ni}_{0.5}\text{O}_4$ ($x = 0.1, 0.3, 0.5, 1.0$, and 1.30 for (a) through (e) respectively) spinels synthesized by a mechanochemical synthesis technique followed by a 10 hour 800°C air anneal. Dashed lines are also provided for the (111), (311) and (400) spinel reflections in order to demonstrate the shift in diffraction peaks correlating to a systematic increase in the lattice parameter. While exhibiting only a minor secondary phase, Figure 7-7e marks a titanium rich NiTiO_3 phase, which is once revoked from further considerations. Here, almost complete solubility of titanium within the spinel host lattice is in agreement with previous reports^{376,377} and comes as little surprise when considering the 14.1% difference in ionic radii between $\text{Ti}^{4+}/\text{Mn}^{4+}$ as compared to 35.8% between $\text{Zr}^{4+}/\text{Mn}^{4+}$.

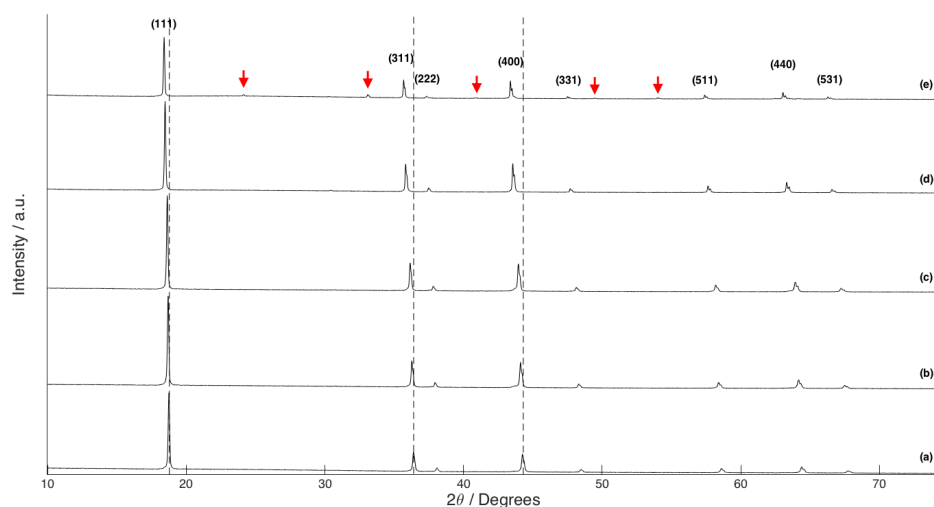


Figure 7-7: Powder X-ray diffraction data of titanium doped spinel samples of nominal composition $\text{LiMn}_{1.5-x}\text{Ti}_x\text{Ni}_{0.5}\text{O}_4$ ($x = 0.1, 0.3, 0.5, 1.0, 1.3$) for (a) – (e) respectively synthesized at 800°C in air .

Table 7-3 compares the refined lattice parameters of Ti-doped spinels discussed previously against those already demonstrated throughout literature. Here, the refined lattice parameters are in good agreement with those previously reported, giving a high level of confidence in the reported stoichiometries and incorporation of Ti onto the intended 16d octahedral sites.

Given that incorporation of the Ti^{4+} onto the spinel host structure has largely increased the lattice parameter, it is of primary interest as to whether or not a sodium spinel can be directly synthesized using the given Ti stoichiometries. Following this methodology, $\text{Li}_{1-y}\text{Na}_y\text{Mn}_{1.5-x}\text{Ti}_x\text{Ni}_{0.5}\text{O}_4$ ($x = 1.0, 1.3$; $y = 0.1, 0.5, 1.0$) target compositions were formed by the same mechanochemical synthesis method in order to determine the stability of Na^+ within the expanded spinel host lattice.

$\text{Li}_{1-y}\text{Na}_y\text{Mn}_{1.5-x}\text{Ti}_x\text{Ni}_{0.5}\text{O}_4$ ($x = 1.0, 1.3$; $y = 0.1, 0.5, 1.0$) samples were annealed both in air and under a pure oxygen atmosphere, with powder XRD data provided in Figure 7-8, Figure 7-9, Figure 7-10, and Figure 7-11 respectively. Throughout Figure 7-9 to Figure 7-11, diffraction peaks marked by arrows correlate to a spinel phase, and those shown throughout (b) – (c) with miller indices correspond to a hexagonal (layered) phase respectively. the minor additional phase(s) present throughout (a) – (c) relate to a multitude of sodiated manganese/nickel oxide phases, and are not considered throughout this section.

Considering the $\text{Li}_{1-y}\text{Na}_y\text{Mn}_{1.5-x}\text{Ti}_x\text{Ni}_{0.5}\text{O}_4$ ($x = 1.0$; $y = 0.1, 0.5, 1.0$) compositions in Figure 7-8 and Figure 7-9, little difference is provided when changing between an air and oxygen atmosphere, predominantly exhibiting a spinel (a) or hexagonal layered phase (b) – (c) with additional phase impurities being largely ignored, as the primary objective of this chapter is to stabilize a spinel crystal structure. Similar annotations and observations can also be made for the $\text{Li}_{1-y}\text{Na}_y\text{Mn}_{1.5-x}\text{Ti}_x\text{Ni}_{0.5}\text{O}_4$ ($x = 1.3$; $y = 0.1, 0.5, 1.0$) compositions in Figure 7-10, and Figure 7-11 and further electrochemical results are provided in the following section.

Table 7-3: Comparison of Ti-doped $\text{LiMn}_{1.5-x}\text{Ti}_x\text{Ni}_{0.5}\text{O}_4$ ($x = 0.1, 0.3, 0.5, 1.0, 1.3$) as compared against previous reports in literature

Sample	REF ³⁷⁶	REF ³⁷⁷	Experimental Data
$\text{LiNi}_{0.5}\text{Mn}_{1.5}\text{O}_4$	8.170(3)	8.169 (P4 ₃ 32)	8.167 (Fd-3m) [§]
$\text{LiNi}_{0.3}\text{Mg}_{0.2}\text{Mn}_{1.5}\text{O}_4$	8.179(3)	-	-
$\text{LiNi}_{0.5}\text{Mn}_{1.45}\text{Ti}_{0.05}\text{O}_4$	-	8.175 (P4 ₃ 32)	-
$\text{LiNi}_{0.5}\text{Mn}_{1.4}\text{Ti}_{0.1}\text{O}_4$	-	8.178 (P4 ₃ 32)	8.175
$\text{LiNi}_{0.5}\text{Mn}_{1.3}\text{Ti}_{0.2}\text{O}_4$	-	8.189 (Fd-3m)	-
$\text{LiNi}_{0.5}\text{Mn}_{1.2}\text{Ti}_{0.3}\text{O}_4$	8.204(5)	8.201 (Fd-3m)	8.199
$\text{LiNi}_{0.5}\text{Mn}_{1.1}\text{Ti}_{0.4}\text{O}_4$	8.218(3)	-	-
$\text{LiNi}_{0.5}\text{Mn}_{1.0}\text{Ti}_{0.5}\text{O}_4$	8.232(5)	8.228 (Fd-3m)	8.227
$\text{LiNi}_{0.5}\text{Mn}_{0.8}\text{Ti}_{0.7}\text{O}_4$	8.262(3)	-	-
$\text{LiNi}_{0.5}\text{Mn}_{0.5}\text{Ti}_{1.0}\text{O}_4$	8.304(3)	8.295 (Fd-3m)	8.299
$\text{LiNi}_{0.5}\text{Mn}_{0.3}\text{Ti}_{1.2}\text{O}_4$	8.324(3)	-	-
$\text{LiNi}_{0.5}\text{Mn}_{0.2}\text{Ti}_{1.3}\text{O}_4$	-	-	8.330
$\text{LiNi}_{0.5}\text{Mn}_{0.15}\text{Ti}_{1.35}\text{O}_4$	8.350(6)	-	-
$\text{LiNi}_{0.5}\text{Ti}_{1.5}\text{O}_4$	8.361(6)	-	-

[§] Lattice parameter based off of $\text{LiNi}_{0.44}\text{Mn}_{1.56}\text{O}_4$ composition

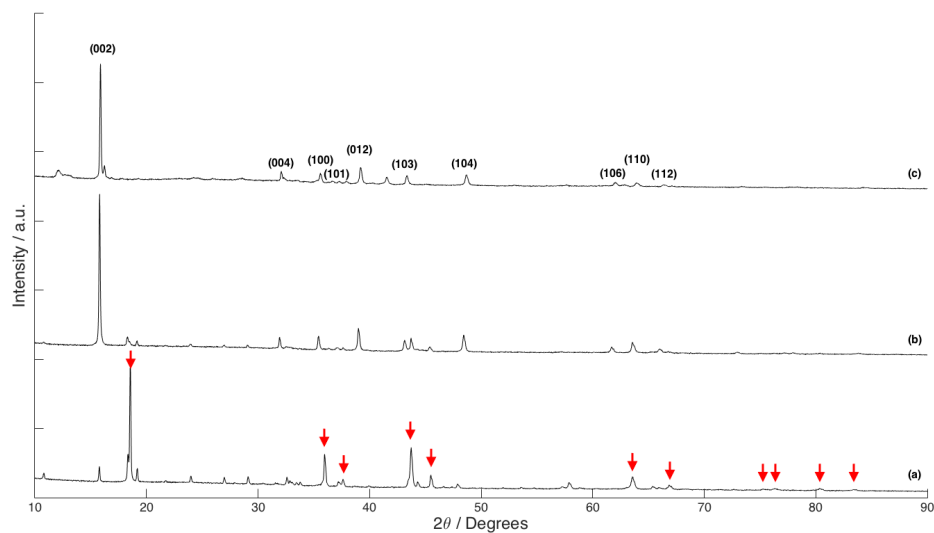


Figure 7-8: Powder XRD of $\text{Li}_{1-y}\text{Na}_y\text{Mn}_{0.5}\text{TiNi}_{0.5}\text{O}_4$ target compositions annealed at 800°C in air for 12 hours

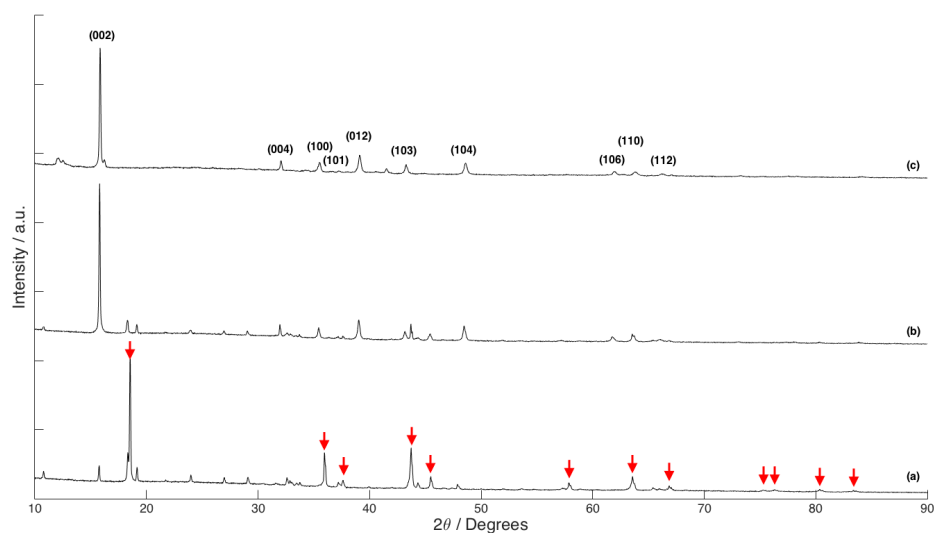


Figure 7-9: Powder XRD of $\text{Li}_{1-y}\text{Na}_y\text{Mn}_{0.5}\text{TiNi}_{0.5}\text{O}_4$ target compositions annealed at 800°C under pure oxygen flow for 12 hours

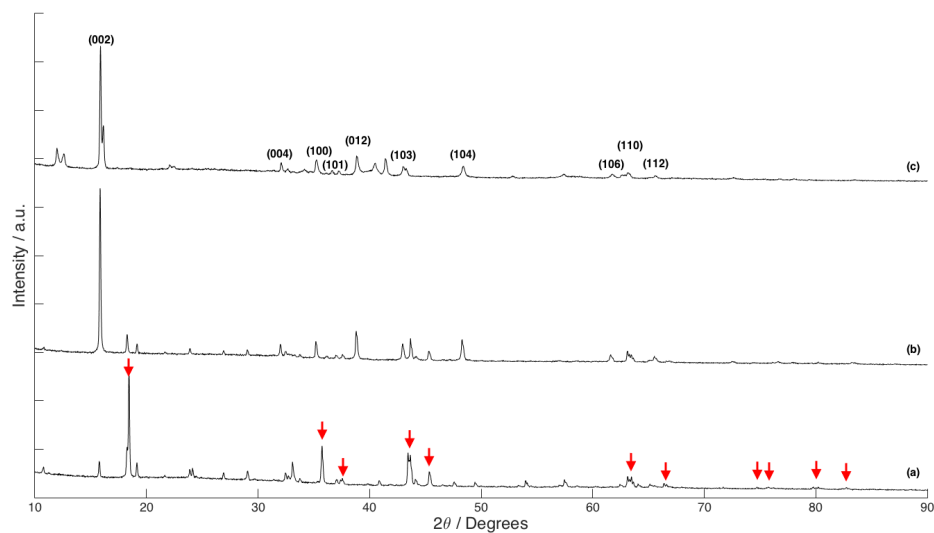


Figure 7-10: Powder XRD of $\text{Li}_{1-y}\text{Na}_y\text{Mn}_{0.5}\text{Ti}_{1.3}\text{Ni}_{0.5}\text{O}_4$ target compositions annealed at 800°C in air for 12 hours

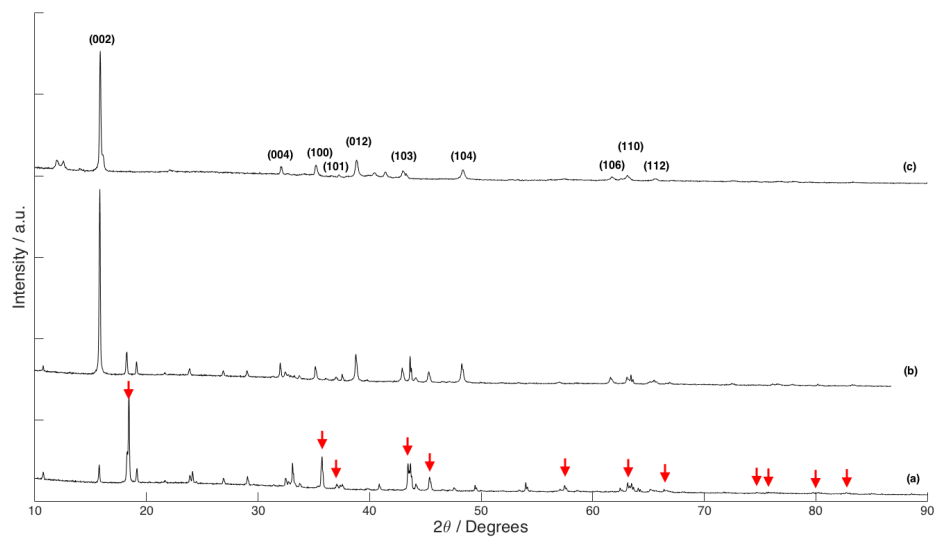


Figure 7-11: Powder XRD of $\text{Li}_{1-y}\text{Na}_y\text{Mn}_{0.5}\text{Ti}_{1.3}\text{Ni}_{0.5}\text{O}_4$ target compositions annealed at 800°C under pure oxygen flow for 12 hours

7.3.2 Electrochemical Results: Synthesized sodium phases

Figure 7-12 provides a voltage profile of the $\text{LiMn}_{1.44}\text{Zr}_{0.06}\text{Ni}_{0.5}\text{O}_4$ spinel cycled against a lithium metal anode with 1M $\text{LiPF}_6\text{-EC/DMC}$ electrolyte. Inset within Figure 7-12 is a cyclic voltammogram using a 0.01 mV/s sweep rate within a similar lithium metal cell; labeled peaks correlate to the active $\text{Ni}^{2+}/\text{Ni}^{4+}$ redox, which has remained relatively invariant from the undoped LMNO spinel reported in Section 4.3. The peaks centered at *ca.* 4.0V show that a significant amount of Mn^{3+} is present, suggesting an oxygen deficient spinel. However, as oxygen deficiency is not of primary concern, the stoichiometry of the $\text{Zr}_{0.06}$ sample is regarded as *ca.* $\text{LiMn}_{1.44}\text{Zr}_{0.06}\text{Ni}_{0.5}\text{O}_4$. Figure 7-12 demonstrates a large amount of electrolyte decomposition throughout the 5.0V charge, which is in agreement with the previously reported surface area of the 500°C annealed $\text{Zr}_{0.02}$ samples (which is expected to be approximately equivalent for the $\text{Zr}_{0.06}$ sample). The following discharge sees an initial capacity of 105 mAh/g, and observes a gradual decline (not shown) due to the considerably high surface areas of active material, resulting in catalytic breakdown of the electrolyte.

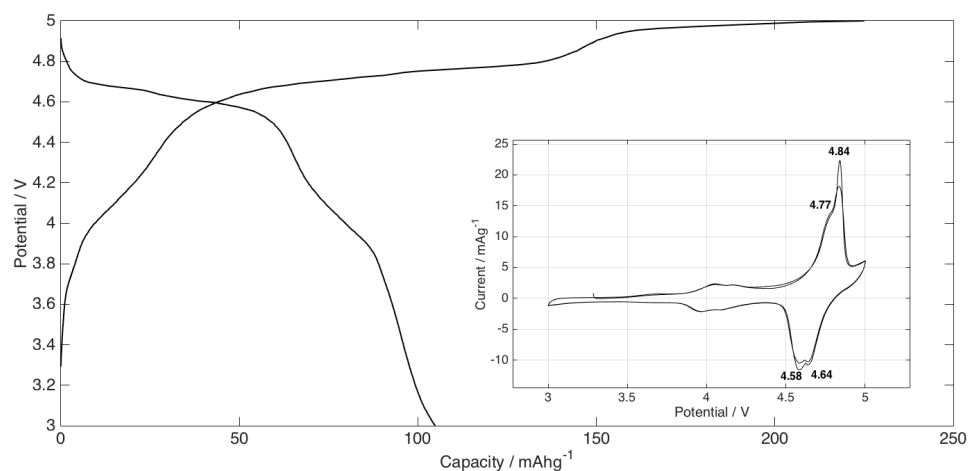


Figure 7-12: Voltage profile of $\text{LiMn}_{1.44}\text{Zr}_{0.06}\text{Ni}_{0.5}\text{O}_4$ spinel (500°C anneal) cycled at 3mA/g, using 1M $\text{LiPF}_6\text{-EC/DMC}$ electrolyte

Following the same electrochemical delithiation process as described previously, Figure 7-13 considers the Na^+ insertion into the $\text{Zr}_{0.06}$ spinel composition at a current rate of 10 mA/g at 24°C. Throughout the initial discharge, a stable voltage plateau is reached at 3.5V (vs. Na/Na^+), followed by a gradual slope in the voltage profile with an additional voltage step occurring at *ca.* 3.0V (resulting from the Mn^{3+} content of the initial $\text{Zr}_{0.06}$ spinel) demonstrating a final discharge capacity of 117 mAh/g. Here, the Na^+ insertion reaction is likely to proceed in a similar manner as that already discussed for Fλ-MNO and

P λ -MNO spinel samples: by an initial two-phase reaction followed by single-phase Na⁺ insertion onto residual 8a tetrahedral sites. Further comments are provided in the discussion section.

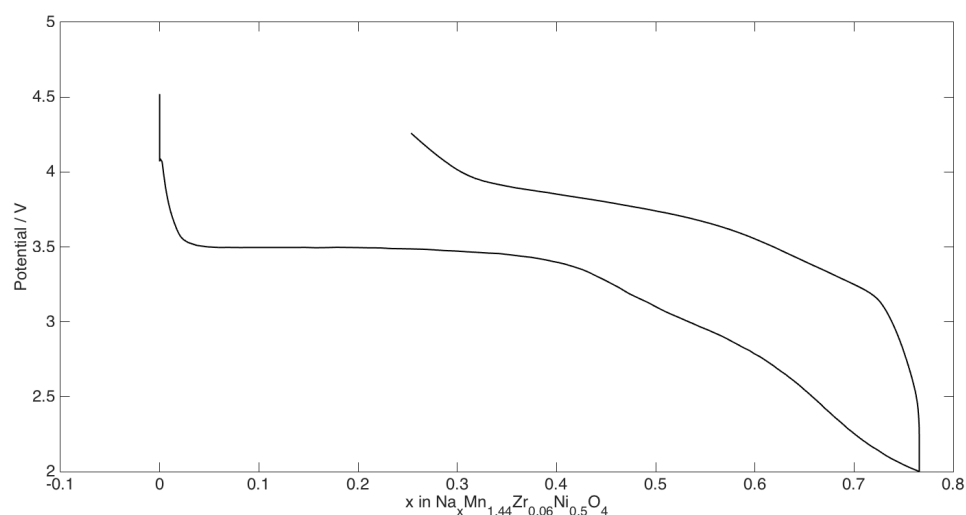


Figure 7-13: Galvanostatically cycled λ -Zr_{0.06} vs. Na/Na⁺ using 1M NaClO₄-PC:FEC2% at 24°C at 10 mA/g. 2.0 – 4.25V

Figure 7-14 shows the voltage profile of LiMn_{1.5-x}Ti_xNi_{0.5}O₄ ($x = 0.3, 0.5, 1.0, 1.3$) vs. Li/Li⁺ coin cells cycled at 10 mA/g, 24°C. Throughout Figure 7-14 discharge capacities see a progressive decline as a function of increasing Ti content. In fact, little evidence of the Ni²⁺/Ni⁴⁺ redox is present for the LiMn_{1.5-x}Ti_xNi_{0.5}O₄ ($x = 1.0, 1.3$) samples, as seen by the limited high-voltage discharge capacities, and from *ex-situ* XRD measurements performed on charged cathodes; suggesting minor delithiation occurring throughout the 5.0V charge protocol.

Due to the apparent electrochemical ‘inactivity’ of high Ti content spinel samples, and sufficient formation of a λ -Ti_{0.3} phase (delithiated Ti_{0.3}), the Ti_{0.3} composition was used in a similar manner as described throughout Chapter 5 in order to study the Na⁺ insertion process into λ -Ti_{0.3}. Figure 7-15 shows the galvanostatic discharge/charge throughout the first 2 cycles at 24°C with a 10 mA/g current rate using the same 1M NaClO₄-PC:FEC2% electrolyte used in the previous chapters. Further comments are provided in the discussion section.

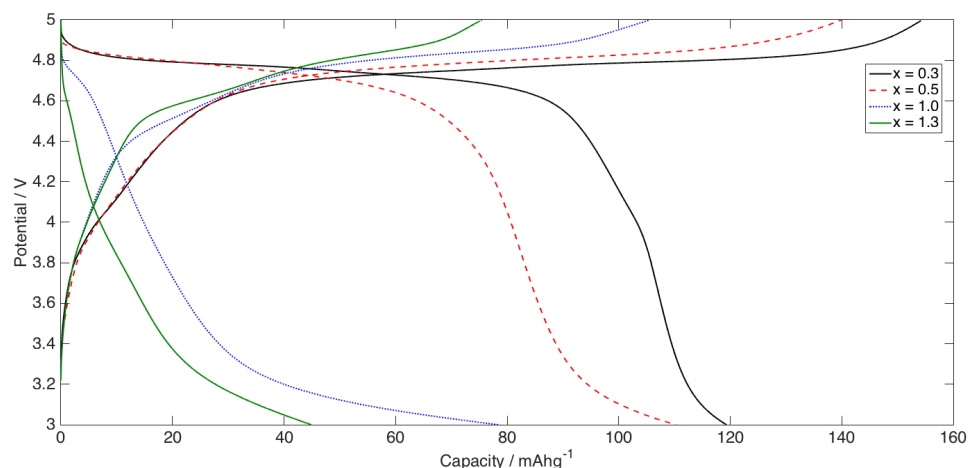


Figure 7-14: Galvanostatic voltage profiles of $\text{LiMn}_{1.5-x}\text{Ti}_x\text{Ni}_{0.5}\text{O}_4$ ($x = 0.3, 0.5, 1.0$, and 1.3) compositions cycled at 10 mA/g at 24°C using $1\text{M NaPF}_6\text{-EC/DMC}$ electrolyte

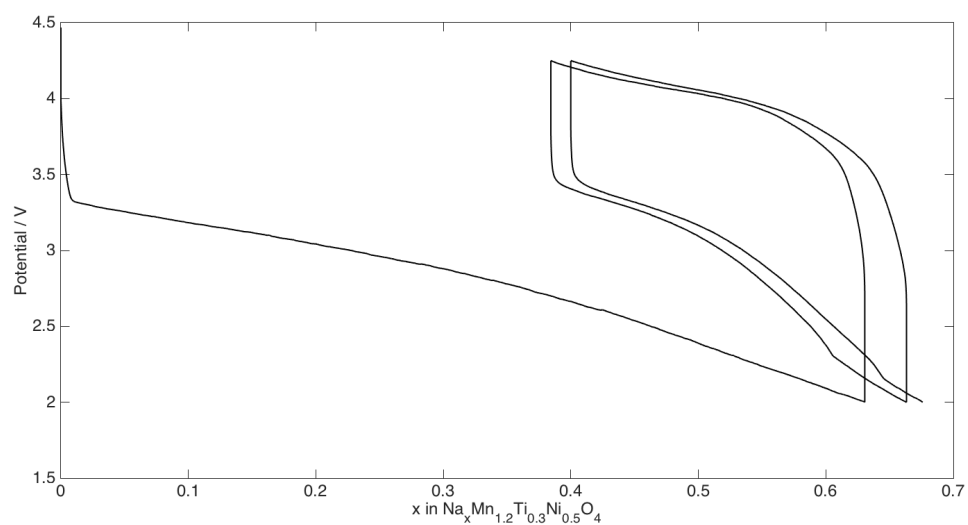


Figure 7-15: Galvanostatic voltage profile of electrochemically delithiated $\text{Mn}_{1.2}\text{Ti}_{0.3}\text{Ni}_{0.5}\text{O}_4$ cycled against a sodium metal anode using $1\text{M NaClO}_4\text{-PC:FEC2\%}$ electrolyte at 24°C , 10 mA/g

Although the $\text{Li}_{1-y}\text{Na}_y\text{Mn}_{1.5-x}\text{Ti}_x\text{Ni}_{0.5}\text{O}_4$ ($x = 1.0, 1.3$; $y = 0.1, 0.5, 1.0$) target compositions mentioned in the previous section notably did not yield a sodiated spinel phase, Figure 7-16 provides their respective voltage profiles at 24°C with a 10 mA/g applied current. The $\text{Li}_{1-y}\text{Na}_y\text{Mn}_{1.5-x}\text{Ti}_x\text{Ni}_{0.5}\text{O}_4$ ($x = 1.3$; $y = 0.1, 0.5, 1.0$) samples in Figure 7-16b see considerably lower capacities as compared to the $x = 1.0$ compositions (Figure 7-16a), further supporting potential concerns surrounding electrical conductivity with high Ti containing samples. As a whole, the $y = 0.5$ compositions ($\text{Li}_{0.5}\text{Na}_{0.5}$) see the greatest capacities, potentially arising from the additional Li^+ de/insertion processes. Due to the relatively similar nature of the

$y = 0.5$ and the $y = 1.0$ compositions, it is expected that a similar de/insertion process is taking place between the two layered compositions, and that the superior nature of the $y = 0.5$ samples is due to the initial Li content; being the result of the initial synthesis composition.

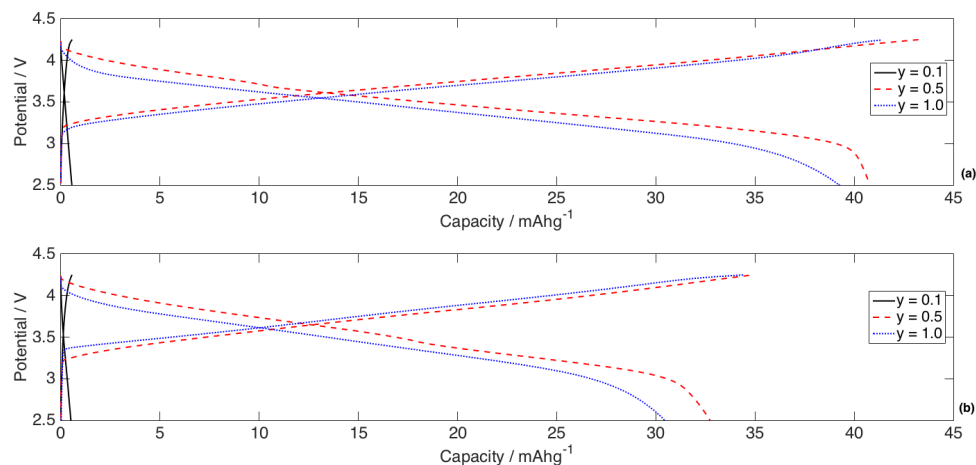


Figure 7-16: Galvanostatic voltage profiles of $\text{Li}_{1-y}\text{Na}_y\text{Mn}_{1.5-x}\text{Ti}_x\text{Ni}_{0.5}\text{O}_4$ ($x = 1.0$ (a), $x = 1.3$ (b); $y = 0.1, 0.5, 1.0$) compositions cycled at 10 mA/g at 24°C using 1M NaClO_4 -PC:FEC2% electrolyte

7.4 Discussion

Zr and Ti-doped spinels demonstrate strikingly similar voltage characteristics as compared to the parent LMNO. Considering the $\text{Zr}_{0.06}$ composition, the low temperature Pechini synthesis technique has resulted in a large amount of Mn^{3+} as can be seen by both the redox reaction occurring at *ca.* 4.0V in both the galvanostatic voltage profile and the cyclic voltammogram shown in Figure 7-12. The evidence of a large quantity of Mn^{3+} may also explain the relatively high reported lattice parameters across the Zr_x spinel compositions annealed at 500°C, due to the relatively larger ionic radii of Mn^{3+} with respect to Mn^{4+} .

Preliminary data on Na^+ insertion into the delithiated $\text{Zr}_{0.06}$ spinel (λ - $\text{Zr}_{0.06}$) suggests a similar reaction pathway as that previously seen in Chapter 5. In particular, the $\text{Zr}_{0.06}$ composition only affords *ca.* a +0.01Å increase in the lattice parameter (with respect to the F-LMNO spinel mentioned in the earlier chapters), which does not appear to have sufficiently enlarged the 8a tetrahedral sites such to drive the Na^+ insertion reaction to a predominantly single-phase de/insertion reaction mechanism. However, it is likely that the two-phase reaction products will be considerably different from those reported for F λ -MNO and P λ -MNO by nature of the moderately expanded spinel crystal structure; potentially motivating future works

in this area. While additional work should be done to validate the Additional comments are provided in the following chapter.

Here, utilization of the 500°C Zr_{0.06} composition was chosen due to the slightly larger reported lattice parameter in comparison to the 700°C and 800°C annealed samples. Considering the lower reported surface areas of the 700/800°C Zr_{0.06} compositions, it is expected that these samples would demonstrate significantly less catalytic decomposition of the electrolyte. However, due to the limited solubility, and hence limited extent of expansion the Zr-substitution affords, additional physical/electrochemical characterization was not explored.

The Ti-doped samples solely utilized a solid-state synthesis method due to incompatibility concerns surrounding titanium precursors. Primary electrochemistry investigations demonstrate that the Ti-doped spinel becomes progressively more electrochemically inactive as a function of increasing Ti content, eventually showing no evidence of the Ni²⁺/Ni⁴⁺ redox at the considered Ti_{1.0} and Ti_{1.3} compositions. While this has been attributed to low electrical conductivity of the Ti-O bonds, initial efforts to increase the electrical conductivity of the Ti-doped samples through formation of a carbonaceous nanocomposite still suffer similar difficulties as those discussed in literature,³⁷⁷ and may suggest additional limiting factors at play.

The Ti_{0.3} composition was chosen for study in an analogous sodium-metal cell, as this sample demonstrated the greatest high voltage capacity, while still considerably expanding the parent LMNO spinel structure. Ti_{0.3} cathodes were initially delithiated as described previously in Chapter 4. Figure 7-15 considers the same 2.0 – 4.25V voltage window as previously discussed for the (F/P) λ -MNO samples in Chapter 5, and sees considerable differences in both voltage and the reversible cycling range beyond the initial discharge. While the Ti-doped spinel was suspected to increase the operating voltage of the Na⁺ insertion process, it in fact, has been drastically lowered from *ca.* 3.6V (vs. Na/Na⁺) to *ca.* 2.9V. Additionally, Figure 7-15 is notably more characteristic of a single-phase insertion process, as can be seen by the gradually sloping voltage profile.

Although additional physical and electrochemical characterization of the Na⁺ insertion into the Ti_{0.3} spinel composition is not reported, it is postulated that the expansion of the spinel lattice in this instance has greatly mitigated the initial two-phase Na⁺ insertion reaction previously reported for the (F/P) λ -MNO

spinel, and resulted in a primarily single-phase Na^+ insertion mechanism. Following the initial Na^+ insertion reaction, there appear to be similar deinsertion kinetic limitations as previously discussed for the (F/P)Na-MNO spinels, meriting additional future study. Here, despite the further reduction in operating voltage, it is evident that further structural/electrochemical investigations are necessary to validate the single-phase/two-phase Na^+ insertion reaction.

Lastly, electrochemical properties of the layered sodium phases were also investigated for both the $\text{Ti}_{1.0}$ and $\text{Ti}_{1.3}$ target compositions. Here, the term ‘target composition’ is meant to indicate the relative stoichiometries of the various transition metals prior to annealing, which is expected to deviate from those actually observed due to deviation from the ideal spinel compositions desired. Figure 7-16 considers the $\text{Li}_{1-y}\text{Na}_y\text{Mn}_{1.5-x}\text{Ti}_x\text{Ni}_{0.5}\text{O}_4$ ($x = 1.0, 1.3$; $y = 0.1, 0.5$, and 1.0) compositions within a sodium-metal coin cell. Capacities see a systematic increase with increasing sodium content (excluding $y = 1.0$ samples), with only the $y = 0.5$, and 1.0 samples showing any appreciable capacity, as the $y = 0.1$ composition is still largely a lithium spinel phase; demonstrating equally low activity in a lithium-metal cell.

Based off the preliminary data of $\text{Li}_{1-y}\text{Na}_y\text{Mn}_{1.5-x}\text{M}_x\text{Ni}_{0.5}\text{O}_4$ ($\text{M} = \text{Zr}, \text{Ti}$) target compositions, further predictions can be made regarding the solid-solubility of various transition metal cations within the LMNO parent spinel. In particular, due to the relatively low differences in their ionic radii with respect to Mn^{4+} , it is anticipated that $\text{M} = \text{V}, \text{Cr}, \text{Fe}$, and Ru will show similar solid-solubility limits as those previously seen for $\text{M} = \text{Ti}$; and $\text{M} = \text{Tc}, \text{Mo}, \text{W}, \text{Ta}$, and Nb are likely to exhibit some limited solid-solubility as demonstrated by the Zr-doped samples.

7.5 Conclusion

Substitutional doping of physically large cations onto the 16d octahedral sites has demonstrated to be effective at increasing the average lattice parameter of the $\text{LiMn}_{1.5-x}\text{M}_x\text{Ni}_{0.5}\text{O}_4$ ($\text{M} = \text{Zr}, \text{Ti}$) spinel compositions. Although only preliminary data is provided, it is believed that the expansion of the lattice parameter has promoted Na^+ insertion onto the 8a tetrahedral sites by a predominantly single-phase insertion reaction as seen through galvanostatically discharged sodium-metal cells. However, additional physical and electrochemical characterization is needed to further bolster this claim. Similar behavior is also predicted for a range of other doped spinel compositions, *i.e.* $\text{LiMn}_{1.5-x}\text{M}_x\text{Ni}_{0.5}\text{O}_4$ ($\text{M} = \text{V}, \text{Cr}, \text{Fe}, \text{Ru}$) due to the similarity in ionic radii relative to Mn^{4+} .

Direct synthesis of a sodium spinel $\text{Li}_{1-y}\text{Na}_y\text{Mn}_{1.5-x}\text{M}_x\text{Ni}_{0.5}\text{O}_4$ ($\text{M} = \text{Zr}, \text{Ti}$) has not been demonstrated, as systematic increasing quantities of Na continually result in the formation of a layered hexagonal crystal structure, potentially indicating that the sodium spinel is a metastable phase, due to the large steric effects that arise from the relatively large size of Na^+ .

8 Future work

8.1 Future work relevant to high voltage electrode materials

Utilization of 4.7V $\text{LiMn}_{1.5-\delta}\text{Ni}_{0.5-\delta}\text{O}_4$ (Fd-3m and P4₃32) in an analogous sodium metal cell has demonstrated that there is a considerably larger drop in operating voltage of *ca.* 1.1V than that predicted from differences in standard redox potentials; suggesting that additional factors such as the electronic structure and differences in charge density are of significant importance for adapting existing high-voltage lithium chemistries to analogous sodium systems. The large drop in voltage may in fact be of considerable utility, as a number of cathode compositions with active redox reaction exceeding *ca.* 5.0V (vs. Li/Li^+) have been identified. However, practical use in a Li-ion cell is not possible due to limitations of modern electrolytes. In fact, implementing such chemistries in a Na-ion cell may drop the voltage sufficiently to operate within the stability ranges of common electrolytes.

The methods and procedures discussed throughout this work may serve as a template against which further testing and optimization of high-voltage Na-ion cathodes (derived from high-voltage Li-ion cathodes) may be derived.

8.2 Future work relevant to high-voltage spinel

Within the previous chapters, (F/P) λ -MNO cathodes have demonstrated a range of interesting features which are of further interest. The questions and points of interest that arise are:

- (1) Why is there a difference in reaction mechanism when holding FNa-MNO in a fully discharged state for prolonged periods of time?
- (2) FNa-MNO and PNa-MNO cathode exhibit drastically different reaction pathways; where does this originate?
- (3) How can the multiphasic nature of high rate discharged cathodes be explained? Is the proposed core/shell model valid?
- (4) Does the λ -Zr_{0.06} spinel observe any superior reaction kinetics/reaction pathways as a result of the Zr-substitution?

- (5) What type of Na^+ insertion reaction mechanism(s) is/are taking place within the Ti-doped ($\text{Ti}_{0.3}$) spinel? Is this an ordered (P4_332) or disordered (Fd-3m) structure?
- (6) Is Na^+ truly residing on the centers of the 8a tetrahedral sites? Is there any partial occupation of the adjacent 16c sites?
- (7) Can additional expanded spinel structures be formed using additional transition metals? What is their specific benefit/advantage over the (F/P) λ -MNO parent spinel?
- (8) Can a direct synthesis method be used to form a sodium spinel in the discharged state?

References

1. Prodromidis, G. N. & Coutelieris, F. A. Innovative Energy Storage for Off-Grid RES-Based Power Systems : Integration of Flywheels with Hydrogen Utilization in Fuel Cells. *Am. Soc. Civ. Eng.* **140**, 1–10 (2014).
2. Beacon Power LCC. Flywheel Energy Storage System. **62**, 991–1001 (2013).
3. Li, W., Chau, K. T., Ching, T. W., Wang, Y. & Chen, M. Design of a High-Speed Superconducting Bearingless Machine for Flywheel Energy Storage Systems. *IEEE Trans. Appl. Supercond.* **25**, 5–8 (2014).
4. Müllner, F., Neudorfer, H. & Recheis, M. highFly – Entwicklung eines Flywheels als elektrischer Energiespeicher für den mobilen Einsatz. *e i Elektrotechnik und Informationstechnik* **132**, 87–94 (2014).
5. Hedlund, M., Lundin, J., de Santiago, J., Abrahamsson, J. & Bernhoff, H. Flywheel Energy Storage for Automotive Applications. *Energies* **8**, 10636–10663 (2015).
6. Rehman, S., Al-Hadhrami, L. M. & Alam, M. M. Pumped hydro energy storage system: A technological review. *Renew. Sustain. Energy Rev.* **44**, 586–598 (2015).
7. Attya, A. B. T. & Hartkopf, T. Utilising stored wind energy by hydro-pumped storage to provide frequency support at high levels of wind energy penetration. *IET Gener. Transm. Distrib.* **9**, 1485–1497 (2015).
8. Yao, E., Wang, H., Liu, L. & Xi, G. A Novel Constant-Pressure Pumped Hydro Combined with Compressed Air Energy Storage System. *Energies* **8**, 154–171 (2014).
9. Song, W. *et al.* High-voltage NASICON Sodium Ion Batteries: Merits of Fluorine Insertion. *Electrochim. Acta* **146**, 142–150 (2014).
10. U.S. Geological Survey. *Mineral Commodity Summaries 2015*. US Geological Survey (2015). doi:10.3133/70140094
11. Brett, C. M. A. & Brett, A. M. O. *Electrochemistry Principles, Methods, and Applications*. (1993).
12. Gellings, P. J. & Bouwmeester, H. J. M. *The CRC Handbook of Solid State Electrochemistry*. (1997).
13. Ning, X. *et al.* Self-healing Li–Bi liquid metal battery for grid-scale energy storage. *J. Power Sources* **275**, 370–376 (2015).
14. Vasiladiotis, M., Cherix, N., Rufer, A. & The, A. Impact of Grid Asymmetries on the Operation and Capacitive Energy Storage Design of Modular Multilevel Converters. **62**, 6697–6707 (2015).
15. Tant, J., Driesen, J., Geth, F. & Belmans, R. Balanced and unbalanced inverter strategies in battery storage systems for low-voltage grid support. *IET Gener. Transm. Distrib.* **9**, 929–936 (2015).
16. Dufo-López, R. *et al.* Techno-economic analysis of grid-connected battery storage. *Electr. Power Syst. Res.* **127**, 128–135 (2015).
17. Koller, M., Borsche, T., Ulbig, A. & Andersson, G. Review of grid applications with the Zurich 1MW battery energy storage system. *Electr. Power Syst. Res.* **120**, 128–135 (2015).
18. Singh, M., Lopes, L. A. C. & Ninad, N. A. Grid forming Battery Energy Storage System (BESS) for a highly unbalanced hybrid mini-grid. *Electr. Power Syst. Res.* **127**, 126–133 (2015).
19. Oliveira, L. *et al.* Environmental performance of electricity storage systems for grid applications, a life cycle approach. *Energy Convers. Manag.* **101**, 326–335 (2015).

20. Balcombe, P., Rigby, D. & Azapagic, A. Energy self-sufficiency, grid demand variability and consumer costs: Integrating solar PV, Stirling engine CHP and battery storage. *Appl. Energy* **155**, 393–408 (2015).
21. Thackeray, M. M. Lithiated Oxides for Lithium Ion Batteries. *J. Electrochem. Soc.* **142**, 2558–2563 (1995).
22. Wang, J. M., Hu, J. P., Ouyang, C. Y., Shi, S. Q. & Lei, M. S. Cobalt suppressed Jahn–Teller effect in for lithium ion batteries. *Solid State Commun.* **151**, 234–237 (2011).
23. Wang, H., Xia, H., Lai, M. O. & Lu, L. Enhancements of rate capability and cyclic performance of spinel $\text{LiNi}_0.5\text{Mn}_{1.5}\text{O}_4$ by trace Ru-doping. *Electrochem. commun.* **11**, 1539–1542 (2009).
24. Wang, H., Tan, T. A., Yang, P., Lai, M. O. & Lu, L. High-Rate Performances of the Ru-Doped Spinel $\text{LiNi}_0.5\text{Mn}_{1.5}\text{O}_4$: Effects of Doping and Particle Size. *J. Phys. Chem. C* **115**, 6102–6110 (2011).
25. Wang, M. & Navrotsky, A. Enthalpy of formation of LiNiO_2 , LiCoO_2 and their solid solution, $\text{LiNi}_{1-x}\text{Co}_x\text{O}_2$. *Solid State Ionics* **166**, 167–173 (2004).
26. Wang, L., Li, H., Huang, X. & Baudrin, E. A comparative study of Fd-3m and P4332 ' $\text{LiNi}_0.5\text{Mn}_{1.5}\text{O}_4$ '. *Solid State Ionics* **193**, 32–38 (2011).
27. Xiong, L. *et al.* The electrochemical performance of sodium-ion-modified spinel LiMn_2O_4 used for lithium-ion batteries. *J. Solid State Electrochem.* **18**, 713–719 (2013).
28. Xu, G., Liu, Z., Zhang, C., Cui, G. & Chen, L. Strategies for improving the cyclability and thermo-stability of LiMn_2O_4 -based batteries at elevated temperatures. *J. Mater. Chem. A* **3**, 4092–4123 (2015).
29. Yue, H., Huang, X., Lv, D. & Yang, Y. Hydrothermal synthesis of $\text{LiMn}_2\text{O}_4/\text{C}$ composite as a cathode for rechargeable lithium-ion battery with excellent rate capability. *Electrochim. Acta* **54**, 5363–5367 (2009).
30. Zhou, X., Chen, F. & Yang, J. Core@shell sulfur@polypyrrole nanoparticles sandwiched in graphene sheets as cathode for lithium–sulfur batteries. *J. Energy Chem.* **24**, 448–455 (2015).
31. Ma, L., Hendrickson, K. E., Wei, S. & Archer, L. A. Nanomaterials: Science and applications in the lithium–sulfur battery. *Nano Today* **10**, 315–338 (2015).
32. Wang, J.-G., Xie, K. & Wei, B. Advanced engineering of nanostructured carbons for lithium–sulfur batteries. *Nano Energy* **15**, 413–444 (2015).
33. Wei, M. *et al.* Facile assembly of partly graphene-enveloped sulfur composites in double-solvent for lithium–sulfur batteries. *Electrochim. Acta* **178**, 564–570 (2015).
34. Wu, S., Ge, R., Lu, M., Xu, R. & Zhang, Z. Graphene-based nano-materials for lithium–sulfur battery and sodium-ion battery. *Nano Energy* **15**, 379–405 (2015).
35. Zhang, J. *et al.* Hollow sulfur@graphene oxide core–shell composite for high-performance Li–S batteries. *J. Alloys Compd.* **650**, 604–609 (2015).
36. Wang, F. *et al.* Conversion Reaction Mechanisms in Lithium Ion Batteries : Study of the Binary Metal Fluoride Electrodes Conversion Reaction Mechanisms in Lithium Ion Batteries : Study of the Binary Metal Fluoride Electrodes Rutgers University , Department of Materials Sc. 18828–18836 (2011). doi:10.1021/ja206268a
37. Capsoni, D., Bini, M., Ferrari, S., Quartarone, E. & Mustarelli, P. Recent advances in the development of Li-air batteries. *J. Power Sources* **220**, 253–263 (2012).
38. Dawoud, B., Amer, E. & Gross, D. Experimental investigation of an adsorptive thermal energy storage. *Int. J. energy Res.* **31**, 135–147 (2007).

39. Ma, Z. *et al.* A review of cathode materials and structures for rechargeable lithium-air batteries. *Energy Environ. Sci.* **8**, 2144–2198 (2015).
40. Marchini, F. *et al.* Surface Study of Lithium–Air Battery Oxygen Cathodes in Different Solvent–Electrolyte pairs. *Langmuir* **31**, 9236–9245 (2015).
41. Mehta, M., Bevara, V. & Andrei, P. Maximum theoretical power density of lithium–air batteries with mixed electrolyte. *J. Power Sources* **286**, 299–308 (2015).
42. Sergeev, A. V., Chertovich, A. V., Itkis, D. M., Goodilin, E. A. & Khokhlov, A. R. Effects of cathode and electrolyte properties on lithium–air battery performance: Computational study. *J. Power Sources* **279**, 707–712 (2015).
43. Sevim, M., Şener, T. & Metin, Ö. Monodisperse MPd (M: Co, Ni, Cu) alloy nanoparticles supported on reduced graphene oxide as cathode catalysts for the lithium-air battery. *Int. J. Hydrogen Energy* **40**, 10876–10882 (2015).
44. Sun, Y. Lithium ion conducting membranes for lithium-air batteries. *Nano Energy* **2**, 801–816 (2013).
45. Wang, J., Li, Y. & Sun, X. Challenges and opportunities of nanostructured materials for aprotic rechargeable lithium–air batteries. *Nano Energy* **2**, 443–467 (2013).
46. Wang, X. *et al.* Gas transport evaluation in lithium–air batteries with micro/nano-structured cathodes. *J. Power Sources* **274**, 762–767 (2015).
47. Sakuma, M., Suzuki, K., Hirayama, M. & Kanno, R. Reactions at the electrode/electrolyte interface of all-solid-state lithium batteries incorporating Li–M (M=Sn, Si) alloy electrodes and sulfide-based solid electrolytes. *Solid State Ionics* (2015). doi:10.1016/j.ssi.2015.07.010
48. Shi, Z. Electrochemical Properties of Li–Zn Alloy Electrodes Prepared by Kinetically Controlled Vapor Deposition for Lithium Batteries. *Electrochem. Solid-State Lett.* **3**, 312 (1999).
49. Hudak, N. S. & Huber, D. L. Nanostructured Lithium–Aluminum Alloy Electrodes for Lithium-Ion Batteries. *Electrochem. Soc.* **33**, 1–13 (2011).
50. Ong, S. P. *et al.* Voltage, stability and diffusion barrier differences between sodium-ion and lithium-ion intercalation materials. *Energy Environ. Sci.* **4**, 3680 (2011).
51. Andriollo, M. *et al.* Energy intensive electrochemical storage in Italy: 34.8MW sodium–sulphur secondary cells. *J. Energy Storage* (2015). doi:10.1016/j.est.2015.12.003
52. Manthiram, A. & Yu, X. Ambient Temperature Sodium–Sulfur Batteries. *Small* 1–7 (2015). doi:10.1002/sml.201403257
53. Yu, X. & Manthiram, A. Na₂S–Carbon Nanotube Fabric Electrodes for Room-Temperature Sodium–Sulfur Batteries. *Chemistry* **78712**, 4233–4237 (2015).
54. Sudworth, J. L. The sodium/nickel chloride (ZEBRA) battery. *J. Power Sources* **100**, 149–163 (2001).
55. Doeff, M. M. *et al.* Electrochemical Insertion of Sodium into Carbon. *J. Electrochem. Soc.* **140**, 169–170 (1993).
56. Bernardo, P. *et al.* Influence of graphite edge crystallographic orientation on the first lithium intercalation in Li-ion battery. *Carbon N. Y.* **91**, 458–467 (2015).
57. Ni, J., Huang, Y. & Gao, L. A high-performance hard carbon for Li-ion batteries and supercapacitors application. *J. Power Sources* **223**, 306–311 (2013).
58. Senyshyn, A., Mühlbauer, M. J., Dolotko, O. & Ehrenberg, H. Low-temperature performance of Li-ion batteries: The behavior of lithiated graphite. *J. Power Sources* **282**, 235–240 (2015).

59. Park, J., Park, S. S. & Won, Y. S. In situ XRD study of the structural changes of graphite anodes mixed with SiO_x during lithium insertion and extraction in lithium ion batteries. *Electrochim. Acta* **107**, 467–472 (2013).
60. Zhang, W. *et al.* In-situ synthesis of magnetite/expanded graphite composite material as high rate negative electrode for rechargeable lithium batteries. *J. Power Sources* **223**, 119–124 (2013).
61. Johnsen, R. E. & Norby, P. Capillary-based micro-battery cell for *in situ* X-ray powder diffraction studies of working batteries: a study of the initial intercalation and deintercalation of lithium into graphite. *J. Appl. Crystallogr.* **46**, 1537–1543 (2013).
62. Zhu, Z., Cheng, F., Hu, Z., Niu, Z. & Chen, J. Highly stable and ultrafast electrode reaction of graphite for sodium ion batteries. *J. Power Sources* **293**, 626–634 (2015).
63. Komaba, S. *et al.* Electrochemical Na insertion and solid electrolyte interphase for hard-carbon electrodes and application to Na-ion batteries. *Adv. Funct. Mater.* **21**, 3859–3867 (2011).
64. Prabakar, S. J. R., Jeong, J. & Pyo, M. Nanoporous hard carbon anodes for improved electrochemical performance in sodium ion batteries. *Electrochim. Acta* **161**, 23–31 (2015).
65. Lotfabad, E. M. *et al.* High-density sodium and lithium ion battery anodes from banana peels. *ACS Nano* **8**, 7115–7129 (2014).
66. Shi, X., Zhang, Z., Fu, Y. & Gan, Y. Self-template synthesis of nitrogen-doped porous carbon derived from zeolitic imidazolate framework-8 as an anode for sodium ion batteries. *Mater. Lett.* **161**, 332–335 (2015).
67. Wan, F. *et al.* Nanoeffects promote the electrochemical properties of organic Na₂C₈H₄O₄ as anode material for sodium-ion batteries. *Nano Energy* **13**, 450–457 (2015).
68. Luo, X.-F. *et al.* Graphene nanosheets, carbon nanotubes, graphite, and activated carbon as anode materials for sodium-ion batteries. *J. Mater. Chem. A* **3**, 10320–10326 (2015).
69. Wang, H. *et al.* Nitrogen-Doped Porous Carbon Nanosheets as Low-Cost, High-Performance Anode Material for Sodium-ion Batteries. *ChemSusChem* **6**, 56–60 (2013).
70. Cao, Y. *et al.* Sodium ion insertion in hollow carbon nanowires for battery applications. *Nano Lett.* **12**, 3783–3787 (2012).
71. Kang, Y.-J., Jung, S. C., Choi, J. W. & Han, Y.-K. Important Role of Functional Groups for Sodium Ion Intercalation in Expanded Graphite. *Chem. Mater.* **27**, 5402–5406 (2015).
72. Wang, X. *et al.* Sulfur covalently bonded graphene with large capacity and high rate for high-performance sodium-ion batteries anodes. *Nano Energy* **15**, 746–754 (2015).
73. Leblanc, D. *et al.* Silicon as anode for high-energy lithium ion batteries: From molten ingot to nanoparticles. *J. Power Sources* **299**, 529–536 (2015).
74. Legrain, F., Malyi, O. I. & Manzhos, S. Comparative computational study of the energetics of Li, Na, and Mg storage in amorphous and crystalline silicon. *Comput. Mater. Sci.* **94**, 214–217 (2014).
75. Jung, S. C., Jung, D. S., Choi, J. W. & Han, Y. K. Atom-level understanding of the sodiation process in silicon anode material. *J. Phys. Chem. Lett.* **5**, 1283–1288 (2014).
76. Komaba, S. *et al.* Redox reaction of Sn-polyacrylate electrodes in aprotic Na cell. *Electrochem. commun.* **21**, 65–68 (2012).
77. Ellis, L. D., Wilkes, B. N., Hatchard, T. D. & Obrovac, M. N. In Situ XRD Study of Silicon, Lead and Bismuth Negative Electrodes in Nonaqueous Sodium Cells. *J. Electrochem. Soc.* **161**, A416–A421 (2014).
78. Shimizu, M., Usui, H., Fujiwara, K., Yamane, K. & Sakaguchi, H. Electrochemical behavior of SiO as an anode material for Na-ion battery. *J. Alloys Compd.* **640**, 440–443 (2015).

79. Han, X., Li, T. & Hu, L. Tin Anode for Sodium-Ion Batteries Using Natural Wood Fiber as a Mechanical Buffer and Electrolyte Reservoir. *Nano Lett.* **13**, 3093–3100 (2013).
80. Liu, Y. *et al.* Tin-Coated Viral Nanoforests as Sodium-Ion Battery Anodes. *ACS Nano* **7**, 3627–3634 (2013).
81. Kanchan, M. *et al.* Tin and graphite based nanocomposites : Potential anode for sodium ion batteries. *J. Power Sources* **225**, 316–322 (2013).
82. Chevrier, V. L. & Ceder, G. Challenges for Na-ion Negative Electrodes. *J. Electrochem. Soc.* **158**, A1011 (2011).
83. Wang, J. W., Liu, X. H., Mao, S. X. & Huang, J. Y. Microstructural Evolution of Tin Nanoparticles during In Situ Sodium Insertion and Extraction. (2012).
84. Chen, W. & Deng, D. Deflated Carbon Nanospheres Encapsulating Tin Cores Decorated on Layered 3-D Carbon Structures for Low-Cost Sodium Ion Batteries. *ACS Sustain. Chem. Eng.* **3**, 63–70 (2015).
85. Kim, I. T., Kim, S. O. & Manthiram, A. Effect of TiC addition on SnSb-C composite anodes for sodium-ion batteries. *J. Power Sources* **269**, 848–854 (2014).
86. Abel, P. R., Fields, M. G., Heller, A. & Mullins, C. B. Tin–Germanium Alloys as Anode Materials for Sodium-Ion Batteries. *ACS Appl. Mater. Interfaces* **6**, 15860–15867 (2014).
87. Lu, Y. C. *et al.* Electrochemical properties of tin oxide anodes for sodium-ion batteries. *J. Power Sources* **284**, 287–295 (2015).
88. Kim, I. T., Allcorn, E. & Manthiram, A. Cu₆Sn₅–TiC–C nanocomposite anodes for high-performance sodium-ion batteries. *J. Power Sources* **281**, 11–17 (2015).
89. Kim, I. T., Allcorn, E. & Manthiram, A. High-Performance MxSb–Al₂O₃–C (M=Fe, Ni, and Cu) Nanocomposite-Alloys Anodes for Sodium-ion Batteries. *Energy Technol.* **1**, 319–326 (2013).
90. Fan, S. *et al.* Rapid fabrication of a novel Sn–Ge alloy: structure–property relationship and its enhanced lithium storage properties. *J. Mater. Chem. A* **1**, 14577 (2013).
91. Cho, Y. J. *et al.* Germanium-tin alloy nanocrystals for high-performance lithium ion batteries. *Phys. Chem. Chem. Phys.* **15**, 11691–5 (2013).
92. Bodnarchuk, M. I., Kravchyk, K. V., Krumeich, F., Wang, S. & Kovalenko, M. V. Colloidal Tin–Germanium Nanorods and Their Li-Ion Storage Properties. *ACS Nano* **8**, 2360–2368 (2014).
93. Zhang, Y. *et al.* Ultrafine tin oxide on reduced graphene oxide as high-performance anode for sodium-ion batteries. *Electrochim. Acta* **151**, 8–15 (2015).
94. Kalubarme, R. S., Lee, J.-Y. & Park, C.-J. Carbon Encapsulated Tin Oxide Nanocomposites: An Efficient Anode for High Performance Sodium-Ion Batteries. *ACS Appl. Mater. Interfaces* **7**, 17226–17237 (2015).
95. Mullins, C. B. Sn – Cu Nanocomposite Anodes for Rechargeable Sodium-Ion Batteries. *ACS Appl. Mater. Interfaces* **5**, 8273–8277 (2013).
96. Jow, T. R. The Role of Conductive Polymers in Alkali-Metal Secondary Electrodes. *J. Electrochem. Soc.* **134**, 1730 (1987).
97. Lin, X. *et al.* Improved electrochemical property of Pb(NO₃)₂ by carbon black, graphene and carbon nanotube. *Electrochim. Acta* **137**, 767–773 (2014).
98. Li, P. *et al.* Comparison of morphology and electrochemical behavior between PbSbO₂Cl and PbCl₂/Sb₄O₅Cl₂. *J. Electroanal. Chem.* **731**, 128–132 (2014).
99. Wang, D. *et al.* Facile fabrication of Pb(NO₃)₂/C as advanced anode material and its lithium

- storage mechanism. *Electrochim. Acta* **120**, 110–121 (2014).
100. Mortazavi, M., Ye, Q., Biribilis, N. & Medhekar, N. V. High capacity group-15 alloy anodes for Na-ion batteries: Electrochemical and mechanical insights. *J. Power Sources* **285**, 29–36 (2015).
 101. Mortazavi, M., Deng, J., Shenoy, V. B. & Medhekar, N. V. Elastic softening of alloy negative electrodes for Na-ion batteries. *J. Power Sources* **225**, 207–214 (2013).
 102. Li, K., Su, D., Liu, H. & Wang, G. Antimony-Carbon-Graphene Fibrous Composite as Freestanding Anode Materials for Sodium-ion Batteries. *Electrochim. Acta* **177**, 304–309 (2015).
 103. Darwiche, A. *et al.* Performance and mechanism of FeSb₂ as negative electrode for Na-ion batteries. *J. Power Sources* **280**, 588–592 (2015).
 104. Hou, H. *et al.* Antimony nanoparticles anchored on interconnected carbon nanofibers networks as advanced anode material for sodium-ion batteries. *J. Power Sources* **284**, 227–235 (2015).
 105. Duan, J., Zhang, W., Wu, C., Fan, Q. & Zhang, W. Self-wrapped Sb / C nanocomposite as anode material for High-performance sodium- ion batteries. *Nano Energy* **16**, 479–487 (2015).
 106. Liu, J. *et al.* Three-dimensionally interconnected nickel–antimony intermetallic hollow nanospheres as anode material for high-rate sodium-ion batteries. *Nano Energy* **16**, 389–398 (2015).
 107. Su, D., Dou, S. & Wang, G. Bismuth: A new anode for the Na-ion battery. *Nano Energy* **12**, 88–95 (2015).
 108. Zhao, Y. & Manthiram, A. Bi_{0.94}Sb_{1.06}S₃ Nanorod Cluster Anodes for Sodium-Ion Batteries: Enhanced Reversibility by the Synergistic Effect of the Bi₂S₃–Sb₂S₃ Solid Solution. *Chem. Mater.* **27**, 6139–6145 (2015).
 109. Zhao, Y. & Manthiram, A. High-Capacity, High-Rate Bi–Sb Alloy Anodes for Lithium-Ion and Sodium-Ion Batteries. *Chem. Mater.* **27**, 3096–3101 (2015).
 110. Jung, H.-G., Jang, M. W., Hassoun, J., Sun, Y.-K. & Scrosati, B. A high-rate long-life Li₄Ti₅O₁₂/Li[Ni_{0.45}Co_{0.1}Mn_{1.45}]O₄ lithium-ion battery. *Nat. Commun.* **2**, 516 (2011).
 111. Zou, W. *et al.* Microspherical Na₂Ti₃O₇ prepared by spray-drying method as anode material for sodium-ion battery. *Solid State Ionics* **262**, 192–196 (2014).
 112. Yan, Z. *et al.* A tightly integrated sodium titanate-carbon composite as an anode material for rechargeable sodium ion batteries. *J. Power Sources* **274**, 8–14 (2015).
 113. Wu, L. *et al.* Unfolding the Mechanism of Sodium Insertion in Anatase TiO₂ Nanoparticles. *Adv. Energy Mater.* **5**, (2015).
 114. Xu, Y. *et al.* Nanocrystalline anatase TiO₂: a new anode material for rechargeable sodium ion batteries. *Chem. Commun.* **49**, 8973 (2013).
 115. Huang, J. P. *et al.* Electrochemical sodium storage of TiO₂(B) nanotubes for sodium ion batteries. *RSC Adv.* **3**, 12593 (2013).
 116. Xiong, H., Slater, M. D., Balasubramanian, M., Johnson, C. S. & Rajh, T. Amorphous TiO₂ Nanotube Anode for Rechargeable Sodium Ion Batteries. *J. Phys. Chem. Lett.* **2**, 2560–2565 (2011).
 117. Ge, Y. *et al.* Copper-doped Li₄Ti₅O₁₂ / carbon nano fi ber composites as anode for high-performance sodium-ion batteries. *J. Power Sources* **272**, 860–865 (2014).
 118. Wu, X., Wu, W., Wang, K., Chen, W. & He, D. Synthesis and electrochemical performance of flower-like MnCo₂O₄ as an anode material for sodium ion batteries. *Mater. Lett.* **147**, 85–87 (2015).
 119. Liu, Y. *et al.* Mesoporous Co₃O₄ sheets / 3D graphene networks nanohybrids for high-

- performance sodium-ion battery anode. *J. Power Sources* **273**, 878–884 (2015).
120. Kumar, P. R., Jung, Y. H., Bharathi, K. K., Lim, C. H. & Kim, D. K. High capacity and low cost spinel Fe₃O₄ for the Na-ion battery negative electrode materials. *Electrochim. Acta* **146**, 503–510 (2014).
 121. Zhang, X. *et al.* MgFe₂O₄/reduced graphene oxide composites as high-performance anode materials for sodium ion batteries. *Electrochim. Acta* **180**, 616–621 (2015).
 122. Jiménez Sandoval, S., Yang, D., Frindt, R. & Irwin, J. Raman study and lattice dynamics of single molecular layers of MoS₂. *Phys. Rev. B* **44**, 3955–3962 (1991).
 123. Chang, K. & Chen, W. L-cysteine-assisted synthesis of layered MoS₂/graphene composites with excellent electrochemical performances for lithium ion batteries. *ACS Nano* **5**, 4720–4728 (2011).
 124. Hwang, H., Kim, H. & Cho, J. MoS₂ nanoplates consisting of disordered graphene-like layers for high rate lithium battery anode materials. *Nano Lett.* **11**, 4826–4830 (2011).
 125. Bhandavat, R., David, L. & Singh, G. Synthesis of surface-functionalized WS₂ nanosheets and performance as li-ion battery anodes. *J. Phys. Chem. Lett.* **3**, 1523–1530 (2012).
 126. Hu, Y. *et al.* Fabrication of MoS₂-Graphene Nanocomposites by Layer-by-Layer Manipulation for High-Performance Lithium Ion Battery Anodes. *ECS J. Solid State Sci. Technol.* **2**, M3034–M3039 (2013).
 127. Zhou, X., Wan, L.-J. & Guo, Y.-G. Facile synthesis of MoS₂@CMK-3 nanocomposite as an improved anode material for lithium-ion batteries. *Nanoscale* **4**, 5868 (2012).
 128. Windom, B. C., Sawyer, W. G. & Hahn, D. W. A Raman Spectroscopic Study of MoS₂ and MoO₃: Applications to Tribological Systems. *Tribol. Lett.* **42**, 301–310 (2011).
 129. David, L., Bhandavat, R. & Singh, G. MoS₂/graphene composite paper for sodium-ion battery electrodes. *ACS Nano* **8**, 1759–1770 (2014).
 130. Qin, W. *et al.* MoS₂-reduced graphene oxide composites via microwave assisted synthesis for sodium ion battery anode with improved capacity and cycling performance. *Electrochim. Acta* **153**, 55–61 (2015).
 131. Fu, Z.-W. *et al.* Electrochemical Reaction of Lithium with Cobalt Fluoride Thin Film Electrode. *J. Electrochem. Soc.* **152**, E50–E55 (2005).
 132. Tan, J. *et al.* The electrochemical performance and mechanism of cobalt (II) fluoride as anode material for lithium and sodium ion batteries. *Electrochim. Acta* **168**, 225–233 (2015).
 133. Slater, M. D., Kim, D., Lee, E. & Johnson, C. S. Sodium-Ion Batteries. *Adv. Funct. Mater.* **23**, 947–958 (2013).
 134. Palomares, V. *et al.* Na-ion batteries, recent advances and present challenges to become low cost energy storage systems. *Energy Environ. Sci.* **5**, 5884 (2012).
 135. Zhang, Y. *et al.* An aqueous capacitor battery hybrid device based on Na-ion insertion-deinsertion in λ -MnO₂ positive electrode. *Electrochim. Acta* **148**, 237–243 (2014).
 136. Whitacre, J. F., Shanbhag, S., Mohamed, A., Polonsky, A. & Carlisle, K. A Polyionic , Large-Format Energy Storage Device Using an Aqueous Electrolyte and Thick-Format Composite NaTi₂ (PO₄)₃ / Activated Carbon Negative Electrodes. **2**, 1–13 (2014).
 137. Park, J. *et al.* Charge-discharge properties of tin dioxide for sodium-ion battery. *Mater. Res. Bull.* **58**, 186–189 (2014).
 138. Liu, H., Zhou, H., Chen, L., Tang, Z. & Yang, W. Electrochemical insertion/deinsertion of sodium on NaV₆O₁₅ nanorods as cathode material of rechargeable sodium-based batteries. *J. Power Sources* **196**, 814–819 (2011).

139. Ding, J. J., Zhou, Y. N., Sun, Q. & Fu, Z. W. Cycle performance improvement of NaCrO₂ cathode by carbon coating for sodium ion batteries. *Electrochem. commun.* **22**, 85–88 (2012).
140. Wu, L., Buchholz, D., Bresser, D., Gomes Chagas, L. & Passerini, S. Anatase TiO₂ nanoparticles for high power sodium-ion anodes. *J. Power Sources* **251**, 379–385 (2014).
141. Wang, Y., Su, D., Wang, C. & Wang, G. SnO₂@MWCNT nanocomposite as a high capacity anode material for sodium-ion batteries. *Electrochem. commun.* **29**, 8–11 (2013).
142. Ponrouch, A., Goñi, A. R. & Palacín, M. R. High capacity hard carbon anodes for sodium ion batteries in additive free electrolyte. *Electrochem. commun.* **27**, 85–88 (2013).
143. Oh, S. M. *et al.* Advanced Na[Ni_{0.25}Fe_{0.5}Mn_{0.25}]O₂/C-Fe₃O₄ sodium-ion batteries using EMS electrolyte for energy storage. *Nano Lett.* **14**, 1620–1626 (2014).
144. Pol, V. G. *et al.* Spherical Carbon as a New High-Rate Anode for Sodium-ion Batteries. *Electrochim. Acta* **127**, 61–67 (2014).
145. Wen, J. W. *et al.* Li and Na storage behavior of bowl-like hollow Co₃O₄ microspheres as an anode material for lithium-ion and sodium-ion batteries. *Electrochim. Acta* **132**, 193–199 (2014).
146. Han, S. C., Bae, E. G., Lim, H. & Pyo, M. Non-crystalline oligopyrene as a cathode material with a high-voltage plateau for sodium ion batteries. *J. Power Sources* **254**, 73–79 (2014).
147. Jian, Z. *et al.* Carbon coated Na₃V₂(PO₄)₃ as novel electrode material for sodium ion batteries. *Electrochem. commun.* **14**, 86–89 (2012).
148. Barpanda, P., Liu, G., Mohamed, Z., Ling, C. D. & Yamada, A. Structural, magnetic and electrochemical investigation of novel binary Na_{2–x}(Fe_{1–y}Mn_y)P₂O₇ (0 ≤ y ≤ 1) pyrophosphate compounds for rechargeable sodium-ion batteries. *Solid State Ionics* **2**, (2014).
149. Song, W. *et al.* Exploration of ion migration mechanism and diffusion capability for Na₃V₂(PO₄)₂F₃ cathode utilized in rechargeable sodium-ion batteries. *J. Power Sources* **256**, 258–263 (2014).
150. Chihara, K., Chujo, N., Kitajou, A. & Okada, S. Cathode properties of Na₂C₆O₆ for sodium-ion batteries. *Electrochim. Acta* **110**, 80–85 (2013).
151. Kitajou, A., Yamaguchi, J., Hara, S. & Okada, S. Discharge/charge reaction mechanism of a pyrite-type FeS₂ cathode for sodium secondary batteries. *J. Power Sources* **247**, 391–395 (2014).
152. Wang, W. *et al.* Single crystalline VO₂ nanosheets: A cathode material for sodium-ion batteries with high rate cycling performance. *J. Power Sources* **250**, 181–187 (2014).
153. Barpanda, P. *et al.* Sodium iron pyrophosphate: A novel 3.0 v iron-based cathode for sodium-ion batteries. *Electrochem. commun.* **24**, 116–119 (2012).
154. Fei, H., Liu, X., Li, H. & Wei, M. Enhanced electrochemical performance of ammonium vanadium bronze through sodium cation intercalation and optimization of electrolyte. *J. Colloid Interface Sci.* **418**, 273–276 (2014).
155. Wang, H. *et al.* Electrochemical properties of P₂-Na_{2/3}[Ni_{1/3}Mn_{2/3}]O₂ cathode material for sodium ion batteries when cycled in different voltage ranges. *Electrochim. Acta* **113**, 200–204 (2013).
156. Yuan, Z., Xuehang, W., Wenwei, W. & Kaituo, W. Synthesis and electrochemical performance of Na_{0.7}Fe_{0.7}Mn_{0.3}O₂ as a cathode material for Na-ion battery. *Ceram. Int.* **40**, 13679–13682 (2014).
157. Komaba, S. *et al.* Fluorinated ethylene carbonate as electrolyte additive for rechargeable Na batteries. *ACS Appl. Mater. Interfaces* **3**, 4165–4168 (2011).
158. Singh, G. *et al.* Electrochemical performance of NaF_x(Ni_{0.5}Ti_{0.5})_{1–x}O₂ (x = 0.2 and x = 0.4)

- cathode for sodium-ion battery. *J. Power Sources* **273**, 333–339 (2015).
159. Vassilaras, P., Toumar, A. J. & Ceder, G. Electrochemical properties of $\text{NaNi}_{1/3}\text{Co}_{1/3}\text{Fe}_{1/3}\text{O}_2$ as a cathode material for Na-ion batteries. *Electrochem. commun.* **38**, 79–81 (2014).
 160. Yu, S. *et al.* A promising cathode material of sodium iron–nickel hexacyanoferrate for sodium ion batteries. *J. Power Sources* **275**, 45–49 (2015).
 161. Yuan, D. *et al.* P2-type $\text{Na}_{0.67}\text{Mn}_{0.65}\text{Fe}_{0.2}\text{Ni}_{0.15}\text{O}_2$ Cathode Material with High-capacity for Sodium-ion Battery. *Electrochim. Acta* **116**, 300–305 (2014).
 162. Nose, M. *et al.* $\text{Na}_4\text{Co}_{2.4}\text{Mn}_{0.3}\text{Ni}_{0.3}(\text{PO}_4)_2\text{P}_2\text{O}_7$: High potential and high capacity electrode material for sodium-ion batteries. *Electrochem. commun.* **34**, 266–269 (2013).
 163. Nose, M. *et al.* $\text{Na}_4\text{Co}_3(\text{PO}_4)_2\text{P}_2\text{O}_7$: A novel storage material for sodium-ion batteries. *J. Power Sources* **234**, 175–179 (2013).
 164. Honma, T. *et al.* Crystallization behavior of sodium iron phosphate glass $\text{Na}_{2-x}\text{Fe}_{1+0.5x}\text{P}_2\text{O}_7$ for sodium ion batteries. *J. Non. Cryst. Solids* **404**, 26–31 (2014).
 165. Ma, D. *et al.* In situ generated FeF_3 in homogeneous iron matrix toward high-performance cathode material for sodium-ion batteries. *Nano Energy* **10**, 295–304 (2014).
 166. Li, H., Bai, Y., Wu, F., Li, Y. & Wu, C. Budding willow branches shaped $\text{Na}_3\text{V}_2(\text{PO}_4)_3/\text{C}$ nanofibers synthesized via an electrospinning technique and used as cathode material for sodium ion batteries. *J. Power Sources* **273**, 784–792 (2015).
 167. Hatchard, T. D. & Obrovac, M. N. Evaluation of Electrolyte Salts and Solvents for Na-Ion Batteries in Symmetric Cells. *J. Electrochem. Soc.* **161**, A1748–A1752 (2014).
 168. Jiang, Y. *et al.* Transition metal oxides for high performance sodium ion battery anodes. *Nano Energy* **5**, 60–66 (2014).
 169. Zhao, J. *et al.* Electrochemical and thermal properties of P2-type $\text{Na}_{2/3}\text{Fe}_{1/3}\text{Mn}_{2/3}\text{O}_2$ for Na-ion batteries. *J. Power Sources* **264**, 235–239 (2014).
 170. B., S., G., A., P., A. & S., R. Synthesis of Carbon coated Nano- $\text{Na}_4\text{Ni}_3(\text{PO}_4)_2\text{P}_2\text{O}_7$ as a Novel Cathode Material for Hybrid Supercapacitors. *Electrochim. Acta* **169**, 447–455 (2015).
 171. Mohd Noor, S. A., Howlett, P. C., Macfarlane, D. R. & Forsyth, M. Properties of sodium-based ionic liquid electrolytes for sodium secondary battery applications. *Electrochim. Acta* **114**, 766–771 (2013).
 172. Chen, C.-Y. *et al.* Charge–discharge behavior of a $\text{Na}_2\text{FeP}_2\text{O}_7$ positive electrode in an ionic liquid electrolyte between 253 and 363 K. *Electrochim. Acta* **133**, 583–588 (2014).
 173. Matsumoto, K. *et al.* The $\text{Na}[\text{FSA}][\text{C}_2\text{C}_1\text{im}][\text{FSA}]$ ($\text{C}_2\text{C}_1\text{im}^+$: 1-ethyl-3-methylimidazolium and FSA^- : bis(fluorosulfonyl)amide) ionic liquid electrolytes for sodium secondary batteries. *J. Power Sources* **265**, 36–39 (2014).
 174. Ding, C. *et al.* $\text{Na}[\text{FSA}][\text{C}_3\text{C}_1\text{pyrr}][\text{FSA}]$ ionic liquids as electrolytes for sodium secondary batteries: Effects of Na ion concentration and operation temperature. *J. Power Sources* **269**, 124–128 (2014).
 175. Monti, D., Jonsson, E., Palacin, M. R. & Johansson, P. Ionic liquid based electrolytes for sodium-ion batteries: Na^+ solvation and ionic conductivity. *J. Power Sources* **245**, 630–636 (2014).
 176. Yamamoto, T. *et al.* Thermodynamic studies on Sn–Na alloy in an intermediate temperature ionic liquid NaFSA–KFSA at 363 K. *J. Power Sources* **237**, 98–103 (2013).
 177. Ziegler, M. J. & Madura, J. D. Solvation of metal cations in non-aqueous liquids. *J. Solution Chem.* **40**, 1383–1398 (2011).

178. Izutsu, K., Nakamura, T., Miyoshi, K. & Kurita, K. Potentiometric study of complexation and solvation of lithium ions in some solvents related to lithium batteries. *Electrochim. Acta* **41**, 2523–2527 (1996).
179. Ponrouch, a *et al.* Towards high energy density sodium ion batteries through electrolyte optimization. *Energy Environ. Sci.* **6**, 2361–2369 (2013).
180. Kim, K. M. *et al.* Improvement of lithium-ion battery performance at low temperature by adopting polydimethylsiloxane-based electrolyte additives. *Electrochim. Acta* **136**, 182–188 (2014).
181. Xia, L., Xia, Y. & Liu, Z. Thiophene derivatives as novel functional additives for high-voltage LiCoO₂ operations in lithium ion batteries. *Electrochim. Acta* **151**, 429–436 (2015).
182. Yang, J. *et al.* In-situ Coating of Cathode by Electrolyte Additive for High-voltage Performance of Lithium-ion Batteries. *Electrochim. Acta* **158**, 202–208 (2015).
183. Chen, J. *et al.* Interface modification in high voltage spinel lithium-ion battery by using N-methylpyrrole as an electrolyte additive. *Electrochim. Acta* **178**, 127–133 (2015).
184. Schmitz, R. W. *et al.* Investigations on novel electrolytes, solvents and SEI additives for use in lithium-ion batteries: Systematic electrochemical characterization and detailed analysis by spectroscopic methods. *Prog. Solid State Chem.* **42**, 65–84 (2014).
185. Zhu, Y., Casselman, M. D., Li, Y., Wei, A. & Abraham, D. P. Perfluoroalkyl-substituted ethylene carbonates: Novel electrolyte additives for high-voltage lithium-ion batteries. *J. Power Sources* **246**, 184–191 (2014).
186. Petibon, R., Rotermund, L. M. & Dahn, J. R. Evaluation of phenyl carbonates as electrolyte additives in lithium-ion batteries. *J. Power Sources* **287**, 184–195 (2015).
187. Xia, J., Ma, L. & Dahn, J. R. Improving the long-term cycling performance of lithium-ion batteries at elevated temperature with electrolyte additives. *J. Power Sources* **287**, 377–385 (2015).
188. Zheng, X. *et al.* High-voltage performance of LiNi_{1/3}Co_{1/3}Mn_{1/3}O₂/graphite batteries with di(methylsulfonyl) methane as a new sulfone-based electrolyte additive. *J. Power Sources* **293**, 196–202 (2015).
189. Xue, L., Lee, S.-Y., Zhao, Z. & Angell, C. A. Sulfone-carbonate ternary electrolyte with further increased capacity retention and burn resistance for high voltage lithium ion batteries. *J. Power Sources* **295**, 190–196 (2015).
190. Pires, J. *et al.* Tris(2,2,2-trifluoroethyl) phosphite as an electrolyte additive for high-voltage lithium-ion batteries using lithium-rich layered oxide cathode. *J. Power Sources* **296**, 413–425 (2015).
191. Wagner, R. *et al.* Vinyl sulfones as SEI-forming additives in propylene carbonate based electrolytes for lithium-ion batteries. *Electrochem. commun.* **40**, 80–83 (2014).
192. Kim, H. *et al.* An azamacrocyclic electrolyte additive to suppress metal deposition in lithium-ion batteries. *Electrochem. commun.* **58**, 25–28 (2015).
193. Alias, N. & Mohamad, A. A. Advances of aqueous rechargeable lithium-ion battery: A review. *J. Power Sources* **274**, 237–251 (2015).
194. Sauvage, F., Baudrin, E. & Tarascon, J. M. Study of the potentiometric response towards sodium ions of Na_{0.44}-xMnO₂ for the development of selective sodium ion sensors. *Sensors Actuators, B Chem.* **120**, 638–644 (2007).
195. Whitacre, J. F., Tevar, A. & Sharma, S. Na₄Mn₉O₁₈ as a positive electrode material for an aqueous electrolyte sodium-ion energy storage device. *Electrochem. commun.* **12**, 463–466 (2010).
196. Whitacre, J. F. *et al.* An aqueous electrolyte, sodium ion functional, large format energy storage device for stationary applications. *J. Power Sources* **213**, 255–264 (2012).

197. Jung, Y. H., Lim, C. H., Kim, J.-H. & Kim, D. K. Na₂FeP₂O₇ as a positive electrode material for rechargeable aqueous sodium-ion batteries. *RSC Adv.* **4**, 9799 (2014).
198. Li, Z., Ravnsbæk, D. B., Xiang, K. & Chiang, Y.-M. Na₃Ti₂(PO₄)₃ as a sodium-bearing anode for rechargeable aqueous sodium-ion batteries. *Electrochem. commun.* **44**, 12–15 (2014).
199. Vujković, M. & Mentus, S. Fast sodiation/desodiation reactions of electrochemically delithiated olivine LiFePO₄ in aerated aqueous NaNO₃ solution. *J. Power Sources* **247**, 184–188 (2014).
200. Scordilis-Kelley, C. Alkali Metal Reduction Potentials Measured in Chloroaluminate Ambient-Temperature Molten Salts. *J. Electrochem. Soc.* **139**, 694 (1992).
201. Fuller, J., Osteryoung, R. A., Carolina, N. & Carlin, R. T. Rechargeable Lithium and Sodium Anodes in Chloroaluminate Molten Salts Containing Thionyl Chloride. **142**, 3632–3636 (1995).
202. Kim, K., Lang, C., Moulton, R. & Kohl, P. A. Electrochemical Investigation of Quaternary Ammonium/Aluminum Chloride Ionic Liquids. *J. Electrochem. Soc.* **151**, A1168 (2004).
203. Lang, C. M., Kim, K. & Kohl, P. a. Catalytic additives for the reversible reduction of sodium in chloroaluminate ionic liquids. *Electrochim. Acta* **51**, 3884–3889 (2006).
204. Fukunaga, A. *et al.* Intermediate-temperature ionic liquid NaFSA-KFSA and its application to sodium secondary batteries. *J. Power Sources* **209**, 52–56 (2012).
205. Nohira, T., Ishibashi, T. & Hagiwara, R. Properties of an intermediate temperature ionic liquid NaTFSA–CsTFSA and charge–discharge properties of NaCrO₂ positive electrode at 423K for a sodium secondary battery. *J. Power Sources* **205**, 506–509 (2012).
206. Yamamoto, T. *et al.* Charge–discharge behavior of tin negative electrode for a sodium secondary battery using intermediate temperature ionic liquid sodium bis(fluorosulfonyl)amide–potassium bis(fluorosulfonyl)amide. *J. Power Sources* **217**, 479–484 (2012).
207. Chagas, L. G., Buchholz, D., Wu, L., Vortmann, B. & Passerini, S. Unexpected performance of layered sodium-ion cathode material in ionic liquid-based electrolyte. *J. Power Sources* **247**, 377–383 (2014).
208. Kumar, D. & Hashmi, S. a. Ion transport and ion-filler-polymer interaction in poly(methyl methacrylate)-based, sodium ion conducting, gel polymer electrolytes dispersed with silica nanoparticles. *J. Power Sources* **195**, 5101–5108 (2010).
209. Kumar, D. & Hashmi, S. a. Ionic liquid based sodium ion conducting gel polymer electrolytes. *Solid State Ionics* **181**, 416–423 (2010).
210. Kumar, D., Suleman, M. & Hashmi, S. a. Studies on poly(vinylidene fluoride-co-hexafluoropropylene) based gel electrolyte nanocomposite for sodium–sulfur batteries. *Solid State Ionics* **202**, 45–53 (2011).
211. Chikkannanavar, S. B., Bernardi, D. M. & Liu, L. A review of blended cathode materials for use in Li-ion batteries. *J. Power Sources* **248**, 91–100 (2014).
212. Jian, Z., Yu, H. & Zhou, H. Designing high-capacity cathode materials for sodium-ion batteries. *Electrochem. commun.* **34**, 215–218 (2013).
213. Kim, J. R. & Amatucci, G. G. Structural and Electrochemical Investigation of Na⁺ Insertion into High-Voltage Spinel Electrodes. *Chem. Mater.* **27**, 2546–2556 (2015).
214. Parant, J.-P., Olazcuaga, R., Devalette, M., Fouassier, C. & Hagenmuller, P. Sur quelques nouvelles phases de formule Na_xMnO₂ (x ≤ 1). *J. Solid State Chem.* **3**, 1–11 (1971).
215. Mendiboure, A., Delmas, C. & Hagenmuller, P. Electrochemical Intercalation and Deintercalation of Na_xMnO₂ Bronzes. *J. Solid State Chem.* **57**, 323–331 (1985).
216. Sauvage, F., Laffont, L., Tarascon, J. M. & Baudrin, E. Study of the insertion/deinsertion

- mechanism of sodium into Na_{0.44}MnO₂. *Inorg. Chem.* **46**, 3289–3294 (2007).
217. Amatucci, G. G., Tarascon, J. M. & Klein, L. C. CoO₂, The End Member of the LiCoO₂ Solid Solution. *Electrochem. Soc.* **143**, 1114–1123 (1996).
 218. Motohashi, T. *et al.* Synthesis and properties of CoO₂, the x = 0 end member of the Li_xCoO₂ and Na_xCoO₂ systems. *Chem. Mater.* **19**, 5063–5066 (2007).
 219. Motohashi, T. *et al.* Electrochemical synthesis and properties of CoO₂, the x = 0 phase of the A_xCoO₂ systems (A = Li, Na). **12** (2008). doi:10.1063/1.2828525
 220. Delmas, C., Braconnier, J. J., Fouassier, C. & Hagenmuller, P. Electrochemical intercalation of sodium in na_xCoO₂ bronzes. *Solid State Ionics* **3/4**, 165–169 (1981).
 221. Kikkawa, S., Miyazaki, S. & Koizumi, M. Deintercalated NaCoO₂ and LiCoO₂. *J. Solid State Chem.* **62**, 35–39 (1986).
 222. Yabuuchi, N. *et al.* P2-type Na_x[Fe_{1/2}Mn_{1/2}]O₂ made from earth-abundant elements for rechargeable Na batteries. *Nat. Mater.* **11**, 512–517 (2012).
 223. Paulsen, J. M., Donaberger, R. A. & Dahn, J. R. Layered T2-, O6-, O2-, and P2-Type A_{2/3}[M'²⁺ 1/3 M⁴⁺ 2/3]O₂ Bronzes, A = Li, Na; M' = Ni, Mg; M = Mn, Ti. *Chem. Mater.* **12**, 2257–2267 (2000).
 224. Mortemard de Boisse, B., Carlier, D., Guignard, M. & Delmas, C. Structural and Electrochemical Characterizations of P2 and New O3-Na_xMn_{1-y}FeyO₂ Phases Prepared by Auto-Combustion Synthesis for Na-Ion Batteries. *J. Electrochem. Soc.* **160**, A569–A574 (2013).
 225. Lu, Z., Donaberger, R. A. & Dahn, J. R. Superlattice ordering of Mn, Ni, and Co in layered alkali transition metal oxides with P2, P3, and O3 structures. *Chem. Mater.* **12**, 3583–3590 (2000).
 226. Eriksson, T. a. *et al.* Influence of Substitution on the Structure and Electrochemistry of Layered Manganese Oxides. *Chem. Mater.* **15**, 4456–4463 (2003).
 227. Paulsen, J. M. & Dahn, J. R. Studies of the layered manganese bronzes, Na_{2/3}[Mn_{1-x}M_x]O₂ with M = Co, Ni, Li, and Li_{2/3}[Mn_{1-x}M_x]O₂ prepared by ion-exchange. *Solid State Ionics* **126**, 3–24 (1999).
 228. Paulsen, J. M., Larcher, D. & Dahn, J. R. O2 Structure Li_{2/3}[Ni_{1/3}Mn_{2/3}]O₂: A New Layered Cathode Material for Rechargeable Lithium Batteries III. Ion Exchange. **147**, 2862–2867 (2000).
 229. Paulsen, J. M., Larcher, D. & Dahn, J. R. O2 Structure Li_{2/3}[Ni_{1/3}Mn_{2/3}]O₂: A New Layered Cathode Material for Rechargeable Lithium Batteries III. Ion Exchange. *J. Electrochem. Soc.* **147**, 2862–2867 (2000).
 230. Delmas, C., Braconnier, J.-J. & Hagenmuller, P. No Title. *Mater. Res. Bull.* **17**, 117 (1982).
 231. Delmas, C., Braconnier, J.-J., Maazaz, A. & Hagenmuller, P. No Title. *Rev. Chim. Min.* **19**, 343 (1982).
 232. Delmas, C., Braconnier, J.-J., Fouassier, C. & Hagenmuller, P. No Title. *Solid State Ionics* **3**, 165 (1981).
 233. Braconnier, J. J., Delmas, C. & Hagenmuller, P. No Title. *Mater. Res. Bull.* **17**, 993 (1982).
 234. Chen, C. Y. *et al.* Electrochemical and structural investigation of NaCrO₂ as a positive electrode for sodium secondary battery using inorganic ionic liquid NaFSA-KFSA. *J. Power Sources* **237**, 52–57 (2013).
 235. Yu, C.-Y. *et al.* NaCrO₂ cathode for high-rate sodium-ion batteries. *Energy Environ. Sci.* **8**, 2019–2026 (2015).

236. Xia, X. & Dahn, J. R. NaCrO₂ is a Fundamentally Safe Positive Electrode Material for Sodium-Ion Batteries with Liquid Electrolytes. *Electrochem. Solid-State Lett.* **15**, A1–A4 (2011).
237. Komaba, S., Takei, C., Nakayama, T., Ogata, A. & Yabuuchi, N. Electrochemical intercalation activity of layered NaCrO₂ vs. LiCrO₂. *Electrochem. commun.* **12**, 355–358 (2010).
238. Kubota, K. *et al.* New Insight into Structural Evolution in Layered NaCrO₂ during Electrochemical Sodium Extraction. *J. Phys. Chem. C* 141208113557000 (2014). doi:10.1021/jp5105888
239. Zhou, Y.-N. *et al.* Phase transition behavior of NaCrO₂ during sodium extraction studied by synchrotron-based X-ray diffraction and absorption spectroscopy. *J. Mater. Chem. A* **1**, 11130–11134 (2013).
240. Barker, M. G. & Hooper, A. J. Preparation and X-ray Powder Diffraction Patterns of the Sodium Vanadates NaVO₃, Na₄V₂O₁₄, and Na₃VO₄. *Dalton* **15**, 1513 (1973).
241. Didier, C. *et al.* Electrochemical Na-Deintercalation from NaVO₂. *Electrochem. Solid-State Lett.* **14**, A75 (2011).
242. Brohan, L. & Marchand, R. Properties physiques des bronzes MxTiO₂. *Solid State Ionics* **9-10**, 419–424 (1983).
243. Murphy, D. W., Cava, R. J., Zahurak, S. M. & Santoro, A. Ternary Li_xTiO₂ phases from insertion reactions. *Solid State Ionics* **9-10**, 413–418 (1983).
244. Maazaz, A., Delmas, C. & Hagemuller, P. A. A Study of the Na_xTiO₂ system by electrochemical deintercalation. *J. Incl. Phenom.* **1**, 45–51 (1983).
245. Szajwaj, O., Gaudin, E., Weill, F., Darriet, J. & Delmas, C. Investigation of the new P'3-Na_{0.60}VO₂ phase: structural and physical properties. *Inorg. Chem.* **48**, 9147–9154 (2009).
246. Vassilaras, P., Ma, X., Li, X. & Ceder, G. Electrochemical Properties of Monoclinic NaNiO₂. *J. Electrochem. Soc.* **160**, A207–A211 (2012).
247. Viret, M. *et al.* β-NaFeO₂, a new room-temperature multiferroic material. *Mater. Res. Bull.* **47**, 2294–2298 (2012).
248. Takeda, Y., Akagi, J., Edagawa, A., Inagaki, M. & Naka, S. A Preparation and Polymorphic relations of Sodium Iron Oxide (NaFeO₂). *Mater. Res. Bull.* **14**, 1167 (1980).
249. Lee, E. *et al.* New Insights into the Performance Degradation of Fe-Based Layered Oxides in Sodium-Ion Batteries: Instability of Fe³⁺/Fe⁴⁺ Redox in α-NaFeO₂. *Chem. Mater.* 150911160228008 (2015). doi:10.1021/acs.chemmater.5b02918
250. Yoshida, H., Yabuuchi, N. & Komaba, S. NaFe_{0.5}Co_{0.5}O₂ as high energy and power positive electrode for Na-ion batteries. *Electrochem. commun.* **34**, 60–63 (2013).
251. Yabuuchi, N. *et al.* P2-type Na_x[Fe_{1/2}Mn_{1/2}]O₂ made from earth-abundant elements for rechargeable Na batteries. *Nat. Mater.* **11**, 512–517 (2012).
252. Takeda, Y. *et al.* Sodium deintercalation from sodium iron oxide. *Mater. Res. Bull.* **29**, 659–666 (1994).
253. Kikkawa, S., Miyazaki, S. & Koizumi, M. Sodium deintercalation from α-NaFeO₂. *Mater. Res. Bull.* **20**, 373–377 (1985).
254. Blesa, M. C. *et al.* α-NaFeO₂: ionic conductivity and sodium extraction. *Solid State Ionics* **126**, 81–87 (1999).
255. Tabuchi, M. *et al.* Preparation of AFeO₂, (A = Li, Na) by hydrothermal method. *Solid State Ionics* **79**, 220–226 (1995).

256. Shirane, T. *et al.* SOLID Structure and physical properties of lithium iron oxide , LiFeO₂ , synthesized by ionic exchange reaction. *Solid State Ionics* **79**, 227–233 (1995).
257. Tabuchi, M. *et al.* Li⁺/Na⁺ exchange from alpha-NaFeO₂ using hydrothermal reaction. *Solid State Ionics* **90**, 129–132 (1996).
258. Hirayama, M., Tomita, H., Kubota, K. & Kanno, R. Structure and electrode reactions of layered rocksalt LiFeO₂ nanoparticles for lithium battery cathode. *J. Power Sources* **196**, 6809–6814 (2011).
259. Abdel-Ghany, a. E., Mauger, A., Groult, H., Zaghib, K. & Julien, C. M. Structural properties and electrochemistry of alpha-LiFeO₂. *J. Power Sources* **197**, 285–291 (2012).
260. Suresh, P., Shukla, a. K. & Munichandraiah, N. Synthesis and characterization of LiFeO₂ and LiFe_{0.9}Co_{0.1}O₂ as cathode materials for Li-ion cells. *J. Power Sources* **159**, 1395–1400 (2006).
261. Wang, X., Liu, G., Iwao, T., Okubo, M. & Yamada, A. Role of Ligand-to-Metal Charge Transfer in O3-Type NaFeO₂–NaNiO₂ Solid Solution for Enhanced Electrochemical Properties. *J. Phys. Chem. C* **118**, 2970–2976 (2014).
262. Chen, H., Freeman, C. L. & Harding, J. H. Charge disproportionation and Jahn-Teller distortion in LiNiO₂ and NaNiO₂: A density functional theory study. *Phys. Rev. B* **84**, 085108 (2011).
263. Ouyang, S.-D., Quan, Y.-M., Liu, D.-Y. & Zou, L.-J. A Comparative Investigation on the JT Effect in Triangular Compounds of NaMnO₂ , NaNiO₂ and NaTiO₂. *Chinese Phys. Lett.* **28**, 067102 (2011).
264. Dhariwal, M., Maitra, T. & Singh, I. Comparative study of NaTiO₂ and NaNiO₂ using first principle calculations. **824**, 824–825 (2013).
265. Braconnier, J. J., Delmas, C. & Hagenmuller, P. Etude par desintercalation electrochimique des systemes Na_xCrO₂ et Na_xNiO₂. *Mater. Res. Bull.* **17**, 993–1000 (1982).
266. Xu, J. *et al.* Identifying the Critical role of Li Substitution in P2-Na_x[Li_yNi_{1-y-z}Mn_{1-y-z}]O₂ (0<x,y,z<1) Intercalation Cathode Materials of High-Energy Na-ion Batteries. *Chem. Mater.* **26**, 1260–1269 (2014).
267. Li, X. *et al.* O3-type Na(Mn_{0.25}Fe_{0.25}Co_{0.25}Ni_{0.25})O₂: A quaternary layered cathode compound for rechargeable Na ion batteries. *Electrochem. Commun.* **49**, 51–54 (2014).
268. Stoyanova, R. *et al.* Stabilization of over-stoichiometric Mn⁴⁺ in layered Na_{2/3}MnO₂. *J. Solid State Chem.* **183**, 1372–1379 (2010).
269. Paulsen, J. M. Layered Li-Mn-Oxide with the O2 Structure: A Cathode Material for Li-Ion Cells Which Does Not Convert to Spinel. *J. Electrochem. Soc.* **146**, 3560 (1999).
270. Chou, F. C., Abel, E. T., Cho, J. H. & Lee, Y. S. Electrochemical De-intercalation, Oxygen Non-stoichiometry, and Crystal Growth of Na_xCoO₂-d. *J. Phys. Chem. Solids* **66**, 155–160 (2005).
271. Shu, G. *et al.* Searching for stable Na-ordered phases in single-crystal samples of γ-Na_xCoO₂. *Phys. Rev. B* **76**, 184115 (2007).
272. Berthelot, R., Carlier, D. & Delmas, C. Electrochemical investigation of the P2–Na_xCoO₂ phase diagram. *Nat. Mater.* **10**, 74–80 (2011).
273. Huang, F.-T. *et al.* X-ray and electron diffraction studies of superlattices and long-range three-dimensional Na ordering in gamma-Na_xCoO₂ (x = 0.71 and 0.84). *Phys. Rev. B* **79**, 014413 (2009).
274. Huang, Q. *et al.* Coupling between electronic and structural degrees of freedom in the triangular lattice conductor Na_xCoO₂. *Phys. Rev. B* **70**, 184110 (2004).
275. Armstrong, a. R. & Bruce, P. G. Synthesis of layered LiMnO₂ as an electrode for rechargeable lithium batteries. *Nature* **381**, 499–500 (1996).

276. Bordet-Le Guenne, L., Deniard, P., Biensan, P., Siret, C. & Brec, R. Structural study of two layered phases in the $\text{Na}_x\text{Mn}_y\text{O}_2$ system. Electrochemical behavior of their lithium substituted derivatives. *J. Mater. Chem.* **10**, 2201–2206 (2000).
277. Inada, R. *et al.* Properties of aerosol deposited NASICON-type $\text{Li}_{1.5}\text{Al}_{0.5}\text{Ge}_{1.5}(\text{PO}_4)_3$ solid electrolyte thin films. *Ceram. Int.* **5**, 0–32 (2015).
278. Lalère, F. *et al.* An all-solid state NASICON sodium battery operating at 200 °C. *J. Power Sources* **247**, 975–980 (2014).
279. Anantharamulu, N. *et al.* A wide-ranging review on Nasicon type materials. *J. Mater. Sci.* **46**, 2821–2837 (2011).
280. Masquelier, C. & Croguennec, L. Polyanionic (phosphates, silicates, sulfates) frameworks as electrode materials for rechargeable Li (or Na) batteries. *Chem. Rev.* **113**, 6552–6591 (2013).
281. Barpanda, P., Oyama, G., Nishimura, S.-I., Chung, S.-C. & Yamada, A. A 3.8-V earth-abundant sodium battery electrode. *Nat. Commun.* **5**, 4358 (2014).
282. Arai, H., Okada, S., Sakurai, Y. & Yamaki, J. Cathode performance and voltage estimation of metal trihalides. *J. Power Sources* **68**, 716–719 (1997).
283. Gocheva, I. D. *et al.* Mechanochemical synthesis of NaMF_3 (M = Fe, Mn, Ni) and their electrochemical properties as positive electrode materials for sodium batteries. *J. Power Sources* **187**, 247–252 (2009).
284. Nishijima, M. *et al.* Cathode properties of metal trifluorides in Li and Na secondary batteries*. *J. Power Sources* **190**, 558–562 (2009).
285. Badway, F., Pereira, N., Cosandey, F. & Amatucci, G. G. Carbon-Metal Fluoride Nanocomposites. *J. Electrochem. Soc.* **150**, A1209 (2003).
286. Barsoum, M. W. *Fundamentals of Ceramics*. (2003).
287. Komaba, S. *et al.* Electrochemical Insertion of Li and Na Ions into Nanocrystalline Fe_3O_4 and $\alpha\text{-Fe}_2\text{O}_3$ for Rechargeable Batteries. *J. Electrochem. Soc.* **157**, A60–A65 (2010).
288. Ling, C. & Mizuno, F. Phase stability of post-spinel compound AMn_2O_4 (A = Li, Na, or Mg) and its application as a rechargeable battery cathode. *Chem. Mater.* **25**, 3062–3071 (2013).
289. Yabuuchi, N., Yano, M., Kuze, S. & Komaba, S. Electrochemical behavior and structural change of spinel-type $\text{Li}[\text{Li}_x\text{Mn}_{2-x}]\text{O}_4$ ($x=0$ and 0.2) in sodium cells. *Electrochim. Acta* **82**, 296–301 (2012).
290. Berg, H. & Thomas, J. O. Neutron diffraction study of electrochemically delithiated LiMn_2O_4 spinel. *Solid State Ionics* **126**, 227–234 (1999).
291. Berg, H., Rundlöf, H. & Thomas, J. O. The LiMn_2O_4 to MnO_2 phase transition studied by in situ neutron diffraction. *Solid State Ionics* **144**, 65–69 (2001).
292. Molenda, J. *et al.* Electrochemical and chemical deintercalation of LiMn_2O_4 . *Solid State Ionics* **157**, 73–79 (2003).
293. Hunter, J. C. Preparation of a new crystal form of manganese dioxide: $\lambda\text{-MnO}_2$. *J. Solid State Chem.* **39**, 142–147 (1981).
294. Li, X., Xu, Y. & Wang, C. Suppression of Jahn-Teller distortion of spinel LiMn_2O_4 cathode. *J. Alloys Compd.* **479**, 310–313 (2009).
295. Mamiya, M. *et al.* Electrochemical properties of transition metal substituted calcium ferrite-type $\text{Li}_x(\text{M}_{0.1}\text{Mn}_{0.9})_2\text{O}_4$ (M = Ni, Ti). *J. Power Sources* **244**, 561–564 (2013).
296. Santhanam, R. & Rambabu, B. Research progress in high voltage spinel $\text{LiNi}_{0.5}\text{Mn}_{1.5}\text{O}_4$ material. *J. Power Sources* **195**, 5442–5451 (2010).

297. Ohzuku, T., Takeda, S. & Iwanaga, M. Solid-state redox potentials for $\text{Li}[\text{Me}_{1/2}\text{Mn}_{3/2}]\text{O}_4$ (Me: 3d-transition metal) having spinel-framework structures: a series of 5 volt materials for advanced lithium-ion batteries. *J. Power Sources* **81-82**, 90–94 (1999).
298. Amine, K., Tukamoto, H., Yasuda, H. & Fujita, Y. Preparation and electrochemical investigation of $\text{LiMn}_{2-x}\text{Me}_x\text{O}_4$ (Me: Ni, Fe, and $x = 0.5, 1$) cathode materials for secondary lithium batteries. *J. Power Sources* **504**, 604–608 (1997).
299. Hagh, N. M. & Amatucci, G. G. Effect of cation and anion doping on microstructure and electrochemical properties of the $\text{LiMn}_{1.5}\text{Ni}_{0.5}\text{O}_4$ spinel. *J. Power Sources* **256**, 457–469 (2014).
300. Kunduraci, M. & Amatucci, G. G. The effect of particle size and morphology on the rate capability of 4.7 V $\text{LiMn}_{1.5}\text{Ni}_{0.5}\text{O}_4$ spinel lithium-ion battery cathodes. *Electrochim. Acta* **53**, 4193–4199 (2008).
301. Patoux, S. *et al.* High voltage spinel oxides for Li-ion batteries: From the material research to the application. *J. Power Sources* **189**, 344–352 (2009).
302. Pasero, D., Reeves, N., Pralong, V. & West, a. R. Oxygen Nonstoichiometry and Phase Transitions in $\text{LiMn}_{1.5}\text{Ni}_{0.5}\text{O}_{4-\delta}$. *J. Electrochem. Soc.* **155**, A282 (2008).
303. Hagh, N. M. & Amatucci, G. G. A new solid-state process for synthesis of $\text{LiMn}_{1.5}\text{Ni}_{0.5}\text{O}_4$ spinel. *J. Power Sources* **195**, 5005–5012 (2010).
304. Yang, J., Zhang, X., Zhu, Z., Cheng, F. & Chen, J. Ordered spinel $\text{LiNi}_{0.5}\text{Mn}_{1.5}\text{O}_4$ nanorods for high-rate lithium-ion batteries. *J. Electroanal. Chem.* **688**, 113–117 (2013).
305. Alcántara, R., Jaraba, M., Lavela, P. & Tirado, J. L. X-ray diffraction and electrochemical impedance spectroscopy study of zinc coated $\text{LiNi}_{0.5}\text{Mn}_{1.5}\text{O}_4$ electrodes. *J. Electroanal. Chem.* **566**, 187–192 (2004).
306. Kunduraci, M. & Amatucci, G. G. Effect of oxygen non-stoichiometry and temperature on cation ordering in $\text{LiMn}_{2-x}\text{Ni}_x\text{O}_4$ ($0.50 \geq x \geq 0.36$) spinels. *J. Power Sources* **165**, 359–367 (2007).
307. Guo, H. *et al.* Effects of sodium substitution on properties of LiMn_2O_4 cathode for lithium ion batteries. *Trans. Nonferrous Met. Soc. China* **20**, 1043–1048 (2010).
308. Yamada, A. Lattice Instability in $\text{Li}(\text{Li}_x\text{Mn}_{2-x})\text{O}_4$. *J. Solid State Chem.* **122**, 160–165 (1996).
309. Cho, J. & Thackeray, M. M. Structural Changes of LiMn_2O_4 Spinel Electrodes during Electrochemical Cycling. *J. Electrochem. Soc.* **146**, 3577–3581 (1999).
310. Patoux, S. *et al.* High voltage nickel manganese spinel oxides for Li-ion batteries. *Electrochim. Acta* **53**, 4137–4145 (2008).
311. Dedryvere, R. *et al.* Electrode/Electrolyte Interface Reactivity in High-Voltage Spinel $\text{LiMn}_{1.6}\text{Ni}_{0.4}\text{O}_4/\text{Li}_4\text{Ti}_5\text{O}_{12}$ Lithium-ion Battery. *J. Phys. Chem. C* **114**, 10999–11008 (2010).
312. Zhong, Q., Bonakdarpour, A., Zhang, M., Gao, Y. & Dahn, J. R. Synthesis and Electrochemistry of $\text{LiNi}_x\text{Mn}_{2-x}\text{O}_4$. *J. Electrochem. Soc.* **144**, 205–213 (1997).
313. Kim, J.-H., Myung, S.-T., Yoon, C. S., Kang, S. G. & Sun, Y.-K. Comparative Study of $\text{LiNi}_{0.5}\text{Mn}_{1.5}\text{O}_4$ -d and $\text{LiNi}_{0.5}\text{Mn}_{1.5}\text{O}_4$ Cathodes Having Two Crystallographic Structures: $\text{Fd}3m$ and P4332 . *Chem. Mater.* **16**, 906–914 (2004).
314. Huot, B. J. & Balema, V. Mechanochemical Effect of Severe Plastic Deformations : Metal Alloys , Hydrides and Molecular Solids. *Mater. Matters* **5**, 1–9 (2011).
315. Pechini, M. Method of Preparing Lead and Alkaline Earth Titanates and. *U.S. Patent 3,330.697* (1967).
316. Vivekanandhan, S., Venkateswarlu, M. & Satyanarayana, N. Effect of different ethylene glycol

- precursors on the Pechini process for the synthesis of nano-crystalline $\text{LiNi}_{0.5}\text{Co}_{0.5}\text{VO}_4$ powders. *Mater. Chem. Phys.* **91**, 54–59 (2005).
317. Jafta, C. J., Mathe, M. K., Manyala, N., Roos, W. D. & Ozoemena, K. I. Microwave-assisted synthesis of high-voltage nanostructured $\text{LiMn}_{1.5}\text{Ni}_{0.5}\text{O}_4$ spinel: Tuning the Mn^{3+} content and electrochemical performance. *ACS Appl. Mater. Interfaces* **5**, 7592–7598 (2013).
 318. Meza, E., Ortiz, J., Ruíz-León, D., Marco, J. F. & Gautier, J. L. Lithium-nickel cobalt oxides with spinel structure prepared at low temperature. XRD, XPS, and EIS measurements. *Mater. Lett.* **70**, 189–192 (2012).
 319. Wu, S. H. & Su, H. J. Electrochemical characteristics of partially cobalt-substituted $\text{LiMn}_{2-y}\text{Co}_y\text{O}_4$ spinels synthesized by Pechini process. *Mater. Chem. Phys.* **78**, 189–195 (2003).
 320. Fu, F. *et al.* A hierarchical micro/nanostructured $0.5\text{Li}_2\text{MnO}_3 \cdot 0.5\text{LiMn}_{0.4}\text{Ni}_{0.3}\text{Co}_{0.3}\text{O}_2$ material synthesized by solvothermal route as high rate cathode of lithium ion battery. *Electrochem. commun.* **44**, 54–58 (2014).
 321. Kunduraci, M. & Amatucci, G. G. Synthesis and Characterization of Nanostructured 4.7 V $\text{Li}_x\text{Mn}_{1.5}\text{Ni}_{0.5}\text{O}_4$ Spinel for High-Power Lithium-Ion Batteries. *J. Electrochem. Soc.* **153**, A1345 (2006).
 322. Dinnebier, R. E. & Billinge, S. J. L. *Powder Diffraction Theory and Practice*. (2008).
 323. Will, G. *Powder Diffraction: The Rietveld Method and the Two-Stage Method*. (Springer, 2006).
 324. Cheetham, A. K., Fender, B. E. F. & Cooper, M. J. Defect structure of calcium fluoride containing excess anions II. Diffuse scattering. *J. Phys. C Solid State Phys.* **4**, 3107–3121 (1971).
 325. Von Dreele, R. B. in *Powder Diffraction: Theory and Practice* 266–279
 326. Ohzuku, T., Ueda, A. & Yamamoto, N. Zero-Strain Insertion Material of $\text{Li}[\text{Li}_{1/3}\text{Ti}_{5/3}]\text{O}_4$ for Rechargeable Lithium Cells. *J. Electrochem. Soc.* **142**, 1431 (1995).
 327. Asahina, H., Kurotaki, M., Yonei, a., Yamaguchi, S. & Mori, S. Real-time X-ray diffraction measurement of carbon structure during lithium-ion intercalation. *J. Power Sources* **68**, 249–252 (1997).
 328. Märkle, W., Colin, J. F., Goers, D., Spahr, M. E. & Novák, P. In situ X-ray diffraction study of different graphites in a propylene carbonate based electrolyte at very positive potentials. *Electrochim. Acta* **55**, 4964–4969 (2010).
 329. Marco, R. De & Veder, J.-P. In situ structural characterization of electrochemical systems using synchrotron-radiation techniques. *TrAC Trends Anal. Chem.* **29**, 528–537 (2010).
 330. Balasubramanian, M., Sun, X., Yang, X. & McBreen, J. In situ X-ray diffraction and X-ray absorption studies of high-rate lithium-ion batteries. *J. Power Sources* **92**, 1–8 (2001).
 331. Chung, K. Y. *et al.* In situ X-ray diffraction studies on the mechanism of capacity retention improvement by coating at the surface of LiCoO_2 . *J. Power Sources* **174**, 619–623 (2007).
 332. Chen, Y.-C. *et al.* Structure studies on $\text{LiMn}_{0.25}\text{Fe}_{0.75}\text{PO}_4$ by in-situ synchrotron X-ray diffraction analysis. *J. Power Sources* **189**, 790–793 (2009).
 333. Nam, K.-W. *et al.* In situ X-ray diffraction studies of mixed LiMn_2O_4 – $\text{LiNi}_{1/3}\text{Co}_{1/3}\text{Mn}_{1/3}\text{O}_2$ composite cathode in Li-ion cells during charge–discharge cycling. *J. Power Sources* **192**, 652–659 (2009).
 334. Nam, K. W., Yoon, W. S. & Yang, X. Q. Structural changes and thermal stability of charged $\text{LiNi}_{1/3}\text{Co}_{1/3}\text{Mn}_{1/3}\text{O}_2$ cathode material for Li-ion batteries studied by time-resolved XRD. *J. Power Sources* **189**, 515–518 (2009).
 335. Yoon, W. S. *et al.* Structural study of the coating effect on the thermal stability of charged MgO -

- coated LiNi_{0.8}Co_{0.2}O₂ cathodes investigated by in situ XRD. *J. Power Sources* **217**, 128–134 (2012).
336. Brant, W. R., Schmid, S., Du, G., Gu, Q. & Sharma, N. A simple electrochemical cell for in-situ fundamental structural analysis using synchrotron X-ray powder diffraction. *J. Power Sources* **244**, 109–114 (2013).
 337. Leriche, J. B. *et al.* An Electrochemical Cell for Operando Study of Lithium Batteries Using Synchrotron Radiation. *J. Electrochem. Soc.* **157**, A606 (2010).
 338. He, H., Huang, C., Luo, C. W., Liu, J. J. & Chao, Z. S. Dynamic study of Li intercalation into graphite by in situ high energy synchrotron XRD. *Electrochim. Acta* **92**, 148–152 (2013).
 339. Bai, J., Hong, J., Chen, H., Graetz, J. & Wang, F. Solvothermal Synthesis of LiMn_{1-x}Fe_xPO₄ Cathode Materials: A Study of Reaction Mechanisms by Time-Resolved in Situ Synchrotron X-ray Diffraction. *J. Phys. Chem. C* 150123095009006 (2015). doi:10.1021/jp508600u
 340. Doeff, M. M. *et al.* Characterization of electrode materials for lithium ion and sodium ion batteries using synchrotron radiation techniques. *J. Vis. Exp.* e50594 (2013). doi:10.3791/50594
 341. Borkiewicz, O. J., Wiaderek, K. M., Chupas, P. J. & Chapman, K. W. Best Practices for Operando Battery Experiments: Influences of X-ray Experiment Design on Observed Electrochemical Reactivity. *J. Phys. Chem. Lett.* **6**, 2081–2085 (2015).
 342. Wilson, B. E., Smyrl, W. H. & Stein, A. Design of a Low-Cost Electrochemical Cell for In Situ XRD Analysis of Electrode Materials. *J. Electrochem. Soc.* **161**, A700–A703 (2014).
 343. Hartung, S., Bucher, N., Bucher, R. & Srinivasan, M. Electrochemical cell for in operando X-ray diffraction measurements on a conventional X-ray diffractometer. *Rev. Sci. Instrum.* **86**, 086102 (2015).
 344. Morcrette, M. *et al.* In situ X-ray diffraction techniques as a powerful tool to study battery electrode materials. *Electrochim. Acta* **47**, 3137–3149 (2002).
 345. Shen, Y., Pedersen, E. E., Christensen, M. & Iversen, B. B. An electrochemical cell for in operando studies of lithium/sodium batteries using a conventional x-ray powder diffractometer. *Rev. Sci. Instrum.* **85**, 104103 (2014).
 346. Wachtman, J. B. *Characterization of Materials*. (1993).
 347. Burba, C. M. & Frech, R. In situ transmission FTIR spectroelectrochemistry: A new technique for studying lithium batteries. *Electrochim. Acta* **52**, 780–785 (2006).
 348. Ma, R. *et al.* Ex situ FTIR spectroscopy study of LiVPO₄F as cathode material for lithium-ion batteries. *Ionics (Kiel)*. 725–730 (2012). doi:10.1007/s11581-012-0807-8
 349. Li, J. T., Chen, Q. S. & Sun, S. G. In situ microscope FTIR studies of methanol adsorption and oxidation on an individually addressable array of nanostructured Pt microelectrodes. *Electrochim. Acta* **52**, 5725–5732 (2007).
 350. Li, J.-T. *et al.* In situ microscope FTIR spectroscopic studies of interfacial reactions of Sn–Co alloy film anode of lithium ion battery. *J. Electroanal. Chem.* **649**, 171–176 (2010).
 351. Berkes, B. B., Jozwiuk, A., Sommer, H., Brezesinski, T. & Janek, J. Simultaneous acquisition of differential electrochemical mass spectrometry and infrared spectroscopy data for in situ characterization of gas evolution reactions in lithium-ion batteries. *Electrochem. commun.* **60**, 64–69 (2015).
 352. Meazah, A. *et al.* Comparative Study on the Solid Electrolyte Interface Formation by the Reduction of Alkyl Carbonates in Lithium ion Battery. *Electrochim. Acta* **136**, 274–285 (2014).
 353. Domi, Y. *et al.* In situ AFM study of surface film formation on the edge plane of HOPG for lithium-ion batteries. *J. Phys. Chem. C* **115**, 25484–25489 (2011).

354. Michalska, M. *et al.* Structural and morphological studies of manganese-based cathode materials for lithium ion batteries. *J. Alloys Compd.* **632**, 256–262 (2015).
355. Brunauer, S., Emmett, P. & Teller, E. Adsorption of Gases in Multimolecular Layers. *J. Am. Chem. Soc.* **60**, 309–319 (1938).
356. Sing, K. S. W. Adsorption methods for the characterization of porous materials. *Adv. Colloid Interface Sci.* **76-77**, 3–11 (1998).
357. Hakuman, M. & Naono, H. A New Method of Calculating Pore Size Distribution: Analysis of Adsorption Isotherms of N(2) and CCl(4) for a Series of MCM-41 Mesoporous Silicas. *J. Colloid Interface Sci.* **241**, 127–141 (2001).
358. Naono, H., Hakuman, M. & Nakai, K. Determination of Pore Size Distribution of Mesoporous and Macroporous Silicas by Means of Benzene-Desorption Isotherms. *Journal of Colloid and Interface Science* **165**, 532–535 (1994).
359. Takai, S. *et al.* Tracer diffusion coefficients of lithium ion in LiMn₂O₄ measured by neutron radiography. *Solid State Ionics* **256**, 93–96 (2014).
360. James, S. D. No Title. *Electrochim. Acta* **21**, 157 (1976).
361. L'vov, A. L., Gnilomedov, A. A., Selemenov, A. P. & Protasov, E. N. No Title. *Elektrokhimiya* **11**, 1322 (1975).
362. Melendres, C. A. No Title. *J. Electrochem. Soc.* **124**, 650 (1977).
363. Wagner, C. No Title. *J. Chem. Phys.* **21**, 1819 (1953).
364. Wen, C. J. Thermodynamic and Mass Transport Properties of 'LiAl'. *J. Electrochem. Soc.* **126**, 2258 (1979).
365. Weppner, W. & Huggins, R. A. No Title. *J. Solid State Chem.* **22**, 297 (1977).
366. Weppner, W. & Huggins, R. A. No Title. *J. Electrochem. Soc.* **124**, 1569 (1977).
367. Li, J., Xiao, X., Yang, F., Verbrugge, M. W. & Cheng, Y. T. Potentiostatic intermittent titration technique for electrodes governed by diffusion and interfacial reaction. *J. Phys. Chem. C* **116**, 1472–1478 (2012).
368. Funabiki, A. Stage Transformation of Lithium-Graphite Intercalation Compounds Caused by Electrochemical Lithium Intercalation. *J. Electrochem. Soc.* **146**, 2443 (1999).
369. Levi, M. D. & Aurbach, D. Frumkin intercalation isotherm - a tool for the description of lithium insertion into host materials: a review. *Electrochim. Acta* **45**, 167–185 (1999).
370. Zhu, Y. & Wang, C. Galvanostatic intermittent titration technique for phase-transformation electrodes. *J. Phys. Chem. C* **114**, 2830–2841 (2010).
371. Gmitter, A. J., Gural, J. & Amatucci, G. G. Electrolyte development for improved cycling performance of bismuth fluoride nanocomposite positive electrodes. *J. Power Sources* **217**, 21–28 (2012).
372. Boisse, B. M. De, Carlier, D., Guignard, M., Bourgeois, L. & Delmas, C. P2-NaxMn_{1/2}Fe_{1/2}O₂ phase used as positive electrode in Na batteries: Structural changes induced by the electrochemical (De)intercalation process. *Inorg. Chem.* **53**, 11197–11205 (2014).
373. Tong, W., Yoon, W. S. & Amatucci, G. G. Electrochemically active silver molybdenum oxyfluoride perovskite: Synthesis and in situ electrochemical characterization. *J. Power Sources* **195**, 6831–6838 (2010).
374. Hwang, B. J., Wu, Y. W., Venkateswarlu, M., Cheng, M. Y. & Santhanam, R. Influence of synthesis conditions on electrochemical properties of high-voltage Li_{1.02}Ni_{0.5}Mn_{1.5}O₄ spinel

- cathode material. *J. Power Sources* **193**, 828–833 (2009).
375. Shannon, R. D. Revised Effective Ionic Radii and Systematic Studies of Interatomic Distances in Halides and Chalcogenides. *Acta Cryst.* **A32**, 751–767 (1976).
376. Gryffroy, D. & Vandenberghe, R. E. Cation distribution, cluster structure and ionic ordering of the spinel series $\text{LiNi}_{0.5}\text{Mn}_{1.5-x}\text{Ti}_x\text{O}_4$ and $\text{LiNi}_{0.5-y}\text{Mg}_y\text{Mn}_{1.5}\text{O}_4$. *J. Phys. Chem. Solids* **53**, 777–784 (1992).
377. Kim, J.-H., Myung, S.-T., Yoon, C. S., Oh, I.-H. & Sun, Y.-K. Effect of Ti Substitution for Mn on the Structure of $\text{LiNi}_{0.5}\text{Mn}_{1.5-x}\text{Ti}_x\text{O}_4$ and Their Electrochemical Properties as Lithium Insertion Material. *J. Electrochem. Soc.* **151**, A1911 (2004).